Université catholique de Louvain
Ecole polytechnique de Louvain
Institut de Mécanique, Matériaux et Génie Civil
(iMMC)

Experimental studies on HCCI combustion of Biomass Syngas towards Tar Tolerant operation

Subir S. Bhaduri

Composition du jury:
Prof. G. Winckelmans (UCL), President
Prof. H. Jeanmart (UCL), Supervisor
Prof. F. Contino (VUB, Belgium)
Prof. Y. Bartosiewicz (UCL)
Prof. B. Johansson (LTH, Sweden)
Prof. S. Verhelst (UGhent, Belgium)

Thesis submitted in fulfillment of the requirements for Docteur en Sciences de l'ingénieur.
Louvain-la-Neuve, September 2015.

Copy Left 2015
Subir S. Bhaduri

Acknowledgments

I take this opportunity to heartily thank my supervisors/mentors/guides Prof. Hérve Jeanmart and Prof. Francesco Contino, who encouraged me to think about quality and clarity, tolerated me and my weired ways, and waited patiently while I tried to figure out stuff. Without their guidance and appropriately timed *kicks in the arse*, I would not have completed anything in any quality, whatsoever. The novel concept discussed in this thesis is their brain child, and its apparent simplicity but underlying complexity is what amazed me and made it so interesting. I thank them once again for coming up with this beautiful and appropriate concept.

To Mr. Ernst Breuer, for inspiring the engine sides of me. To the Service Public de Wallonie (SPW) for their generous funding which made it all possible, and especially to Dr. Gilles Tihon of SPW for the great support.

I thank the jury members who patiently went through the thesis draft and suggested many important points/comments/mistakes through which I learned a lot about the subject.

I must thank our great technical staff Yan L. (Lily), Frank H., Julien V., Françoise V., and Nicolas C., for accommodating so many of my unplanned and untimely requests without any complaints. They have happily given me the unquantifiable support before, during and after the experiments. Great technical help and friendship was offered by Dr. Jean-Marie S. during this period.

And a big toast to my dear friends at TFL (in no order): Isabelle H., Gäel L., Benjamin B., Ehsan T., Haddy, Lucio D., Stéphane B., Véronique D., Pierre S., Yves M., Panagiotis A., Catherine D., Nicolas P, Nicolas B. and everyone else. To my friends outside of TFL: Marie-anne N., Amit K.C. and others. You all made my life and stay here very pleasant and beautiful. From general problems to issues related to our works and life in general, you have been there and shared with me immensely, for which I am very grateful.

I must thank my friend, mentor and father-like figure, Prof. Michel Vandyke, for inspiring me to be creative and improve the art of sharing life with others. Our common passions for making things with our own hands and our discussions about the Stirling engine, mechanical clocks and other innovative machines with the ample sprinkling of world politics and society, have all played key roles during this thesis, keeping my spirits up and active.

I came this far because of my family, which inspires me through its diversity and a commonly shared understanding that struggle is essential and beautiful. Without their love and acceptance of who I am, life would have been very difficult. Especially to Ma, for keeping me on the ground and inspiring me to aspire for the better and Pa, for inspiring the creativity in me in unknown ways. To Suchita, Boudi & Dada and my little friend Arindam, for helping me see that passions come in so many colors.

All this could not have been meaningful without the acceptance, understanding and support of my long suffering friend and companion, Ila. You motivated and encouraged me to plan, open up, appreciate quality and to include more of my heart's viewpoints into my life. And you stand by me, even after all the great personal sacrifices. Also, I deeply thank my extended family from Ila's side, for the understanding and support given to me for all the past many years.

I owe my special thanks to the unknown people behind the great open source tools I have used : LaTeX, Python and OpenOffice/LibreOffice. And to the selfless people on Stack Exchange and similar websites + blogs. You inspire me to be, to share the best possible, and have fun doing that :)

To the people of my host country for about 4 years, Belgium, for accepting me as one of their own. I have never seen a more peaceful and accommodating people, and it will remain a lifetime's experience. I owe to you guys.

Abstract

Biomass syngas needs to be cooled before being usable in a conventional spark-ignition engine, in order to avoid knock. The tar impurities of raw biomass syngas condense due to this cooling process, which leads to the clogging and subsequent damage of critical process parts. Thus, in addition to cooling, the syngas needs to be purified of the tars, which adds to the cost and complexity of the gasification power plant. A novel technique is being investigated where the syngas temperature is kept above the tar dew point (about 250°C) throughout the process, and thus, tar condensation and its related problems can potentially be avoided. A Homogeneous Charge Compression Ignition (HCCI) engine is suitable for such an application. The objective of this thesis is to experimentally study HCCI combustion with biomass syngas at intake temperatures above the tar dew point.

Chapter 1, reviews the broad context of gasification and the associated tar impurities, where it argues that the SI engine, due to its limited intake temperature flexibility, significantly contributes in the making of tars into problematic compounds. The novel method of using the HCCI engine at intake temperatures above the tar dew point is introduced, along with listing the multiple challenges foreseen with such an approach. Of these challenges, two are identified which forms the main experimental works described in this thesis.

The test bench, which includes a 435cc single-cylinder air cooled engine, and the associated instruments are discussed in Chapter 2. Chapter 3 discusses the various post processing methods used during this work which computes the rate of heat release from the raw in-cylinder pressure data, along with a host of other parameters. Thereafter, the main experimental works are described in Chapters 4, 5 and 6.

In a real-world scenario, the syngas composition varies with time. To understand the HCCI combustion in response to such variations, studies with artificial syngas compositions were carried out, as described in Chapter 4. In these experiments, the time component was omitted and the focus was on determining the impacts of various possible syngas compositions as well as operating conditions on the HCCI combustion. It was found that increasing H_2 content of syngas advanced the combustion which lead to the undesirable pressure ringing (equivalent to *knock* in SI engines). At an intake temperature of 250°C and intake pressure of 1.2 bar, a maximum IMEP of 2.8 bar and an Indicated Efficiency (IE) of 35% could be attained with dry and pure syngas compositions. Since the raw syngas would also contain water and tars, the effects of these components were studied. Syngas moisture dampened the HCCI combustion, thus improving the IMEP potential. Two representative tar compounds (naphthalene and toluene) were used and it was observed that tars, due to their high heating values and higher heat capacities, had positive effects on HCCI combustion. Additionally, the effects of intake pressure and temperature

were also studied with the conclusion that high intake pressures and low intake temperatures improved the engine performance.

Since the HCCI engine lacks a direct control method, studies were carried out to explore the use of Exhaust Gas Recirculation (EGR) as a control method, as discussed in Chapter 5. EGR was found to successfully delay the combustion initiation and thus, in combination with the equivalence ratio which advanced the combustion, an effective HCCI control method for this context was demonstrated. An improvement in the maximum IMEP from 2.8 bar at EGR=0, to 3.3 bar at EGR=25% was achieved, a significant gain of about 25%.

Studies with real syngas were carried out to investigate the effect of time variations in the syngas composition, as discussed in Chapter 6. Syngas from a two-stage downdraft gasifier was used in its cooled and purified form so as to reduce the complexity of the process and form a basis for future hot syngas experiments. Two experiments were carried out with time durations of 3 hours and 24 hours. For the 3 hours experiments, the gasifier was in a transient stage (warming up) and thus supplied syngas with a lower heating value. Decent HCCI combustion stability was observed which is interesting in the light of the highly sensitive nature of the HCCI combustion. For the 24 hours test, the gasifier was operating at its designed conditions, resulting in a higher heating value syngas. During the 24 hours test, the engine combustion was not stable and wide variations were observed. Additionally, high amounts of NO_x emissions were recorded. The reasons for both the cyclic instabilities and high NO_x could not be confirmed, however, some hypotheses are proposed.

Finally, Chapter 7 concludes the findings of this thesis and reflects on the advantages and limitations of the concept as well as on the limitations of this thesis. Planned works following this thesis in the near and distant future are listed.

Major publications/Conferences

- Subir Bhaduri, Francesco Contino, Hervé Jeanmart, and Ernst Breuer. The effects of biomass syngas composition, moisture, tar loading and operating conditions on the combustion of a tar-tolerant HCCI (Homogeneous Charge Compression Ignition) engine. *Energy*, 87(0):289–302, 2015
- Subir Bhaduri, Hervé Jeanmart, Ernst Breuer, and Francesco Contino. Studies of EGR in Biomass Syngas fueled tar tolerant HCCI engines. In *Ninth Mediterranean Combustion Symposium*, Rhodes, Greece, 2015

Contents

1 Introduction **3**
- 1.1 Motivation - Gasification and the tar problem . . . 4
  - 1.1.1 The Gasification process . . . 5
  - 1.1.2 Syngas impurities . . . 8
  - 1.1.3 Gasification Engineering . . . 14
  - 1.1.4 Syngas and the IC engine . . . 20
  - 1.1.5 Summary . . . 26
- 1.2 The proposed solution . . . 27
  - 1.2.1 The HCCI engine . . . 27
  - 1.2.2 Syngas use in HCCI engines . . . 32
  - 1.2.3 Foreseeable challenges . . . 37
  - 1.2.4 Thesis outline . . . 38

2 Experimental Setup **41**
- 2.1 The test bench hardware . . . 41
  - 2.1.1 Determination of critical parameters . . . 42
  - 2.1.2 The experimental Test Bench . . . 42
- 2.2 The instrumentation . . . 49
  - 2.2.1 Slow instruments and controls . . . 50
  - 2.2.2 Fast instruments . . . 52
  - 2.2.3 The NI hardware . . . 53

3 Post-Processing of experimental data **57**
- 3.1 General formulations . . . 57
- 3.2 Computing the Heat Release . . . 63
  - 3.2.1 Determination of the ratio of specific heats . . . 65
  - 3.2.2 Determining the heat loss term . . . 68
  - 3.2.3 Determining the bulk gas temperature or trapped mass 72
  - 3.2.4 Summary of HR computation . . . 80
- 3.3 Calibration of Experimental data . . . 82
  - 3.3.1 Determination of the effective compression ratio . . . 83
  - 3.3.2 Determination of the TDC offset . . . 86

3.3.3 Determination of pegging . . . 90
3.3.4 Pressure filtering . . . 93
3.4 Uncertainty Analysis . . . 97

4 Influences of syngas compositions and operating conditions 101
4.1 Formulation of the BCE . . . 102
4.2 Experimental Results . . . 103
4.2.1 Variations in the dry and pure syngas composition . . . 104
4.2.2 Effect of moisture in syngas . . . 113
4.2.3 Effect of Tars . . . 115
4.2.4 Effect of variations in p_{in}, T_{in} . . . 116
4.3 Conclusion . . . 121

5 Exhaust Gas Recirculation for control of HCCI combustion 123
5.1 A brief overview of the EGR technique . . . 124
5.2 Formulation . . . 126
5.3 The diluting effects of EGR . . . 128
5.4 Experimental Details . . . 131
5.5 Experimental results . . . 133
5.5.1 Thermal effects of EGR . . . 133
5.5.2 Global trends due to EGR . . . 137
5.6 Conclusion . . . 142

6 Experiments with real, cooled and purified syngas 145
6.1 Introduction . . . 145
6.2 The two-stage downdraft gasifier . . . 146
6.3 Test Bench and experimental changes . . . 146
6.4 Experiments and results . . . 150
6.4.1 The 3h test . . . 150
6.4.2 The 24h test . . . 160
6.5 Conclusion and analysis . . . 171

7 Conclusions and future directions 173
7.1 Merits and Demerits of the Concept . . . 175
7.2 Limitations of this thesis . . . 176
7.3 Future work . . . 177

Bibliography 178

A Schematic of LabVIEW codes 193
A.1 RTOS code . . . 193
A.2 FPGA codes . . . 195

B Uncertainty formulations **199**
B.1 Uncertainties from the MFC and EGA 200
B.2 Uncertainties in the Balanced Chemical Equation 200
B.3 Uncertainty in the pressure data 200
B.4 Volume 202
B.5 Indicated Efficiency IE 204
B.6 IMEP 204
B.7 Cumulative gross heat release, Q_{net} 205
B.8 CA50 206

C BCE formulation, calibration of pumps and uncertainties for Chapter 4 **209**
C.1 General BCE formulation 209
C.2 Calibration of Syringe and Peristaltic Pumps 212
C.2.1 Syringe Pump 212
C.2.2 Peristaltic Pump 215
C.3 Uncertainties in the BCE 217
C.3.1 Heat input per cycle 218
C.3.2 LHV of air+fuel mixture 218
C.3.3 Combustion Efficiency 219

D BCE formulation for Chapter 5 **221**
D.1 Formulation of EGR : BCE assuming complete combustion . . 221
D.1.1 Specifying the inputs 222
D.1.2 Decoding data from flow measurements 223
D.1.3 Formulation of the BCE with incomplete combustion . . 224
D.2 Uncertainties in the BCE 226

Nomenclature

γ	Ratio of specific heat capacities
λ_g	Air to biomass gasification equivalence ratio
$\overline{R}$	Universal Ideal gas constant = 8.314 $J/mol/K$
ϕ	Fuel to air equivalence ratio
ϕ_{BCE}	Fuel to air equivalence ratio derived from the Balanced Chemical Equation
ϕ_{FIN}	Fuel to air equivalence ratio for fresh intake mixture, before being mixed with EGR gases
M_i	Molecular mass of species i
m_i	Mass of species i
n_i	Number of moles of species i
R_c	Compression Ratio
x_i	Molar concentration of species i
BCE	Balanced Chemical Equation
BDC	Bottom Dead Center
CA10	Crank angle where 10% of fuel in a cycle has been burnt
CA50	Crank angle where 50% of fuel in a cycle has been burnt
CA90	Crank angle where 90% of fuel in a cycle has been burnt
CAD	Crank Angle Degrees
CE	Combustion Efficiency
CGE	Cold Gas Efficiencies
CHP	Combined Heat and Power

CI Compression Ignition engine

DD Downdraft gasifier

EGA Exhaust Gas Analyzer

EGR Exhaust Gas Recirculation

EVC Exhaust Valve Close timing

EVO Exhaust Valve Open timing

GGA Gasifier Gas Analyzer

H_2/CO Hydrogen to carbon monoxide molar or volumetric ratio

H_2/CO_2 Hydrogen to carbon dioxide molar or volumetric ratio

HCCI Homogeneous Charge Combustion Ignition

ICE Internal Combustion Engine

IE Indicated Efficiency

IMEP Indicated Mean Effective Pressure

IVC Intake Valve Close timing

IVO Intake Valve Open timing

LHV Lower Heating Value

MBT Maximum Brake Torque

p_{in} Intake pressure

PAH Polyaromatic Hydrocarbons

SI Spark Ignition

T_{in} Intake temperature

TDC Top Dead Center

UD Updraft gasifier

Chapter 1

Introduction

Biomass has been the mainstay energy source throughout the human history with a renewal of interest in recent years due to the impending fossil energy crisis. There are immense advantages of biomass derived energy, such as its widespread availability, renewable and carbon neutral potential, as well as the relative ease and versatility of its conversion technologies. However, the huge energy demand of the current population and its increasing living standards (about 550 EJ/year) cannot be met through biomass alone (as of 2011, about 320 EJ/year including all agriculture and commercial forestry) [1]. Thus, adhering to the sustainable limits of biomass exploitation for energy is of extreme importance [2]. Apart from the sustainability concerns, in terms of the bioenergy technologies, the various properties of biomass such as its low energy density, high water content, heterogeneity, and others, pose significant challenges [3].

Biomass can be converted into usable forms of energy through biological or thermo-chemical pathways, for example the reader may refer to the technical and economical review by Gerssen-Gondelach et al. [4]. In terms of thermochemical pathways for small scale systems, the low electrical efficiencies, the comparatively higher costs of direct combustion technologies or the complications in the use of pyrolysis technologies, make the alternative route of energy production through biomass gasification very promising [5, 6, 7, 8]. Indeed, studies on the biomass-gasification-energy routes with various end-use technologies have been evaluated in the range of 0.1-300 MW of theoretical biomass heat input by many authors [6, 7, 8]. The consensus points to the combination of biomass gasification with the reciprocating Internal Combustion Engine (ICE) as being the most appropriate in terms of its economy and efficiency, especially for small scale applications below 1 MW of electrical capacity. However, as pointed out by Dornburg and Faaij [7] and Skorek-Osikowska et al. [9] in studies carried out within the European context, factors such as government subsidies and the relatively high cost of biomass feedstock, play critical roles

in the competitiveness of this technology.

The domain of this thesis pertains to small scale gasification of biomass (less than 1 MW thermal input) for the purpose of Combined Heat and Power (CHP) production achieved through the use of ICEs. A major challenge in this technological pathway arises from the impurities contained in the *syngas* produced from biomass gasification, especially the *tar* impurities. The destruction or filtering of tars is a long standing challenge and requires elaborate efforts which impede the commercial acceptance of this technology. In terms of solutions to the tar problem, three approaches can be undertaken: 1) Cutting the tar production within a gasifier, classified as *primary methods* of dealing with tars 2) Filtering/destroying the tars downstream of a gasifier, classified as *secondary methods* and 3) Utilizing tar tolerant end-use devices. While the first two options form the core subject of research in biomass gasification, the third option remains highly unexplored and forms the approach taken in this thesis work. The broad objective of this thesis is to present experimental investigations related to the scarcely explored combination of biomass gasification and a *Homogeneous Charge Combustion Ignition* (HCCI) engine, with the novel difference of operating the HCCI engine with high temperature impure syngas-air mixtures, in order to bypass the problems posed by the tars. The success of this technique can potentially reduce or eliminate the need to bother about tar production (primary methods) or tar filtration (secondary methods).

This chapter is divided into two broad sections. Section 1.1 presents the contextual motivation for this thesis, where the process of biomass gasification, the types and nature of the impurities and the features of the conventional Spark Ignition (SI) engine are reviewed. Section 1.2 starts by discussing the novel combination of using an HCCI engine fueled with high temperature syngas, as a means to avoid the tar related issues. The essential works related to this approach are reviewed in Section 1.2.2, followed by a discussion on the main foreseen challenges. This chapter concludes in Section 1.2.4 where the challenges explored within this thesis are presented, in the form of a thesis outline.

1.1 Motivation - Gasification and the tar problem

Biomass gasification is an old process dating back to the 19th century and its interesting history can be followed in [10]. The use of biomass gasification to fuel IC engines became popular in the last few decades. However, the issue of the tar impurities, as of date, plagues the process of biomass-gasification to electricity production through the ICE pathway. The following account presents a brief outline of the various aspects within the conventional chain of syngas production through biomass gasification, its intermediate conditioning

and the its eventual use in a conventional SI engine.

Section 1.1.1 presents the outline of the fundamental gasification process. This is followed by a brief overview of the syngas impurities in Section 1.1.2, which are of much interest in this thesis. Section 1.1.3 describes the gasification engineering which begins with the fundamental gasifier designs relevant to the context of small scale gasification, along with a brief overview of the existing ways to address the challenges due to the various impurities. Thereafter, Section 1.1.4 describes the conventional end-use technology of the SI engine used within the context, including a discussion on the features of syngas as an IC engine fuel. And finally, Section 1.1.5 summarizes the main observations of this section which clears the ground for the introduction of the novel solution in the second part of this chapter.

1.1.1 The Gasification process

The main objective of biomass gasification is to transform the solid biomass into non-condensable gases such as CO and H_2 with maximum conversion efficiency. Typically, gasification is a four step process consisting of endothermic drying, pyrolysis and gasification stages on one hand and exothermic oxidation on the other hand, as visualized in Figure 1.1. The overview presented here follows mostly from the works of Basu [5] and Reed et al. [10].

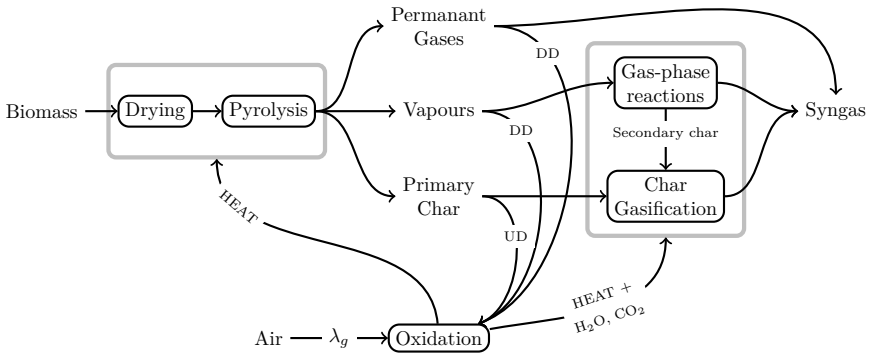


Figure 1.1: *Schematic of a typical air blown biomass gasification process. The drying and pyrolysis of biomass first take place, followed by partial oxidation and gasification reactions. The choice of fuel required for the oxidation process depends on the gasifier design, which have been marked as 'UD' for updraft and 'DD' for downdraft gasifiers. Here λ_g stands for the gasification equivalence ratio.*

The gasification process begins through a *drying* step wherein the biomass is heated from an ambient temperature to about 120-160°C, causing the release of water contained within the biomass. Thereafter, the process of *pyrolysis* begins where the complex biomass molecules undergo thermal decomposition

resulting into solids or *primary chars* which are about 85% pure carbon (C), non-condensable gases (CO, CO_2, CH_4, etc.), and condensable vapors (H_2O, $C_aH_yO_x$, etc.). Depending on the pyrolysis temperature, the rate of heating and the residence/exposure time of the biomass, the distribution of pyrolysis products between solids, vapors and gases are affected significantly [11]. Lower temperatures and longer times result in higher production of char, while moderate temperatures of about 500°C and short residence times favor the formation of vapors. Considering the context of gasification, where higher non-condensable gas yields are desirable, pyrolysis at high temperatures (about 750-900°C) with longer residence times (>3s) could be considered. However, such high pyrolysis temperatures would require higher amounts of heat and yet would not complete the conversion into gases. Thus, the pyrolysis is carried out up till moderate temperatures of about 500 °C with long residence times. Thereafter, the remaining solids and vapors undergo the process of *gasification* wherein the char is reduced by CO_2 and H_2O available from the pyrolysis and combustion reactions, while the vapors undergo thermal cracking or gas phase reactions, resulting into the desired non-condensable gases.

All these reactions being endothermic in nature, require exothermic oxidation reactions to provide for the necessary supply of heat. The typical gasification is of the auto-thermal type, wherein a partial oxidation of the biomass feedstock is carried out through a limited supply of oxygen (by air or in purified form) at air to biomass equivalence ratio, λ_g <1. For example, as per Reed et al. [10], the combustion of about 6-10% of dry biomass by weight could supply enough heat to pyrolyze the remaining biomass at 600°C.

Overall, gasification transforms the solid biomass predominantly into a gas mixture consisting of the fuel gases CO, H_2 and a small quantity of CH_4, inert gases such as CO_2, N_2 (if air is used as gasifying medium) and water vapor, along with impurities such as un-cracked vapors (tars), particles and trace gases. The solids remaining after the gasification process consist of some unconverted carbon in the form of char, minerals such as Ca, K, and others.

The gasification process is sensitive to many parameters [5, 12, 13, 14]. A few of these are outlined here:

Gasification temperature has the most critical effect on the process. High temperatures improve the biomass-to-syngas conversion efficiency resulting in higher gas yields and most importantly cause the conversion / destruction of tar impurities into non-condensable fuel gases. However, this benefit is countered by the larger portion of the feedstock diverted for the partial oxidation processes required for increasing the gasification temperature. As a result, the share of inert gases (N_2, CO_2 and H_2O) originating from the higher supply of air and the subsequent combustion, increases in the output syngas decreasing its Lower Heating Value (LHV). Additionally, challenges of higher loss of heat from the gasifier wall, loss

of thermal efficiency due to the additional cooling required for the low temperature syngas requirements of a conventional SI engine, higher engineering costs due to the need of sophisticated construction materials, increased potential for the melting, slagging and agglomeration of ashes, and others, may occur. As of specific interest to the concept discussed in this thesis, while higher gasification temperatures result in lesser amounts of tars, the tar compounds produced from these high temperatures have higher tar dew points. As will be see in Section 1.2, the tar dew point is a crucial parameter in the context of developing a tar-tolerant end-use system.

The gasifying agent significantly influences the LHV of the syngas [5, 6, 15]. In cases where air is used as the gasifying medium, the un-reacted N_2 is included in the output syngas which results in a low LHV of about 4-6 MJ/kg. To improve the syngas energy density, various oxidizing agents such as oxygen rich air and steam are used, resulting in energy densities of about 10-18 MJ/kg [5, 15]. However, the improvements in LHV by using agents other than air incur additional costs and complexities of equipment (for O_2 rich gasification) and heat sources (for allo-thermal steam gasification).

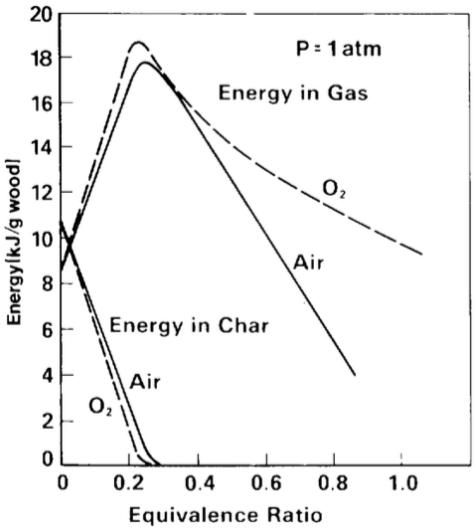


Figure 1.2: *The chemical energy content of output syngas and char as a function of the gasification equivalence ratio (gasifying agent to biomass ratio) as adapted from Reed et al. [10].*

Gasification ratio could be defined as the ratio of air mass to biomass mass used in the gasification process, assuming a self-sustaining or auto-thermal operation. Reed et al. [10] present a plot, represented here in Figure 1.2, showing the energy content of the output syngas as well as the char as

a function of the gasification equivalence ratio, for two gasifying agents, air and pure oxygen. The maximum energy content in the syngas occurs for an equivalence ratio of ≈ 0.25. As the equivalence ratio increases, the additional combustion raises the gasification temperature, but at the cost of the combustible portions of the output syngas. Due to the lack of inert N_2 when pure O_2 is used as the gasifying agent, the effect of an increased equivalence ratio is less significant, than compared to air gasification.

Feedstock properties If the feedstock contains a lot of minerals, then the chances of slagging and agglomeration increase at high gasification temperatures, thus limiting the use of such feedstock types. Also, the moisture content of feedstock requires un-recoverable heat energy to raise its temperature from ambient to gasification temperatures ($\approx 700°C$) and thus, the feedstock moisture content becomes a crucial factor. Feedstock size is also important as smaller sizes help in the flow of feedstock through the gasifier along with having larger surface areas, which aid the gasification process. However, smaller sizes may also cause large pressure drops and clogging. They may also require additional energy for their production from raw biomass, thus adding to the cost and complexities of the plant.

Additionally, other factors such as the gasification pressure, residence times and gas velocities also play important roles. The tasks of the gasifier designers are to optimize these complex process variables to a desired level, resulting in many gasifier designs, a few of which will be seen in Section 1.1.3. However, the most difficult aspect of gasification is discussed next.

1.1.2 Syngas impurities

Syngas from biomass gasification contains impurities such as particulate matter (soot, char or fly ash and minerals), condensable vapors (tars) and trace chemicals. Of these impurities, the challenges posed by the tars are the most significant, and shall be discussed in the next three sections, Sections 1.1.2.1, 1.1.2.2 and 1.1.2.3. Thereafter, the other impurities are discussed in Section 1.1.2.4.

1.1.2.1 Tar formation and their classification

All tar compounds can be traced back to the pyrolysis stage of the gasification process, but are modulated throughout the process into a myriad variety of forms. The formation and subsequent transformation of tars are influenced by factors such as the gasification and/or local temperatures, residence times of the biomass or tar compounds at particular temperatures, the types of tar compounds (since the reactivities are different), the presence or absence of reacting elements and catalysts, gasification pressure and other factors. The

broad formation and transformation process of tars, as a result of pyrolysis severity, can be summarized as below, which follows from the reviews and discussions provided by Milne et al. [16] and Vreugdenhil et al. [17]:

Primary tars: Pyrolysis results in the decomposition of solid biomass into pyrolysis products consisting of non-condensable gases, volatiles and char, as seen previously. At the pyrolysis conditions, the reaction environment is essentially inert and devoid of reactants such as O_2, H_2O, CO_2 and H_2. The volatiles, which originate in the temperature range 400-700°C as a result of the first stage of pyrolysis, are classified as primary tars. These tars contain mainly oxygenated compounds (containing O atoms) which are closely related and derived from the basic biomass components of cellulose, hemicellulose and lignin. These tars, compared to all the subsequent classes of tars, exhibit the highest reactivities and easily transform into other tar classes due to increases in pyrolysis severity (meaning higher temperatures and/or residence times).

Secondary tars: This class of tars originate in the temperature range from 700-850°C and mostly consist of phenolic and olefin compounds. These tars are a result of gas phase reactions where the high temperatures cause the breaking of chemical bonds of the tar compounds resulting in the formation of radicals. The reactions driven by the radicals may result in the cracking of tars into lighter hydrocarbons or secondary tars and non-condensable gases, especially hydrogen.

Tertiary tars: Additionally, the radicals may participate in recombination reactions forming heavier tar compounds. The latter process, also called *polymerization*, leads to the formation tertiary tars in the temperature range of 850-1000°C and consists of compounds such as methylnaphtahlene, toluene, indene, Polyaromatic Hydrocarbons (PAH) and others. The severity of thermal cracking may additionally lead to the formation of *soot* or char, which are high molecular weight compounds with high carbon content, and hence are solids.

The above classification is based on pyrolysis conditions which essentially occur in an inert environment. Destruction of tars through thermal cracking is limited by various issues.

- The temperatures required for thermal cracking are high, which imply that more oxidation reactions are required for raising the temperatures, which cause a reduction in the LHV of the syngas.
- Severe pyrolysis results in increased amounts of tertiary tars and char, which are more difficult to crack on account of their highly refractive nature (low reactivity) as compared to primary products (primary tars and chars).
- The carbonaceous compounds being in solid form need to be removed from the gas stream before the syngas can be used in IC engines. Thus

a significant amount of potential fuel energy has to be filtered out contributing in decreased overall efficiency of the gasification plant.

Thus, the process of gasification causes reactants such as CO_2 and H_2O to participate and increase the tar (and char) decomposition through chemical reactions. These reactive compounds react with the tar radicals produced during the pyrolysis, resulting in the chemical breakup of tars into the desired non-condensible fuel gases CO and H_2. However, H_2 presence during the gasification stage slows down the tar decomposition reactions. This is because of the higher reactivity of H_2, in comparison with those of CO_2 and H_2O, causes it to react with the tar radicals resulting in the elimination of the radical back into a stable tar molecule. Additionally, H_2 radicals are released from these reforming reactions, further leading to the suppression of tar decomposition reactions and increased formation of the heavier tertiary tars. Thus, the formation and eventual conversion of tars into the output syngas during the gasification process can undergo various complex pathways.

As discussed by Rabou et al. [18], the composition of dry biomass has little or no effect on tar amounts and compositions resulting from gasification. Due to the H_2O reactions with tars, as discussed above, the gasification of high moisture content biomass reduces the amount of tars produced. Although, the temperature is the most influencing factor, increasing the gas (with tar content) residence time at high local temperatures has the same effect as increasing the temperature. Further, catalysts are an effective way to decompose tars and it is interesting to note that biomass char also functions as an effective catalyst.

Apart from the way-of-formation classification just described, tar compounds have been classified based on their chemical and physical properties by the ECN of Netherlands, as presented in Table 1.1. They can also be further differentiated based on their properties such as water solubility, carcinogenic potential, condensation temperature, condensed state properties (solid or liquid, viscosity, etc), reactivity and other aspects [18, 19].

1.1.2.2 Tar dew point

The major challenge posed by the tars arise due to their condensation at a wide range of temperatures ($\approx$ 0-300°C), which depend on the specific tar compounds and their specific concentrations within the lumped tar impurities. The tar dew point is the temperature where the tar content in a gas reaches saturation conditions, thereby beginning to condense. The dew point depends on the classification of tars, as shown in Table 1.1, and also on their concentrations. As discussed by Bergman et al., tar problems do not occur as long as the tars remain in their gaseous phase. The authors also conclude that the tar problems are not related to the amount of tars, but rather to the composition of the tars, which determines the effective tar dew point. This is because the tars with the highest dew points will condense first as the syngas temperatures

Class	Tar description	Examples
1	GC undetectable tars Gravimetric tars, generally $\geq$ 7-rings	Biomass fragments, heaviest tars (pitch)
2	Heterocyclic compounds. Highly water soluble	Phenol, cresol, quinoline, pyridine
3	Aromatic components, important for tar process but not for condensation or solubility	Toluene, xylenes, ethylbenzene (excluding benzene)
4	Light PAH, 2-3 rings. Condense at relatively high concentrations and intermediate temperatures	Naphthalene, indene, biphenyl, antracene
5	Heavy PAH (>4-rings). Condense at relatively high temperature and low concentrations	Fluoranthene, pyrene, crysene
6	GC detectable, not identified components.	Unknowns

Table 1.1: *Tar classification according to the ECN of Netherlands [20].*

decrease after it exists the gasifier. Thus, the tar dew point has a significant role to play in the tar handling processes downstream the gasifier or in its effect on the end-use devices. Additionally, as mentioned by Rabou et al. [18], because the heavier tars (tertiary tars of aromatic nature with higher rings, like Class V and Class I from Table 1.1) have more vapor pressure and the severity of pyrolysis or gasification temperatures increases the production of these heavier tars (as seen in the previous section), the tar dew point increases with gasification temperature.

Figure 1.3, adapted from Bergman et al. [20], shows a wide range of dew points of the main tar classes. Class I tars are not included in the Figure 1.3 due the limitations of the Gas Chromatography/Mass Spectroscopy (GC/MS) systems commonly employed in the measurement of tars. However, they seem to condense in the range of 300-350°C [20]. Due to the wide range of dew point temperatures, it is difficult to pinpoint a specific temperature above which tars can be safely assumed to be non-condensing and thus cause no problems. In Figure 1.3, Class V tars (the top-most trend), having the highest dew point temperature, would dominate the overall tar dew point of a tar mixture containing them. As shall be seen in Section 1.1.3, various gasifiers produce different set of tar compounds with their associated dew-points and in different quantities. For example, a modern optimized gasifier, such as the downdraft gasifier (see Section 1.1.3.2) would produce tars less than 100 mg/Nm^3 of syngas. In contrast, gasifier designs not optimized for reduced tars production, such as the updraft gasifier (see Section 1.1.3.1), may produce tars more than a few g/Nm^3. If it is assumed that the tars produced in either of these gasifiers contain the easily condensing Class V tars, then the corresponding conservative tar

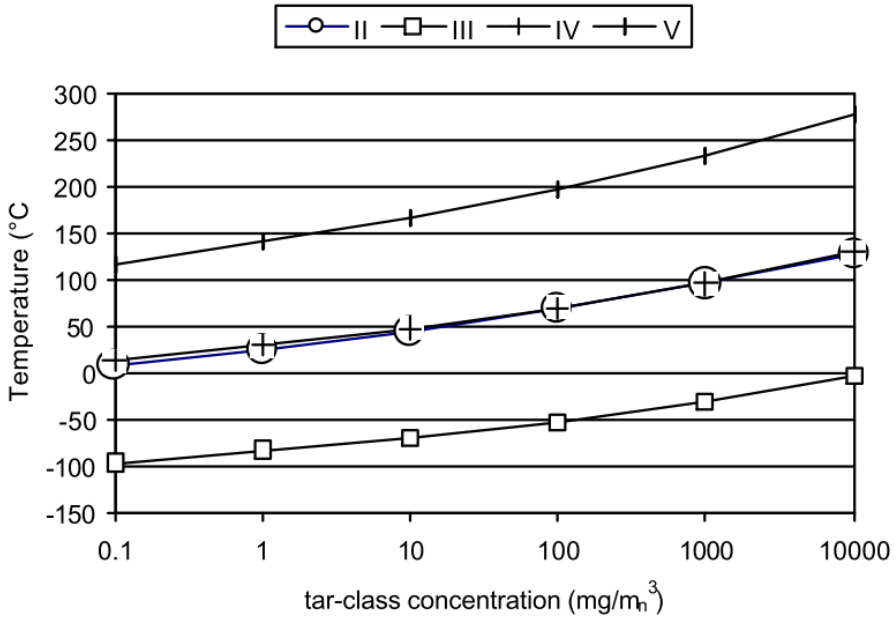


Figure 1.3: *Tar dew point temperatures according to the concentration of tar classes. Image adapted from Bergman et al. [20].*

dew point estimates, according to Figure 1.3, would be approximately 200°C for the downdraft gasifier and somewhat above 250°C for the updraft gasifier. However, the content and composition of tars vary significantly with gasifier designs, operating conditions and other factors, and thus, the effective tar dew point can not be fixed beforehand.

A conservative estimate of 250° C can be assumed as a working temperature, if the condensation of tars has to be avoided.

1.1.2.3 Tar related issues

The problems arising due to tars could be classified into the following broad categories (see [16, 18, 21]):

Tar deposition: Tars, in their condensed form, are sticky and have a high viscosity. Cyclonic filters, used as a primary step for particle filtration from raw syngas, must be operated above the tar dew points ($\approx$ 250 °C) so as to prevent the tars from condensing on the walls. If not done so, the condensed tars may eventually trap the particulate impurities, increase the plugging of particle drains and decrease the overall cyclonic separation efficiency. Fine particle filtration methods, using bag house filters or candle filters, must also be maintained above the tar dew point so as to

avoid the blocking of the pores by condensed tars. The tars also condense on the surfaces of the heat exchangers necessary for cooling syngas, decreasing their efficacy as well as reducing the overall flow. Tar deposits may additionally trap particulate matter leading to abrasive actions between moving parts or make surfaces sticky, which may constrain the free movement of parts.

Tar maturation/polymerization : Excessive gasification temperatures can result in thermal cracking of tar compounds or inversely cause their polymerization into heavier and more refractive compounds, which are often precursors of soot, as discussed in the previous section. Soot can form combustion chamber deposits, which may alter combustion processes [22, 23]. They can also settle on condensed tars and jam or clog critical moving parts. Additionally, soot emissions are an environmental hazard due to their sizes and ill effects on the human respiratory system. Polymerized tars, being chemically more stable, are much more difficult to clean or destroy through thermal, catalytic or physical processes. As discussed by Houben et al. [24], tar maturation or polymerization can also take place with time, forming sticky and dark brown or black syrup, which may eventually become hard and brittle.

Tar purification: Tars, due to their chemical diversity and nature, require physical capture and agglomeration or coalescence, instead of simple cooling for the purpose of filtration. However, tars are known to be very difficult to coalesce, thus requiring complex procedures for even 90% tar removal [6]. Additionally, tars are hydrocarbons and thus represent the energy lost from the syngas if they have to be filtered out.

Tar disposal: Many tar compounds are toxic by nature and their emissions need to be monitored. A very common method of tar and particulate filtering is through wet scrubbing, which produces a toxic waste water stream that needs to be purified before being let out in the environment. The purification of this water stream or other mediums used for tar scrubbing becomes more complicated due to the solubilities of the various tar compounds.

As of the effects of tar deposition inside an engine, not many studies are available from open literature. However, the consensus of tar deposition and subsequent damages to the engine is very strong in the industry. Studies carried out by Hasler and Nussbaumer [25] on an engine run with syngas containing tars of about 50 mg/Nm^3, found heavier tars (Class I and V probably) forming the largest share of the deposited mass (about 85%) on the engine internals, compared to the lighter tars, such as the light PAH compound, naphthalene. Ahrenfeldt et al. [23] carried out studies to test the formation of combustion chamber deposit (CCD) due to tar loaded biomass syngas at a laboratory scale. Simulated syngas with representative tar compounds were used. However, no

deposits were found in the test conditions.

1.1.2.4 Other Syngas impurities

After tars, the particulate impurities are the most important. Particles can clog filters, scrape piston-cylinder surfaces, mix with the engine oil or accumulate with the tars on certain surfaces which may further complicate tar related problems. However, the physical removal of particles is a proven and effective technology, unlike the case of tars.

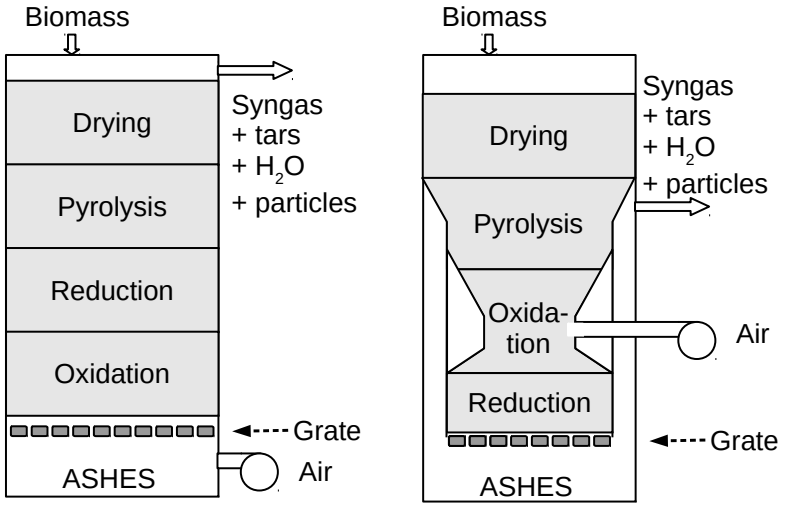
Syngas also contains traces of alkali metals which condense at temperatures lower than 600°C. In vapor form, alkali metals may damage ceramic particulate filters and thus the syngas needs to be cooled to below 600°C before the use of such filters for fine particle filtering [6]. Alkali metals are also known to cause corrosion of turbine blades which operate at very high temperatures, however, such is not the case with IC engines and thus they need not be bothered with within this context [6]. N_2 related compounds such as ammonia occur in the biomass in the form of fuel bound nitrogen. In the process of gasification and end-use, these compounds may give rise to emissions either in the form of NO_x or ammonia [6, 26]. Unlike fossil fuels, the sulfur content in biomass is low and thus its removal is not deemed necessary for most of the applications, except for gas turbines [6]. Chlorine content in biomass, from the spraying of pesticides, herbicides and fertilizers during the growth phase of biomass, can cause corrosion of engine piston surfaces and thus may require cleaning.

1.1.3 Gasification Engineering

Biomass gasification is carried out in a variety of forms with the intent of delivering high quality syngas to the end-use devices such as ICE, gas turbines, fuel cells or used for direct combustion in steam boilers or Stirling cycle engines. In the current state of gasification technology, the raw syngas from the gasifiers often does not meet the stringent input requirements of end-use devices, and therefore intermediate syngas conditioning steps are used. The end use technologies themselves have differing requirements in terms of syngas quality. To summarize, the broad motivations of biomass-gasification-energy engineering in the pursuit of developing a capable system could be listed as:

- High LHV syngas.
- High conversion efficiency of biomass to syngas in terms of energy.
- Low content of impurities, especially the tars.
- High tolerance of the end-use devices to syngas impurities.
- Scalability of the system for various power classes.
- Low overall costs of power production.
- Flexibility in the use of different biomass types.

Often these requirements are conflicting and the best compromise is searched for. Biomass gasification combines the processes of drying, pyrolysis, gasification and combustion into a compact package to produce the desired quality of syngas. Gasifiers can be classified into fixed/moving bed and fluidized bed designs. The fixed beds are generally of a simpler nature and are appropriate for small scale applications such as decentralized power or CHP, whereas the fluidized bed types, having high throughput, are more suitable for large scale operations [6, 7]. In the context of this project, two principle fixed bed gasifier designs are relevant, namely the Up Draft (UD) or counter-current gasifier, and, the Down Draft (DD) or co-current gasifier.



(a) Updraft gasifier (UD) *(b) Downdraft gasifier (DD)*

Figure 1.4: *Schematic representations of the most common fixed bed biomass gasifiers. Both these gasifiers are mounted in vertical orientation with respect to the ground, with gravity providing the major force for biomass and its derivative solids to flow through the gasification process.*

1.1.3.1 The Updraft Gasifier

The Updraft gasifier (UD) is the simplest of all gasifier designs, and its schematic is shown in Figure 1.4a. Such a gasifier is characterized by the counter flows of biomass and the gases, including the gasifying medium. The biomass flows from the top towards the bottom of the gasifier while the gases move up, from the bottom towards the top. The oxidation zone is the lowest part and mostly contains solid char and ash resting on a grate. The gasifying agent is supplied at this zone, which results in the important heat releasing oxidation reactions,

converting the solid char into ash. The combustion residue (ash) falls through the grate and is collected at the bottom, whereas the hot oxidation products (mostly CO_2, N_2, H_2O and others) rise upwards, encountering the descending pyrolysis char from the upper lying pyrolysis stage. Reduction reactions take place at this stage, where the char is thermally cracked into the desirable non-condensable gases and carbon free ash. The hot gases further rise from the reduction zone, with a lesser amount of sensible heat, into the pyrolysis zone. Here the descending dried biomass is decomposed into pyrolysis products. Since the volatiles are in their gaseous form, they mostly follow the flow of gases towards the top, instead of the downward flow of the solid char. Beyond the pyrolysis zone, the relatively cooler gases still have enough sensible heat which is utilized for drying the incoming fresh biomass. Some of the volatiles condense on the cooler biomass particles, while the rest escape with the non-condensable gases.

The presence of high temperature gases, with the absence of any oxidizer compounds (which are ideally consumed at the partial-oxidation stage), drives the sequential reduction, pyrolysis and drying processes. Finally, the syngas exits the gasifier at the top, along with a large proportion of the pyrolysis volatiles, at temperatures in the range of 300-400°C.

The major features of the UD gasifier can be summarized as below:

1. Since the pyrolysis products of the condensible type remain in their vapor form and do not pass through the high temperature oxidation or reduction zones, they either condense on the colder biomass in the drying zone or exit with the syngas. This results in very high concentrations of tar in the syngas, often up to 100 g/Nm^3 [16].
2. Due to the collisions of the upward rising gases with the biomass in the pyrolysis and drying stages, less particles are carried over by the syngas, resulting in low particulate impurities in the syngas.
3. Since the oxidation zone is at very high temperatures and all the solid pyrolysis/gasification residues must pass through this region, the fixed carbon of the biomass char is almost completely released, leaving behind only mineral rich ashes. Thus, high carbon conversion efficiencies are achieved.
4. The high temperatures at the bottom grate can cause clinkering of ash compounds, and thus, biomass feedstock with low ash content needs to be used with this type of gasifier.
5. Since the rising gases do not encounter the high temperature oxidation and reduction zones, the large amount of moisture released from the drying stage exits the gasifier with the syngas, resulting in a high moisture loaded syngas. Additionally, since this water is not heated to the gasification temperatures, an important fraction of the unrecoverable heat energy is saved. Thus, feedstock with higher water content can be used, as it does not interfere/deteriorate the gasification process.

6. The heat released from the partial-oxidation stage is efficiently transfered to the reduction, pyrolysis and drying stages of the process, thus resulting in low exit temperatures of the syngas and a consequent higher thermal efficiency. This also implies that lesser combustion is required to supply the heat necessary for the gasification process, resulting in low concentrations of inert components in the syngas and a subsequently high LHV of the syngas.
7. The low exit temperature of the syngas implies that lesser cooling is required for the syngas to meet the requirements of most conventional end-use applications, thus resulting in a higher Cold Gas Efficiency (CGE).
8. Since the pyrolysis components do not undergo severe pyrolysis reactions, the tar content of syngas from this gasifier contains significant amounts of primary tars which have subsequently lower tar dew points.
9. Of the three components of pyrolysis, the oxidation of char supplies the major source of heat for the gasification process.

Despite the various advantages, the high content of tars in the syngas from this type of gasifier is a major disadvantage in the context of its use with a conventional SI engine. In order to avoid extensive and costly gas cleaning downstream the gasifier, which would be required if such a syngas is to be used in the conventional tar *intolerant* SI engines (more on this in Section 1.1.4), other gasification designs are found to be more appropriate. Hence, the application of the UD gasifier is mostly limited to boilers for heat generation or external combustion engines.

1.1.3.2 The Downdraft Gasifier

In a Down Draft or DD gasifier, the biomass and the gasification agent flows in the downward direction, as shown in Figure 1.4b. In contrast to the UD gasifier design, the oxidation zone is maintained at the central portion of the gasifier, above the reduction zone. Fresh biomass is dried by the heat of the oxidation zone due to radiative heat transfer, as well as from the flow of hot syngas around the walls of the gasifier which act as heat exchanger surfaces. The dried biomass moves downward to the pyrolysis zone. Again, in contrast to the opposite directions of flows of the pyrolysis char and gases (including the volatiles) seen in the UD gasifier, the flow of all pyrolysis products are in the downward direction, entering into the high temperature oxidation zone. This results in the thermal cracking of the volatiles into the desired non-condensable gases. Chars products, from primary pyrolysis reactions as well as from the decomposition reactions of volatiles, thereafter accumulate above the grate at the bottom of the gasifier. The high temperatures and the long residence times at this stage causes the reduction of char. The resultant products, with high content of sensible heat, pass through the reduction zone into the ash region. Since the ash are fine particles, they are entrained in the gas flow, resulting in

high particulate contamination of the output syngas. The walls of the gasifier are so designed so that the high temperature syngas can exchange its sensible heat with the pyrolysis and drying stages of the process, thereby improving the thermal efficiency of the gasifier.

The main features of the DD gasifier can be summarized as follows:

1. The passing of pyrolysis products through the combustion and reduction zone cracks almost all of the tars, producing one of the least tar content syngas amongst all the gasifier designs. Tar loading less than 1 g/Nm^3 can be achieved.
2. Due to its passing from the ash zone, syngas from this gasifier contains high amounts of particulate impurities.
3. The syngas, even after exchanging its sensible heat with the cooler pyrolysis and drying stages through the heat exchanger surface, retains a significant amount of sensible heat and exits the gasifier with temperatures at around 500-600°C. This loss of gasification heat requires to be compensated by higher rates of combustion, ultimately resulting in a lower thermal efficiency and a lower LHV of syngas, as compared to an UD gasifier.
4. Due to the high exit temperature of syngas, low CGE results when used with conventional cold-gas end-use devices.
5. The overall construction is relatively complicated engineering-wise, as compared to an UD gasifier.
6. Due to the passing of the volatiles through the high temperature oxidation and reduction zones, the tars from this type of gasifier mostly belong to the tertiary class, containing high concentrations of PAH. Their dew points are thus higher than those from an UD gasifier.
7. In contrast to UD gasifier, the oxidation of non-condensible gases and volatiles (which have relatively high reactivity as compared to char) supplies the heat for the process.

Despite the various disadvantages of the DD gasifier in comparison to the UD gasifier, the low tar output of the syngas makes it the most popular design for small power generation applications.

However, the low tar content of DD gasification still remains above the requirements of IC engines (less than 50 mg/Nm^3, as shall be seen in Section 1.1.4.2). Often, transient operations during the start of the gasification process, or during biomass addition processes, may disturb the chemical equilibrium of these systems, resulting in increased tar outputs.

The following section presents a brief overview of methods used to interface the raw syngas from the gasifiers with the requirements of end-use devices.

1.1.3.3 Improvements and intermediate gas conditioning

The end-use requirements posed by IC engines amount to about 50 mg/Nm^3 of particulate matter and about 100 mg/Nm^3 for tars [16]. However, the data compiled by Milne et al. [16] shows many different values of tar loading, quoted from different works, often reaching as low as 10 mg/Nm^3. From the experience gained over the many years by the staff utilizing the gasifier setup at the author's laboratory, the latter value seems to be more reasonable.

Gasifier	Tars [mg/Nm^3]	Particles [mg/Nm^3]	Ref
UD	10,000-150,000	100-3000	Review by [27]
UD	80,000	-	[28]
1-stage DD	10-6000	100-8000	Review by [27]
2-stage DD	20	-	[29]
2-stage DD	19-34	-	[30]
2-stage DD	<1	5	[31]

Table 1.2: *Comparison between the UD, DD and two-stage DD gasifiers in terms of tars and particles.*

Table 1.2 shows some examples of biomass syngas tar loadings, from updraft and downdraft gasifiers. The gap between the outputs of these gasifiers and the engine requirements have to be met by tar filtration methods which form the secondary measures. The extremely high values of tar production from UD gasifiers make them unsuitable for IC engine power generation. However, this may not be true for large plants, such as the Harbøre in Denmark, with a 5.2 MW thermal input UD gasifier operating in CHP mode with IC engine power plants [28]. As for the conventional single stage DD gasifier, the tar tolerance capacity of the IC engine is at least an order of magnitude lesser than the syngas produced by such gasifiers. Thus, there is a wide gap between the simple gasifiers and the engine requirements, creating the need for improvements. Much of the current research in the domain of biomass gasification is split into two approaches classified into *primary* and *secondary* methods, as mentioned before.

Technology	Retention Efficiency [%]
Wash tower	10-25
Venturi Scrubber	50-90
Wet electrostatic precipitator	0-60
Fabric filter	0-50
Rotational Particle Separator	30-70
Fixed bed tar absorber	50
Catalytic tar cracker	>95

Table 1.3: *Comparison of tar retention efficiency of different secondary measures, as reviewed by Hasler and Nussbaumer [27]*

Devi et al. [32] provide a review of primary methods which include techniques such as optimizing the physical gasification process parameters or using catalysts in the gasifiers so as to reduce the production of tarry compounds. Multi-stage gasifier designs have been developed which separate the gasification process into many stages so as to have more freedom in optimizing the key stages, relatively independent of other stages. One such branch of designs, the two-stage downdraft gasifier, has gained much acceptance (see for example [30, 33, 34]). Table 1.2 shows the typical tar loading of syngas from some two-stage DD gasifiers. As it is evident, this class of gasifier produces syngas of optimum quality in terms of tars, and apparently seems to be suited for direct use with IC engines, without the need for intermediate secondary measures. As an example, consider a 2-stage downdraft gasifier setup at the author's laboratory. The work of this thesis is based on the gas properties resulting from its functioning and shall be discussed in more detail in Chapter 6. This system develops syngas with tar content often in the range of 20 mg/Nm^3. However, this low tar content is representative of optimum and stable working conditions, which is not the case during transient operations, such as during the start of the gasifier or in case of changes in the feedstock quality, and others. Thus, to ensure consistent syngas quality, intermediate syngas conditioning steps are required even for low tar two-stage DD gasifiers.

The intermediate secondary methods can be divided into various sub-classes, such as physical filtering (scrubbing, cyclonic particulate filters, bag or candle filters, etc.), thermal hot gas cleaning and catalytic hot gas processes. Reviews of such methods can be found in [27, 35, 26]. Table 1.3 presents an example summary of the tar retention abilities of some of the most common tar filtration or conversion devices used for small scale gasification setups, as reviewed by Hasler and Nussbaumer [27]. The low retention abilities of many of these devices imply that multiple stages have to be utilized to arrive at the syngas of a desired quality. The complexity of secondary measures are significantly reduced for 2-stage downdraft gasifiers due to the effectiveness of primary measures, but they are nevertheless complex and maintenance prone.

Combinations of DD gasifiers with sophisticated intermediate cooling and cleaning mechanisms have been put into practice, and yet the challenges posed by tars persist, as repeated by many authors [18, 21]. As seen in the next section, the very low tar tolerance of gasification based power systems is directly linked to the use of conventional SI engines in this context.

1.1.4 Syngas and the IC engine

The gasification+ICE combination is the most popular of biomass gasification technologies implemented throughout the world, but limited to small scale of operations. The popularity is primarily due to the availability, economy and established know-how of the IC engines, originating from the automotive

and stationary power generation domains. Also, minimal customizations are required to adapt the commercially available petrol/diesel/gas engines to syngas operation. Compared to other conversion technologies (except external combustion engines), the IC engines also have the highest tolerance to syngas impurities [16]. And finally, the reliability and high syngas-to-electricity conversion efficiencies at the small scale, make them aptly suited to this domain [8].

Some studies using Compression Ignition (CI) engines operating in a dual-fuel mode can be found, where syngas supplements a large portion of the main diesel fuel and is premixed with air, likewise in a Spark Ignition (SI) engine (for example see [36]). The basic difference between these two modes of combustion is the replacement of the spark plug by a pilot ignition, both of which are used to initiate stable flames which can then burn the syngas. However, the SI engine has been the most popular IC engine technology in this domain.

Section 1.1.4.1 presents an overview of the functioning and limits of the SI engine, based on which Section 1.1.4.2 presents the particular features and issues of syngas used as SI engine fuel.

1.1.4.1 Overview of the SI engine

The following account has been summarized from Heywood [37] and additional sources, as quoted.

In a SI engine, the fuel is premixed with air and injected at the intake port after which it is compressed. At a predetermined position during the compression, a spark-plug is fired resulting in a flame-front which expands from the position of the spark towards the rest of the un-burnt fuel. The SI engine combustion is controlled by the critical timing of the spark. Apart from spark timing, the SI engine is also influenced by many factors such as the design of the combustion chamber, the compression ratio, the pressure and temperature of the gases before the combustion as well as the fuel properties such as the laminar flame speeds, octane rating and mixture properties such as mixture turbulence, homogeneity, equivalence ratio (ϕ) and others. The maximum extents of the SI engine operation is limited by the phenomena of engine *knock* on one hand and high cycle-to-cycle variations on the other hand. Between the high cyclic variability and the knock regions, there exists an optimum Maximum Brake Torque (MBT) region, where the maximum performance of a SI engine can be realized.

Spark timing is an important control which can be exercised on the SI engine, in accordance with changing conditions or load demands. In case of advanced spark timing, the combustion is initiated early in the cycle and causes the cylinder pressure to rise much before the piston reaches the Top Dead Center (TDC). Such a combustion results in negative influences such as increased frictional and heat losses. Additionally, as the flame front progresses through-

out the chamber, the *end-gas regions* are subjected to increased compression, both due to volumetric compression as well as compression due to the expanding combustion gases. In such situations, the increased temperatures may lead to autoignitions even before the flame can consume the end-gas, leading to the phenomenon of *knock*. As pointed out by Pöschl and Sattelmayer [38], specific distributions of thermal inhomogeneities, within the compressed charge, are necessary for sequential autoignition processes to occur in an SI engine, which amplify the pressure waves resulting in audible knock. In knocking condition, the combustion rates may rise by 5 to 25 times the normal [37], which, along with the high audible noise and vibrations, may cause drastic increases in the heat transfer between the gas and the engine walls and subsequently damage the engine. In contrast to knocking combustion, excessively delayed spark timing results in combustion which occurs much after the TDC, where the decreasing pressures and temperatures resulting from volume expansion decrease the flame propagation speed. As a consequence, the volume expansion completes (meaning the exhaust valves open) much before the combustion is completed, resulting in the loss of performance, high emissions of partially burnt fuel (high CO and hydrocarbon emissions) and low combustion efficiency.

The occurrence of knocking conditions are not just limited to advanced spark timings, but are created whenever the temperatures in the end-gas regions reach beyond the auto-ignition temperature. This can be caused by many factors such as high intake temperatures or compression ratios for the specific fuel used, or may directly be linked to the composition and properties of the fuel. An interesting example is that of H_2, which has a high propensity to auto-ignite due to its low ignition energy and wide flammability range, and yet in an SI engine, the high flame speeds of H_2 leads to decreased occurrence of knock. This is in contrast to methane or natural gas which are relatively difficult to auto-ignite, and yet lead to knocking tendencies more than H_2. Along with these examples of knock behavior being influenced by fuel types, the functioning of a SI engine through its dependence on flame propagation places important limitations on the maximum spark advance, the maximum compression ratio and the maximum intake temperature possible to be used. The latter aspect of limited maximum intake temperature is a crucial factor within the discussions in this thesis.

Cyclic variability is an inherent aspect of the IC engines. In case of the SI engine, this variability arises due to the high sensitivity of the spark-to-flame front development process to the conditions around the spark plug (see [39]). Additionally, the flame speed and structure may also be influenced by thermal and species inhomogeneities within the charge. The inherent cyclic variations severely increase if the sparking conditions are less than optimal, and thus subject to the random influences of local inhomogeneities and turbulent flows within the chamber. In case of spark igniting a lean mixture, the low availability of fuel, in addition to high heat losses which normally occur due

to the presence of the colder spark plug surface near the primary flame kernel, causes the flame to be disturbed. As a consequence, this results in increased cyclic variations. To compensate for the reduced flame speed resulting from the use of a lean mixture, the spark timing has to be advanced. However, the advancing of the spark timing distances the spark-to-flame process from its optimal conditions, further increasing the cyclic variations. On further leaning of the mixture, partial combustion or misfires can occur. Thus, the functioning of a conventional SI engine is limited to near stoichiometric mixtures.

For optimal performance, an engine should have the maximum fuel-to-mechanical energy efficiency (brake efficiency) while having minimal emissions of CO, Hydrocarbons (HC), NO_x and soot and operating well within the smooth regimes bound by knock and cyclic variations. Lean operation meets many of these requirements. With lean operation, the combustion efficiency increases due to the increased availability of oxygen. Additionally, due to the reduced flame speeds and resulting wide combustion duration, the combustion temperatures decrease, resulting in lower NO_x emissions. The ratio of specific heats (γ) also increases, causing the thermal efficiency to increase due to the higher compression temperatures achieved with the same compression ratio. However, it must be noted that knock can occur even in lean operations where the knock tendencies are aided due to the increased adiabatic compression temperatures, as mentioned by Topinka et al. [40]. Further, in lean operation, the throttling losses incurred by the SI engine decreases significantly, thereby increasing the overall efficiency.

In summary, although the SI engine posses an important control 'handle' in terms of spark timing, its functioning is limited by knock imposed restrictions on the intake temperature and compression ratio on one hand, and the limited scope for lean operation, due to cyclic variability, on the other. The fuel properties are important factors too, which affect both these limits, in addition to the power produced. The next section discusses how syngas fares as a fuel for the SI engine.

1.1.4.2 Syngas as SI engine fuel

Syngas as an IC engine fuel has been a subject of many studies due to its major differences from fossil fuels. The LHV of the syngas from an air-blown gasifier at atmospheric pressures is about 4-6 MJ/kg (kg of syngas fuel), compared to fossil fuels such as petrol (44 MJ/kg) or natural gas (45 MJ/kg). Apparently, the use of syngas would cause significant *de-rating* in the output power, however, since syngas contains a large portion of inert gases, N_2 and CO_2, the energy content of the stoichiometric air ratio is not far from that of the fossil fuels. In stoichiometric conditions, a syngas mixture would amount to about 2.04 MJ/kg at Air to Fuel mass Ratio $AFR_{m,stoic}$=1.2, compared to petrol, which would have about 2.8 MJ/kg at $AFR_{m,stoic} = 14.6$ and natural gas, about 2.9

MJ/kg at $AFR_{m,stoic} = 14.5$ [37]. Tinaut et al. [41] predicted a power de-rating of a syngas fueled SI engine to be about $1/3^{rd}$ of the power when fueled with conventional fossil fuels.

The compression ratios usable with SI engines depend on the propensity of the fuel to cause knock, as well as the initial charge conditions. For liquid fuels, the *octane number* is used, where a high octane number implies a higher knock limited compression ratio. However, for gaseous fuels, the *Methane Number (MN)* is more applicable. According to its definition, the gas CH_4 has a MN of 100, whereas H_2 has a MN of 0, implying that these gases have the highest and lowest resistance to knock, respectively. For example, a fuel with MN=x below 100 would correspond to a composition with x molar fractions of CH_4 and $(100 - x)$ molar fractions of H_2. In contrast, a fuel with MN> 100 would correspond to a composition with CH_4 <100% with the rest consisting of the knock suppressor, CO_2. The values of MN are evaluated empirically.

Arunachalam and Olsen [42] carried out an experimental evaluation of simulated syngas compositions from five different biomass gasifiers, determining their methane numbers from 53 to 131. For the experimental procedure, a variable compression ratio engine was used with artificially blended syngas mixtures at varying equivalence ratios. A predetermined knock intensity was achieved for a syngas blend at a particular compression ratio. Thereafter, this knock intensity was matched by a reference gas mixture of CH_4, H_2 and CO_2 at the same compression ratio to determine the MN for the syngas blend. This procedure was repeated for the five test syngas compositions. The lower end of the methane number range implies high content of H_2 in the syngas compared to CO_2 and thus a high propensity to knock, whereas the upper end of this range implies a lower H_2 content relative to other compositions, and thus a lower propensity to knock. The MN of natural gas lies in the range of MN=75 to 97. The authors found that the CO_2 component of syngas acted as an efficient knock suppressor due to its high heat capacity which dampened the combustion rates, whereas H_2 acted as a knock inducer due to its high flame speeds and ease of ignition. It was found that a 1% increase in CO_2 or H_2, allowed for a respective *increase* or *decrease*, in the knock limited critical compression ratio by 0.32 or 0.14 units, respectively. Thus, the positive aspects of knock suppressing abilities of CO_2 overpowers the negative knock inducing tendencies of H_2, by a factor of two. Therefore, it theoretically implies that syngas with MN greater than the MN of natural gas, could be burnt at higher compression ratios without encountering knock, as compared to the highest knock limited compression ratio of about 15 for natural gas (see [43]).

Of the five compositions compared in the paper by Arunachalam and Olsen, two are of interest in this discussion, the compositions from the IISc gasifier (see [44]) and the Viking gasifier (see [31, 34]). The syngas from from the IISc gasifier matches with that from the 2-stage downdraft gasifier setup functioning at the author's laboratory (more in Chapters 4 and 6), and corresponds

to MN≈125. Accordingly, Sridhar et al. [45] reported operating a SI engine with a compression ratio of 17.1 with syngas from this gasifier. Surprisingly, in case of the Viking gasifier, the syngas has a low MN=54, which is much less than that of natural gas and yet Ahrenfeldt [46] reported knock free operation at a compression ratio of 18.5, which is much higher than the knock limited compression ratio of 15 for natural gas. Also, in contrast to the methane number discussions so far, the accumulated experience of operating SI engines with the syngas from the author's laboratory gasifier indicates higher propensity to knock, compared to natural gas operation. Also, the methane number does not capture the presence of CO in the syngas. Thus, the methane number may not be a reliable knock index for syngas.

Another important aspect of syngas in relation to the SI engine is its flame speed. Hernandez et al. [47] reported that the syngas flame speed increases with the LHV of syngas while it reduces due to the presence of moisture. In terms of magnitude, the flame speed of syngas was found to be higher than that of CH_4, but lower than iso-octane. Thus, compared to fossil fuels, syngas is relatively more knock resistant whereas the comparison between CH_4 and natural gas in terms of knock resistance depends on the syngas composition.

Many works reviewing the SI engine adapted to be used with biomass gasification syngas can be found, for example see the reviews by [48, 49], while some examples are discussed here. Sridhar et al. [45] discussed SI operation with syngas in a converted diesel engine at compression ratios from 11.5 to 17, without encountering engine knock. This was attributed to the presence of hydrogen. In terms of performance, an indicated efficiency of 32% and an IMEP of 5.9 bar were observed at the compression ratio of 17. Additionally, the authors compared the operations with syngas fuel to diesel fuel and found that power de-rating amounted to about 16%. As an interesting observation, it was found that syngas operation resulted in increased wall heat losses as compared to diesel, even if the performance was lower. One reason could be due to the fact that in SI combustion, the premixed mixture burns near the walls and hence contributes to the increased heat transfer, unlike in CI combustion where the fuel is consumed essentially away from the walls. The same authors, in another paper [50], analyzed syngas operation in SI as well as in dual-fueled CI engine with diesel as the injected ignition fuel in the latter engine. In the dual fuel case, a maximum indicated efficiency of about 28% was recorded for syngas+diesel mode where as it was about 33% with neat diesel operation. Additionally, the exhaust temperatures in the duel-fuel experiments were found to be much higher than in neat diesel mode, thus contributing to the decreased efficiency. The reason for such loss of efficiency was attributed to the two fuels (diesel and syngas) competing for the excess air which delayed the combustion resulting in increased exhaust gas temperatures. In the same paper, the authors also discussed experiments with neat syngas in a 12 cylinder turbo-charged SI engine with a compression ratio of 12 and adapted with

a carburettor specifically designed for the purpose. The syngas to shaft power efficiency was reported to be about 28% in this case.

Ahrenfeldt et al. [31] discussed SI engine operation with clean syngas from the *Viking* gasifier. Although no detailed measurements on the SI engine performance were made (in-cylinder pressure, etc), a syngas to electrical efficiency of about 29% and an overall wood-to-electrical efficiency of about 25% were reported. Mohon Roy et al. [36] discussed syngas used in a supercharged duel fuelled (syngas + pilot diesel) CI engine with varying hydrogen content. Equivalence ratios from 0.5 to near stoichiometric with diesel fuel fraction varying from 3.5 to 6.5% were tested. A maximum IMEP of about 15 bar while a maximum indicated efficiency of 38% were reported. Additionally, two syngas compositions were experimented with and the one with higher hydrogen content was found to have superior performance at lean conditions. Ulfvik et al. [51] discussed experiments with an SI engine fueled with neat biomass syngas and operated at a wide range of equivalence ratios, down to the very lean fuel to air equivalence ratio of 0.22. High thermal efficiencies of about 44-48% and high IMEP of about 10 bar were reported. They achieved these results through the use of intake pressure boosting and using a fast burn combustion chamber geometry.

1.1.5 Summary

Through the discussions within this section on biomass gasification and the use of syngas in the SI engine, the following main conclusions can be drawn:

1. The issue of tars are central to the context of biomass gasification. Many efforts are being made to specifically address this issue, but relying mainly on developing low tar syngas either through optimized gasification or through effective tar purification/destruction methods.
2. The nature of tars (Section 1.1.2.2) gives a very interesting insight about alleviating tar related problems, i.e. operate above the tar dew point temperature. If this insight were to be used, assuming an impure raw syngas stream containing tars of about 1 g/Nm^3, a conservative working temperature of about 250°C could be sufficient.
3. The traditionally used SI engine in this domain offers significant benefits with its low cost and availability, along with decent performance in terms of efficiency and power. However, its operation is limited by the knock limited maximum intake temperature (less than 100°C).

In essence, the SI engine plays a significant role in creating tar related challenges, which places significant loads on the upstream gasifier and gas conditioning systems to produce the practically challenging tar-free syngas. The following section proposes to use an alternative engine which holds the potential for achieving a much interesting tar tolerant biomass-gasification-CHP system.

1.2 The proposed solution

A Homogeneous Charge Compression Ignition (HCCI) engine can operate in a wide variety of intake temperatures, unlike a SI engine. Thus, a tar tolerant gasification-engine system with a suitably adapted HCCI engine as the end-use device is proposed. If such a system is realized, the following benefits can be foreseen:

1. Low cost and simple updraft gasifiers could be used, without much consideration for the associated high tar content. It would also benefit from the lower particulate emissions of this class of gasifiers, allowing for simpler particle cleaning technologies. Also, since these gasifiers have low exit temperatures, close enough to the proposed high temperature engine intake, the overall thermal efficiency could be improved.
2. In case of downdraft gasifiers, the operations could be optimized for higher LHV and efficiency instead of producing the least tar content syngas.
3. Due to the reduction in the severity of intermediate tar purification systems, the pressure drop across the gasifier would decrease, thereby increasing the volumetric efficiency of such an engine. However, this should be considered together with the overall loss of volumetric efficiency resulting from the high temperature operation.
4. Low temperature gasification could be pursued since one of the main motivations for high temperature gasification is the production of low tar syngas. Low temperature gasification has many benefits such as ability to use high ash content feedstock, production of tars with lower tar dew (implying lower intake temperatures could be used), and so on.
5. And finally and most importantly, the high capital and maintenance costs of tar purification systems could be avoided.

Operation with tar laden syngas has been discussed by some authors in the domain of gas turbines due to their ability to operate at high intake temperatures, for example see [52]. However, the capital investment costs and the complexities of gas turbines limit them to large power plants. Additionally, they are much more critical of particulate and other impurities contained in raw syngas, in comparison to IC engines [6]. Thus, the HCCI engine fits appropriately to experiment with this approach, at the reasonable scale of small gasification systems. The following section describes in brief the HCCI engine, followed by a discussion on related works.

1.2.1 The HCCI engine

Consider the schematic representation of the SI, CI and HCCI engines in Figure 1.5. As seen before, the SI engine compresses a premixed homogeneous mixture of air and fuel and at a predetermined position, initiates a spark, which causes

a flame front to propagate throughout the combustion chamber. In contrast, a CI engine compresses only air to high temperatures. Near the TDC, the fuel is injected into the hot air, leading to its spontaneous auto-ignition. The HCCI engine combines the features of the SI and CI engines, where it compresses a premixed homogeneous charge of air and fuel (like the SI engine) to the point of autoignition (like the CI engine).

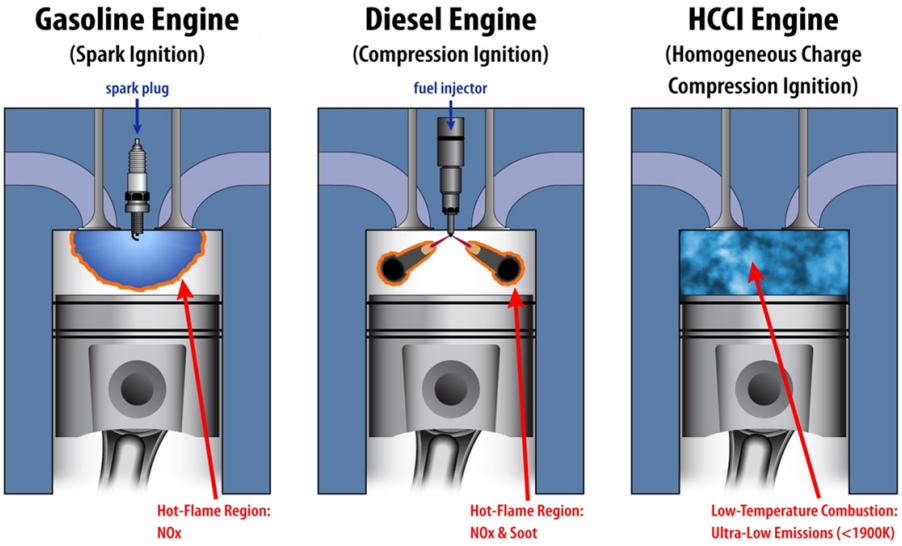


Figure 1.5: *A schematic of the SI, CI and the HCCI engines. (Image credits: Green Research Group of MIT, USA*[1]*.)*

Due to the naturally occurring or induced in-homogeneities present within the combustion volume of the HCCI engine, the initial points of auto-ignition occur only at the hottest regions with the highest local equivalence ratios. These initial auto-ignitions release heat and induce the surrounding regions to auto-ignite, primarily through the process of compression heating and to a minor extent, through the process of deflagration [53, 54]. In contrast to the SI engine, where the unburned end-gas condition must be far from the autoignition condition in order to avoid knocking, most of the gas in the HCCI engine exists close to the autoignition condition. This implies that the rate of auto-ignition driven combustion can become considerably higher than the flame based SI engine combustion. Thus, to avoid rapid and violent combustion, the HCCI mixture is leaned to appropriate levels, often with the fuel to air equivalence ratio in the range of 0.2 to 0.4.

[1] http://cheme.scripts.mit.edu/green-group/wp-content/uploads/2013/11/engines.png

Advantages and limitations of the HCCI engine

One of the significant advantages of the HCCI engine is its low temperature auto-ignition driven combustion which results in very low NO_x emissions, unlike the high temperature flame based combustion of the SI and CI engines. Additionally, the HCCI engine is capable of operating very lean, and thus results in low soot formation. Another advantage is that the auto-ignitions occur almost simultaneously throughout the chamber, thus coming close to the ideal isochoric combustion which holds the promise of increased efficiency. Further, with respect to the subject of this thesis, the HCCI engine can be adapted for a wide range of intake temperature conditions, which implies that this engine technology can burn impure syngas containing tars, without condensing them.

However, the HCCI engine also poses major challenges. One of the main challenges is the lack of a method to initiate the autoignition process in a HCCI engine, unlike the availability of sparking in a SI engine or fuel injection in a CI engine. Control is highly desirable as there always exists an optimum combustion phasing which results in optimal performance at varying conditions. Lack of control implies that many factors influence and essentially shift the combustion phasing away from the optimal. In case of the HCCI engine, this implies that many influencing parameters need to be controlled simultaneously so that combustion occurs at an optimal position. This is further complicated as a result of changing loads or changes in parameters which can not be controlled, such as the time varying syngas composition, as shall be discussed in Chapter 6.

Another challenge is that of combustion efficiency. Autoignition processes are strongly influenced by temperature differences, and may fail to occur at the engine walls which are cooler than the compressed gas. In regions where the surface to volume ratio is very large, like found in the crevice regions, autoignitions may never take place during the cycle. This results in high emissions of partly burnt fuel in the form of hydrocarbons and CO with consequent lower combustion efficiencies. The crevice regions are also responsible for combustion inefficiencies in the SI engine since the stoichiometric mixture enters these regions during compression and combustion and reenters the combustion chamber only during expansion. The flame in the SI engine, being sensitive to the wall temperatures, is quenched at the crevices and fails to burn these gases. When the crevice gases reenter the main chamber, the conditions are less favorable for their combustion, thus leading to combustion efficiencies of about 95-98%. However, in an HCCI engine, the main combustion chamber walls and the consequent boundary layer also contribute to the loss of combustion efficiency, in addition to the crevice regions [55]. In stark contrast to the SI and HCCI engines, due the non-premixed nature of combustion in a CI engine, the crevice regions have negligible effect, thus resulting in higher combustion efficiencies of about 99%.

In the HCCI engine, combustion efficiency increases when higher equivalence ratios are used which lead to higher temperatures and the resulting heat subsequently decreases the effects of colder chamber walls. Due to obvious reasons, higher temperatures of the engine walls (as a result of lesser engine body cooling) can significantly improve the combustion efficiency. And lastly, combustion efficiency is increased when the combustion takes place near or before the TDC where the high temperatures and pressures ensure minimal wall cooling effects. Thus, factors such as the equivalence ratio, intake temperature, species and thermal inhomogeneities, residual gas fractions, wall temperatures being influenced by past cycles and others, and others, need to be monitored and controlled since they have critical influences on the overall HCCI combustion process.

Limits of HCCI combustion

Cyclic variability in the HCCI engine is produced by the many parameters which affect the autoignition process. These phenomena impact the average wall temperatures and residual gas fractions, which in turn influence the autoignition processes in the subsequent cycles. At the lowest limits of the equivalence ratio, the corresponding low magnitude of combustion results in lower temperature increases which in turn fail to autoignite the surrounding gases, unless higher compression states are reached as the cycle progresses. Further, the late and slow combustion may last well into the expansion stages of the compressed volume, where the temperatures decrease and quench the chemical process. In such combustion scenarios, along with higher combustion inefficiencies, the wall temperatures fluctuate cycle-by-cycle and with cycles influencing each other. Additionally, such weak combustion processes also tend to be more sensitive to the many influencing parameters, the combined effect being large cyclic dispersions.

In contrast, if the equivalence ratio or the intake temperature or the compression ratio are too high, the combustion phasing advances and the rate of combustion increases dramatically. The resulting increase in the thermal efficiencies due to the increased pressure volume work area, the increase in the combustion efficiency resulting in the low CO and HC emissions and the higher power availability, soon become overshadowed by the consequences of high pressure oscillations. A summary of HCCI related pressure oscillations or *ringing*, based on articles by Eng [56], Saxena and Bedoya [57], is presented here. Due to the inherent inhomogeneities across the combustion chamber of a HCCI charge, a sequential combustion generally occurs, starting from the most favorable regions to the rest of the chamber. At high equivalence ratios, certain regions experience very high rates of heat release and subsequent volumetric expansion, while other regions experience compression forces due to the lack of combustion. The dynamic and temporal developments of these ‘hotspots’ and

'coldspots' give rise to pressure oscillations traversing the chamber. The end effect appears similar to that of SI engine knock, however the fundamental processes causing these oscillations are different, as elaborated by Eng [56]. The significant effect of these pressure oscillations are that they cause significant audible noise and result in increased wall heat losses, resulting in decreased efficiencies. Thus, limited amounts of fuel can be used in an HCCI engine, resulting in very low IMEP.

Methods to improve the HCCI combustion

In conclusion of the previous discussions, the challenges of the HCCI combustion can summarized as A) Significant control efforts are required to maintain or counter the non-optimal effects of the many influencing factors and B) Due to pressure ringing, the maximum IMEP that can be achieved is severely limited, in comparison to a similarly sized SI or CI engine. To overcome these issues and allow the potential benefits of HCCI combustion to dominate, major research efforts are underway, which can be classified into three major fronts:

Combustion control: Combustion control methods are of great interest which can influence the start of combustion as well as the duration of combustion. The key parameter is the equivalence ratio or the fueling rate which needs to be changed according to the requirements of load. However, to control/counter the resulting shift in the combustion phasing, measures such as modulation of the thermal and species inhomogeneities within the chamber (for example see Kodavasal et al. [58]), modulating the heat capacity of the charge through Exhaust Gas Recirculation (for example, as done in Chapter 5) or dynamically changing the compression ratio (for example see Christensen et al. [59]), have been used. A transitory control strategy has been developed, called the Spark Assisted Compression Ignition, that bridges the gap between HCCI and SI operation through the use of sparking and thus achieves a higher load range and control (for example see Persson et al. [60] and Lavoie et al. [54]). Injection of inert components such as H_2O have also been explored (see Christensen and Johansson [61]). The use of intake boost may also be used, however the primary intention of such an effort is to maximize the IMEP (for example see Olsson et al. [62]).

Fuel properties: Since HCCI combustion essentially depends on the chemical kinetics related to auto-ignition processes, the fuel properties are of critical importance. As seen previously for syngas in Section 1.1.4, the methane number or MN is an important parameter in terms of auto-ignition of gaseous fuels, though not completely representing the syngas properties. Liquid fuels for HCCI engines have been studied, for example see Risberg [63]. Lu et al. [64] give a detailed account of the various aspects of fuels for HCCI applications.

Diagnostic tools: The HCCI engine, in the current state of technology, heavily depends on in-cylinder pressure sensors and associated electronics to monitor the state of combustion. Technologies such as ion current sensing (Vressner et al. [65]) and audio and vibrational monitoring (Cheng et al. [66]) to decipher CA50 values, are some of the techniques being investigated for simplifying the monitoring aspect of this class of engines.

1.2.2 Syngas use in HCCI engines

Based on the discussions in Section 1.1.4 and Section 1.2.1, syngas as an HCCI engine fuel can be expected to offer multiple advantages. In order to achieve auto-ignition, the charge in an HCCI engine requires to be preheated before the compression begins. In the context of biomass gasification, this requirement of the HCCI engine is quite fitting, as the high exit temperatures of the syngas ($\approx 400 - 500°$C from a downdraft gasifier) can be utilized. The proposed method depends on mixing the high temperature syngas with ambient or appropriately heated air to achieve the desired intake temperature above the tar dew point. Also the piping and intermediate devices such as particle filtering cyclones and candle filters will cause the syngas to cool down, thus implying that special heat exchangers for syngas cooling may not be required. Such an arrangement holds the promise of increased thermal efficiency of the power plant. Additionally, the HCCI engine itself has the potential for higher thermal efficiency and lower NO_x emissions compared to a SI engine, which can be another major advantage in this context.

A major benefit of the combination of HCCI engine with syngas is the disappearance of the vast difference between the low LHV of the syngas and the high LHVs of fossil or liquid fuels. This occurs at lean equivalence ratios which are in the domain of HCCI engines, as seen in Figure 1.6. A similar discussion can be found in Haggith et al. [67]. For such comparisons, the *FuelMEP*[2], as shall be formally introduced in Section 3.1 of Chapter 3, is a convenient parameter. The FuelMEP describes the fuel energy content of a fuel+air mixture, but normalized by the displacement of the engine, resulting in a quantity analogous to the IMEP. Eq. (1.1) describes the FuelMEP as a function of the mass weighted LHV (in MJ/kg) of the fuel along with physical state parameters (at some reference state 0) of pressure (p_0), temperature (T_0) and mixture parameters such as the specific gas constant (R_{charge}), the air-to-fuel stoichiometric mass ratio ($\text{AFR}_{m,stoic}$) and the equivalence ratio (ϕ).

$$\text{FuelMEP} = \frac{p_0}{R_{\text{charge}} \cdot T_0} \cdot \frac{\text{LHV}_{\text{fuel}}}{\frac{\text{AFR}_{m,stoic}}{\phi} + 1} \tag{1.1}$$

In Figure 1.6, petrol and syngas (typical composition with LHV=5 MJ/kg) as fuels mixed with air are considered at various equivalence ratios. As the ϕ

[2]Originally developed at LTH, Lund, Sweden.

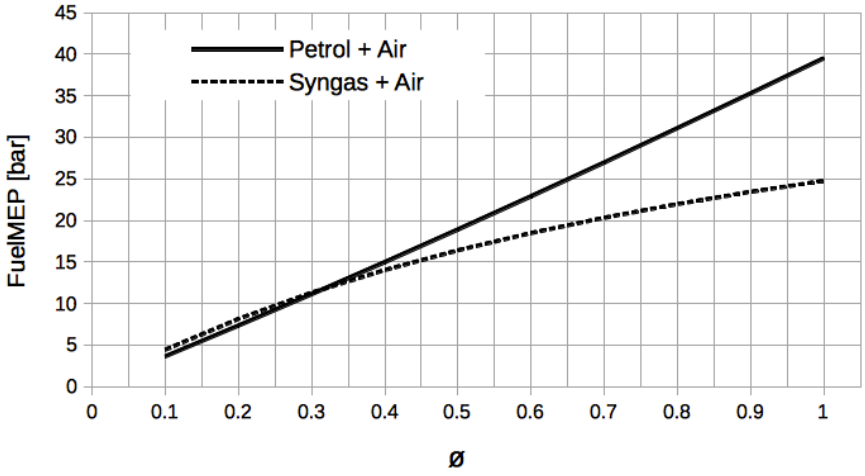


Figure 1.6: *FuelMEP comparison between petrol and syngas mixtures with air, at various equivalence ratios ϕ. At $\phi = 0.32$ the FuelMEPs are equal.*

approaches 0.3, the FuelMEP corresponding to the high LHV petrol becomes equal to that of the low LHV syngas. In further lean conditions, the FuelMEP corresponding to syngas becomes higher than that of petrol. It must be noted that although the difference between the fuel air mixtures are essentially eliminated at these low equivalence ratios, the power derating continues to remain due to the use of low equivalence ratios. Additionally, it is interesting to note that the trend for FuelMEP of syngas is not linear, in constrast to that of petrol. This can be attributed to the very low $\text{AFR}_{m,stoic}$ of syngas ($\approx$1.2) which results in the non-linear term $\text{AFR}_{m,stoic}/\phi$ to have significant impact on the overall value of FuelMEP. Additionally, the R_{charge} does not change for sygnas as a function of ϕ since the molecular weight of syngas being very near to that of air or combustion products. As for the petrol, these non-linear effects are relatively weaker and therefore the FuelMEP trend appears to be linear.

Ref	R_c	RPM	T_{in} [°C]	LHV [MJ/kg]	H_2/CO	H_2/CO_2	ϕ	IE [%]	IMEP [bar]
[68]	24	1500	100	4.4-8.9	1.1-4.28	0.67-4	0.2-0.4	42	3
[69]	22.5	1050	75-145	6.07	1.5	2	0.15-0.28	48	8.3
[70]	21.2	1800	104	-	-	-	0.26,0.3	30	-
[71]	22	1523	130-190	4.26-4.55	0.4-1.33	3-5	0.35-0.46	34	3.45

Table 1.4: *A summary of experimental works regarding the use of biomass syngas in HCCI engines. The LHV values correspond to simulated syngas. Here R_c indicates the compression ratio, T_{in} stands of intake temperature, ϕ stands fo the fuel to air equivalence ratio, IE indicates the Indicated Efficiency while IMEP indicates the Indicated Mean Effective Pressure.*

Syngas as an HCCI fuel has been explored only recently and in relatively small numbers. A common issue studied in this domain concerns the coupling of the varying nature of syngas composition to the inherently sensitive HCCI combustion, which is predominantly driven by chemical kinetics. These syngas variations can be characterized in terms of the variations in the volumetric concentrations of H_2 and CO, represented in the form of H_2/CO ratio. Variations in the inert components of syngas (N_2 and CO_2) also significantly influence the combustion through indirect means by changing the ratio of molar specific heats of the mixture. Table 1.4 summarizes the main parameters of the few papers available in open literature (according to the author of this thesis) regarding the combination of HCCI engines with biomass syngas, which are discussed in brief below.

The first dedicated work, proposing and experimenting with the use of biomass syngas in HCCI engines, as known to the author of this thesis, was conducted by Yamasaki et al. [68]. They carried out a detailed experimental evaluation of the role of various syngas components on HCCI combustion using artificially generated syngas, on a modified SI engine. They found the H_2/CO_2 ratio as having the most significant effect on the combustion timing and duration. H_2 is known to have a low ignition energy and thus has the propensity to burn early in the cycle, at very high rates. On the other hand CO_2 has a low specific heat ratio (about 1.29 at 20°C) which absorbs the produced heat and dampens the combustion rates. The effect of CO was found to contribute only to the amount of heat released and having a very low influence on the combustion rates and timing. This was so because CO-to-CO_2 reactions are sensitive to temperatures and are thus initiated later during the combustion, as elaborated by Aceves et al. [55]. Yamasaki et al. further compared the results between SI and HCCI modes of operation for the same engine, but conducted with different compression ratios (9.5 for SI and 24 for HCCI) and equivalence ratios (0.5-0.8 for SI and 0.2-0.4 for HCCI). The thermal efficiency of HCCI engines were found to be about 10 points higher than the corresponding SI engine for the same amount of indicated work output. However, at the similar values of IMEP, CO and HC emissions were found to be far higher for the HCCI mode than in the SI mode. The low peak combustion temperatures resulting from the lean HCCI operation resulted in negligible NO_x emissions compared to the SI operation. The authors thus showed the important advantages of HCCI to this domain, in terms of thermal efficiency and low NO_x, and disadvantages in terms of CO and HC emissions.

Achilles et al. [69] carried out similar experiments with artificial syngas, based on syngas compositions from the Viking gasifier of Technical University of Denmark (DTU). These experiments were compared with natural gas experiments on the same engine with the same compression ratio. They found that at the same equivalence ratio, natural gas HCCI operation had a longer combustion duration compared to syngas, which can be understood by the high

content of H_2 in the syngas that burns much earlier in a cycle in comparison with the largely CH_4 content of natural gas. This high content of auto-ignition resistant CH_4 also required higher intake temperatures compared to those of syngas. However, the same reasons also resulted in the use of higher equivalence ratios for natural gas compared to syngas, thus producing a maximum IMEP of 9.6 bar for natural gas, compared to the maximum IMEP of 8.3 bar for syngas. At high equivalence ratios with high combustion temperatures, CO emissions of syngas were much higher compared to natural gas, while the NO_x emissions were negligible for both the fuels. For both the natural gas as well as syngas, higher equivalence ratios resulted in higher indicated efficiencies, around 48%. The presence of inert components of CO_2 and N_2 in syngas helped in achieving stable combustion compared to the natural gas operation at similar equivalence ratios. In these experiments the role of compositions were not studied. Intake boosting was found to have a significant positive effect on the IMEP.

Bika et al. [70] studied HCCI combustion fueled by combinations of pure H_2 and CO as representative of syngas from various sources, from fossil coal to biomass. However, the experiments did not include the inert components, CO_2 and N_2, which as seen in the previous works have crucial impact on HCCI combustion. Due to this composition, the values of LHV_{syngas}, or H_2/CO or H_2/CO_2 ratios have not been indicated in Table 1.4. Thus, the results of this work cannot be relevant with the biomass gasification context, but is included here for the sake of discussion on the influences of H_2/CO ratio. Similar to the conclusions discussed previously, increasing the H_2/CO ratio advanced the combustion, while decreasing this ratio required the authors to use higher intake temperatures for realizing combustion. The authors observed high heat transfer losses from the charge to the walls. They postulated that high concentrations of H_2 in the syngas resulted in an increase in the overall thermal conductivity of the charge, which coupled with the high intake temperatures required for HCCI combustion, resulted in increased losses.

Haggith and Sobiesiak [71] carried out simulated syngas experiments with three compositions of syngas. The roles of H_2 and CO were investigated and similar influences, as discussed above, were found. The authors went on to suggest that syngas with lower LHV and lower H_2/CO ratio would be more beneficial for HCCI combustion due to better combustion phasing. However, such syngas compositions would require additional intake temperatures to achieve combustion, and thus decrease the energy density of the intake flow, causing a reduction in the IMEP. Thus, there exists an optimal syngas composition for a fixed set of HCCI operations or vice versa.

Yamasaki and Kaneko [72] in a recent paper carried out detailed numerical simulations studying the influences of fuel as well as inert syngas components on HCCI combustion, along with its validation using experimental results presented in [68]. The *CHEMKIN-PRO*[3] software tool was used in combination

[3]http://www.reactiondesign.com/products/chemkin/chemkin-2/

with *GRI-mech 3.0* reaction mechanism [73]. Simulations showed that the compression temperatures were different for different compositions of syngas, even at the same equivalence ratio and same initial conditions of pressure and temperature before the start of compression. The compositions with higher proportion of CO_2 had lower compression temperatures due to their low ratio of specific heat capacities. The maximum temperature difference, before the onset of auto-ignition at -10 Crank Angle Degrees (CAD) before the TDC, were as large as 30 K between syngas compositions which varied in their H_2/CO_2 ratio from 4 to 0.6. Additionally, the authors showed that, regardless of the compositions, the autoignition temperatures were approximately about 1100 K. Since the ignition timing depends on the temperature, the thermal cooling provided by the inert components, especially the CO_2, can thus significantly delay the combustion process, as well as dampen the combustion rate. In terms of the relative influences of H_2 and CO, the H_2 was observed to burn right after the autoignition (beyond 1100 K) and form the dominant part of the initial heat release, whereas CO reactions were initiated in significant proportions only beyond temperatures of about 1800 K. Further analysis by the authors showed that if the CO concentration in the syngas was increased, contradictory influences on the reaction rates of the main chemical reactions were observed, whereas, if the H_2 concentration in the syngas was increased, the reaction rates for all the reactions increased. Thus, they reinforced the observation discussed in the past works that the CO does not influence the rates of heat release, whereas the H_2 significantly does.

As a conclusion, the works carried out in the domain of HCCI engine fueled by biomass primarily focused on exploring the influences of H_2, CO and CO_2 components on HCCI combustion. However, in the context of this present thesis, the following features regarding these studies can be observed:

1. The main intention of the discussed studies were to explore the viability of HCCI engine as an alternative to the conventional SI engine, but confined to the traditional context of utilizing pure and cooled syngas.
2. Some authors discussed the advantages of high intake temperatures in terms of benefiting from the high enthalpy syngas available from biomass gasification, however, these arguments were not developed further.
3. On the experimental side, due to the intention of using cooled and purified syngas, these works were limited to intake temperatures $<200°C$ and compression ratios >20, to achieve stable HCCI combustion.
4. All the works were carried out using artificially generated *dry* compositions of syngas, which is the case in a traditional context. Thus, there was no mention of the influences of syngas water component on HCCI combustion.
5. And most importantly, there were no mentions of the possibility of using the high intake temperature potential of the HCCI technology for addressing the tar related issues of biomass gasification.

The work of this thesis therefore differs significantly from the aforementioned works. Here the attempt is towards developing a system with the primary aim of achieving a tar tolerant operation. To this end, the HCCI technology has been chosen, and as a result, specific challenges from the domain of HCCI engines as well as biomass gasification arise. Amongst these challenges, some would require studies similar to the aforementioned works with purified syngas, whereas, others would be completely specific to this approach.

1.2.3 Foreseeable challenges

In order to appropriately place the work of this thesis, the foreseeable challenges in this pathway need to be considered:

Efficacy of tar tolerance: Although, in principle, the operation at high temperatures would avoid tar condensation, this ability could be challenged by the fact that operational constraints may require the engine body to be operated at much cooler temperatures, and thus may lead to some chances of tar deposition. Additionally, the subsequent destruction of tars through combustion may be hindered by pockets of incomplete combustion, which are a major cause of CO and HC emissions in the HCCI engine [55]. The measurement of tar deposits in the engine would require experiments with long hours of operation with tar loaded syngas (for example as carried out in [25]). Additionally, to assess the destruction of tars through this process, GC/MS measurements at the intake and the exhaust of this engine could be carried out. The high temperatures of combustion may also lead to the polymerization of tars into soot particles, which can add to the concerns of potential engine damage and emissions, thus needing further attention. Although of grave interest in the context, the issues of experimentally verifying the tar tolerance capabilities were not within the scope of this thesis work.

Power de-rating: The issue of power de-rating shall be a significant limitation of this approach. This would arise primarily due to the utilization of an HCCI engine which is associated with its limited load range. This would be further worsened by the high intake temperatures required for the successful avoidance of tar related problems. To match the performance achieved by the SI engine used in this domain, a significantly larger HCCI engine would thus be needed, unless, the power derating issue could be addressed by other means. One possible way could be through boosted HCCI operation. However, the use of compressors with high temperature tar loaded syngas seems a difficult challenge by itself. An effective solution thus could be to use this concept along with pressurized gasification, thus allowing boosted operation without use of compressors or turbo/superchargers.

Maturity of the current HCCI technology: The maturity of HCCI engine has been discussed previously in Section 1.2.1. The viability of this concept will be governed by the economics of operation in comparison to the traditional SI engine which does not require installing special control and monitoring equipments, as shall be needed for ensuring optimal operation with the current state of HCCI engine technology.

Varying syngas compositions and operating conditions: In contrast to other fuels, the composition of syngas is not fixed in time. This would directly effect HCCI operation. This forms the subject of the works discussed in the previous section. However, raw syngas would also contain moisture and tars which would additionally influence the combustion. Since HCCI combustion is influenced by previous cycles through the presence of *wall temperature histories*, the time varying aspect could turn out to be additionally complex.

HCCI phasing control: HCCI combustion phasing needs to be maintained near optimal, so as to have a decent operation in the face of varying operational conditions. This could be achieved through the use of techniques such as EGR or varying in the intake temperature or the compression ratio.

1.2.4 Thesis outline

Of the challenges mentioned above, only the last two could be explored in this thesis. The work of this thesis has thus been divided into the following chapters:

Chapter 2 discusses the test bench constructed for experiments of this thesis.

Chapter 3 discusses various post-processing methodologies used throughout this thesis for evaluating the experimental data.

Chapter 4 studies the influences of artificially created syngas compositions, including moisture and tars, along with controlled intake temperatures and pressures on HCCI combustion under conditions relevant to the concept. The use of artificial mixtures and operating conditions ensures that the experimental procedures are characterized by repetition, reliability and precise control, so that the main tendencies between the causes and their consequences appear clearly.

Chapter 5 studies the use of EGR as a HCCI combustion control technique. These studies were again carried out with artificial syngas as well as artificial EGR, for the same reasons as discussed for Chapter 4.

Chapter 6 discusses experiments with real syngas from a real gasifier as used in the HCCI engine at the conditions relevant to this concept. However, the real syngas in its cooled and purified form was used due to the technical feasibility of such operations. This gas was heated at the test bench to simulate the intended above tar dew point operating conditions.

Chapter 7 summarizes the main conclusions of this thesis and reflects on the viability of the concept. It also discusses some of the ongoing and planned works in this direction.

Chapter 2

Experimental Setup

The objectives of setting up a test bench were:

1. Ability to create various compositions of syngas, which may include moisture or tar components.
2. Allow a homogeneous mixture of air and syngas to enter the engine at temperatures up to 270°C, at a wide range of equivalence ratios and at speeds up to 1500 RPM.
3. Record high-resolution (0.1 crank angle degrees) in-cylinder pressure data along with other important details, such as exhaust emissions and intake conditions of pressure and temperature, in order to produce heat release curves.

The aim of this chapter is to present the general characteristics of the test bench, while specific modifications according to the requirements of different experiments are elaborated in their respective chapters. This chapter been split into two parts. Section 2.1 discusses the mechanical section of the test bench which includes a single cylinder engine and an electric motor/brake. This is followed by a discussion on the instrumentation hardware in Section 2.2, which also includes the control and acquisition hardware.

2.1 The test bench hardware

The characteristics of an experimental test bench which would allow for the desired experimental investigations, were not known beforehand. Therefore, a design study was necessary, which had been accomplished before the beginning of this thesis by F. Contino and is discussed in detail in [74, 75]. Here, for the sake of continuity, only the main results of the aforementioned design study are presented. This is followed by a description of the actual test bench.

Base Engine	Diesel
Displacement	500 cc
Piston crown shape	Shallow bowl
RPM	1500
Compression ratio range	10 to 13
Intake pressure range	1 to 1.2 bar
Equivalence ratio	0.5 to 0.7

(a)

N_2	0.48
CO_2	0.11
CO	0.22
H_2	0.18
CH_4	0.01
LHV_{syngas} [MJ/kg]	4.52

(b)

MPRR	<10 bar/CAD [80]
CA50	-5 to 10 CAD [80]
Maximum pressure	<100 bar

(c)

Table 2.1: *CFD simulation input parameters and constraints used to determine the main characteristics of the test bench. (a) Idealized engine parameters. (b) Syngas composition. (c) CFD simulation constraints.*

2.1.1 Determination of critical parameters

One of the most critical design parameter is the compression ratio (R_c) which significantly affects engine performance and in the case of HCCI engines, would directly affect the combustion timing and duration. Thus, numerical studies using Computational Fluid Dynamics (CFD) were carried out by Contino et al. using the Tabulation of Dynamic Adaptive Chemistry (TDAC) method [76, 77, 78, 79]. The CFD techniques outperform zero dimensional models as they better estimate the heat release rates while taking into account the temperature inhomogeneities occurring due to wall heat transfers. Contino et al. have validated the current methodology in various contexts and have shown that it can be used to predict the maximum pressure and Maximum Pressure Rise Rate (MPRR), as well as ignition timings [76, 77, 78, 79].

The evaluated configuration of engine and gas composition are presented in Table 2.1. The inputs of compression ratio (R_c), equivalence ratio (ϕ) and the intake pressure (p_{in}) were adjusted so that the constraints given in Table 2.1c were satisfied. Based on these constraints, the CFD studies predicted that R_c=12 would be suitable for p_{in}=1.2 bar at an upper limit of $\phi = 0.5$.

The next section describes the features of the test bench, built around the important value of compression ratio determined from the CFD studies.

2.1.2 The experimental Test Bench

A schematic of the experimental test bench is shown in Figure 2.1. The discussions in this section are based on the schematic representation, while a few images of the test bench are embedded in support of the schematic.

An air-cooled single cylinder diesel engine was selected for carrying out the

modifications which would result in an appropriate HCCI engine. The base engine was originally a diesel engine for industrial use and thus had a rigid construction. Being air-cooled and of single cylinder configuration, this engine offered ease of machining and instrumentation (see Figure 2.2a). The cylinder head was machined for mounting a pressure sensor (see Figure 2.2b). The standard piston with deep bowl, as seen in Figure 2.2c, was modified into a shallow bowl shape, as seen in Figure 2.2d. Since, HCCI engines are known for high emissions of CO and HC from the crevice regions due to lack of favorable autoignition conditions in those regions [55], the piston was machined to have a minimal crevice region. Also, in order to avoid excessive heat losses and the consequent cooling of the gas mixture (so as to avoid tar condensation), a low turbulence shallow bowl piston crown design was adopted, as seen in Figure 2.2d. The original compression ratio was reduced from about 19 to the required 12, as discussed in Section 2.1.1 above. Additionally, the diesel injector was replaced by a spark plug (see Figure 2.2b) in order to examine spark assisted HCCI, but experiments in this regard were not carried out in this study. The specifications of the modified engine are listed in Table 2.2.

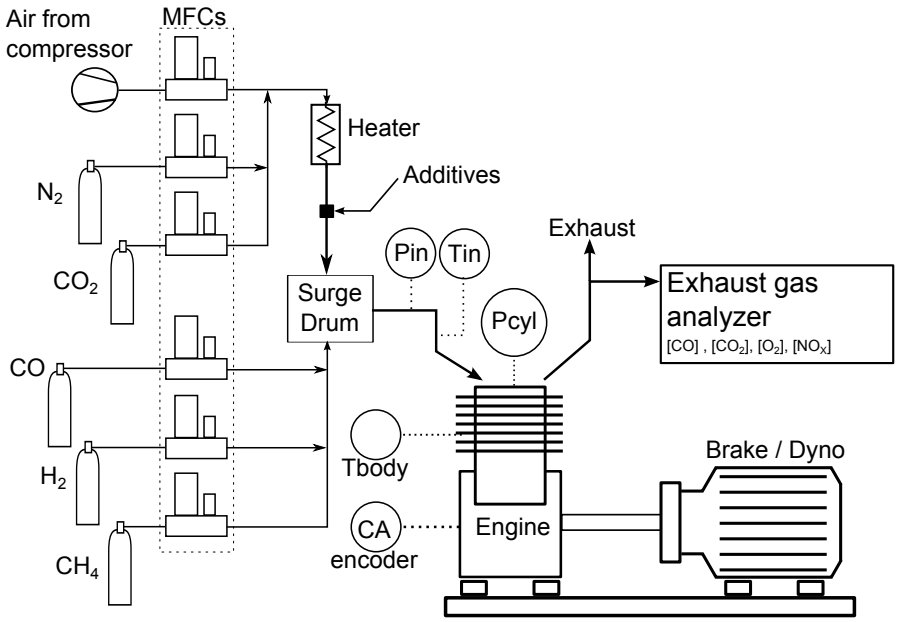


Figure 2.1: *A schematic representation of the HCCI test bench.*

Engine Type	Air cooled, Mono-cylinder 4-stroke, Diesel
Make	Yanmar L100V
Displacement	435 cc
Original Compression ratio	19
Modified Compression ratio (R_c)	12
Intake valve closure (IVC)	53° aBDC
Exhaust valve opening (EVO)	53° bBDC
Bore	86 mm
Stroke	75 mm
Length of conrod (L)	120.5 mm
Crank radius (r)	37.5 mm

Table 2.2: *Specifications of the HCCI engine.*

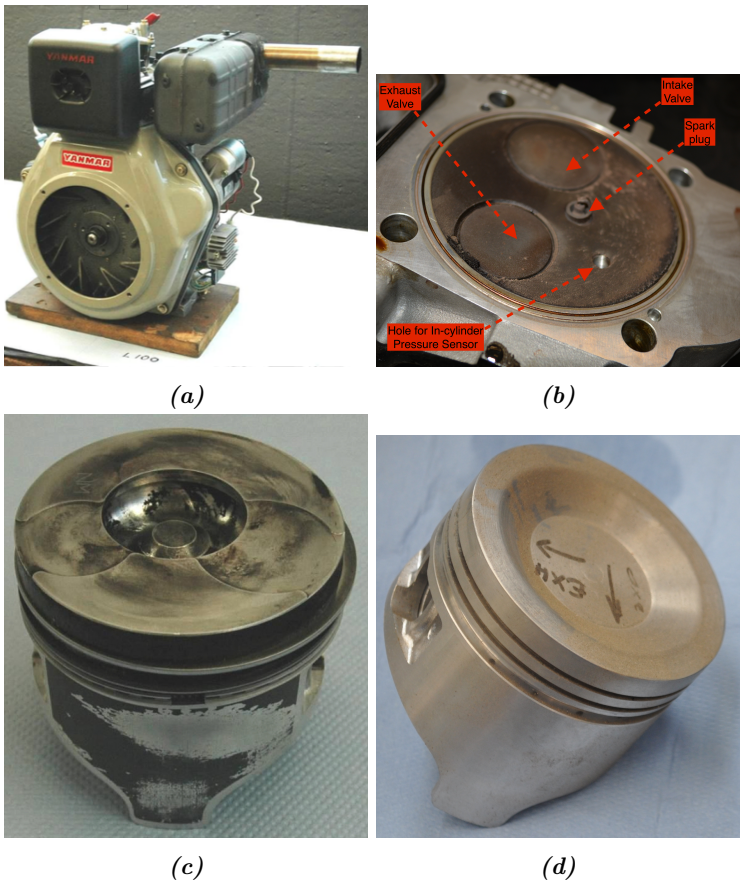


Figure 2.2: *(a) The original single cylinder air-cooled engine, Yanmar LV100. (b) The flat cylinder head which was machined to include a pressure sensor.(c) The original piston with $R_c = 19$ and a high swirl crown design. (a) The modified piston with $R_c = 12$ and a low turbulence shallow bowl design.*

As seen in the schematic Figure 2.1, six Mass Flow Controllers (MFCs) supply all the gases required for the test bench operation, when experiments with simulated syngas are carried out. The air MFC is connected to an air compressor, while the other MFCs are supplied with gas bottles. These MFCs are controlled digitally through a single RS432 communication channel in a multi-drop configuration. The gases are supplied at ambient conditions and at about 7 bar pressure. Figure 2.3 shows an image of the 6 MFCs, of which 5 are connected to their respective bottles while that of the air is connected to an air-compressor.



Figure 2.3: *The major part of the experiments were carried out using simulated syngas of various compositions. The test bench has six mass flow controllers of which the first one is for air, while the remaining are for syngas.*

The intake side of the test bench can be seen in Figure 2.4. Once let into the system by the MFCs, the air and the inert components of syngas, N_2 and CO_2, pass through a 2 kW electric heater with an upper limit of 400°C. A 3-way flow splitting valve (electronically controlled) has been added to the air and inert gas flows such that some of gases can bypass the heater. This allows for a fast control of the intake temperature of the engine. However, this feature of the test bench was not used in any of the experiments discussed in this thesis, but may form part of a future investigation into the development of HCCI combustion control strategies. Further, the hot gases mix with the cold fuel gases from another line in a simple T-junction. This mixture enters a 10 liters capacity surge drum that can be assumed to create a homogeneous mixture and also act as a buffer to absorb the oscillations of the engine intake.

In addition to the MFC flows, additives such as water or tars can be injected into the system, through the additives port just before the surge tank (see the

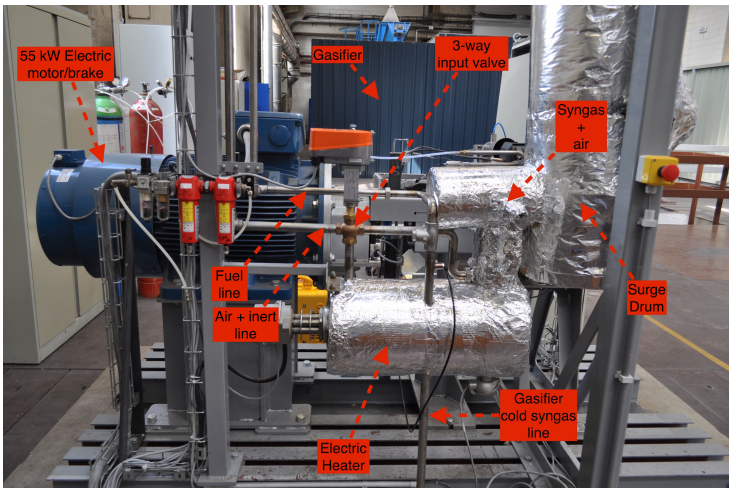
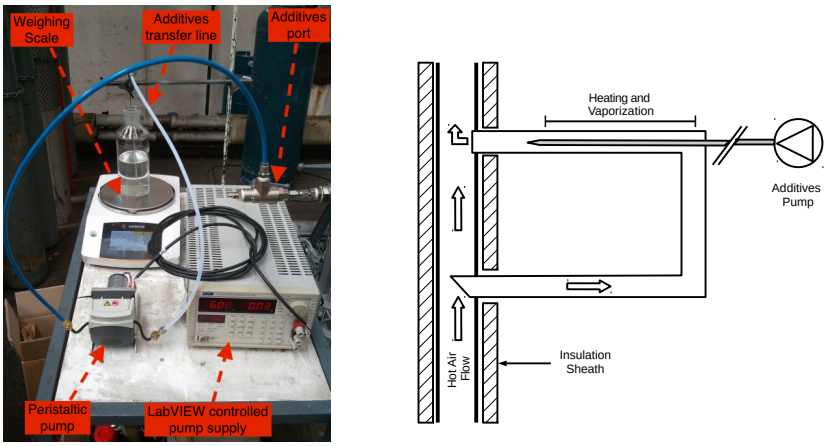


Figure 2.4: *A view of the test bench from the intake side. The air and the inert components of the syngas (N_2 and CO_2) pass through a 2 kW electric heater. The cold fuel components of syngas (H_2, CO and CH_4) mix with the hot air, N_2 and CO_2 flows at a 'T' junction before entering a surge drum. For experiments in Chapter 6, real syngas from the gasifier (seen in the rear of the test bench) has been used, which is sucked from the gasifier through a special pipeline, as pointed at the lower right of the image.*

schematic in Figure 2.1). For high flows, such as that required for simulating the moisture content of syngas, a peristaltic pump was used, as shown in Figure 2.5a. The in-house developed/assembled peristaltic pump can be controlled through a variable power supply, which itself can be controlled through the LabVIEW control software. As seen in Figure 2.5a, the peristaltic pump water from a flask at a constant rate and injects it into the air+syngas flow. The rate of water drawn can be measured from the change in weight of the flask with time, as measured by a high sensitivity electronic mass balance. For small volume flows, such as for simulating the tar content of the syngas, a syringe pump was used instead of the peristaltic pump. Figure 2.5b shows how the liquids (water or tars) are injected into the system. A diagonally cut tube is inserted into the hot air/CO_2/N_2 flow downstream the electric heater, such that some of the hot gases are directed into the insert. This small flow of hot gases heats up a narrow tube through which the liquid additives are pumped, forming vapors of the liquids which are carried on to the main flow. In the main flow, any remaining droplets of additives are vaporized. Thereafter, the large surge tank ensures the homogeneous mixing of all the gases.

The mixtures of syngas and air at high temperatures can be very dangerous because of the low flammability limit of H_2 gas. Also, during strong combustion events occurring at the engine, hot gases can flow back into the intake tubing, which can increase the chances of an explosion. Thus, the surge drum, for safety



(a) *(b)*

Figure 2.5: *(a) A peristaltic pump is used to simulate the moisture content of syngas. It draws water from a flask on a weighing scale, the change in which over time gives the flow rate of the water. In a similar fashion, a syringe pump (not shown in the figure) is used to simulate tars. (b) Schematic of the way additives such as tars and water in liquid form can be injected into the system.*

reasons, is equipped with a safety valve, as seen in Figure 2.6, that is designed to vent out excess pressure to the atmosphere, if the pressure inside crosses beyond 2 bar (absolute). Often, due to the debugging and learning curve undergone by the author during the course of programming the LabVIEW control system (discussed in the Appendix Section A), high equivalence ratios of syngas and air mixtures have been mistakenly injected into a running engine system (high intake temperatures), consequently leading to a few number of explosions. But thanks to the safety valve, these explosions were easily vented towards the high sealing of the laboratory, thereby mitigating any harm. Further, downstream of the drum are the intake pressure and temperature sensors. In Figure 2.6, the large distance between the engine and the intake pressure sensor must be noted. Additionally, the pressure sensor is connected to the intake runner through an intermediate needle valve (not clearly visible in the figure) which can be adjusted so that the sensor registers only a long time average of intake pressure. This approach was chosen due to the fact that a single cylinder engine would have high amplitudes of intake pressure oscillations which would lead to spurious intake pressure readings. As for the intake temperature sensor (k-type thermocouple not visible in the image), it is placed very near to the intake valve opening to record accurate intake temperatures.

The modified Yanmar engine can be seen in Figure 2.6. An adjustable opening to the engine flywheel-cum-fan has been attached, to control the surface temperature of the engine cylinder. This is necessary since the HCCI combustion is highly sensitive to engine wall temperatures and thus, for consistency

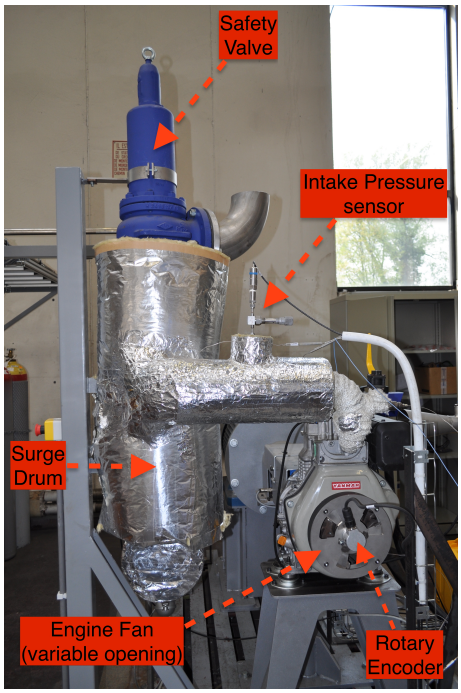


Figure 2.6: *A front facing image of the test bench showing the modified Yanmar engine which is connected to a 10L surge drum which has a large safety valve attached to it. The air-cooled engine's body temperature can be controlled by adjusting the fan opening manually. The rotary encoder provides the basic clock pulse timing which the pressure sensor-charge amplifier (not shown in the figure) uses to sample the in-cylinder pressures. An intake pressure sensor is mounted at a distance from the intake valve opening to avoid transient pressure data.*

during the experiments, the body temperature is controlled using this contraption. It must be noted here that the engine cylinder temperature is measured at the engine surface (approximately at the mid position of the full piston stroke), and thus is not an accurate representation of the in-cylinder wall temperatures. However, since the objective is to have consistency, this approach suffices. The Figure 2.6 also shows the rotary encoder, which will be seen in more detail in Section 2.2.2.

Figure 2.7 shows the test bench from the exhaust side. The exhaust emissions are sampled by a high temperature sampling probe and intermediate sampling system which will be discussed in detail in Section 2.2.1. The engine is driven by a WEG 55 kW three-phase induction motor which acts as a brake as well as a motor. The reason why such a large motor was selected, compared to the small power of the Yanmar engine was because it is planned that the small engine would eventually be replaced by a larger 4-cylinder engine. A Mitsubishi FR-A741-55k frequency inverter controls the RPM as well absorbs

any power generated by the engine by delivering it to the grid.

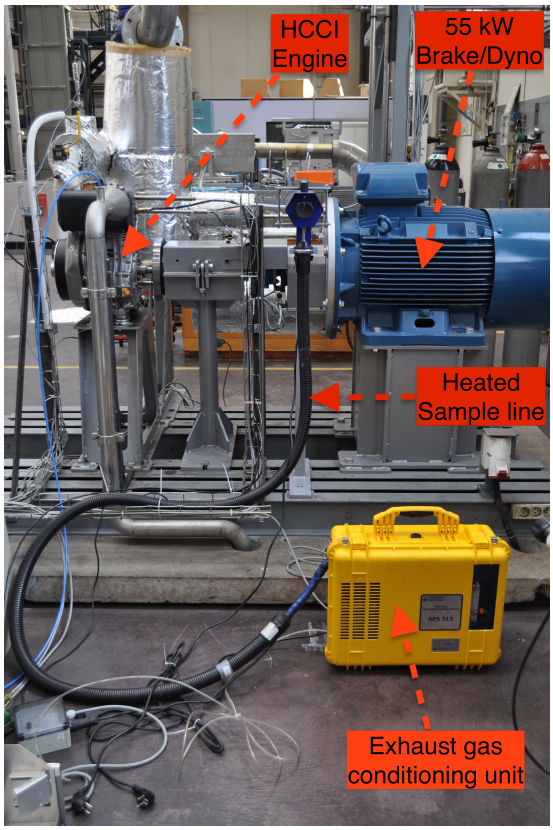


Figure 2.7: *The side view of the test bench showing the HCCI engine on the left and the 55 kW electric brake/dyno on the right. It also shows the exhaust sampling and conditioning unit for emission measurement.*

2.2 The instrumentation

An overview of the instrumentation hardware and software used in the test bench is presented in a simplistic form in Figure 2.8. The National Instrument (NI) hardware and software combination interfaces between the human operator and the test bench. The operator exercises some controls based on the visible information on the LabVIEW® front end which displays relevant data from the online processing of data acquired from the acquisition section. The controls are directed to the various instruments on the far right of the figure which modulate the flow, or the intake temperature or regulate the RPM of the engine. The test bench responds to these controls which are detected by respective sensors and subsequently the data is acquired by the acquisition sec-

tion. Based on the discretion of the operator, the overall data can be recorded into the hard disk for later offline post processing, which forms the subject of Chapter 3.

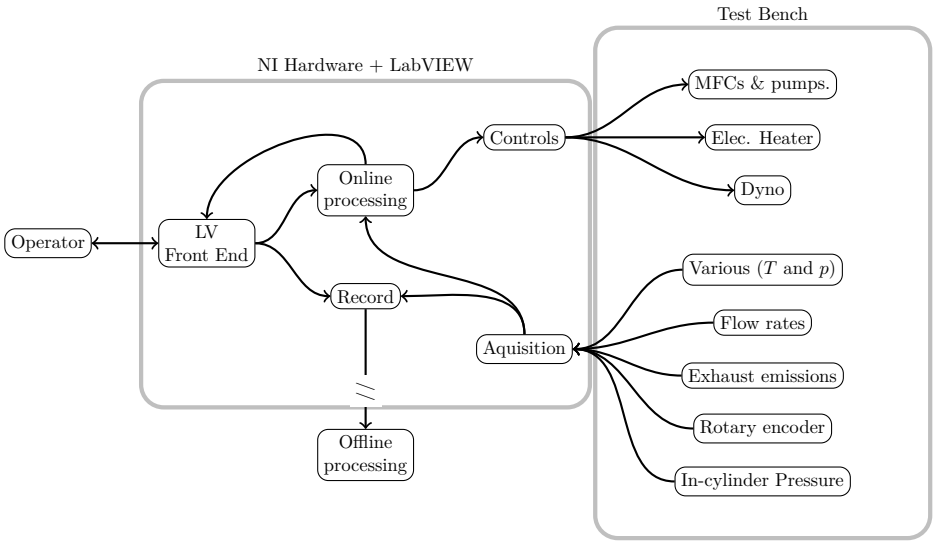


Figure 2.8: *An overview of the test bench instrumentation hardware and software controls. The latter have been implemented in the LabVIEW® environment.*

In the following sections, the instruments of control and acquisition are discussed while the last section discusses the National Instrument data acquisition and control hardware. The major acquisition and control equipments are listed in Table 2.3 and split according to their operational speeds into slow and fast instruments.

2.2.1 Slow instruments and controls

In slow instruments, the acquisition of data is carried out at low frequencies. The slow data is averaged over 10 seconds, with 4 samples acquired each second, resulting in a moving average of over 40 samples. The major slow acquisition instruments are the MFCs and the Exhaust Gas Analyzer (EGA). The MFCs accept control inputs as well as carry out measurements on the flow and thus return the measurement outputs. Using MFCs and pumps, the critical parameters such as the equivalence ratio (ϕ) and the intake pressure (p_{in}) can be controlled. The EGA measures the emissions after the combustion process and gives data about O_2, CO_2, CO and NO_x concentrations in the exhaust. Here it must be noted that even though the syngas contains some amount of CH_4, the HC measurements were not carried out in the exhaust due to a lack of the required equipments. However, since the CH_4 content is less than 1% by volume in the syngas, and the operation is lean, it can be assumed that the

	Instrument	Make/Type	Details
Slow Controls	RPM	Mitsubishi FR-A741-55k	0-400 base + 0-120 control
	Electric Heater	Ohmewatt bvba/sprl	15-400°C + PID control
	Mass Flow Controllers	Brooks Nv.	Air : 180 nL/min
			N_2 : 55 nL/min
			CO_2 : 15 nL/min
			CO : 25 nL/min
			H_2 : 25 nL/min
			CH_4 : 1.5 nL/min
	Peristaltic Pumps	Inhouse	≈ 2-5.5 g/min
	Syringe Pumps	Inhouse	≈ 0.17-0.4 ml/min
Slow Acq.	Intake Pressure	Kistler 4260	0-5 bar(abs.) range
	Exhaust Pressure	Kistler 4260	0-5 bar(abs.) range
	Intake Temperature	K-type Thermocouple	0-400 °C range
	Body Temperature	K-type Thermocouple	0-400 °C range
	Exhaust gas analyzer	Testo 350 M/XL	$[O_2]$: 0-25%
			$[CO_2]$: 0-50%
			[CO] : 0-20,000 ppm(% Vol)
			[NOx] : 0-100 ppm (% Vol)
Fast Acq.	Rotary encoder	Heidenhain ROD 426	3600 div./cycle
	In-cylinder Pressure	AVL GH15D	0-250 bar (abs.) range
	Charger Amplifier	AVL FlexIFEM 2P2E	0-14400 pC (720 bar max)

Table 2.3: *Major acquisition (*Acq.*) and control instruments used in the test bench.*

lack of HC measurements should not cause significant errors in the analyses.

Although the equivalence ratio, ϕ, can be determined from the MFCs and the pump values, a relatively independent determination of the equivalence ratio can be carried out by combining the intake flow data from the MFCs and pumps with data from the emissions through the formulation of a Balanced Chemical Equation (BCE), as shall be seen in Chapters 4 and 5 and their respective appendices. The resulting equivalence ratio, ϕ_{BCE}, must ideally be the same as ϕ for cases where there are no additional inputs, such as Exhaust Gas Recirculation (EGR). In reality, however, minor differences can exist and these differences can help in identifying instrumental faults or process uncertainties. This aspect of the *closure of the BCE with known intake flows and exhaust emissions* was one of the most problematic challenges faced with the current setup and which ultimately resulted in identifying faults with an old EGA device used previously, before settling for the current EGA, the Testo 350 M/XL.

Additionally, the gas sampled at the engine exhaust at temperatures >200°C may contain non-negligible concentrations of engine oil and particulate matter and significant concentrations of water, which can damage the analyzer. Although the Testo analyzer has an in-built gas conditioning system, it was realized that it would be safer to add an external dedicated Exhaust Gas Conditioning Unit (EGCU) to ensure the best precision of the output data as well

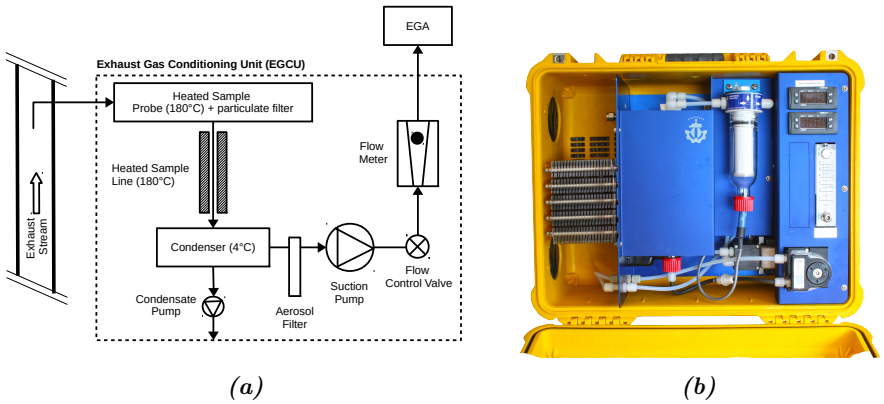


Figure 2.9: *(a) A simplified schematic of the Exhaust Gas Conditioning Unit (EGCU) used to sample and condition the exhaust emissions before being measured by the Exhaust Gas Analyzer (EGA) (b) Internals of the EGCU, called the Ankersmid Portable System (APS), manufactured by Ankersmid Sampling in Belgium. (www.ankersmidsampling.com)*

as safeguard the operation of the EGA for long term testing. Accordingly, a modular EGCU was purchased from Ankersmid Sampling, Belgium. As seen in Figure 2.9a, a suction pump of the EGCU creates a suction at the end of a sample probe inserted into the exhaust stream. The sample probe is equipped with a particle filter (2 μm) and is heated to temperatures of about 180°C. This ensures that vapors of the engine lubricant and water in the exhaust gases remain in their vapor forms and do not clog the filter surface, while at the same time allowing the filter to block any particulate matter. A heated sample tube (up to 180 °C) connects between the sampling probe and the sample EGCU, to ensure that the vapors (of oil and water) do not condense anywhere in the sample line and obstruct the flow. At the EGCU, the sample gases are cooled, from 180 to 4°C, by passing them through a 2-stage Peltier cooling unit. A continuously operating peristaltic pump removes the condensate. The cleaned sample gases pass through the suction pump on their way to the EGA. An intermediate flow control valve along with a flow meter allows for the adjustment of the net flow according to the requirements of the EGA input. Experiments detailed in the first two experimental chapters, Chapter 4 and Chapter 5, were carried out without the EGCS, which was acquired only later and used for the experiments covered in Chapter 6.

2.2.2 Fast instruments

The main fast acquisition parameters comprise of the in-cylinder pressure measurement system and the rotary encoder. The in-cylinder system consists of a piezoelectric pressure sensor and a charge amplifier. The in-cylinder pres-

sure sensors are designed to have a high accuracy and bandwidth, along with high tolerance to harsh temperatures and environmental conditions. When the cylinder pressure changes, the flexing of the diaphragm of a piezoelectric sensor causes a charge to develop on it. This charge is sensed by the charge amplifier which amplifies and converts it into a scaled voltage, acquired by the data acquisition system. Since the charge on the sensor decays due to self-discharge, the sensor-amplifier combination cannot measure static pressure but only dynamic pressure changes, necessitating the use of additional post processing of the amplified signal, as shall be seen in detail in the Section 3.3.3 of Chapter 3. So that the pressure information could be acquired, stored and used in computations, it needs to be sampled to create a discrete set of sequential data. In the current implementation, a 3600 pulses/cycle rotary encoder attached rigidly to the main engine shaft (see Figure 2.6) provides the triggers for the pressure acquisition system, resulting in 90 kilo samples/second of pressure data rate at an RPM of 1500.

The rotary encoder outputs square-wave signals on three channels A, B and Z. Signal A provides a rising edge with 3600 equally spaced pulses for each revolution of the encoder shaft, while the signal from channel B is similar to A, but is phase shifted by 90 degrees. This availability of shifted signals allows for easily detection of the direction of rotation. The third channel, Z, outputs a single pulse for every 360° rotation of the shaft. The encoder is mounted on to the shaft in such manner so that the signal Z peaks as near as possible to the Top Dead Center (TDC) position. This TDC reference signal is crucial to interpret the relative positions of signals from channels A and B so as to determine of the crank angle degrees of rotation. However, inaccuracies in the mounting of the encoder necessitates further post-processing as described in the next chapter in Section 3.3.2.

All these instruments are interfaced through a National Instrument (NI) controller and acquisition hardware which is discussed in the following section.

2.2.3 The NI hardware

A control system for the test bench must have the following features:

1. High rates of data acquisition.
2. Continuous data storage and fast processing times.
3. A human interface to monitor the parameters.

A real-time operating system with deterministic Input/Output (IO) capabilities is needed for such applications. The large amount of data acquisition and live processing is possible with Field Programmable Gate Array (FPGA) systems where the logic can be hard-wired into the hardware with the ease of programming. Due to these reasons, the NI CompactRIO system was found to be appropriate for the application.

NI hardware	Part. label	Notes
CompactRIO	cRIO-9022	FPGA
Chassis	cRIO-9114	8 slots
Analog input	9205	32 ch multiplexing
Analog input	9215	16-bit 4-ch independent, for pressure
Analog output	9264	4-ch independent
Digital input	9425	32-ch.
Digital input (high speed)	9411	6-ch. for CAD
Digital input (high speed)	9411	6-ch. for torque
Digital output	9476	32-ch.

Table 2.4: *National Instrument data Acquisition and Control hardware used in the test bench.*



Figure 2.10: *The CompactRIO real-time embedded industrial controller containing 8 cards for various data acquisitions and controls interfaced by an FPGA.*

The CompactRIO system is an embedded controller system containing an inbuilt Real-Time (RT) processor which can be coupled to a reconfigurable FPGA unit and wide variety of IO modules. The RT module provides deterministic communication with the downstream FPGA unit that has a high bandwidth interface with IO modules, along with providing fast computational abilities. Additionally, the CompactRIO can interface with a host PC to provide the human interface or front end. In Figure 2.11 the structure of such a system is depicted. Essentially the FPGA is programmed to become a hard wired circuit, but without the problems of huge labor that would be required to produce such a system. In other words,the FPGA adds a layer of abstraction to the complicated electronics and liberates the user with a generic motherboard that can be programmed for a wide range of applications.

The programming is done on the host computer using LabVIEW RT and FPGA modules and is transferred to the VxWorks RT Operating System (RTOS) that the CompactRIO controller runs on. The FPGA code is converted into Hardware Description Language (HDL) and set onto the FPGA. Special loops are used within the programming of both the RTOS and the FPGA to lay down the priorities and loop timings, which must be performed

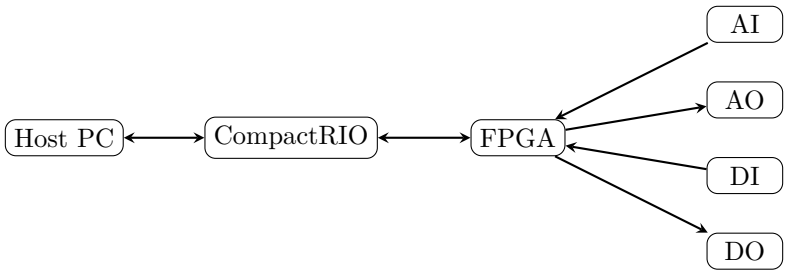


Figure 2.11: *The NI CompactRIO hardware structure*

in predetermined time without fail. The predetermined times can be calculated based on known operating frequency of the in-built clock of the controller. If a certain loop fails to achieve the set time, it passes error messages thus indicating the programmer to improve the programs into more efficient ones and retry. The resulting acquisition, processing and control logic has very low latency and high robustness and reliability.

The CompactRIO controller module has a 533 Mhz processor with 256 mb DRAM and 2 GB of storage capabilities. This module is attached to a 8-slot chassis (NI 9114) which includes the Xilinx Virtex-5 Reconfigurable I/O (RIO) FPGA unit. Additionally, the 8 modules listed in Table 2.4 make available all the IO ports to which numerous instruments listed in the previous sections are connected. A host computer, running Windows® 7 OS is attached to the CompactRIO system (CRIO+chasis+IO modules) which is loaded with the LabVIEW® software platform to program as well as to function as an interface. An Ethernet connection allows communication as well as data transfer from the limited memory of the CompactRIO system to the host PC.

The 32 channel AI module is used for all the slow processes. It was however found unsuitable for the high speed pressure data as this module acquires its data through a multiplexing algorithm that scans through the 32 channels while using the same Analog to Digital Converter (ADC) unit. Thus, although the native sample rate of this module is 100 kS/sec, the multiplexed rate is in effect divided by 32 and thus does not match the requirements. Additionally, the multiplexing causes a phenomenon called 'ghosting', where the signal of a previously sampled channel influences the currently sampled channel. Due to this, an additional 4-channel dedicated AI module was used for pressure measurements where each of the 4 channels are mutually independent and can function in parallel at 100 kS/sec. Similarly, with the 32 channel DI, the high speed of acquisition from the rotary encoder required use of a separate DI module with 2000 kS/sec sampling frequency. For precise acquisition of torque signals, an additional high throughput DI card was used.

The logic of accessing the mentioned instruments and connecting them with each other passing through computations is programmed into the controller and

the FPGA using the National Instrument's LabVIEW programming environment. The schematics and a brief overview of the codes developed for this test bench can be found in the Appendix A

Chapter 3

Post-Processing of experimental data

The main aim of the experimental setup and post processing is to obtain an understanding of the HCCI combustion process through the evaluation of experimentally obtained in-cylinder pressure data. The computation of the Rate of Heat Release (RoHR) provides values such as the CA50 and the combustion or burn duration (CA_{90-10}), which help in judging the quality of combustion when correlated to parameters such as the Combustion Efficiency (CE), the Indicated Efficiency (IE), the Indicated Mean Effective Pressure (IMEP), amongst others. The computation process requires that the pressure-volume data be well calibrated and filtered which necessitates a non-trivial processing of the raw experimental data. And finally, all the computations can only be valid if the associated uncertainties are evaluated and presented.

This chapter is split into four parts. Section 3.1 gives a summary of the basic definitions and formulations used in this thesis, with parameters like the ϕ, CA50, CA_{90-10}, IE, IMEP and others. Section 3.2 elaborates the main objective of the post processing effort, which is to compute the RoHR and derive important combustion metrics from it. Section 3.3 discusses the main calibration processes which go into transforming the raw pressure data. This includes calibrating/determining the compression ratio, the TDC error in the crank angle sensor, pegging procedure and filtration of pressure data. And the last section, Section 3.4, presents some evaluations of uncertainty in the experimental data.

3.1 General formulations

This section describes the various terms and definitions used throughout this thesis. The aspects of engine geometry are first defined. Consider Figure 3.1,

where a typical pressure curve has been plotted as a function of the Crank Angle Degree (CAD). The various valve positions such as the Intake Valve Closure and Opening (IVC and IVO) and the Exhaust Valve Closure and Opening (EVC and EVO), have been marked. It must be noted here that the IVC is much later than the Bottom Dead Center (BDC) position at -180 CAD and the difference amounts to 53 CAD. Similarly, the EVO is 53 CAD earlier than the BDC of the expansion stroke. Also, there is a significant positive valve overlap of 40 CAD between the IVO and the EVC.

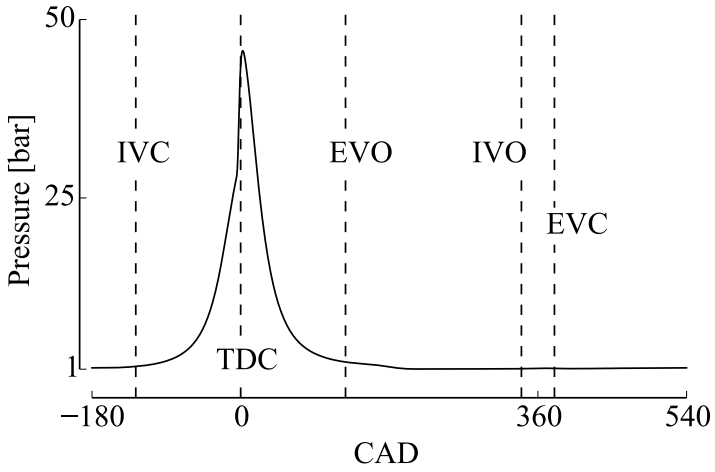


Figure 3.1: *Input and exhaust valve positions marked on a plot of in-cylinder pressure curve. The pressure curve corresponds to equivalence ratio, $\phi = 0.3$, for a dry syngas composition with entry conditions, $p_{in} = 1.2$ bar and $T_{in} = 250^{\circ}C$.*

The geometric compression ratio, R_c, of an engine is defined as the ratio of the maximum to the minimum geometric volumes of a piston cylinder system:

$$R_c = \frac{V_{TDC}}{V_{BDC}} \tag{3.1}$$

Here, V_{BDC} and V_{TDC} depict the cylinder volumes when the piston is at the BDC and at the Top Dead Center (TDC), respectively. The R_c represented here differs from the effective compression ratio, R_c', which is a consequence of the engine valve positions, as marked in Figure 3.1 and more closely represents the compression undergone by the gas in the cylinder. Thus the R_c' is defined as:

$$R_c' = \frac{V_{TDC}}{V_{IVO}} \tag{3.2}$$

In most engines, the IVC position is much later than the BDC of the compression stroke, meaning $V_{IVC} < V_{BDC}$. Thus the effective compression ratio is lesser than the geometric compression ratio, i.e. $R_c' < R_c$. Additionally, en-

gines following the *Otto-Atkinson cycle* have their expansion ratios larger than their compression ratios, however, this shall not be discussed further in this thesis. For the discussions in this thesis, only the geometric compression ratio will be used.

The cylinder volume, $V(\theta)$, is a function of the CAD, with the V_{BDC} and the V_{TDC} being its extremities. The CAD, represented by θ, is set as zero at the compression TDC (see Figure 3.1), i.e. the four stroke cycle spans -180 to 540° in terms of CAD, with the range of -180 to 0 CAD indicating the compression stroke. $V(\theta)$ can be derived from a simple sliding crank-piston geometry (without any pin offset), which depends on the total displaced volume expressed as $V_{stroke} = V_{BDC} - V_{TDC}$, the geometric compression ratio, R_c, and the ratio between the lengths of the connecting rod (L) and the crank radius (r), represented as the term L/r. The cylinder volume and its derivative are expressed as Eq. (3.3) and Eq. (3.4), respectively.

$$V(\theta) = \frac{V_{stroke}}{R_c - 1} + \frac{V_{stroke}}{2}\left(L/r + 1 - cos(\theta) - \sqrt{(L/r)^2 - sin^2(\theta)}\right) \tag{3.3}$$

$$\frac{dV(\theta)}{d\theta} = V_{stroke} \cdot \frac{sin(\theta)}{2} \cdot \left(1 + \frac{cos(\theta)}{\sqrt{(L/r)^2 - sin^2(\theta)}}\right) \tag{3.4}$$

Based on the pressure and volume data, the indicated work and its derivatives, the IE and IMEP, can be computed. The Indicated Efficiency or IE, is a measure of the thermodynamic efficiency, which is based on the area enclosed by a pressure-Volume (pV) diagram and the fuel input ($Q_{fuel/cycle}$), as expressed in Eq. (3.5).

$$\mathrm{IE}_{net} = \frac{100}{Q_{fuel/cycle}} \cdot \int_{-180°}^{540°} p(\theta) \cdot \frac{dV(\theta)}{d\theta} d\theta \tag{3.5}$$

Eq. (3.5) represents the formal method of computing the net IE for a four stroke engine. In case of discrete data, which is acquired from an experimental setup, the equation is modified to involve the discrete volume change, $\Delta V(\theta)$, and a summation of the terms, $\sum p(\theta)\Delta V(\theta)$. In this test bench no back-pressure valve was used in the exhaust manifold. Thus, when intake pressures above the atmospheric were used, the accuracy in the computation of IE_{net} would be negatively affected. This may also cause some errors on the measurement of combustion efficiency due to *shortcut* flow resulting from the valve overlap. However, for efficiency computations, the gross value of IE, computed between the compression and expansion stages of the engine, is used throughout this thesis:

$$\mathrm{IE}_{gross} = \frac{100}{Q_{fuel/cycle}} \cdot \sum_{-180^\circ}^{180^\circ} p(\theta) \cdot \Delta V(\theta) \tag{3.6}$$

The Indicated Mean Effective Pressure or IMEP, is the indicated work per unit swept volume and is expressed as:

$$\mathrm{IMEP}_{net} = \frac{1}{V_{stroke}} \cdot \int_{-180^\circ}^{540^\circ} p(\theta) \cdot \frac{dV(\theta)}{d\theta} d\theta \tag{3.7}$$

Again, likewise done for IE, the gross IMEP is more representative.

$$\mathrm{IMEP}_{gross} = \frac{1}{V_{stroke}} \cdot \sum_{-180^\circ}^{180^\circ} p(\theta) \cdot \Delta V(\theta) \tag{3.8}$$

Since the net values of IE and IMEP are not used, the gross terms IE_{gross} and IMEP_{gross} are henceforth referred to simply as IE and IMEP.

The pressure data can also be utilized to evaluate the high pressure ringing behavior or cyclic dispersions. The Maximum Pressure Rise Rate (MPRR), as computed using Eq. (3.9), is directly correlated to the intensity and rate of combustion which results in the generation of pressure waves within the combustion chamber (known as *ringing* in HCCI and *knock* in SI) [80]. To respect the structural and thermal safety limits of an engine, the MPRR has to be limited to below a certain fixed value, such as 10 bar/CAD for this thesis (as discussed previously in Section 2.1.1).

$$\mathrm{MPRR} = \left[\frac{dp(\theta)}{d\theta}\right]_{max} \tag{3.9}$$

While ringing limits the upper range of tolerable combustion intensity for an engine, excessive variations between consecutive cycles represent the lower limit. These variations are represented by the Coefficient of Variation in the IMEP, computed for each cycle in a sample of N consecutive cycles using the mean $\overline{\mathrm{IMEP}}$ in Eq. (3.10).

$$CoV_{\mathrm{IMEP}} = 100 \cdot \frac{1}{\overline{\mathrm{IMEP}}} \cdot \sqrt{\frac{1}{N} \cdot \sum_{i=0}^{N} (\mathrm{IMEP}_i - \overline{\mathrm{IMEP}})^2} \tag{3.10}$$

As of the parameters which are related to the chemical composition of the charge, the equivalence ratio, denoted by symbol ϕ, is an important one. It is defined as:

$$\phi = \frac{n_{fuel}}{n_{O_2}} \cdot \left[\frac{n_{O_2}}{n_{fuel}}\right]_{stoic} = \frac{m_{fuel}}{m_{O_2}} \cdot \left[\frac{m_{O_2}}{m_{fuel}}\right]_{stoic} = \frac{V_{fuel}}{V_{O_2}} \cdot \left[\frac{V_{O_2}}{V_{fuel}}\right]_{stoic} \tag{3.11}$$

Here, the last terms of each equality is subscripted by '*stoic*', which represents that the ratio is computed at stoichiometric conditions. Since ϕ is a comparison of ratios, the amounts of fuel and air can be either in terms of mass (m), volume (V) or in molar (n) forms. Thus, the ϕ is a purely unit less quantity. Since most of the chemical species computations are in moles, the following definition of ϕ will be used:

$$\phi = \frac{n_{syngas}}{n_{air}} \cdot \left[\frac{n_{air}}{n_{syngas}}\right]_{stoic} \tag{3.12}$$

The composition of the species participating in the combustion reactions can be obtained by forming a Balanced Chemical Equation (BCE). Assuming the atmospheric nitrogen to represent the major constituents of dry air, except oxygen ($N_2 = 78.09$, $Ar = 0.93$ and $CO_2 = 0.03$) [37], the general form of the BCE can be expressed as:

$$\left(\begin{array}{c} n_{syngas} + \dfrac{1}{\phi_{BCE}} \cdot n_{O_2,stoic} \cdot (O_2 + 3.773N_2) \\ + n_{RGF} + n_{EGR} \end{array}\right) \xrightarrow{combustion} n_{products} \tag{3.13}$$

Here, the reactants are composed of syngas, air and the Residual Gas Fraction (RGF). The air is represented by the two factors, the equivalence ratio and stoichiometric moles of O_2 required for the given syngas flow, $n_{O_2,stoic}$. Note that the term ϕ_{BCE} is different from ϕ. While the ϕ is specified at the inputs using MFCs and pumps, the ϕ_{BCE} is a computed value based on the balancing of the reactants (inputs from MFCs and pumps) and the products (exhaust emission measurements). Ideally, $\phi = \phi_{BCE}$, however this differs slightly in practice because of system and instrument uncertainties.

The n_{RGF} indicates the gases trapped inside the cylinder at the end of the exhaust stroke when the exhaust valve closes. These exhaust gases mix with the fresh gases in the intake stroke and can have influences similar to Exhaust Gas Recirculation. In case of a positive valve overlap where the intake valve opens before the exhaust valves closes, depending on the dynamic intake and exhaust conditions, the ensuing gas exchange can result in RGF gases consisting of both the fresh intake along with some of the exhaust gases. In cases where the intake pressures are sufficiently higher than the cylinder or exhaust pressures, some fraction of intake gases may flow directly into the exhaust manifold during the positive overlap constituting a 'shortcut flow'. In case of the present engine, there is a relatively large positive valve overlap of about 40 CAD along with the intake pressure (p_{in}=1.2 bar) being higher than the exhaust pressure (p_{ex} ≈1 bar). However, for the sake of simplicity, it has been assumed that RGF consists only of exhaust products. The n_{RGF} can be estimated using the ideal gas equation Eq. (3.47) with input values from the in-cylinder pressure and the volume at the end of the exhaust stroke, represented

as the Exhaust TDC (ETDC), along with the temperature measured at the exhaust of the engine (T_{ex}):

$$n_{RGF} = \frac{p_{ETDC} \cdot V_{ETDC}}{R \cdot T_{ex}} \tag{3.14}$$

Further, the RGF fraction can be determined from Eq. 3.13 and Eq. 3.14 as:

$$RGF = \frac{n_{RGF}}{n_{products}} \tag{3.15}$$

The exhaust products contain complete combustion products such as H_2O and CO_2, along with products of incomplete combustion, such as CO. Additionally, since the HCCI engine operates lean, the excess oxygen along with N_2 also forms part of the products. For the sake of consistency with EGR computations undertaken in Chapter 5, the RGF gases have been assumed to consist only of complete combustion products, the excess air and N_2, i.e. no CO. This assumption is not far from the reality as the CO emissions in most of the experiments were found to be about 4000 ppm, which amounts to only 0.4% of the exhaust gas by volume. Even for the worst case which occurred with a low hydrogen content syngas at low equivalence ratio of $\phi = 0.22$, the CO emissions amounted to a maximum of 14000 ppm, equivalent to only 1.4% of the total exhaust gas volume. Since the RGF value amounts to about 7-9% of the exhaust gases (computed for this engine through use of Eq. (3.14) and Eq. (3.15)), the inclusion or exclusion of CO in the RGF gases can be assumed to have a negligible effect.

In subsequent chapters, the experiment specific BCE would be mentioned. The BCE provides the crucial molar compositions of the reactants and products, necessary for the computation of the heat release, as shall be seen in Section 3.2. Additionally, the BCE is used to compute mass or volume weighted LHV of the fuel and air mixture. The mass wighted LHV is simply the ratio of energy heat contributed by each individual fuel component of a fuel mixture to the mass of the fuel component, as expressed in Eq. (3.16). Here the LHV of the individual fuel components (LHV_i) and the corresponding molar masses (M_i) are obtained from published experimental data. The mass weighted LHV can be calculated for mixtures of combustible fuel and inert components, such as in case of syngas (LHV_{syngas}), or for mixtures of fuel, inert and oxidizing components, as in case of syngas and air mixtures (LHV_{charge}).

$$LHV = \frac{\sum\limits_{i} LHV_i \cdot n_i \cdot M_i}{\sum_i n_i \cdot M_i} \tag{3.16}$$

As introduced previously in Section 1.2.2, instead of using the mass of fuel consumed in each cycle (m_{fuel}) as a parameter for comparison with other parameters or between other engines, the use of FuelMEP is more appropriate

(for example see [81]). Its defined as:

$$\text{FuelMEP} = \frac{m_{fuel} \cdot \text{LHV}_{\text{fuel}}}{V_{\text{stroke}}} \tag{3.17}$$

Using the definitions of ϕ and $\text{AFR}_{m,stoic}$, the FuelMEP can be simplified, as represented previously in Section 1.2.2:

$$\text{FuelMEP} = \frac{p}{R_{\text{charge}} \cdot T} \cdot \frac{\text{LHV}_{\text{fuel}}}{\frac{\text{AFR}_{m,stoic}}{\phi} + 1} \tag{3.18}$$

The completeness of combustion can be gauged by measuring the Combustion Efficiency or CE, a general form of which is defined in Eq. (3.19). Here, the Q_r and Q_p represent the LHV heat of the reactants and products respectively, as obtained from the BCE in Eq. (3.13).

$$CE = \left(1 - \frac{Q_p}{Q_r}\right) \times 100 \tag{3.19}$$

As done with m_{fuel}, the use of CE results in the parameter QMEP which is a engine-displacement normalized value for the amount of heat released through the burning of the fuel contained in a single cycle

$$\text{QMEP} = \text{FuelMEP} \cdot \text{CE} \tag{3.20}$$

The Thermodynamic Efficiency (TE) shows how efficiently the released heat energy is converted into pressure-volume work while the IE as discussed previously can also be expressed in terms of FuelMEP and the IMEP.

$$\text{TE} = \frac{\text{IMEP}}{\text{QMEP}} \tag{3.21}$$

$$\text{IE} = \frac{\text{IMEP}}{\text{FuelMEP}} \tag{3.22}$$

The TE shall not be used in the discussions, but is mentioned here for the sake of clarity.

3.2 Computing the Heat Release

The RoHR formulation presented here is based on the discussions in Heywood [37]. With the notation U standing for the internal energy, Q for the heat energy and W for pressure-volume (pV) work, the *First Law of Thermodynamics* for a closed system can be written as:

$$\Delta U = Q - W \tag{3.23}$$

The differential form of the First Law equation can be expressed as:

$$nC_v\frac{dT}{d\theta} = \frac{dQ}{d\theta} - p\frac{dV}{d\theta} \tag{3.24}$$

Here C_v is the molar specific heat capacity of the gas mixture, at a particular gas temperature T. The differential form of the ideal gas equation, $pV = n\overline{R}T$, can be expressed as:

$$n\overline{R}\frac{dT}{d\theta} = p\frac{dV}{d\theta} + V\frac{dp}{d\theta} \tag{3.25}$$

Here $\overline{R}$ is the universal gas constant in SI units ($\overline{R} = 8.314$ J/K/Mol) and n is the number of moles which change due to combustion. Substituting Eq. (3.25) in Eq. (3.24) results in:

$$\frac{dQ}{d\theta} = p\frac{dV}{d\theta}\left(\frac{C_v}{\overline{R}} + 1\right) + \frac{C_v}{\overline{R}}V\frac{dp}{d\theta} \tag{3.26}$$

The molar specific heat capacities, C_p and C_v, are related to each other through the equalities $\gamma = C_p/C_v$ and $\overline{R} = C_p - C_v$. Thus, Eq. (3.26) reduces to:

$$\frac{dQ}{d\theta} = \frac{\gamma}{\gamma - 1}\cdot p\cdot\frac{dV}{d\theta} + \frac{1}{\gamma - 1}\cdot V\cdot\frac{dp}{d\theta} \tag{3.27}$$

The heat Q evaluated in Eq. (3.27) represents the heat that is available for the gas, Q_{net}. However, this heat is only a part of the total heat produced from the combustion of fuel, Q_{gross}, while the other part, Q_{loss}, is lost to the cylinder walls in the form of convective heat transfer. Thus,:

$$Q_{gross} = Q_{net} + Q_{loss} \tag{3.28}$$

$$\text{Or} \qquad \frac{dQ_{gross}}{d\theta} = \frac{dQ_{net}}{d\theta} + \frac{dQ_{loss}}{d\theta} \tag{3.29}$$

Thus, to obtain the total heat released, Eq. (3.27) becomes:

$$\frac{dQ_{gross}}{d\theta} = \frac{\gamma}{\gamma - 1}\cdot p\cdot\frac{dV}{d\theta} + \frac{1}{\gamma - 1}\cdot V\cdot\frac{dp}{d\theta} + \frac{dQ_{loss}}{d\theta} \tag{3.30}$$

The integration of Eq. 3.30 over a predetermined window where the combustion takes place results in the important heat release evolution, $Q_{gross}(\theta)$. As an example, results of such computations can be seen in Figure 3.2. The RoHR and its cumulative sum, have been computed for the pressure curve displayed in Figure 3.1, corresponding to conditions of ϕ=0.3, p_{in}=1.2 bar and T_{in}=250°C. The parameters CA10, CA50 and CA90 correspond to the crank angle positions where 10, 50 or 90 % of the fuel has been burnt. For example, at the crank angle where y% of the total fuel has been burnt, the corresponding

heat released would be:

$$Q_y = \frac{y}{100} \cdot (Q_{gross}|_{max} - Q_{gross}|_{min}) \tag{3.31}$$

Thus, the corresponding crank angle to Q_y is designated as CAy. Further, the burn duration, CA_{90-10} is simply the absolute difference between the CA90, considered as the end of the combustion, and CA10, considered as the start of combustion.

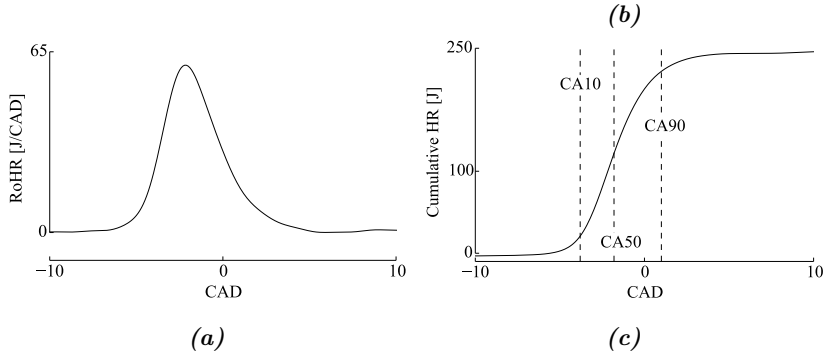


Figure 3.2: *A typical RoHR profile and its cumulative outcome. The cumulative curve helps in determining the important parameters CA10, CA50, CA90 and the burn duration* CA_{90-10}.

The computations required for determining the RoHR and its cumulative sum Q_{gross}, are based on determination of temperature evolution, γ and the estimation of the heat loss term Q_{loss}. The computation of bulk gas temperature shall be dealt with at the end due to its iterative nature.

3.2.1 Determination of the ratio of specific heats

The ratio of specific heats γ and the specific heat themselves are functions of the bulk gas temperature as well as the chemical species involved in the process. Amongst the many methods available in open literature, the method used in this thesis uses the molar concentrations of the involved species before the combustion begins (reactants) and the composition after the combustion ends (products) and the transition from reactants to products is evaluated based on an iterative process based on the Mass Burn Fraction (MBF). The chemical species are determined from Balanced Chemical Equations introduced in Section 3.1 and their specific solving according to the respective chapters (4, 5 and 6).

The C_p of a particular species can be determined based on the bulk gas temperature T using the NASA polynomial (Eq. (3.32)) with the species dependent

temperature coefficients, a_1, a_2, a_3, a_4 and a_5 (see [82]):

$$C_p = \overline{R} \times (a_1 + a_2 T + a_3 T^2 + a_4 T^3 + a_5 T^4) \tag{3.32}$$

The C_p of a gas mixture containing many individual species (i) would be a molar fraction (x_i) weighted sum of the individual C_{p_i}:

$$C_p = \sum C_{p_i} \cdot x_i \tag{3.33}$$

During a chemical reaction, all the species from the reactants and products can not be present at the same time and thus the specific contribution from each species to the bulk gas C_p would be wighted accordingly by their changing molar concentrations. However, these concentrations may not change linearly or in sync with other species due to varying reactivities. Considering the complexities involved in a detailed computation, a simple assumption is used where it is assumed that all reactant species would change in sync with each other as the combustion advances, creating equivalent fractions of products. Thus, the equivalent C_p of the gas mixture or charge can be expressed as:

$$C_p = (1 - MBF) \cdot \left[\sum_{i}^{\text{reactants}} (C_{p_i} \cdot x_i) \right] + MBF \cdot \left[\sum_{j}^{\text{products}} (C_{p_j} \cdot x_j) \right] \tag{3.34}$$

Here MBF stands for the Mass Burn Fraction which contains the information of how the bulk reactants change into bulk products as a result of combustion. From the C_p, the required γ can be deduced using Mayer's relation:

$$\gamma = \frac{C_p}{C_p - \overline{R}} \tag{3.35}$$

The MBF is not known beforehand and thus, an iterative procedure is used, as described in [83]:

1. As a starting condition, the MBF is assumed to be a step function where the composition changes from pure reactants to products at the TDC.
2. The corresponding γ evolution is determined using Eq. (3.34) and Eq. (3.35) between from the Start of Combustion (SOC) position to the End of Combustion (EOC) position.
3. Further, the first estimate of the RoHR is carried out, eventually computing the cumulative heat release.
4. The cumulative heat release is normalized in its amplitude, giving a better estimate of the MBF than the previous step function.
5. These steps can be repeated until a stable RoHR is reached.

Usually, only two iterations are required.

Figure 3.3 shows the evolution of γ as computed from the method just

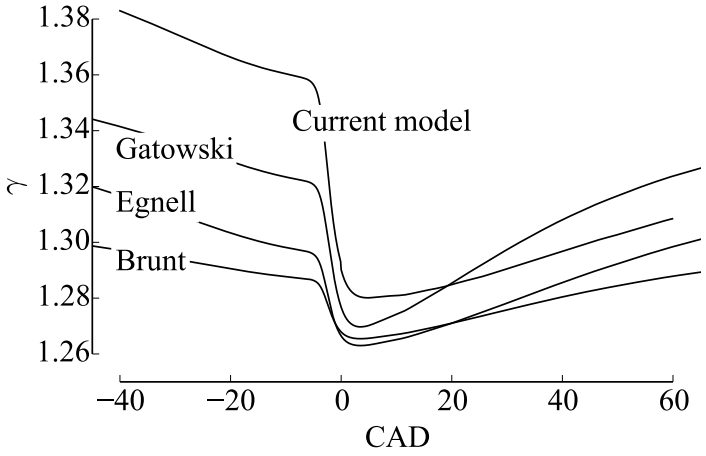


Figure 3.3: *γ estimates from the method described in this text as compared to other methods.*

described, for a test case. Other models, as listed below, have also been used for the sake of comparison. Here the temperature T is in Kelvin.

- Gatowski's model [84]:

$$\gamma = 1.38 - 0.08 \cdot \frac{T - 300}{1000} \tag{3.36}$$

- Brunt's model [85]:

$$\gamma = 1.338 - 6 \times 10^{-5} \cdot T + 1 \times 10^{-8} \cdot T^2 \tag{3.37}$$

- Egnell's model [86] :

$$\gamma = 1.38 - 0.2e^{-\frac{900}{T}} \tag{3.38}$$

Obvious differences exist between the iterative model and the temperature dependent models. This can be attributed to the fact that the latter models do not consider the involved species and their original coefficients, which have been tuned for stoichiometric operations with hydrocarbon fuels, may not be accurate for the current application. Hence, throughout this thesis, the iterative model described in this subsection has been used.

3.2.2 Determining the heat loss term

The rate of heat loss through the wall, $\frac{dQ_{loss}}{d\theta}$, can be expressed in the form of Newton's law of convective cooling:

$$\frac{dQ_{loss}}{d\theta} = h \cdot A \cdot (T - T_{\text{wall}}) \cdot \frac{1}{\omega} \tag{3.39}$$

Here A is the total surface area of the combustion chamber, expressed as $A = A_{\text{cylinder head}} + A_{\text{liner}} + A_{\text{piston}}$. It is assumed here that the surface temperatures are uniform throughout. Further, ω is the angular speed of the crank in CAD/s, T and T_{wall} are the gas and cylinder wall temperatures in Kelvin (K) and h is the coefficient of convective heat transfer in $\text{W/m}^2\text{/K}$.

Several empirical models for determining h have been explored in the literature, for example see [87, 88, 89, 90, 91]. Of the many correlations, the Hohenberg's correlation is simple to implement and effective while, requiring no major tuning effort to match the geometry of the engine [89]. On the other hand, the Woschni correlation, although in popular use for SI and CI type of engines, is ill-suited for the HCCI engine in its original form. Thus, Chang et al. [87] proposed a modified Woschni coefficient model that was adapted to the HCCI combustion by taking experimental measurements of the heat flux at the cylinder walls. For use in the current context, both the Hohenberg correlation as well as the modified Woschni correlation are evaluated.

The Hohenberg correlation can be stated as:

$$h_{\text{Hohenberg}} = \alpha_{\text{scaling}} \cdot V^{-0.06} \cdot p^{0.8} \cdot T^{-0.4} \cdot (S_p + 1.4)^{0.8} \tag{3.40}$$

Here the pressure p is in bars, T in K and V in m^3. The term $\alpha_{scaling}$ is used to adapt the equation to a specific engine geometry. The S_p is the mean piston speed in m/s and defined as:

$$S_p = 4 \cdot r \cdot \frac{\text{RPM}}{60} \tag{3.41}$$

On the other hand, the modified Woschni correlation, henceforth called as the *Chang* correlation, can be expressed as:

$$h_{\text{Chang}} = \alpha_{\text{scaling}} \cdot H^{-0.2} \cdot p^{0.8} \cdot T^{-0.73} \cdot \nu^{0.8} \tag{3.42}$$

Here, H stands for the instantaneous combustion chamber height in meters as a function of θ. The rest of the units are similar to those used in Eq. (3.40), while ν represents a characteristic velocity component which is expressed as:

$$\nu = C_1 \cdot S_p + \frac{C_2}{6} \cdot V_{\text{stroke}} \cdot \frac{T_0}{p_0 V_0} \cdot (p - p_{\text{motoring}}) \tag{3.43}$$

The constants $C_1 = 2.28$ and $C_2 = 0.0034$, while T_0, p_0 and V_0 are reference values. This velocity component uses the motored pressure, p_{motoring}, which can be computed assuming a polytropic compression/expansion:

$$p_{\text{motoring}} = p_0 \left(\frac{V_0}{V} \right)^{\gamma} \tag{3.44}$$

The polytropic exponent, γ, is calculated from the compression phase of the experimental pressure curve, before the beginning of combustion. Further, it is assumed here that the compression and expansion processes of the idealized motoring curve are equivalent, and hence a constant γ is used for generating the motoring pressure curve.

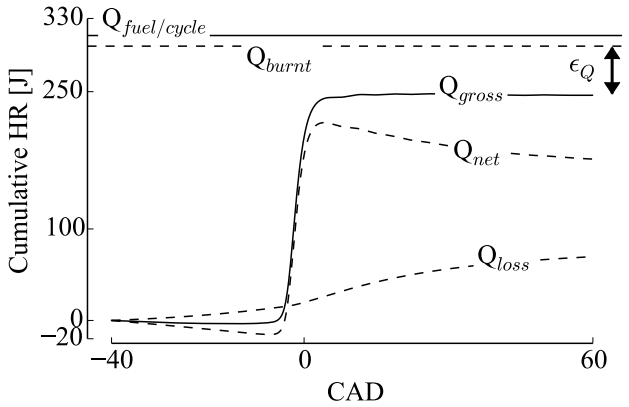


Figure 3.4: *Evolution of various heat release parameters against CAD. Here, the $Q_{gross} = Q_{net} + Q_{loss}$. The flatness before the steep rise of Q_{gross} indicates that the heat losses to the engine walls have been adequately compensated by the heat loss model. Similar compensation can be seen after the combustion ends. However, the gap between the maximum of gross heat released and the experimentally determined burnt fuel energy indicate the underestimation of the heat loss model by a factor of ϵ_Q.*

Next, both the Hohenberg and the Chang models are calibrated as per the engine, and then evaluated for a specific case to understand their differences, if any. Two major aspects need to be considered:

- The shape of the gross heat release curve.
- How well the heat release matches to the fuel burnt inside the engine.

Consider Figure 3.4 which is computed for the pressure curve plotted in Figure 3.1. Here, the cumulative gross heat release, the net heat release and the wall losses are plotted as functions of CAD. The wall losses in this case have been computed using the Hohenberg correlation from Eq. 3.40, but with $\alpha_{\text{scaling}} = 130$. In fact this value of scaling was part of the original Hohen-

berg's equation, as reported in the corresponding literature cited above. Similar curves have been obtained by using Chang correlations, using $\alpha_{\text{scaling}} = 483$. The flatness of the Q_{gross} in Figure 3.4, before the combustion began and after it ended can be subjectively judged as an appropriate fitting of the heat loss model, as well as other parameters that influence the heat release analysis, such as the quality of pressure data, the accuracy of the compression ratio, and others, as shall be seen in detail in Section 3.3. In specific to the topic of heat losses, the flat shapes imply that the convective heat loss models adequately compensate for the wall losses and thus implying that the Q_{gross} is an accurate representative of the in-cylinder combustion processes.

However, Figure 3.4 also indicates three additional terms, the fuel energy contained in the cycle, $Q_{fuel/cycle}$, the actual fuel burnt, Q_{burnt}, and the energy gap between the maximum of the computed Q_{gross} and the Q_{burnt}. The fuel energy burnt in a single combustion cycle can be determined from the CE, which in turn can be determined from the BCE through the use of Eq. (3.19). Thus:

$$Q_{burnt} = Q_{fuel/cycle} \cdot CE \tag{3.45}$$

Ideally, the maximum of the calculated heat release, $Q_{gross,max}$, must match the fuel burnt, Q_{burnt}, but in reality this is hardly the case. The resulting relative % error between the calculation and experimental value of fuel heat released, can be expressed as:

$$\epsilon_Q = \frac{Q_{burnt} - Q_{gross,max}}{Q_{burnt}} \times 100 \tag{3.46}$$

In this error computation, the losses due to blow-by were not included as they were not determined for the current engine setup. In Figure 3.4, the error ϵ_Q is non-zero, which implies that the convective heat loss is underestimated in this case. The usual method is to adjust the α_{scaling} of the heat loss models to minimize the value of ϵ_Q.

Figure 3.5a shows variations in the tuned α_{scaling} values of Hohenberg model (solid lines) and Chang model (dashed lines) for the same example as in Figure 3.4. The main observation that can be made is that, although the relative error between the fuel burnt, Q_{burnt} and the maximum of the gross heat release can be minimized by increasing the α_{scaling}, there is a marked deviation from the flat nature of the curves. In Figure 3.5a, the curves corresponding to 0% modulation of the respective $\alpha_{scaling}$ used for Hohenberg (130) and Chang (483), subjectively seem to be the most accurate, even if they have a large difference from the experimental value. Thus the simple modification of α_{scaling} does not seem to help.

Additionally, it can be explored how the heat loss models behave with changes in the equivalence ratio, and hence the changes in the heat flux at

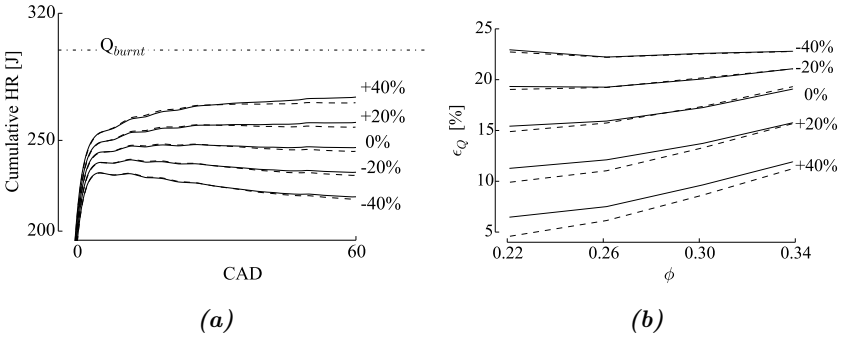


Figure 3.5: *A typical cumulative heat release curve (solid line) along with the cumulative heat lost to the cylinder walls (dashed line). The fuel burnt is marked as horizontal dashed line. The gap between the maximum of gross heat release curve is lesser than the fuel burnt, by error ϵ_Q.*

the walls. Figure 3.5b plots the error ϵ_Q for various values of ϕ using the two heat transfer correlations, Hohenberg (solid lines) and Chang (dashed lines). It is observed that as the ϕ increases, the relative error increases. The errors corresponding to the Chang correlation have a relatively steeper change as the ϕ changes, indicating a less stable model. However, in all cases the heat estimation by the heat release computations have relatively high errors. There could be the following possible reasons:

- The relative error, ϵ_Q does not include any crevice or blow-by losses. For example, Chang et al. [87] have accounted for about 3% blow by losses in their estimation. Thus, the estimation of blow-by losses are required for a better computation of the heat losses.
- There is a positive valve overlap between the opening of the intake valve (IVO) and the closing of the exhaust valve (EVC), during the exhaust stroke, equivalent to 40 CAD. Since the experiments have been conducted with an intake pressure of 1.2 bar, while the exhaust is atmospheric, this would imply that some of the intake gases 'short-cut' out of the engine without undergoing a combustion cycle. Since the experiments were carried out on a mono-cylinder engine, the exhaust gas flow is highly fluctuating. In contrast, the exhaust emission analyzer has a slow sampling process. Thus, it may be possible that the combustion efficiency is overestimated.

As a note, the large relative error, of about 15%, between the computation of the heat released due to combustion and the experimental estimate using CE seems to be normal, for example see Tunestål [92] who reports an overestimation of the Q_{gross} by 10% compared to the experimental values. A recent paper by Broekaert et al. [91] tested the various empirical heat transfer correlations, including the Hohenberg and Chang correlations, against experimentally

measured heat flux for an HCCI engine operated at various operating points. The authors found all the models lacking in their abilities to accurately predict the heat transfer, even after adjusting the various empirical coefficients. However, the model of Hohenberg fared better than Chang in this work, reiterating the conclusion of Soyhan et al. [89] about the suitability of the Hohenberg coefficient for HCCI heat loss analysis.

As a conclusion, with this limited analysis, the Hohenberg model, due to its simple form, has been used throughout this thesis. Additionally, to conserve the flat shaped prediction of the gross heat release, the original $\alpha_{\text{scaling}} = 130$ is used in the Hohenberg correlation.

3.2.3 Determining the bulk gas temperature or trapped mass

One of the most important parameter is the in-cylinder bulk gas temperature, $T(\theta)$. As a first estimate, assuming an ideal gas behavior, $T(\theta)$ can be estimated as being a function of the in-cylinder pressure $p(\theta)$, the volume $V(\theta)$ and the number of moles involved in the compression or expansion process, n:

$$p(\theta) \cdot V(\theta) = n\bar{R}T(\theta) \tag{3.47}$$

Here $\bar{R}$ is the universal gas constant, expressed in the SI units: $\bar{R}$=8.314 $J{\cdot}K^{-1}{\cdot}$ mol^{-1}. Neglecting blow-by, and assuming that n remains constant between the IVC and the EVO (i.e. no combustion), the in-cylinder temperature can be deduced from Eq. (3.47):

$$T(\theta) = \frac{p(\theta)}{p_0} \cdot \frac{V(\theta)}{V_0} \cdot T_0 \tag{3.48}$$

Here, the subscript '0' stands for the reference position of the CAD from where the computation is initiated. Usually, the IVC is used as the reference position since it can be assumed that the mass of gases trapped after this position in the cycle does not change until the EVO position is reached. To further simplify, it can be assumed that the temperature at IVC is nearest to the known intake temperature, T_{in}, thus, $T_0 = T_{IVC} = T_{in}$. The other reference terms in Eq. (3.48), p_{IVC} and V_{IVC}, can be obtained from the experimentally measured in-cylinder pressure and its associated volume (computed from Eq. (3.3)).

However, this evaluation of the in-cylinder temperature is not accurate due to the following assumptions:

1. $T_{in} = T_{IVC}$ is assumed.
2. A constant n is assumed i.e. no combustion takes place.
3. The gas is an ideal gas.
4. Blow-by from the piston rings (and thus a possible change in the n) is neglected.

The assumptions related to ideal gas and blow-by result in negligible uncertainties in the computation process and thus shall be used in this thesis. On the other hand, assumptions of constant n and reference temperature T_{IVC} can lead to significant errors.

Many authors choose to approach the issue through a better determination of the temperature at the IVC, for example see [93]. The approach followed here is to compute the temperature evolution from the trapped mass which does not change throughout the compression, combustion and expansion process. As a simple approximation, the trapped mass is equal to the sum of measured intake mass flow and the residual gases where the intake has been measured. This is the case in this thesis for Chapters 4 and 5. However, in Chapter 6, the test bench functions with an unmeasured syngas flow while the air component is measured. Additionally, due to the presence of pressure waves in the intake manifold, there might be cycle-to-cycle differences in the trapped mass. Thus, identifying the trapped mass per cycle is very desirable.

Modifying the ideal gas equation, Eq. (3.47), the bulk gas temperature can be expressed as:

$$T(\theta) = \frac{p(\theta) \cdot V(\theta)}{n \cdot \overline{R}} = p(\theta) \cdot V(\theta) \frac{M(\theta)}{m \cdot \overline{R}} \tag{3.49}$$

Here $M(\theta)$ is the combustion dependent average molar mass of the gases involved, and m is the mass of the gases trapped inside the combustion chamber. Due to the negligible blow-by assumption, the value of m remains constant throughout the IVC-EVO range. The variation in $M(\theta)$ over the combustion duration can be estimated through a similar process as the one followed for determining the evolution of γ, in the Section 3.2.1. The challenging issue here is the determination of m, which is the subject of many works (for example see [94, 95, 96, 97]). In this thesis, the recently developed techniques of Luján et al. [96] and Broatch et al. [97] have been used since these techniques are based on very few assumptions.

The method is based on two fundamental ideas (readers may refer to the works by Draper [98] and Eng [56] for detailed fundamental discussions on the topic of combustion induced resonance in IC engines) :

- When combustion takes place, pressure oscillations are set up within the chamber. The resonant frequency of these pressure waves, according to the formulations first proposed by Draper [98], can be expressed as:

$$f_{m,n} = \beta_{m,n} \frac{c}{\pi B} \tag{3.50}$$

  Here, $f_{m,n}$ is the resonant frequency of the m, n vibration mode with m and n being the circumferential and radial pressure node numbers. The term $\beta_{m,n}$ represents the corresponding wave number determined from

solving Bessel equations in the cylindrical coordinates of an idealized right circular cylinder engine. c stands for the speed of sound inside the combustion chamber and B is the bore of the cylinder.

- The speed of sound c in turn depends on the instantaneous temperature:

$$c = \sqrt{\frac{\gamma(\theta)\bar{R}T(\theta)}{M(\theta)}} \tag{3.51}$$

Luján et al. [96] combined Eq. 3.50 and Eq. 3.51 and substituted the ideal gas law into it resulting in Eq. (3.52), which relates the experimentally detectable resonance frequencies and the mass of the trapped gases:

$$f_{m,n} = \frac{\beta_{m,n}}{\pi \cdot B}\sqrt{\frac{\gamma(\theta) \cdot p(\theta) \cdot V(\theta)}{m}} \tag{3.52}$$

According to Eng [56], the mode $f_{1,0}$ is the fundamental circumferential vibration mode which contains the bulk of oscillation energy amongst the other possible modes. Thus, the discussion follows around identifying this particular mode. If the combustion chamber is assumed to be exactly a *right circular cylinder*, then Bessel coefficient is $\beta_{1,0} = 1.842$. However, this is not the case due to the presence of different combustion chamber geometries (bowls, penthouse shaped cylinder head, valve seats, crevices etc). Therefore, to determine mass from Eq. 3.52, the procedure reduces to:

- Identifying the resonant frequencies in the pressure trace.
- Replacing the factor $\beta_{1,0}$ with $\beta'_{1,0}$ adapted to the particular engine geometry. The relationship is expressed as:

$$\beta'_{1,0} = \mu(\theta) \cdot \beta_{1,0} = \mu(\theta) \cdot 1.842 \tag{3.53}$$

  Here, μ is the calibration factor which is a function of CAD and the value of which tends towards 1 as the piston moves away from the cylinder crown and the combustion chamber geometry resembles more like a perfect cylinder.
- Determining the trapped mass.

The following subsections discuss the above listed steps.

Identifying the frequencies

The resonant frequencies can be determined through developing a *spectrogram* of the pressure trace of a single pressure cycle. To determine the spectrogram, Luján et al. [96] proposed the method using Short Term Fourier Transforms (STFT). Although a Fourier transform of a single pressure trace would provide the frequencies contained in the trace, it would not provide the time or CAD position where specific frequencies appear in the trace. This issue is solved

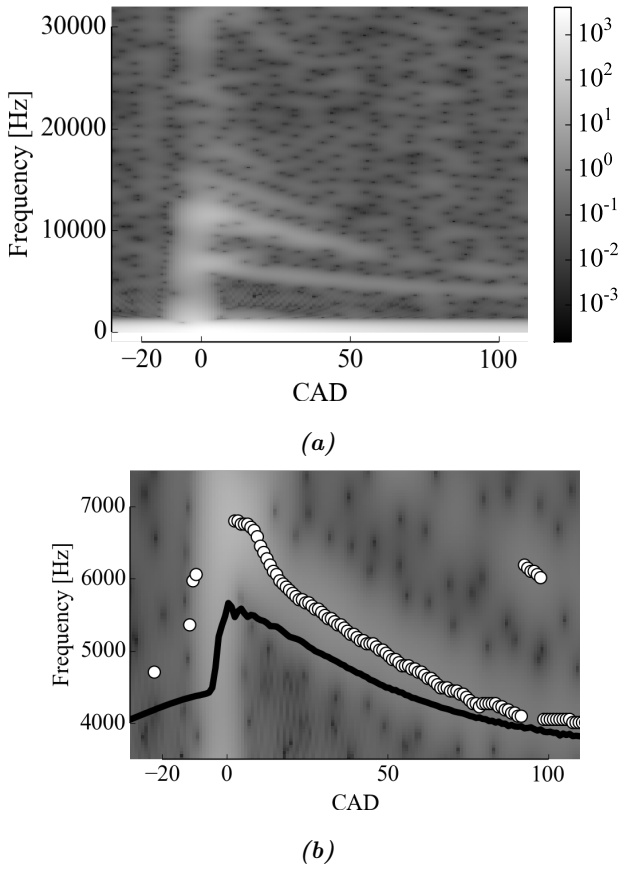


Figure 3.6: Calibration of the mass determination method: *(a) Spectrogram of a single pressure trace through the method of STFT. (b) Dominant first circumferential mode frequency evolution as a function of CAD with the assumption of ideal cylindrical combustion chamber (black continuous line) and with experimentally observed frequency (circular markers).*

through taking the Fourier transforms of a modified pressure trace, which is modified such that only a small section has the original amplitude, whereas the rest of the trace is essentially zero in amplitude. This process is repeated for overlapping *time or CAD frames*, for the rest of the signal. In the end, the net result looks like Figure 3.6a which shows the spectrogram of one in-cylinder pressure trace at $\phi = 0.34$ for a specific syngas composition which results in high intensity combustion (i.e. high MPRR). Multiple resonant frequencies are identifiable as white (high power) regions. The start of combustion can easily be noted at 0 CAD where the high power frequencies originate. As the chamber volume expands, the resonant frequencies decrease along with their amplitudes.

The transformation of the original pressure trace into overlapping frames is

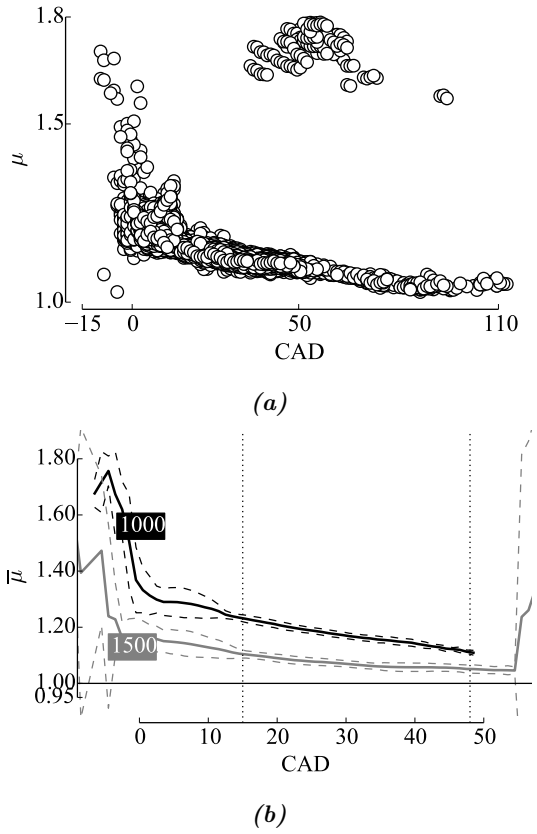


Figure 3.7: Calibration of the mass determination method: *(a) μ coefficients identified for large number of operating points at various ϕ, T_{in}, p_{in} and compositions. (b) The mean and filtered $\overline{\mu}$ data of which only the data between 15CAD-48CAD have been chosen due to low variations. The μ factors differ based on RPM, as shown here.*

done through the use of *windowing functions*, such as the *Blackman-Harris*[1], as proposed by Luján et al. [96]. The width of the windowing function and the overall trace length and position where this operation needs to be carried out significantly effects the construction of the spectrogram and the subsequent identification of the frequencies. Details of these choices have been discussed in [96]. For the studies carried out in this thesis, the pressure trace within the IVC-EVO was used with the (moving) frame size of 25 CAD and an 99% overlap between the frames. Such an operation results in spectrograms similar to the one shown in Figure 3.6a.

Once a spectrogram is constructed, the next task is to identify the dominant frequencies in the range of 2-8 KHz. This range, according to Eng [56], captures

[1]The Blackman-Harris window function is available as a library function in Python Scipy, in the form of *scipy.signal.blackmanharris(frame size)* to which zeros are padded before and after the frame under study so as to have a signal of the same length as the original.

the primary modes of vibrations resulting from combustion which are of interest in this discussion. Figure 3.6b shows the identified dominant frequencies as a function of CAD, in the form of circular markers. Also shown is the theoretical frequency evolution (black continuous line) based on the assumption that the combustion chamber is a right circular cylinder. Thus, the discrepancies due to the combustion chamber geometry are obvious, reinforcing the need for calibrating the multiplier $\mu(\theta)$, using Eq. (3.53).

The $\mu(\theta)$ factor

Figure 3.7a shows the μ computed from various cases of syngas combustion in the test bench HCCI engine, where the intake mass was known (from the operating points discussed in Chapter 4). These *base* cases operated at 1500 RPM and included only those cases where the sole supply of intake gases were controlled through MFCs (no pumps). This implied the best accuracy possible with the current test bench setup. While the RGF mass (based on the simplified treatment discussed in Section 3.1) was included, inaccuracies in its computation as well as the exclusion of blow-by and shortcut losses, could lead to some errors at the μ calibration stage. However, these inaccuracies could not be avoided unless more rigorous procedures for in-cylinder mass determination are utilized. Nevertheless, using this technique, it can be assumed that the accuracy of the resulting mass estimates are at least as good as the ones experimentally obtained in the base cases.

For each base case used to construct Figure 3.7a, the μ was computed at each CAD segment of each of the 100 cycles. Next, the dominant resonant frequencies were identified in the 2-8 kHz range by finding the *maximas* using second order differentials. To eliminate noisy and unclear data, μ was computed for spectrogram points with a high signal to noise ratio using the criteria that the highest frequency in the STFT of a CAD segment must lie in the 2-8 kHz band and must have an amplitude at least 9 times higher than the amplitude of the next highest frequency.

In Figure 3.7a, although most points align together to form a general decreasing trend with increasing CAD, some points clustered around 50 CAD can be observed to deviate significantly from such a trend. This can be explained by the observing the original spectrogram where it can be seen that at 50 CAD, the resonant frequencies from a mode higher than the first circumferential mode also can be found in the window of 2-8kHz. Thus, the μ trend is filtered by only considering μ points which lie within two standard deviations of the mean[2]. The resulting mean $\overline{\mu}$ (solid line) is shown in Figure 3.7b along with the standard deviations (dashed lines). The region between 15 CAD and

[2]The spread in μ at any θ can be considered to obey a normal distribution and thus, the width of 2 standard deviations around the mean can be assumed to capture at least 95% of all the data points.

50 CAD has the least spread and thus is selected as the calibrated $\overline{\mu}$ used in further discussions.

Figure 3.7b also shows the outcome of a similar procedure carried out for experiments discussed in Chapter 5, which were carried out at 1000 RPM. It is surprising to note that the μ differs due to changes in the RPM, which is interesting as μ relates to the geometry of the combustion chamber, which remained the same for both the RPMs. Once possible reason could be that at lower RPMs, the assumption that the CAD and time domains are equivalent does not quite hold true and therefore this results in a different μ profile[3]. Thus,, this aspect needs to be explored further and verified.

Computing the trapped mass

With the $\overline{\mu}$ data available, the computation of mass can be a straightforward calculation by simply substituting the identified frequencies in the range of 15-48 CAD in the realistic version of Eq. (3.52), i.e. where $\beta_{1,0} = 1.842$ is replaced by $\beta'_{1,0} = \overline{\mu(\theta)} \cdot 1.842$. Using this method, multiple estimates of trapped mass at each CAD in the range of 15-48 CAD can be computed. However, this method suffers from the limitations of STFT as having poor frequency and time (or CAD[4]) resolution, as discussed by the same group of authors which proposed the STFT method in another paper by Broatch et al. [97]. As an alternative, Broatch et al. provide an even more interesting and straightforward method for computing the direct mass.

The Fourier transform of a signal $s(t)$ can be written as:

$$A(f) = \int_{-\infty}^{\infty} s(t) e^{-j2\pi ft} dt \tag{3.54}$$

Instead of using constant frequency based amplitude, Broatch et al. proposed a varying mass based transformation of the signal by substituting f from Eq. (3.52):

$$A(m) = \int_{-\infty}^{\infty} s(t) e^{-j2\pi \left[\int_{-\infty}^{\tau} \frac{\overline{\mu(\theta)}\beta_{m,n}}{\pi \cdot B} \cdot \sqrt{\frac{\gamma(\theta) \cdot p(\theta) \cdot V(\theta)}{m}} d\tau \right] t} dt \tag{3.55}$$

When simplified to be used with a pressure signal in the CAD domain, the

[3]Through personal communications with the authors of Luján et al. [96] and Broatch et al. [97]

[4]It must be noted here that there are variations in the angular speed during a cycle, and hence time and CAD are not the same scales. However, overall, this assumption may not lead to significant errors.

above transformation reduces to:

$$A(m) = \frac{1}{f_s} \sum_{\theta=15CAD}^{\theta=48CAD} w(\theta)s(\theta)e^{-j2\pi\frac{1}{f_s}\left[\sum_{\theta=15CAD}^{\theta=48CAD} \frac{\overline{\mu(\theta)}\cdot 1.842}{\pi\cdot B}\cdot\sqrt{\frac{\gamma(\theta)\cdot p(\theta)\cdot V(\theta)}{m}}\right]} \quad (3.56)$$

Here, $w(\theta)$ is a Blackman-Harris window over the pressure trace from 15 CAD to 48 CAD for which the μ was calibrated previously. The rest of the parameters are available from the experiments, except the mass m which has to be computed.

If various possible values of m are substituted in Eq. (3.56), the outcome of this transformation results in a 'resonance' of amplitude when the substituted mass value is equal to the real mass value. This can be seen in Figure 3.8 where the highest amplitude coincides with the mass contained inside the cylinder (measured with MFCs and including the RGF gases). This procedure can be performed for each cycle at each experimental point. However, the robustness of this procedure with differing equivalence ratios, intake temperature and pressure needs to be tested.

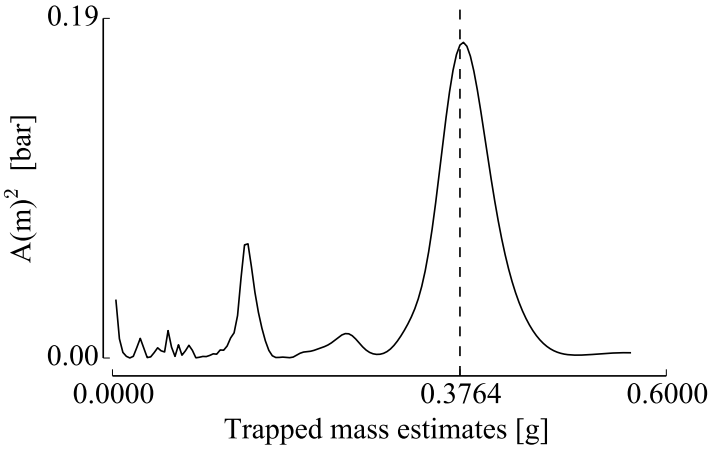


Figure 3.8: *Trapped mass estimation using Broatch et al. method. The dashed line indicates the trapped mass as computed from the MFC values.*

The relative error between the mass estimate provided by the current method (m_{Broatch}) and the experimental based estimation (m_{exp}) could be expressed in the form of:

$$\text{mass error} = \frac{m_{exp} - m_{\text{Broatch}}}{m_{exp}} \times 100 \quad (3.57)$$

Figure 3.9 plots the relative mass errors computed using Eq. 3.57 for the experiments discussed in Chapter 4. The cycle-to-cycle masses computed from the Broatch et al. method were averaged for the 100 cycles of each operating

point, whereas, the experimental mass estimate has a low resolution and remains constant for the complete 100 cycles. The relative mass errors have been computed for various cases of ϕ, p_{in} and T_{in} and can be noted to be within 5%, thus proving the robustness of this technique.

As discussed previously, the accuracy of this method depends on determining the $\overline{\mu(\theta)}$ as accurately as possible. Thus, inaccuracies in the mass estimates of base cases used for calibrating $\overline{\mu(\theta)}$ would be propagated to all subsequent mass estimates using the current method.

3.2.4 Summary of HR computation

The procedure followed to compute the RoHR is summarized as follows:

1. Compute a first approximation to the in-cylinder temperature using Eq. (3.48) with the assumption of T_{in}=T_{IVC}.
2. Assume a step function MBF and compute the γ according to Section 3.2.1.
3. Compute the trapped mass using Eq. (3.56) with inputs of γ and temperature.
4. Compute the temperature using the recently computed mass using Eq. (3.49)
5. Compute the RoHR and the cumulative heat release.
6. Compute the MBF and go back to Step 2 for better approximations.

These steps are repeated twice. All the data contained in this thesis are from such computations, however with certain exceptions:

- The values of CA10, CA50 and CA90 reported in this thesis are based on a mean and filtered pressure trace, built from the 100 cycle data. The procedure for creating such a pressure trace has been discussed in Section 3.3.4. This procedure has been done so to avoid spurious noises arising out of numerical differentiation of noisy pressure data that can create in errors in these combustion metrics. However, these combustion parameters have also been computed for each of the 100 pressure cycles and are helpful to identify the standard deviations from the mean. The Coefficient of Variations have been computed for combustion duration from these datasets.
- The MPRR, IMEP and IE have been computed for each of the 100 cycles and their mean are reported. CoVs have also computed.
- Values of MFCs, ϕ, CE, emissions and thus basically the molar concentrations have been recorded from slow instruments. Therefore, these data are available only for each operational point, instead of cycle by cycle.
- The mass contained per cycle is computed for each of the 100 cycles. Although of little use to the experiments in Chapter 4 and 5, these values are of immense importance to the experiments in Chapter 6.

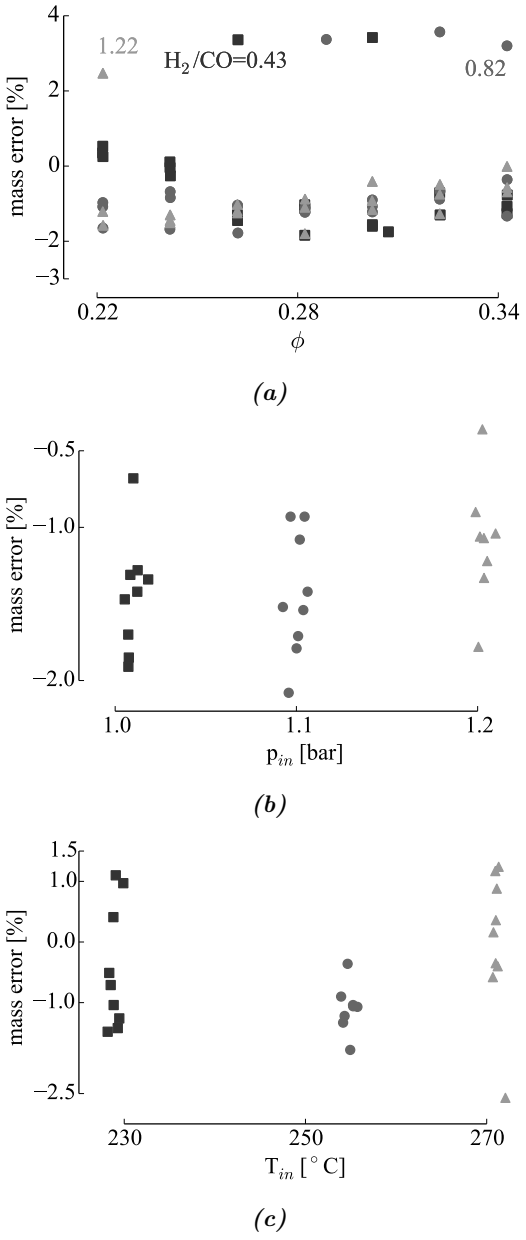


Figure 3.9: *Comparison of the relative errors between mass computed from the MFCs and 100 cycle averaged masses computed from the mass transform method of Broatch et al., for various cases of ϕ, p_{in} and T_{in} for the 1500 RPM experiments. The mass errors are all within 5%.*

In the following section, the determination of key parameters such as the compression ratio, TDC offset and others will be discussed.

3.3 Calibration of Experimental data

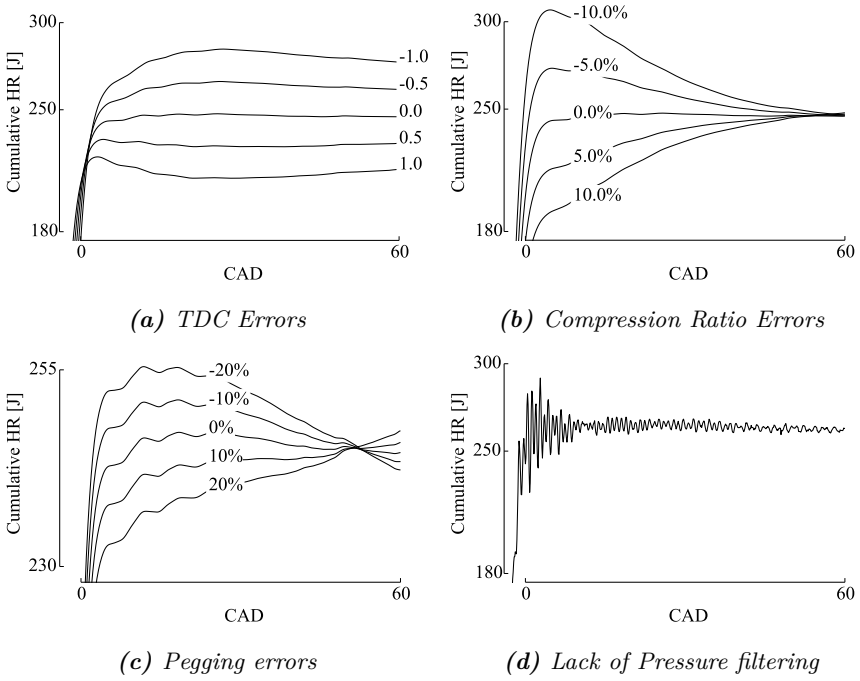
The in-cylinder pressure is the most crucial experimental data which leads to the important RoHR calculations as well as a host of other parameters such as the IE, the IMEP, the MPRR and so on. However, the quality and calibration of pressure data along with the calibration of volume data are non-trivial aspects of in-cylinder pressure measurements. The sources of possible errors can be listed:

- Heat transfer coefficient
- Compression ratio value error
- TDC offset error
- Charge amplifier offset (pegging errors)
- Pressure filtering
- Number of cycles in sample
- Blow-by occurring at the piston rings
- Pressure sensor thermal shock error

Of these errors, the first four are the most critical and have been explored in this thesis, whereas the rest have not been explored.

Figures 3.10a, 3.10b, 3.10c and 3.10d show the respective influences of the errors in the TDC position, the compression ratio, the pegging of the pressure curve and the lack of pressure averaging and filtering, on the computation of the cumulative gross heat release Q_{gross}. In case of TDC errors of just half a degree, the total heat released varies as much by 10%. Since the CA10, CA50 and CA90 determination are based on the difference between the maximum and minimum heat release values (see Eq. 3.31), the TDC error directly effects the CA50 estimation. On the other hand, errors in the compression ratio have a distorting effect on the shape of the HR curve, which again would affect the combustion phasing parameters. A pressure signal, derived from the combination of a piezoelectric in-cylinder pressure sensor and a charge amplifier, is inherently offset from the real pressure due the functioning of the device. This *DC* offset remains constant throughout a cycle, but has to be corrected for to avoid problems in the heat rate determination, as seen in Figure 3.10c . Finally, since the HR calculation uses a derivative of the pressure signal, any noise is greatly amplified thus causing significant disturbances in the HR curve.

Following section presents the various calibration procedures employed in this work to determine minimize the errors arising from the errors in TDC, the compression ratio, pegging and efficient pressure filtering methods.



(a) *TDC Errors*

(b) *Compression Ratio Errors*

(c) *Pegging errors*

(d) *Lack of Pressure filtering*

Figure 3.10: *Sensitivity of the gross heat release computation to four critical parameters. Only the post- combustion phase is plotted to amplify the disturbances. (a) Errors in TDC position correspond to crank angle degrees. (b) Compression ratio estimate varied in % of the computationally determined optimum value of 11.8. (c) Effects of errors in pressure pegging, with the 0% corresponding to no errors. (d) Heat release computed on a single raw pressure trace without any averaging or filtration of noise.*

3.3.1 Determination of the effective compression ratio

One of the most important components of the pressure volume ensemble is the geometrical compression ratio, R_c, used in the determination of the cycle resolved volume (see Eq. (3.3)). The R_c, although being a geometrically defined parameter, suffers from errors due to cylinder and piston manufacturing inaccuracies, unaccounted regions such as crevices, valve seat depressions and loss of compression due to blow-by. Thus, it is necessary that a better estimate of R_c be found out. Of the many available methods proposed in literature [99, 100, 101, 102], the one by Irimescu et al. [100] has been chosen for its intuitive nature and simple implementation.

To determine the effective R_c, the Irimescu method uses RoHR calculations discussed in the previous sections, but carried out on a motoring pressure curve. Due to the heat exchanges between the gas and the cylinder walls, the RoHR curve tends to peak around the TDC, even without any combustion. The authors of the method observed that, independent of the value of R_c used in

the volume calculations, the values of the RoHR at the location of peak pressure (p_{max}) were mostly equal, as shown in Figure 3.11a. The reason behind this behavior is that at the TDC, the volume is minimum and changes slowly with respect to the crank angle. Due to the lack of any combustion, this implies that the differential terms in the RoHR Eq. (3.30) are close to zero. Since the R_c affects the volume, its effect on the RoHR at the TDC is thus negligible, leading to similar heat transfer values across the range of assumed R_c values. Differences occur due to the changes in the compression temperatures which result in different γ, but they are minimal and so can be neglected.

To exploit this phenomenon, theoretical RoHR motoring curves are generated for each of the evaluated R_c using a convective heat transfer coefficient, h_{model}, which is calibrated using the $\alpha_{scaling}$ factor, such that at the position of maximum pressure, p_{max}, the $h_{\text{experimental}} = h_{\text{model}}$. The reason behind this calibration is to match the model RoHR as close as possible to the experimental RoHR. Additionally, such a calibration is carried out at the p_{max} due to this position being independent of the value of R_c. Finally, the value of R_c, where the difference between the experimentally determined RoHR curve and the calibrated theoretical RoHR curve is minimal, is selected as the best estimate. *It must be noted that the R_c evaluated here is related to the ratios between the volumes at the BDC and TDC and not between the volumes at the IVC and the TDC. Also, the computation of the RoHR takes place between predefined SOC and EOC points, which in the current case correspond to 40 CAD before and after the TDC.*

The theoretical pressure curve can be obtained by rewriting the RoHR equation, Eqn (3.30), and equating the gross heat release rate, $\frac{dQ_{gross}}{d\theta} = 0$, resulting in:

$$\frac{dp}{d\theta} = \frac{\gamma - 1}{V}\frac{dQ_{loss}}{d\theta} - \gamma\frac{p}{V}\frac{dV}{d\theta} \tag{3.58}$$

A 4th order Runge-Kutta numerical integration of Eq. (3.58) can be performed to obtain a theoretical motoring pressure curve. Using the experimental and theoretical pressure curves, the respective RoHR curves can be generated. It must be noted here that while calculating the RoHR, the dQ_{gross} is not presumed to be zero and the full equation of Eq. (3.30) is used. Thereafter, at the p_{max} position, a calibration factor C_{cal} is computed such that:

$$C_{cal} = \left[\frac{\frac{dQ_{\text{experimental}}}{d\theta}}{\frac{dQ_{\text{model}}}{d\theta}}\right]_{p_{max}} \tag{3.59}$$

Using C_{cal}, the heat transfer coefficient of the model, h_{model}, can be calibrated such as $h_{g,model,new} = C_{cal} \cdot h_{model,old}$. With the new heat transfer coefficient, $h_{model,new}$, the theoretical pressure (Eq. (3.58)) and the corresponding RoHR are recalculated for a second time. Finally, the residual error between the

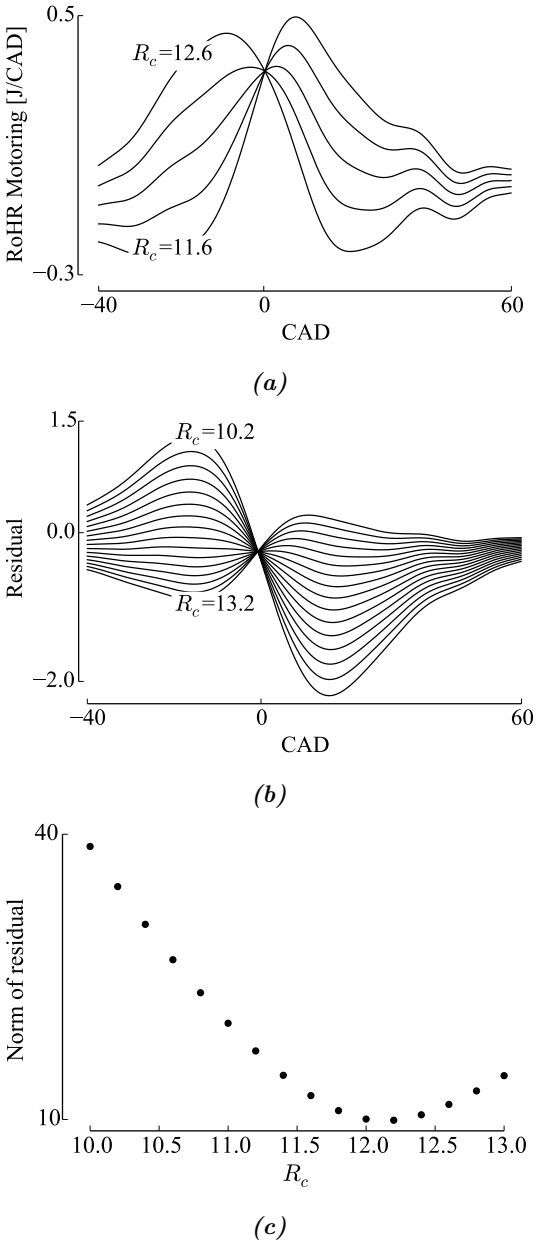


Figure 3.11: *(a) RoHR evaluated from experimental motoring data assuming different R_c values. (b) Residuals computed between experimental RoHR and calibrated theoretical RoHR computed for motoring cases as per the Iremescu method. (c) At $R_c = 12.15$ the norm of the residuals are minimum, which is equal to the geometrically determined R_c.*

experimental RoHR and the calibrated theoretical RoHR curve is evaluated.

$$\text{Residual}_{R_c} = \left[\frac{dQ_{gross}}{d\theta}\right]_{\text{experimental}} - \left[\frac{dQ_{gross}}{d\theta}\right]_{\text{model, calibrated}} \tag{3.60}$$

This procedure is repeated for a range of potential R_c, and the norm of for the residual array is carried out for each: $\|\text{Residual}_{R_c}\|^2$. Figure 3.11b shows the residuals and their norm for a test case. The least error corresponds to R_c=12.15, and is equal to the designed R_c.

3.3.2 Determination of the TDC offset

The TDC offset occurs due to a misalignment in the crank angle rotary encoder, which causes the phase mismatch between the pressure cycle and the volume estimate based on the crank angle encoder values. The requirement of precision on the TDC is about 0.1 CAD due to its critical effect on the estimation of the RoHR as well as the IMEP [103]. There are physical methods to determine the TDC such as the direct physical measurement by a length gauge on the piston crown accessed through the spark plug hole, to using capacitive TDC sensors. However, these methods are either inconvenient to carry out repeatedly or require additional instrumentation which have associated costs. Hence, many numerical methods have been developed for TDC offset determination [104, 105, 106, 107, 108]. In this thesis, the one developed by Tunestål [108] has been implemented.

The Tunestål method is based on a realistic assumption that the heat transfer of a motoring case at the TDC essentially remains constant for a certain width of the CAD range, which is similar to the approach seen in the previous section on R_c determination. Rewriting Eq. (3.58) with the assumption of constant heat flow rate, $\frac{dQ_{gross}}{d\theta} = k$, we have:

$$\frac{dp(\theta)}{d\theta} = (\gamma - 1)k\frac{1}{V(\theta)} - \gamma\frac{p(\theta)}{V(\theta)}\frac{dV}{d\theta} \tag{3.61}$$

Assuming α to be the TDC error, the above equation can be written as:

$$\frac{dp(\theta + \alpha)}{d\theta} = (\gamma - 1)k\frac{1}{V(\theta)} - \gamma\frac{p(\theta + \alpha)}{V(\theta)}\frac{dV}{d\theta} \tag{3.62}$$

Here it should be noted that it is the positioning of the pressure trace that is shifted by the error α with respect to the volume and not the other way around. Letting $k_1 = (\gamma - 1)k$, the unknowns in Eq. (3.62) can be represented by the symbol Λ:

$$\Lambda = \begin{pmatrix} (\gamma - 1)k \\ \gamma \\ \alpha \end{pmatrix} = \begin{pmatrix} k_1 \\ \gamma \\ \alpha \end{pmatrix} \tag{3.63}$$

Let $\epsilon(\theta, \Lambda)$ be defined as the error occurring due to α, such that:

$$\epsilon(\theta, \Lambda) = \frac{dp(\theta + \alpha)}{d\theta} - k_1 \frac{1}{V(\theta)} + \gamma \frac{p(\theta + \alpha)}{V(\theta)} \frac{dV}{d\theta} \tag{3.64}$$

When this equation is evaluated for a set of consecutive crank angle positions near the TDC, say $\theta_1, \cdots, \theta_N$, the error vector can be written as:

$$E(\theta, \Lambda) = \begin{pmatrix} \epsilon(\theta_1; \Lambda) \\ \vdots \\ \epsilon(\theta_N; \Lambda) \end{pmatrix} \tag{3.65}$$

The solution $\hat{\Lambda}$ to the problem could be found by solving this Non-Linear Least Squares (NLLS) problem, i.e. finding an optimal set of the unknowns of Eq. (3.62) such that a residual taken on the error vector shall be minimum:

$$\hat{\Lambda} = \underset{\Lambda}{\operatorname{argmin}} \, ||E(\theta, \Lambda)|| \tag{3.66}$$

Since the dependence of Eq. (3.64) on the first two elements of Λ is linear, while it is non-linear on the last one, Tunestål proposed that the problem be broken into linear and non-linear parts, such that:

$$\Lambda = \begin{pmatrix} \Lambda_l \\ \Lambda_{nl} \end{pmatrix} \quad \text{where} \cdots \begin{cases} \Lambda_l & = \begin{pmatrix} k_1 \\ \gamma \end{pmatrix} \\ \Lambda_{nl} & = \alpha \end{cases} \tag{3.67}$$

Thus, assuming α is known, a set of N linear equations of the form of Eq. (3.62) corresponding to points $\theta_1, \cdots, \theta_N$ near the TDC, can be expressed as a system of linear equations:

$$\Upsilon = \Psi \Lambda_l \tag{3.68}$$

Where:

$$\Upsilon = \begin{pmatrix} \frac{dp(\theta_1+\alpha)}{d\theta} \\ \vdots \\ \frac{dp(\theta_N+\alpha)}{d\theta} \end{pmatrix}, \quad \Psi = \begin{pmatrix} \frac{1}{V(\theta_1)} & \frac{p(\theta_1+\alpha)}{V(\theta_1)}\frac{dV_1}{d\theta} \\ \vdots & \vdots \\ \frac{1}{V(\theta_N)} & \frac{p(\theta_N+\alpha)}{V(\theta_N)}\frac{dV_N}{d\theta} \end{pmatrix}, \quad \text{and} \quad \Lambda_l = \begin{pmatrix} k_1 \\ \gamma \end{pmatrix}$$

This linear problem, assuming α or Λ_{nl} is known, can be solved as:

$$\hat{\Lambda}_l(\Lambda_{nl}) = \Psi^+ \Upsilon \tag{3.69}$$

... where the Ψ^+ is a *Moore-Penrose pseudoinverse* [5] of Ψ and is a commonly used method to determine a best fit linear least squares solution to such a system of linear equations. Once the linear problem is solved, the solution to the overall problem can be expressed as:

$$\hat{\Lambda}_{nl} = \underset{\Lambda_{nl}}{\operatorname{argmin}} \, ||E(\theta; \hat{\Lambda}_l(\Lambda_{nl}))|| \tag{3.70}$$

The solution to Eq. (3.70) could be found by evaluating a range of α values using Eq. (3.69) and simply spotting the value of α which results in the minimum residual (see Figure 3.12a). However, this method, though simple, can take many iterations and the computational cost could become unacceptable when such a method is used in conjunction with processes to find out τ, TDC and pegging errors in an iterative fashion. Thus, Tunestål in [109] has elaborated a method to find the above solution in a minimum number of iterative steps (see Figure 3.12b). The procedure defines a 'loss function', J, which depends on the residual vector D, equal to vector E from Eq. (3.65), such that:

$$J = D^T D \tag{3.71}$$

$$\begin{aligned} \text{where} \quad D &= \Upsilon - \Psi\Lambda = \Upsilon - \Psi(\Psi^T\Psi)^{-1}\Psi^T\Upsilon \\ &= \left[I - \Psi(\Psi^T\Psi)^{-1}\Psi^T\right]\Upsilon = P\Upsilon \end{aligned} \tag{3.72}$$

Here $P = \left[I - \Psi(\Psi^T\Psi)^{-1}\Psi^T\right]$ is a symmetric matrix with $P^T = P$ and $P^2 = P$ as shown in [109]. Thus the loss function becomes:

$$J = D^T D = \Upsilon^T P^T P \Upsilon = \Upsilon^T P \Upsilon \tag{3.73}$$

To find the solution, the loss function J needs to be minimized with respect to α such that $\frac{dJ}{d\alpha} = 0$. Differentiating Eq. (3.73), we have:

$$J' = \frac{dJ}{d\alpha} = \Upsilon^T \frac{dP}{d\alpha}\Upsilon + 2\Upsilon^T P \frac{d\Upsilon}{d\alpha} \tag{3.74}$$

[5] http://mathworld.wolfram.com/Moore-PenroseMatrixInverse.html

It was shown in [109] that the first term can be evaluated as:

$$\Upsilon^T \frac{dP}{d\alpha}\Upsilon = -2D^T \frac{d\Psi}{d\alpha}\Lambda_{nl} \tag{3.75}$$

while the second term can be re-written by taking the transpose of D from Eq. (3.72) such that the overall derivative of the loss function becomes:

$$J' = \frac{dJ}{d\alpha} = 2D^T \left(\frac{d\Upsilon}{d\alpha} - \frac{d\Psi}{d\alpha}\Lambda_{nl}\right) \tag{3.76}$$

Finally, a Newton-Raphson finite difference method is used to find the solution to the equation $J' = 0$. The $(i+1)^{th}$ itertation in the process of finding α can be written as:

$$\alpha_{i+1} = \alpha_i - \frac{J'_i}{J''_i} \tag{3.77}$$

$$\text{Where} \quad J''_i = \frac{d^2 J_i}{d\alpha^2} = \frac{\frac{dJ_i}{d\alpha} - \frac{dJ_{i-1}}{d\alpha}}{\alpha_i - \alpha_{i-1}}$$

As a note, the implementation of Eq. (3.76) in a computation code requires differentiation of Υ and Ψ with respect to α, which are not analytical functions themselves. Let the crank angle θ be expressed in terms of the code level array index number i_θ along with the TDC error α represented i_α. Since the interval of change is $\delta i_\alpha = 1$, the differentiation of the terms Υ and Ψ (see Eq. (3.68)) with respect to i_{alpha} can be expressed as:

$$\frac{d\Upsilon}{d\alpha} = \begin{pmatrix} \frac{\frac{dp[i_{\theta,1}+i_\alpha+1]}{d\theta} - \frac{dp[i_{\theta,1}+i_\alpha-1]}{d\theta}}{2} \\ \vdots \\ \frac{\frac{dp[i_{\theta,N}+i_\alpha+1]}{d\theta} - \frac{dp[i_{\theta,N}+i_\alpha-1]}{d\theta}}{2} \end{pmatrix} \tag{3.78}$$

$$\frac{d\Psi}{d\alpha} = \begin{pmatrix} 0 & \frac{p[i_{\theta,1}+i_\alpha+1]-p[i_{\theta,1}+i_\alpha-1]}{2}\frac{1}{V(\theta_1)}\frac{dV_1}{d\theta} \\ \vdots & \vdots \\ 0 & \frac{p[i_{\theta,N}+i_\alpha+1]-p[i_{\theta,N}+i_\alpha-1]}{2}\frac{1}{V(\theta_N)}\frac{dV_N}{d\theta} \end{pmatrix} \tag{3.79}$$

The convergence generally requires less than 10 iterations and can be stopped when $|\alpha_i - \alpha_{i+1}| < 0.1$ CAD. As seen in Figure 3.12b the convergence is achieved only in 4 iterations and the TDC offset value, $\alpha = -1.6$ CAD, implies that the current pressure trace must be shifted and advanced by 1.6 CAD relative to the volume.

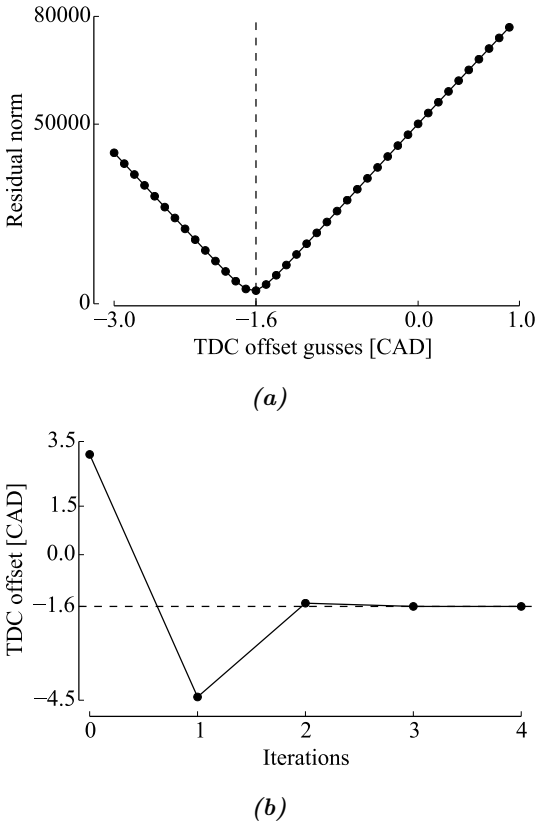


Figure 3.12: *TDC estimation using the Tunestål method. (a) A sequential method of finding the TDC is computationally expensive. (b) On the other hand, the Tunestål method gives the correct TDC offset of -1.6 CAD in only a few iterations.*

3.3.3 Determination of pegging

The issue of pegging arises from the nature of the piezoelectric sensor which only responds to a change in the pressure rather than the actual pressure. The baseline for the signal change needs to be quantified so as to recover the original pressure variations from the data. Generally the pegging offset is a simple DC offset which remains constant throughout a single cycle but may vary between successive cycles. Hence, it is necessary to 'peg' *each* of the acquired pressure cycles. Many ways of pegging have been developed as reviewed by Lee et al. [110].

The most common method of pegging is through the use of an intake pressure sensor. Since an intake pressure sensor is available in the test bench, the intake pressure can be used as a reference to compare with the in-cylinder pressure at a position in the cycle when the gas path between the two pressure sensors are connected, for example, before the IVC position of the compres-

sion stroke. Figure 3.13a shows a typical case where the in-cylinder pressure near the BDC is plotted along with the measured intake pressure. To use the difference between the cylinder pressure sensor signal and the intake pressure signal, a filtering of the in-cylinder pressure signal of decent accuracy would be required. Complicating the intake pegging procedure are the acoustic waves that occur in the intake manifold resulting from oscillating air flow which are not captured by the slow response of the intake pressure sensor which produces only an average value. Lee et al. [110] argued that intake pegging methods may not be sufficiently robust and hence reviewed some theoretical pathways to determine the pegging offset. In this work, a pegging method developed by Tunestål [109] is discussed, utilizing the similar nonlinear least squares estimation methodology as discussed in the previous section. It must be noted here that unlike the TDC and R_c estimations discussed in the previous sections which utilize motoring data, the pegging procedure is a must for all experimental data including those with combustion.

The pegging offset, Δp, resulting from the way a piezoelectric sensor and charge amplifier works can be expressed as an intra-cycle constant term that simply adds to the experimental pressure, p, resulting in the erroneous measured output pressure signal p_m:

$$p_m = p + \Delta p \tag{3.80}$$

It can be assumed that the compression and expansion of the in-cylinder gas follows a polytropic form i.e. $pV^\gamma = C$, where γ is the polytropic exponent and C is a constant. Thus Eq. (3.80) can be re-written as:

$$p_m = \Delta p + C \cdot V^{-\gamma} \tag{3.81}$$

where $C = p_0 V_0^\gamma$ with p_0 and V_0 being reference values. It must be noted that this holds true only before any combustion begins, i.e. before the SOC. Assuming the polytropic exponent γ is known, Eq. (3.81) can be written as a linear system of equations, for N pressure points corresponding to N consecutive crank angle degrees in a single pressure trace. In matrix form this can be expressed as:

$$\Upsilon = \Psi\Lambda \tag{3.82}$$

Where

$$\Upsilon = \begin{pmatrix} p_{m,1} \\ \vdots \\ p_{m,N} \end{pmatrix}, \quad \Psi = \begin{pmatrix} 1 & V_1^{-\gamma} \\ \vdots & \vdots \\ 1 & V_N^{-\gamma} \end{pmatrix}, \quad \Lambda = \begin{pmatrix} \Delta p \\ C \end{pmatrix}$$

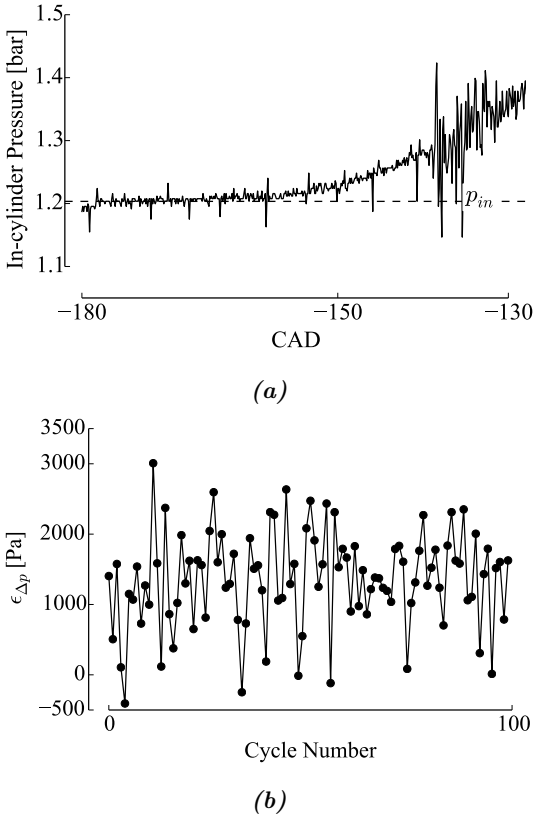


Figure 3.13: *(a) Pegging using the intake pressure sensor. The inherent noise of the in-cylinder pressure sensor along with the possibility of manifold oscillations not captured by the intake pressure sensor make this procedure somewhat less robust. (b) Error computed from taking the difference between the pressure offsets, Δp, computed from Tunestål pegging method and intake pegging method. The Tunestål pegging method shows a larger value as compared to the intake pegging method.*

The vector Λ is the unknown vector and it can be found, like in the previous section, through taking a Moore-Penrose pseudo-inverse. However, γ is generally not known, and hence it must be figured out too. As can be seen in Eq. (3.81), the relationship with γ is non-linear, thus requiring the use of a similar strategy as discussed in the previous section. A loss function J is defined and its minimum is found out using Newton-Raphson finite difference method. Let the residual be defined as:

$$D = \Upsilon - \Psi\Lambda \tag{3.83}$$

As done in Eq (3.73), a loss function J is defined:

$$J = D^T D = \Upsilon^T P \Upsilon \tag{3.84}$$

Where P is the symmetric projection matrix $P = [I - \Psi(\Psi^T\Psi)^{-1}\Psi^T]$. The solution would be to find a particular $\hat{\gamma}$ such that $J' = \frac{dJ}{d\hat{\gamma}} = 0$. Unlike the case in the previous section, Υ is independent of γ and hence J' has a simpler form:

$$J' = \frac{dJ}{d\gamma} = \Upsilon^T \frac{dP}{d\gamma}\Upsilon = -2D^T \frac{d\Psi}{d\alpha}\Lambda = 2CD^T \begin{pmatrix} V_1^{-\gamma}\, lnV_1 \\ \vdots \\ V_N^{-\gamma}\, lnV_N \end{pmatrix} \tag{3.85}$$

Finally, a Newton-Raphson finite difference method can be used to find the solution to $J' = 0$. As done in the last section, the $(i+1)^{th}$ iteration of determining the γ can be written as:

$$\gamma_{i+1} = \gamma_i - \frac{J'_i}{J''_i} \tag{3.86}$$

$$\text{Where} \quad J''_i = \frac{d^2 J_i}{d\gamma^2} = \frac{\frac{dJ_i}{d\gamma} - \frac{dJ_{i-1}}{d\gamma}}{\gamma_i - \gamma_{i-1}} \tag{3.87}$$

With the γ known, it can be re-substituted in Eq. (3.82) and solved to get a better estimate of Δp. Again, the convergence is super-linear and occurs within 5 iterations with the difference between offsets of about 100 Pa.

Figure 3.13b plots an error computed for 100 cycles, by taking a difference between the pegging offset obtained by the Tunestål method and that obtained by the intake pressure method, for each cycle. As for the intake pressure pegging, the pressure data was pegged using only a single intake pressure reading for the 100 cycles. With hindsight, this could have been improved by taking multiple readings per cycle and then averaging it to get more accurate values. To further test the robustness of the Tunestål method, the pressure traces were added random offset values before being analyzed by the two methods. The small difference between the two methods remains constant for as many iterations of random offsets, thus proving the robustness and consistency of the Tunestål method.

3.3.4 Pressure filtering

The final part of the processing of raw experimental pressure data is related to its filtering of signal noise. The first attempt to filtering is to average over a large number of pressure cycles. This is simple but inadequate, as shall be seen following this discussion. For having a good in-cylinder pressure trace, filtering has been suggested, over and above an averaging of many consecutive cycles. Filters such as the Savitzky-Golay have been used, for example see [111]. However, a more sophisticated approach, which can work in most cases along with the ability to retain combustion information is more desirous.

Digital filtering techniques such as low-pass filtering can be used for better quality data, necessary for accurate heat release analysis. The general proce-

dure of constructing such a filter is to first convert the signal from time domain into frequency domain, using Fourier transforms. Thereafter, the higher frequencies are eliminated beyond a certain *cut-off* frequency, thus forming a low-pass filter. The cut-off is carried out in a smooth fashion, such as through the use of a *Hanning window* function, in order to avoid the spurious generation of ripples in the filtered time domain signal (Gibbs effect). Specifying the cutoff frequencies tuned to particular signals are not trivial, and thus Payri et al. [112] describes the procedure of adaptive determination of the cut-off frequencies based on the features of individual pressure cycle. This methodology is followed for all pressure cycles in this thesis and is briefly described here.

The first step is to treat the samples of consecutive raw pressure cycles as a continuous periodic signal, so that it can be converted from time or CAD domain to the corresponding frequency domain by carrying out a Discrete Fourier Transform (DFT) of the signal. With respect to this context it could be assumed that since the RPM was held constant, the angular speed also remains relatively constant which implies that the CAD and time domains are interchangeable. For n_s pressure samples per cycle and n_c consecutive cycles in the sample (in our case n_c=100), the amplitude A of the $n_s \times n_c$ points in the complex frequency domain can be written as:

$$A_i = A_i^{Re} + jA_i^{Im} \quad \text{with} \cdots i = 1, 2, \cdots, n_c \cdot n_s \tag{3.88}$$

The corresponding frequencies can be written as:

$$f_i = \frac{i-1}{n_c \cdot n_s} f_s = \frac{i-1}{n_c} f_0 \quad \text{with} \cdots i = 1, 2, \cdots n_c \cdot n_s \tag{3.89}$$

where f_s is the sampling frequency and f_0 is the frequency of the engine cycle. For convenience, a normalized frequency can be used such as:

$$f_i^n = \frac{f_i}{f_0} = \frac{i-1}{n_c} \quad \text{with} \cdots i = 1, 2, \cdots n_c \cdot n_s \tag{3.90}$$

Assume k_1 and k_2 are the start and the stop cut-off frequencies of interest for filtering a pressure trace. Then, the Hanning window function H can be applied at each point such that the filtered signal $A_{i,filtered}$ results:

$$A_{i,\text{filtered}} = H_i \times A_i \qquad \text{where} \quad H_i = \begin{cases} 1 & k < k_1 \\ cos\left(\frac{\pi}{2} \cdot \frac{k-k_1}{k_2-k1}\right) & k_1 \leq k \leq k_2 \\ 0 & k > k_2 \end{cases} \tag{3.91}$$

This window function implies that the amplitudes of the frequency spectrum are smoothly decreased, starting from k_1 and ending at zero at frequency k_2, in order to avoid Gibbs effect or spurious oscillations, as well as capture the important information contained in the pressure signal. To determine the k_1

and k_2, the frequency domain dataset could be divided into signal harmonics S_k and non-signal harmonics, N_k. Signal harmonics, S_k, are defined as those whose normalized frequencies, f_i^n, are a natural number:

$$S_k = A^{Re}_{(k-1)n_c+1} + jA^{Im}_{(k-1)n_c+1} \tag{3.92}$$

Here $k = 1, 2, \cdots, n_s$. For the non-signal or noise harmonics, their normalized frequencies occur in-between the natural harmonics with about $n_c - 1$ frequency points such that:

$$N_{k,m} = A^{Re}_{(k-1)n_c+1+m} + jA^{Im}_{(k-1)n_c+1+m} \tag{3.93}$$

Here, $k = 1, 2, \cdots, n_s$ and $m = 1, 2, \cdots, n_c - 1$. Each set of $n_c - 1$ noise signals, $N_{k,m}$, can further be associated with the previous signal frequency S_k such that:

$$\{S_k, \{N_{k,m}\}\} \quad \text{with} \quad \begin{cases} k = 1, 2, \cdots, n_s \\ m = 1, 2, \cdots, n_c - 1 \end{cases} \tag{3.94}$$

Let N_k be the mean of the $N_{k,m}$ set of frequencies which may be represented as the mean noise $N_k = N_k^{Re} + jN_k^{Im}$ for the 'k'th signal point S_k. The next step is to apply some statistical testing to establish frequencies at which the signal S_k and its associated noise N_k begin to be in-differentiable from each other. It has been established in the paper, that if at a certain frequency k, the value $S_k - N_k$ lies within the following confidence intervals and the interval also contains the origin ($S_k - N_k$=0), then it can be said that the signal and noise are indistinguishable, with a probability $p = 1 - \alpha$.

$$(S_k^{Re} - N_k^{Re}) \pm t^{\alpha/2}_{nc-2} \cdot s_k^{Re} \sqrt{n_c/(n_c - 1)} \tag{3.95}$$

$$(S_k^{Im} - N_k^{Im}) \pm t^{\alpha/2}_{nc-2} \cdot s_k^{Im} \sqrt{n_c/(n_c - 1)} \tag{3.96}$$

Here s_k represents the standard deviation in the noise frequencies, $N_{k,m}$. The symbol t stands for Student's t-distribution. It was recommended that the probabilities for k_1 and k_2 should correspond to probabilities of 98% and 80%, respectively.

The results of the Payri filtering process can be seen in Figure 3.14. In Figure 3.14a, 100 raw pressure cycles have been plotted against the CAD. The pressure traces are from an operating condition corresponding to $\phi = 0.34$, which is near the ringing limit represented by the MPRR of 10 bar/CAD. In such conditions the cycles have higher fluctuations near the TDC which is captured by the figure. Figure 3.14a also plots the average of the 100 cycles, along with the Payri filtered pressure trace, however, they are indistinguishable from each other. But the real difference between the raw data, the 100 cycle average and the Payri filtered pressure trace can be found in their differential forms

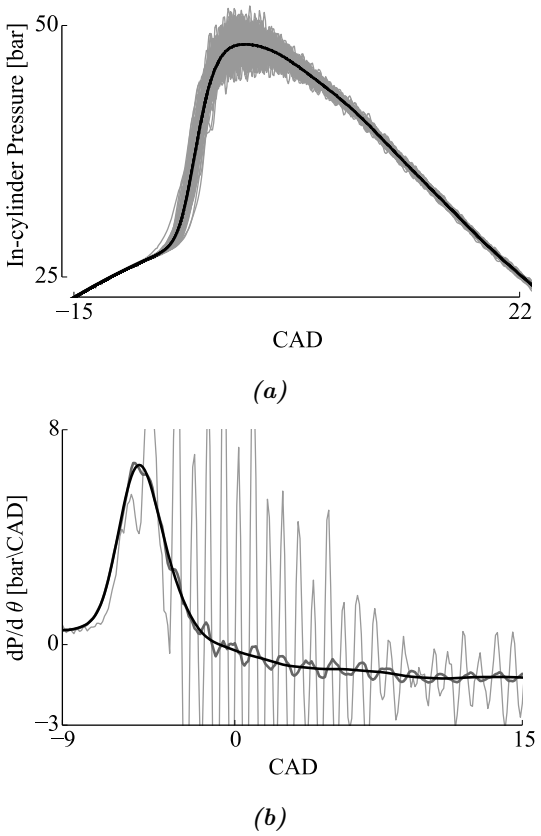


Figure 3.14: *The effect of averaging and filtering or noise prone raw pressure data. (a) Raw pressure data for 100 cycles along with the 100 cycle average and the mean and filtered pressure trace according to the method proposed by Payri et al.. The 100 cycle average is indistinguishable from the Payri filtered trace. (b) The noise is magnified on differentiation of the pressure traces. In light gray, the derivative of a single raw pressure trace. In contrast, the derivative of the 100 cycle average pressure trace (darker grey) has less noise, however it still is of lesser quality than the smooth derivative of the Payri filtered pressure trace (black).*

as shown in Figure 3.14b, which is used for RoHR computations. The simple raw pressure differential has high amounts of fluctuation. The regularity of the oscillations point towards HCCI ringing phenomenon, rather than instrument related random noise. However, for computation of RoHR, such ringing data can cause spurious effects. Figure 3.14b also shows the differential of the 100 cycle average pressure trace which has smaller oscillations than the raw trace. However, the differential corresponding to the Payri filtered pressure trace has no oscillations, while tracing along the 100 cycle average very well.

The Payri method has been used extensively throughout the data discussed in this thesis. However, the computation have also included raw pressure traces

(after some low pass filtering below 20 kHz) which contain important information about inter-cycle variations for various parameters.

3.4 Uncertainty Analysis

The propagation of uncertainty from the experiments to the final results have been summarized in Figure 3.15. The left hand side in Figure 3.15 lists the various sources of fundamental instrument level uncertainties, which contribute to the uncertainties in the intermediate parameters, and which are themselves used in calculations of the uncertainties in the final parameters. The *Type A* or *Type B* analysis is also marked in the connecting arrows and are relevant at the fundamental stages. It should be noted here that the uncertainty calculations in the in-cylinder temperature and the ratio of specific heat, γ, have not been carried out due to their computations being based up on assumptions (in case of temperatures, for example ideal gas behavior) and empirical models (in case of γ, the NASA polynomials), the evaluations of which will require more elaborate efforts than were feasible in the current time frame.

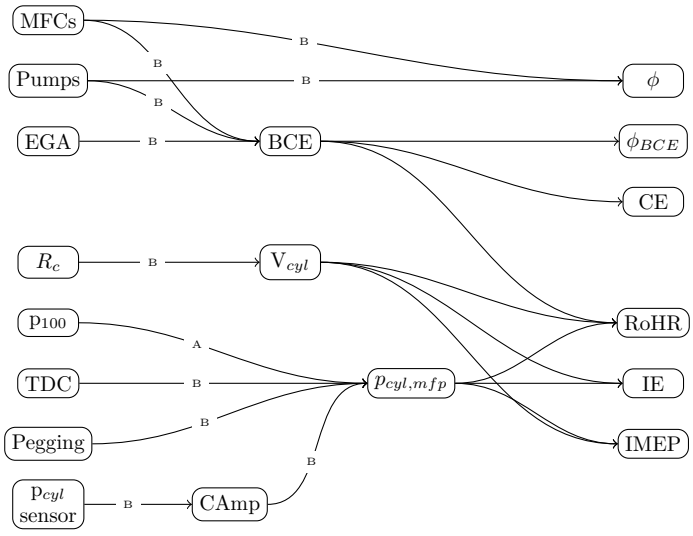


Figure 3.15: *Overview of the uncertainty work flow. Type A and B are marked in the connecting arrows at the base level of uncertainty calculations which start from the left and proceed towards the right.*

The formulations for the computation of uncertainties represented in Figure 3.15 have been discussed in detail in Appendix B. Table 3.1 lists some of the uncertainties in the key parameters used throughout the thesis. The first thing to notice is the high uncertainty in the in-cylinder pressure measurement. This is due to the large magnitude of uncertainty the pressure sensor offers at the lowest values near the BDC. Therefore, for the computation of CA10 and

Parameter	U95
m	0.8%
ϕ	2%
CE	3%
Tars	4 g/Nm^3
H_2O	3 % of syngas flow
$p_{cycle,max}$ Type B	17 %
$p_{cycle,max}$ Type A	3.6%

Table 3.1: *Maximum U95 uncertainties, either in absolute point or relative.*

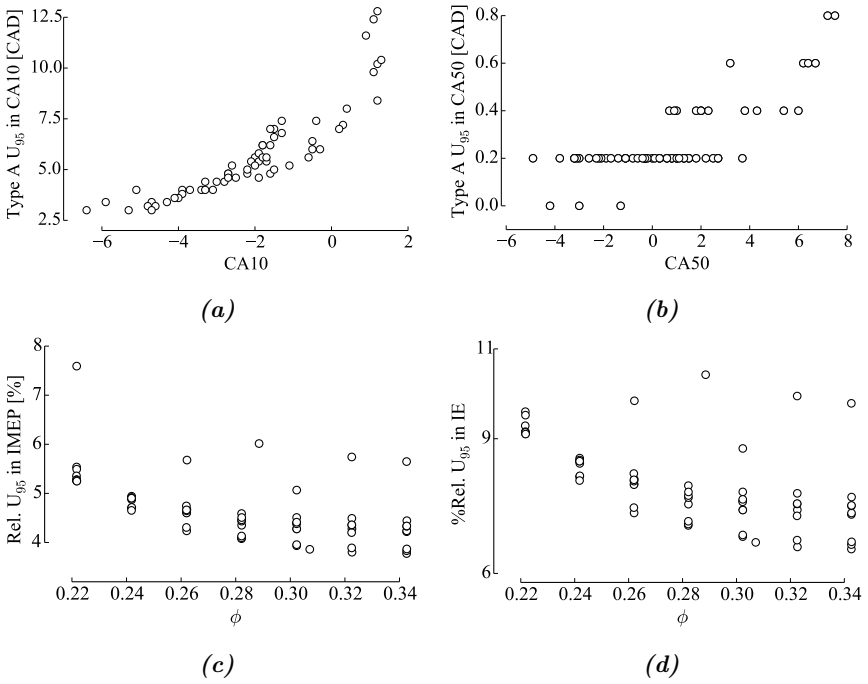


Figure 3.16: *Uncertainties in some main parameters: (a) As combustion advances the associated uncertainty decreases. This uncertainty has been computed on the 100 cycles pressure data and does not include the inherent instrument level uncertainty in the pressure sensing system, hence Type A. (b) Similarly for CA50, as the combustion advances the uncertainty decreases. (c and d) As the ϕ increases, the computed uncertainties on the IMEP and IE decreases since the combined uncertainty of the pressure trace decreases.*

CA50, only Type A uncertainties in the in-cylinder pressure have been used, resulting in Figures 3.16a and 3.16b. As can be observed, the burn angle uncertainties decrease as the combustion advances. This behavior is explained in Appendix B.8. Uncertainty computations in IE and IMEP have included Type A+B uncertainties in the pressure data and are plotted in Figures 3.16c

and 3.16d. These uncertainties decrease as the equivalence ratio increases and similar trends have also been found when the combustion advances, albeit not as clearly.

It must be noted here that all the uncertainties mentioned in this section have a confidence level of 95% (hence the label U95), and therefore have noticeably higher values, almost twice than that of standard uncertainty which has a confidence level of only 68%. Additionally, for the sake of clarity, these uncertainties are not indicated in the plots presented in the following chapters.

Chapter 4

Influences of syngas compositions and operating conditions

This chapter is an expanded/updated version of

Subir Bhaduri, Francesco Contino, Hervé Jeanmart, and Ernst Breuer. The effects of biomass syngas composition, moisture, tar loading and operating conditions on the combustion of a tar-tolerant HCCI (Homogeneous Charge Compression Ignition) engine. *Energy*, 87(0):289–302, 2015

This chapter describes experimental investigations carried out regarding HCCI combustion with high temperature syngas and air mixtures, in order to establish the influencing factors. The nature of HCCI combustion in terms of indicated performance (IE and IMEP), combustion phasing (CA50 and burn duration CA_{90-10}) and emissions (CE, NO_x and CO emissions) has been studied as a response to the following factors:

1. Variations in the H_2/CO ratio of the dry syngas.
2. Syngas moisture content.
3. Syngas tar content.
4. Intake pressure, p_{in}, and temperature, T_{in}.

These experiments have used simulated syngas compositions with simulated representative tar compounds and injected water, thus benefiting from repeatability and controlled variability. Section 4.1 establishes the Balanced Chemical Equation (BCE) relevant to this chapter, which include the tars and moisture content of simulated syngas. The next sections discuss the experimental results starting from Section 4.2.1 which discusses the effects of H_2/CO ratio, followed

by syngas moisture content in Section 4.2.2, syngas tars content in Section 4.2.3 and engine operating factors of p_{in} and T_{in} in Section 4.2.4.

4.1 Formulation of the BCE

The objectives of formulating and solving the BCE can be summarized as below:

1. Define what are the reacting components and the product components going and coming out of the engine system.
2. Determine the flow rates which can be specified to the MFCs and pumps to simulate the various compositions.
3. Based on the complete information about the BCE, compute various data such as molar fractions of gases, combustion efficiency, LHV, etc.

Based on the generic form of the BCE from Eq. 3.13 in Chapter 3, the general form of the BCE for this chapter can be expressed as:

$$\left(\begin{array}{l} n_{\text{dry syngas}} + n_{\text{additives}} \\ + \dfrac{1}{\phi_{BCE}} \cdot n_{O_2,stoic} \cdot (O_2 + 3.762N_2) \\ + n_{RGF} \end{array}\right) \xrightarrow{combustion} n_{products} \tag{4.1}$$

Notice here that the EGR term has been dropped. The complete BCE, with all the species, can be expressed as follows:

$$\begin{aligned} &\left(\begin{array}{l} n_{S,N_2}\, N_2 + n_{S,CO_2}\, CO_2 + n_{S,CO}\, CO \\ + n_{S,H_2}\, H_2 + n_{S,CH_4}\, CH_4 \end{array}\right)_{\text{dry syngas}} \\ &+ \left(\begin{array}{l} n_{S,C_7H_8}\, C_7H_8 \\ + n_{S,C_{10}H_8}\, C_{10}H_8 \\ + n_{S,H_2O}\, H_2O \end{array}\right)_{\text{tars and moisture}} \\ &+ \frac{1}{\phi_{BCE}}\, n_{O_2,stoic}\, (O_2 + 3.76N_2) \\ &+ RGF \left(\begin{array}{l} \overline{n_{E,H_2O}}\, H_2O + \overline{n_{E,CO_2}}\, CO_2 \\ + \overline{n_{E,O_2}}\, O_2 + \overline{n_{E,N_2}}\, N_2 \end{array}\right) \\ &\xrightarrow{combustion} \\ &\qquad \left(\begin{array}{l} n_{E,H_2O}\, H_2O + n_{E,CO_2}\, CO_2 \\ + n_{E,CO}\, CO + n_{E,O_2}\, O_2 + n_{E,N_2}\, N_2 \end{array}\right) \end{aligned} \tag{4.2}$$

Here the first bracket denotes the simulated dry syngas components, the second represents the added tars and moisture, while the third and fourth represent the air and residual gas fraction (RGF) components respectively. It must be remembered here that the letter 'n' represents the moles of the respective species

at the IVC position of the HCCI cycle. The subscript S represents a syngas component while E represents an exhaust component. The ϕ_{BCE} stands for the equivalence ratio calculated through this formulation by solving it. The term $n_{O_2,stoic}$ represents the stoichiometric oxygen required for the combustion of the given amount of syngas fuel, termed as n_{syngas}. Two kinds of additives have been included into the BCE, tars and water. In the case of tars, two kinds of representative tar compounds, toluene (C_7H_8) and naphthalene ($C_{10}H_8$) have been used during the experiments related to tars, as described in Section 4.2.3. Experiments with syngas moisture (n_{S,H_2O}) are discussed in Section 4.2.2.

Since the RGF gases have been assumed to be constituted of complete combustion products resulting from a lean combustion, its components have been marked with $\overline{overline}$ in order to distinguish them from exhaust components measured by the exhaust gas analyzer.

The Appendix C.1 details the procedure for evaluating the BCE expressed in Eq. (4.2). It also includes the method of computing the RGF and its constituents, based on Eq. (3.14) and Eq. (3.15) introduced in Chapter 3. Additionally, the combustion efficiency or CE from Eq. (3.19) can be deduced from the BCE with the Q_p calculated from the unburnt CO emissions whereas Q_r is calculated from the reactants. The uncertainties in the BCE are crucial to deduce the uncertainties in the CE and the uncertainties in the heat input per cycle, $Q_{fuel/cycle}$, necessary for determining the uncertainties in the indicated efficiency, IE. The procedures for determining these uncertainties are mentioned in Appendix C.3.

4.2 Experimental Results

The experimental procedure carried out throughout this chapter, as well as in Chapter 5, has the following underlying characteristics:

- The engine body temperatures were held constant at $T_{body} = 110 \pm 5°C$. This temperature range was decided upon through empirical observations and is one that can be reliably maintained for all the experiments described in this chapter, as well as in Chapters 5 and 6, using the manual control of engine fan opening. A higher engine body temperature would benefit the completeness of combustion, but will also advance the combustion phasing and its subsequent ill effects on the upper limit of equivalence ratio and the IMEP. Additionally, higher engine temperatures are detrimental to the engine health. The influences of changing T_{body} were not evaluated explicitly in this thesis.
- The data was recorded only when the CO emissions, measured from the Exhaust Gas Analyzer (EGA), became stable. This condition can be assumed to imply stabilized operating conditions as the CO emissions were found to be highly sensitive to the changes in the engine body temper-

ature, which itself changes due to changes in the operating conditions and the strength of combustion related to the equivalence ratio. During the experiments, the CO emissions stabilized the slowest, as compared to other parameters such as the CO_2 and O_2 emissions, engine body temperatures, etc.

- At each experimental point, three repeat experiments were carried out to evaluate the experimental stability. Additionally, these repetitions were not sequential, but were carried out by a random intermixing between the various experimental points (i.e. between different ϕ) to further represent the experimental trends as inclusive of the uncontrollable random variations in the test conditions.

4.2.1 Variations in the dry and pure syngas composition

The syngas composition varies as a function of time for any gasifier which may cause fluctuations in the engine performance. The time variation aspect has been studied in Chapter 6. In order to study the response of HCCI combustion to the compositional variations, experiments with three dry compositions, representative of the typical syngas from the two-stage downdraft gasifier at the authors' laboratory (see Chapter 6), were carried out. The tested compositions differed only in their H_2 and CO concentrations, as listed in Table 4.1. The compositions are ordered according to low, nominal and high values of H_2/CO as well as H_2/CO_2 ratios. The low Lower Heating Value (LHV) of the compositions can be attributed to air being used as the gasifying agent. Thus, about 59% of the bulk syngas volume consists of inert components (N_2, CO_2 and some Ar) which results in the low LHV. The table also mentions the LHV of the mixture of each of the three compositions with air at stoichiometric conditions as well as at equivalence ratio of 0.3, from which it can be concluded that for all practical purposes, the influence of the variations in the LHV, due to the variations in the H_2/CO or H_2/CO_2 ratios, can be neglected.

In this section, the effects of dry syngas compositions, characterized by their changing H_2/CO and H_2/CO_2 ratios, on HCCI combustion have been evaluated. During the experiments, the equivalence ratio, ϕ, was changed from 0.22 to 0.34, in steps of 0.02 while the operational parameters of intake temperature and pressure were held relatively constant at $T_{in} = 250 \pm 5°C$ and p_{in}=1.2 bar.

Figure 4.1 shows the variations in the CA50 and the combustion duration (CA_{90-10}), as a function of the equivalence ratio ϕ for the three compositions. The heat content of a combustion process is directly linked with the ϕ. Due to the critical dependency of autoignition processes on the temperature and the fuel chemistry, inhomogeneities in the thermal and species distribution throughout the compressed volume cause the autoignition reactions to initiate only at certain favorable spots. These initial reactions, depending on the ϕ, influence

Fuel Type (H_2/CO)	Low	Nominal	High
x_{H_2}	0.12	0.18	0.22
x_{CO}	0.28	0.22	0.18
x_{N_2}	0.48	0.48	0.48
x_{CO_2}	0.11	0.11	0.11
x_{CH_4}	0.01	0.01	0.01
H_2/CO	0.43	0.82	1.22
H_2/CO_2	1.1	1.64	2.0
A/F$_{stoic}$ [kg$_{air}$/kg$_{fuel}$]	1.14	1.21	1.26
LHV$_{syngas}$ [MJ/kg]	4.34	4.52	4.65
LHV$_{mix,stoic}$ [MJ/kg]	2.03	2.04	2.05
LHV$_{mix,\,\phi=0.3}$ [MJ/kg]	0.90	0.90	0.89

Table 4.1: *Three standardized dry syngas compositions have been used in the experiments, represented by their molar fractions x, which are representative of the variations observed in the downdraft two-stage gasifier installed at the author's laboratory. The compositions are characterized by their H_2/CO ratios as low, nominal and high. The same sequence is also true for the respective H_2/CO_2 ratios.*

the surrounding gas temperatures which in turn lead to further autoignitions and eventually a thermal runaway. Thus, as the ϕ increases, the autoignition processes accelerate, resulting in the advancement of combustion (see Figure 4.1a) and the consequent reduction in the burn duration (see Figure 4.1b). The CO-rich syngas composition (H_2/CO=0.43) lags behind in the trends of CA50 compared to the other compositions which are relatively H_2-rich. For example, at ϕ=0.28 the lag amounts to a large 3 CAD. This lag and its consequences, as shall be seen in the following sections, can be attributed to the differences in the rates of combustion of CO and H_2.

HCCI combustion can be characterized by the auto-ignition delay times for the different species involved. As discussed in Hernandez et al. [113] and in the review of previous works in Section 1.2.2, the mixtures with higher H_2 content have shorter auto-ignition delays compared to mixtures with lower H_2 content. Thus, as seen in Figure 4.1, at low ϕ, the slow combustion of CO in the CO-rich syngas results in the correspondingly longer combustion durations and later CA50 positions. Due to the rapid expansion in the gas volume after the TDC, the resulting temperature drop decreases the combustion rate of CO rich syngas at low ϕ, and eventually quenches it. On the other hand, for the H_2 rich syngas, the higher combustion rates result in the appropriate combustion phasing. Thus, a short combustion duration with the CA50 position near the TDC is necessary in order to avoid quenching. Alternatively, if a closed control loop HCCI was implemented, adjusting the control parameters could have compensated for the ϕ and fuel composition dependent changes in the combustion phasing.

The quality or completeness of combustion can be assessed through the

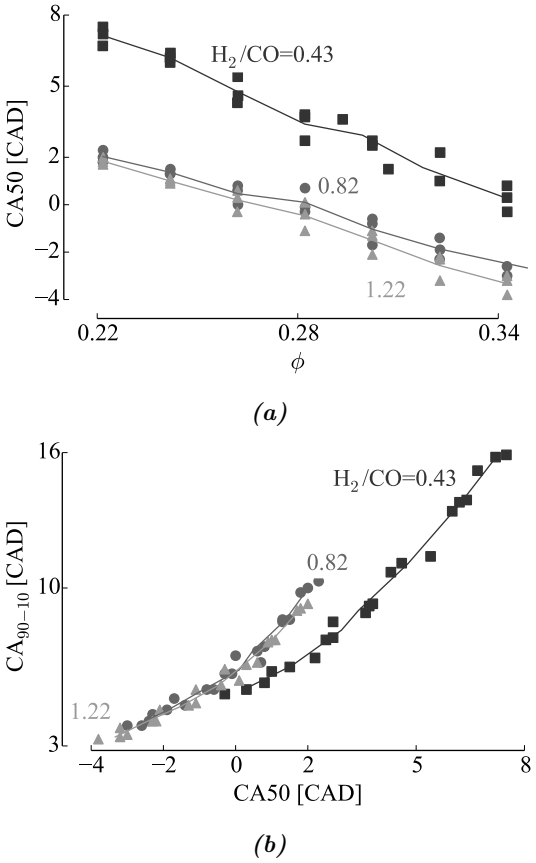


Figure 4.1: *Variations in HCCI combustion phasing as a function of ϕ, for different H_2/CO mixture ratios. (a) CA50 of the slow burning 0.43 mixture lags behind the fast burning H_2-rich mixtures. (b) The CA50 position and the burn duration are almost linearly related.*

combustion efficiency, using Eq. (3.19). The CE of the three compositions, as a function of the CA50, are shown in Figure 4.2a. As described previously, the combustion of CO-rich syngas at ϕ=0.22 is quenched due to its late phasing and as a consequence, a large portion of the fuel remains un-burnt. This results in the low CE of approximately 80%. In the context of syngas as a fuel in HCCI engines, due to the absence of any significant quantities of hydrocarbons, the bulk of CO emissions can be linked directly to the un-burnt CO component of the original fuel, as see in Figure 4.2b. It must be noted that the maximum CE of H_2-rich syngas mixtures are higher because all the experiments were stopped at $\phi = 0.34$. Higher ϕ with CO-rich syngas would have achieved equivalent CE as the H_2-rich mixtures achieve at lower ϕ. Also, the rate of decrease in the unburnt CO is much higher for the H_2-rich syngas, because of the higher availability of H_2 which provides the much needed heat

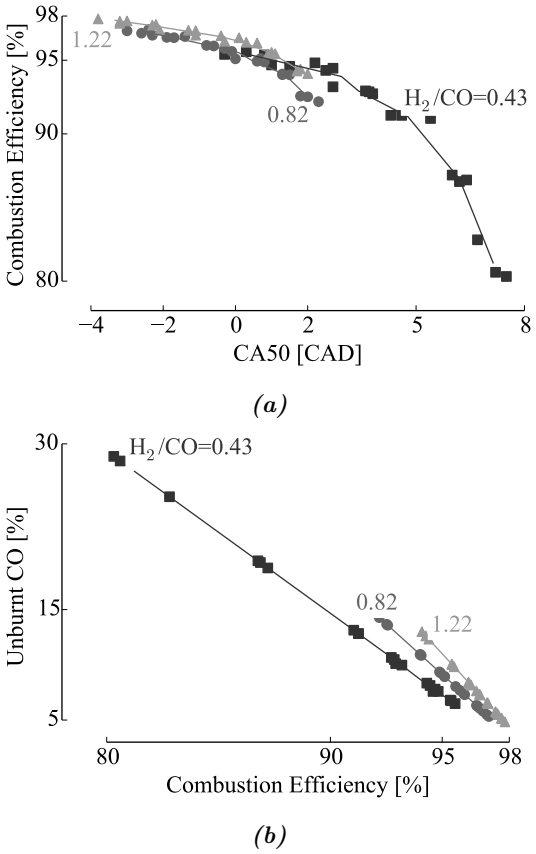


Figure 4.2: *CE and unburnt portion of CO measured in the emissions, as functions of CA50 for various H_2/CO mixture ratios. Advanced combustion and shorter burn durations caused by increasing ϕ (or H_2 content) are least affected by the volume expansion after the TDC, and hence have a better combustion efficiency. Consequently, emissions of CO decrease.*

for accelerating CO combustion. Even at an advanced CA50, the colder crevice regions still remain unfavorable for combustion and thus lead to the sub-100% combustion efficiencies observed in Figure 4.2 [55].

Advanced combustion and the resulting shorter combustion duration leads to higher peak cycle temperatures, T_{max}, as seen in Figure 4.3a. The strong linear relationship between CA50 and the peak temperature can be explained as being directly related to the almost linear relationship of CA50 with ϕ (see Figure 4.1a). The shift in the trends between the lower H_2 content syngas and the higher ones is also similar. The negative consequence of high combustion temperatures is the production of NO_x, as seen in the Figure 4.3b. However, these emissions are still low compared to the SI and CI engines due to the relatively cooler combustion temperatures, characteristic of the HCCI engine.

The effects of H_2/CO ratio on the NO_x can be observed to be negligible or within the uncertainty of the exhaust analyzer (U95≈5 ppmv).

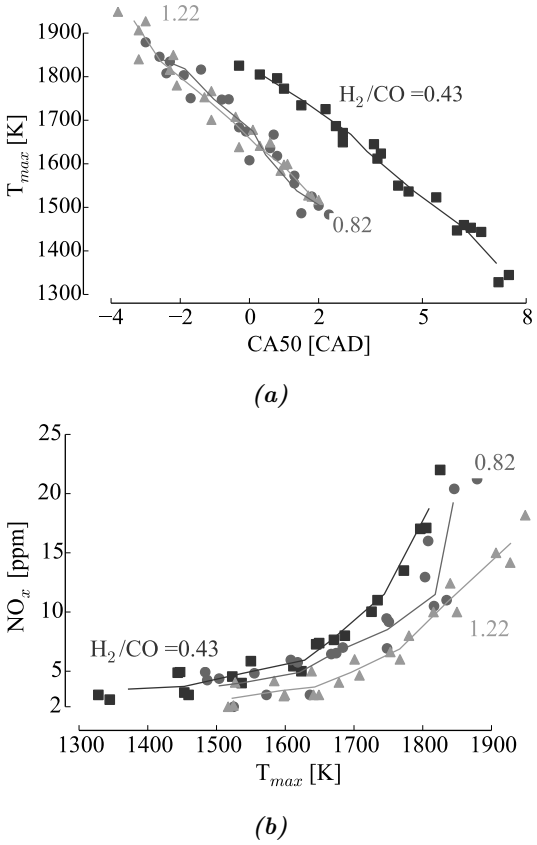
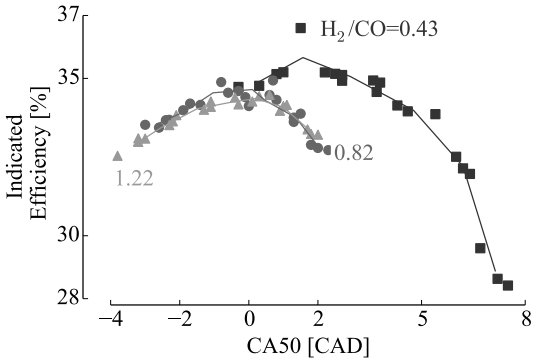


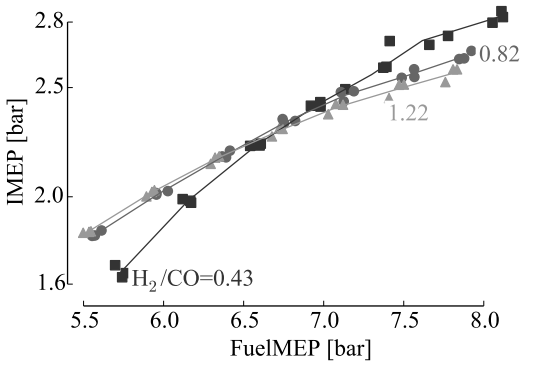
Figure 4.3: *Experimental NO_x measurements as a function of the peak cycle temperature, T_{max}, which is also a strong function of ϕ, and hence the CA50.*

Although the CE displays how much of the fuel has been burnt, the IE indicates the indicated work output as compared to the fuel input. The IE, as seen in Figure 4.4a, has a maximum when the CA50 is near the TDC. However, for the CO-rich syngas (H_2/CO=0.43), the IE maximum has a relatively higher value than the maximums from other compositions. This higher efficiency of the 0.43 mixture occurs at a relatively late CA50=2 CAD and at a high $\phi \geq 0.30$. The resulting short combustion duration due to a high ϕ remains unaffected by the volume expansion, thus contributing positively to the overall cyclic work. On the other hand, for mixture ratios of 0.83 and 1.22, since the CA50 is already near the TDC even at the low ϕ=0.22, the increase in ϕ causes an increased portion of the combustion to occur before the TDC. This results in increased frictional, as well as, wall heat transfer losses. Thus, the heat released is not well utilized resulting in a decrease in the IE, the peak of which

occurs very near the TDC for the H_2-rich compositions. Figure 4.4b shows the increase in the IMEP as a function of the increasing amounts of fuel contained in the combustion chamber, represented by the FuelMEP. The higher IMEP for the CO-rich syngas at higher FuelMEP can be attributed again to the better combustion phasing, similar to the behavior of the IE.



(a)



(b)

Figure 4.4: *(a) As ϕ increases, the CA50 advances with maximum IE occurring near and after the TDC. (b) The IMEP improves with FuelMEP and is also responsive to the better combustion phasing of the 0.43 mixture.*

Figure 4.5a shows large variations in the CA_{90-10} parameter represented by the coefficient of variations (CoV), computed over 100 cycles. These variations show a peculiar tendency to increase at the regions prone to high pressure ringing (advanced CA50 before the TDC) or to larger cyclic variations (later CA50 after the TDC). Additionally, the syngas with lower H_2/CO seems to have the most stability over a relatively larger variation in the CA50, as compared to the H_2-rich compositions. The tendencies in these variations are similar to those found for the IE in Figure 4.4a. In fact, since the IE discussed here is the average of 100 cycles, it is obvious that large variations in the combustion phasing

or duration will decrease the average IE. Also the peak in the IE matches exactly to the most stable points in the CA_{90-10} of Figure 4.5a, reinforcing the link between decreased performance and combustion phasing variations. The high variations in the CA_{90-10} for the H_2-rich compositions around the narrow region of CA50=0 can be understood better when the variations are plotted against the FuelMEP in Figure 4.5b. This reinforces the earlier statement that the variations in the combustion duration increase either due to the late combustion resulting from lower fueling rate, or due to earlier combustion due to the higher fueling rates. Additionally, Figure 4.5b shows that the 0.43 mixture has a more stable combustion even at higher fueling rates. Although the variations in the combustion duration are large, it does not necessarily translate into unacceptable performance, as shall be seen in terms of the CoV of IMEP.

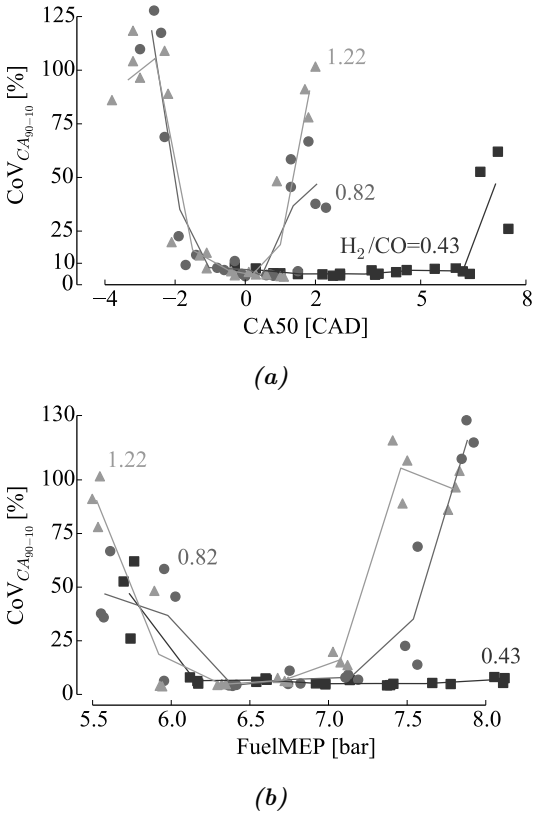


Figure 4.5: *The CA_{90-10} shows wide variations and has tendencies similar to that of IE. This behavior can be better explained by the FuelMEP which dictates if there is pressure ringing or variations resulting from weak combustion.*

The HCCI load range is limited by large variations between the cycles occurring at low FuelMEP and excessive MPRR, indicative of high pressure ringing,

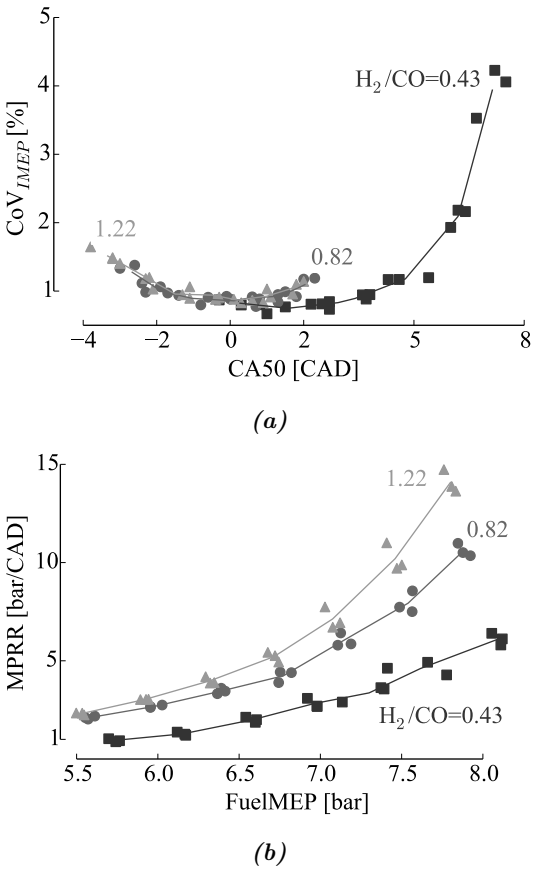


Figure 4.6: *Limits of HCCI combustion in terms of CoVs of the IMEP as a function of the CA50 and the MPRR as a function of the FuelMEP, for different H_2/CO ratios. HCCI load range is constrained between <5% CoV_{IMEP} and <10 bar/CAD of MPRR.*

occurring at higher FuelMEP. At low FuelMEP, HCCI combustion occurs late and is spread over many crank angle degrees (long combustion duration) and thus highly sensitive to factors such as the cylinder wall temperatures and thermal inhomogeneities within the charge. Thus, as the wall temperatures are modified inconsistently by each cycle, the consecutive cycles are affected. The resulting variability between the cycles is represented by the Coefficient of Variation in the IMEP (CoV_{IMEP}), computed for each operational point over 100 cycles. An upper limit of 5 % in the CoV_{IMEP} is generally accepted as representing stable combustion [80]. The CoV_{IMEP}, plotted as a function of CA50 in Figure 4.6a, indicates the overall stability of the HCCI combustion throughout the experimented range. However, when the combustion is delayed, the CoV_{IMEP} increases, with the maximum increase corresponding to the case of the slow burning CO-rich syngas at ϕ=0.22. This is the similar effect found

in case of the CoV of the CA_{90-10} in Figure 4.5b for low FuelMEP.

As the FuelMEP increases, the advanced and shorter combustion produces higher values of MPRR, as seen in Figure 4.6b. The MPRR is correlated to high pressure ringing phenomena and can therefore be utilized as a measure of ringing, with limits often determined through subjective operator experience [80]. The presence of ringing (correlated to MPRR) results in emissions of high amplitude audible noises and increases the heat loss to chamber walls, which decreases the thermal efficiency. In case of this test bench, a MPRR limit of 10 bar/CAD was found to be reasonable. The MPRR increase is accelerated with H_2-richness which can be attributed to the short ignition delays and fast H_2 reactions, as has been found by the other researchers in this domain [68, 69, 70, 71, 114]. Thus, the H_2 component increases the ringing tendency of syngas and places an upper limit on the usable HCCI load range. From Figure 4.6b it is evident that the increase in the MPRR as a function of FuelMEP is lower as the H_2 content in syngas decreases. Thus, the utilization of larger FuelMEP, or larger values of ϕ, is possible with the CO-rich syngas, as compared to the H_2-rich syngas.

In conclusion, it can be said that for optimal combustion behavior of the HCCI engine, leading to the maximum IE or IMEP, it must have the following characteristics:

- The combustion initiation or ignition delay must be such that a major portion of the combustion occurs after the TDC. This would reduce pressure ringing, friction and heat losses resulting in better overall efficiency. Such a combustion could be directly related to a decreased H_2 content in the syngas, or could result from an appropriate use of a combustion control strategy.
- The combustion must also be fast enough, so that it is not affected by the negative influences of volume expansion. Faster combustion rates (while not having a significantly advanced combustion) could be achieved at higher FuelMEP with fuels with increased CO content, which has a significantly higher reaction rate at higher temperatures compared to at lower temperatures [72].

Thus, if a control strategy is implemented which is able to maintain the CA50 at a constant position irrespective of the changes in fuel composition (increase or decrease in H_2/CO ratio, for example) or in the FuelMEP (controlled by ϕ) or in other influencing factors, the rate of combustion would become the dominant deciding factor with regards to optimal combustion. In such circumstances, the fastest possible combustion at a slightly later CA50 is most desirable.

4.2.2 Effect of moisture in syngas

Raw syngas from biomass gasifier contains approximately 10% of water by volume. Since the use of syngas in conventional IC engines has been concerned with cooled, purified and dry compositions, the effects of moisture content on the engine performance has not been explored widely. However water as an additive has been studied in IC engines operated with conventional fuels for its anti-knock effects as well as for reducing NO_x emissions (for example see [115]). In case of HCCI engines operated with conventional fuels, the objective of water injection has been to control the ignition timing by manipulating the rates of combustion as discussed in [61].

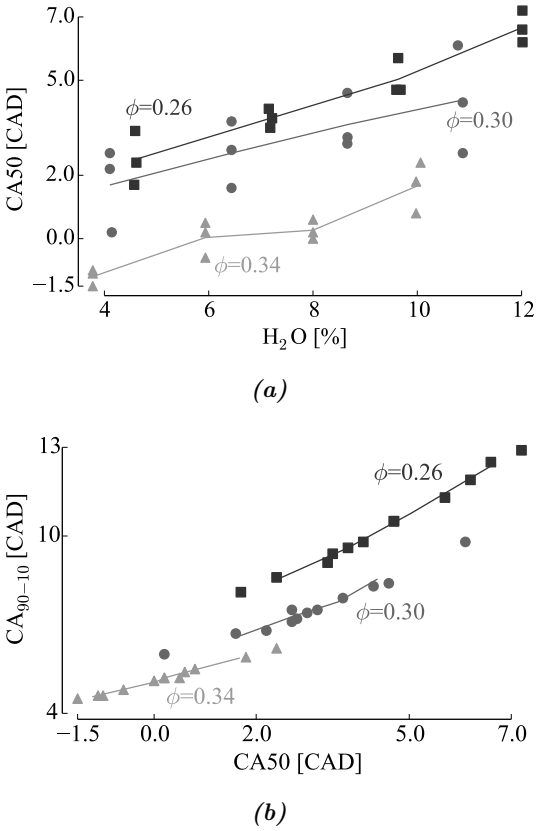


Figure 4.7: *Effects of water content on the CA50 and burn duration for various ϕ. Water slows down the combustion processes which retards the CA50 and causes the combustion duration to increase.*

Since the objective of the current work is to function with raw syngas, the pure and dry syngas discussed in the previous section is 'wetted' with water at varying proportions to simulate real case scenarios. A peristaltic pump has been used for injecting water into the hot gas flow just before the mixing drum

so that the water is fully vaporised and is assumed to have become a part of the homogeneous fuel-air mixture. For the experiments, the syngas of nominal composition with H_2/CO=0.82 was chosen and the engine was operated at T_{in}=250°C and p_{in}=1.2 bar. Experiments were carried out at three ϕ values of 0.26, 0.30 and 0.34 while the volumetric percentage of water in the syngas was varied from approximately 4 to 12 %.

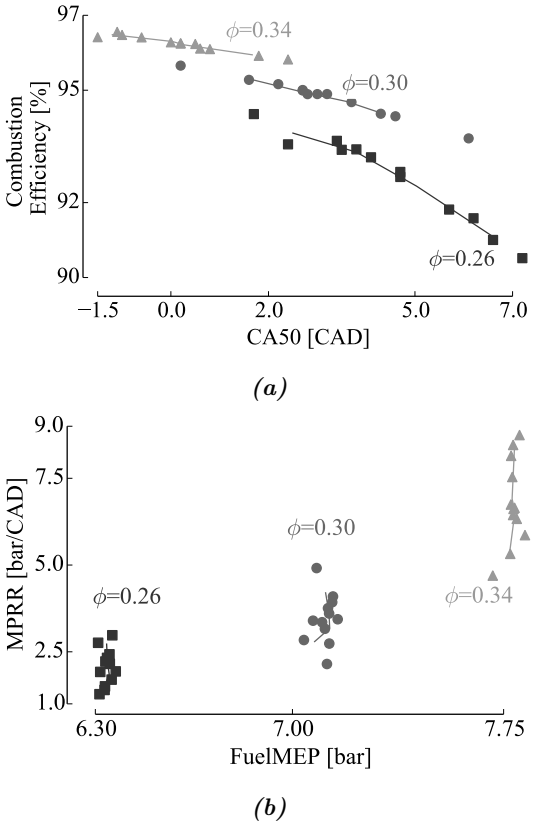


Figure 4.8: *(a) A negative effect of increasing water content of syngas is the decreased combustion efficiency. (b) However, the presence of moisture decreases the MPRR significantly.*

The main effect of increasing the water content of syngas was found to be the increasing delay in the CA50 and the corresponding increase in the combustion duration CA_{90-10}, as seen in the Figure 4.7. Compared to the combustion phasing and duration of pure syngas (as seen in Figure 4.1) for the highest ϕ=0.34, the CA50 delayed by more than 2 CAD when the water content was increased from 0 to a low 4%. Due to the combustion delay caused by water, the retarded combustion caused the CE to decrease, as seen in the Figure 4.8a. The decreasing trend can be attributed to the twin effects of the

drop in the combustion temperatures caused by the cooling effect of water, and the increasing influence of volume expansion due to larger combustion duration associated with late combustion phasing. However, the presence of moisture in the syngas has the beneficial effect of decreasing the MPRR significantly, as seen in Figure 4.8b. This is more evident for the $\phi = 0.34$ case, where an increase in H_2O content of syngas from 4% to 10% by volume, resulted in a decrease in the MPRR from about 8 bar/CAD to about 5 bar/CAD, a decrease of more than 30%.

With the increase in the water content of the syngas, minor improvements in the IE and IMEP were observed, mainly due to the retarded phasing. The delay in CA50 as well as the reduction in the MPRR due to the increased water content can allow operation at higher FuelMEP. Similar effects can be found through the use of EGR in HCCI engines.

4.2.3 Effect of Tars

The effect of the tars on the IC engines have not been sufficiently documented in available literature. Hasler and Nussbaumer [25] carried out some tests on the tar deposits formed in a SI engine after several hundred hours of operation with syngas containing tars <50 mg/Nm^3. Heavy tars, classified as those with boiling points higher than 200 °C were found having more tendency of forming deposits, compared to the comparatively lighter Polyaromatic Hydrocarbons (PAH) tars. As mentioned before in Section 1.2.3, the testing for tar depositions for the current setup was not feasible. However, on an immediate basis, the tar content in the syngas would alter the fuel chemistry due to its varying concentrations, high LHV, influences on chemical kinetics, etc. Thus, instead of studies with a detailed tar composition, which is essential in the study of tar deposition, the amount of tars was considered as of more relevance to the objectives of this thesis. Amongst the wide variety of tar compounds found in the biomass syngas, naphthalene ($C_{10}H_8$) and toluene (C_7H_8) have been chosen as the representative tar compounds for the current set of experiments, due to their significant proportions in the tar distribution and their wide acceptance as model tar compounds (for example see [116]).

Naphthalene, being a solid at room temperature, was dissolved in toluene and a saturated solution was created with the solubility constant of M=2.635 mol/L. The quantities of the compounds were determined from the molar ratios known from the assumption of a saturated mixture. The mixtures were injected in the liquid form using a 10 ml syringe pump. The total tar (toluene+naphthalene) injection rates varied in the range of 3.5 g/Nm^3 to about 17 g/Nm^3 of syngas flow, which are much higher than the nominally expected 50 mg/Nm^3 from a modern two stage gasifier. The solution was injected through the contraption shown in Figure 2.5b of Chapter 2, so that the hot gases (which are above the boiling points of the tars in the solution) in the

stream would vaporize the liquid droplets and produce a homogeneous mixture with the rest of the gases. The ϕ of pure syngas input was held constant at 0.3, while the injection rates of tars were changed. The range of tars injected from 3.5 to 17 g/Nm^3 stands equivalent to a change in the ϕ of neat syngas with (H_2/CO=0.82) from 0.30 to 0.34. It must be noted that modern two-stage gasifiers, such as the one at the author's laboratory, produce approximately 20 mg/Nm^3 of tars, instead of the minimum 3.5 g/Nm^3 used in these experiments. The significant amounts used here were to see if at all there could be flexibility of such a concept to be used with high tar producing gasifiers.

Figure 4.9a shows the changes in the CA50 due to the increasing FuelMEP caused by either increasing the ϕ of neat syngas, or through the addition of tars. The combustion phasing seems to be most sensitive to pure syngas, followed by the syngas containing the tar toluene. The tar mixture of toluene and naphthalene shows the least effect on the CA50. Figure 4.9b shows the reduced MPRR due to syngas which contains tars in contrast to pure syngas. This can be reasoned because tars have higher heat capacities and therefore their being present in the syngas leads to a delayed combustion initiation and stronger combustion damping. Figure 4.9c shows that since tars are fuel, their addition increases the IMEP. Thus, tars are beneficial components of syngas due to their high heat capacities in combination with high LHV, and are especially well suited to be used in an HCCI engine.

As a note, these experiments could have benefited from the measurements of hydrocarbon emissions, due to the significant quantities of tar used. Such a measurement would have allowed to estimate the completeness of combustion for the tars. Alternatively, detailed GC/MS measurements of the emissions could have been used to further understand the characteristics of tar combustion. However, such instrumentation was unfortunately not available at the time of the experiments.

4.2.4 Effect of variations in $\mathbf{p}_{in}$, $\mathbf{T}_{in}$

For exploring the sensitivity of HCCI combustion to the variations in p_{in} and T_{in}, experiments were carried out for a fixed fuel composition at the nominal H_2/CO=0.83 and at three ϕ values of 0.26, 0.30 and 0.34. While exploring the sensitivity to p_{in}, the T_{in} was held constant at 250°C, whereas, while exploring the sensitivity to T_{in}, the p_{in} was held at a constant 1.2 bar.

An increase in the p_{in} results in greater charge densities while having lesser impact on the compression temperature. The higher temperatures resulting from combustion of larger amounts of fuel advance the CA50, as seen in Figure 4.10a. However, the ϕ does not represent the increased fueling, which is better reflected by the use of FuelMEP, as shown in Figure 4.10b. Thus, the consequences of pressure boosting simply transforms into an effect equivalent to using a higher amount of fueling rate, with the advantage of maintaining

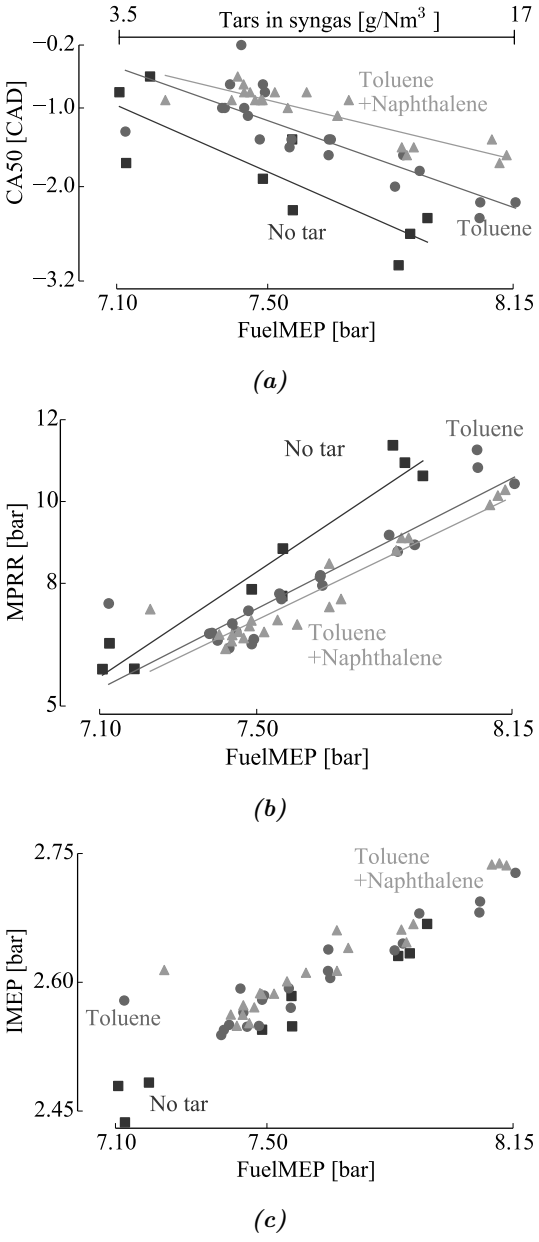


Figure 4.9: *Effects of syngas tars on HCCI combustion as a function of FuelMEP of the syngas+tar input. (a) The effects of naphthalene or toluene on the CA50 are comparatively lesser than pure syngas (No tar), even at very large concentrations. The range of tars injected, in terms of g/Nm^3, is also indicated. (b) Due to the delayed CA50 caused by use of tars, the MPRR produced is lesser than for pure syngas. (c) Higher IMEP is achieved due to the high LHV of* ***impure syngas****, as compared to pure syngas.*

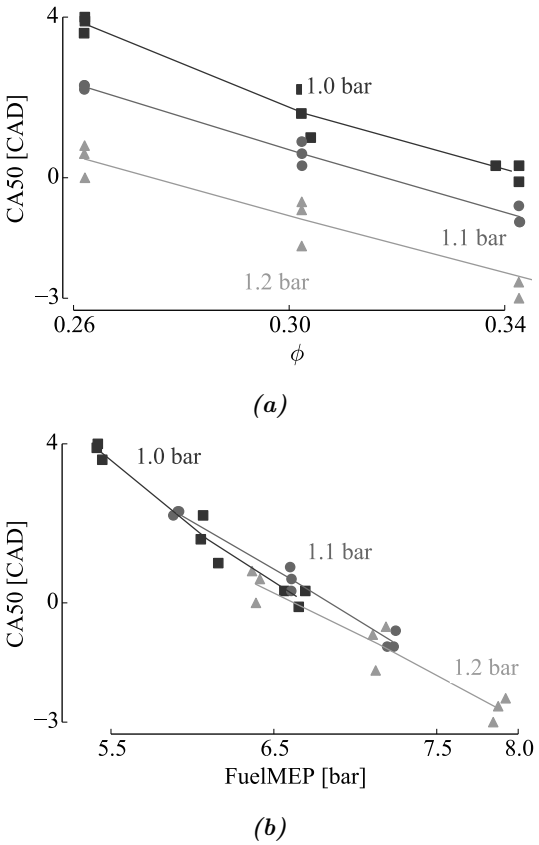


Figure 4.10: *The CA50 represented as function of ϕ and FuelMEP, for different p_{in}. The increased pressure boost simply becomes equivalent to an increased fueling rate.*

the ϕ.

The direct consequence can be seen in the IMEP plot in Figure 4.11a. In contrast, the reader may refer to the previous discussion on the relationship between the FuelMEP and the IMEP (see Figure 4.4b) where the combustion phasing differences caused by differing H_2/CO mixture compositions caused differences in the IMEP, even at the same FuelMEP. This is not the case here, the only difference being that of the pressure.

In Figure 4.11b, the MPRR can be observed to decrease with the pressure boosting, while the FuelMEP remains constant. For example, at FuelMEP=6.5 bar, the decrease in the MPRR is about 2 bar/CAD for an increase in the intake pressure by 0.2 bar (from p_{in}=1.0 bar to p_{in}=1.2 bar). This can be attributed to the higher concentration of gases with higher heat capacity (air) as a consequence of pressure boosting, which dampens the combustion thus reducing the MPRR. Thus, pressure boosting is an effective method of increasing the fueling

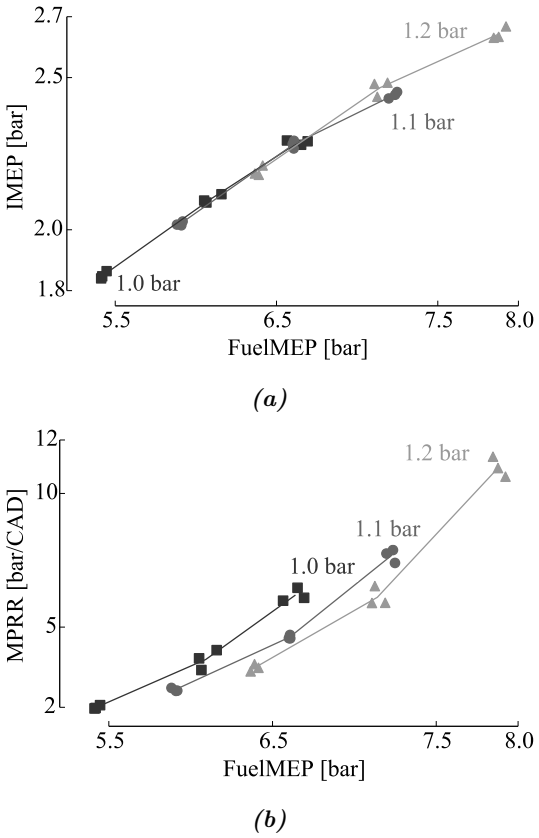


Figure 4.11: *Effects of variation in the p_{in} on the IE and the IMEP at different ϕ. As p_{in} increases, the advance in the CA50 reduces the IE while the IMEP improves almost proportionally.*

capacity of an HCCI engine without the consequence of increased ringing.

The parameter T_{in} has a significant impact on HCCI combustion. The primary effect can be seen on the CA50 trends plotted in Figure 4.12a for different T_{in} of 230, 250 and 270 °C. For the high T_{in}=270°C, the autoignition process begins well in advance of the TDC and is accelerated due to the volume compression, resulting in very short combustion durations and advanced CA50 values. As an example, at ϕ=0.30, an increase in the T_{in} by about 20°C from 230 to 250°C, advances the CA50 by about 8 CAD and in the 250 to 270°C range, by about 3.5 CAD. Consequently, the combustion duration decreases significantly, as seen in Figure 4.12b.

The first consequence is the increase in the MPRR, as seen in Figure 4.13a. The MPRR for T_{in}=270°C increases beyond the 10 bar/CAD limit. Once again, the parameter FuelMEP helps in isolating the effects. At a constant FuelMEP, for example at FuelMEP=7 bar, the increase in intake temperature

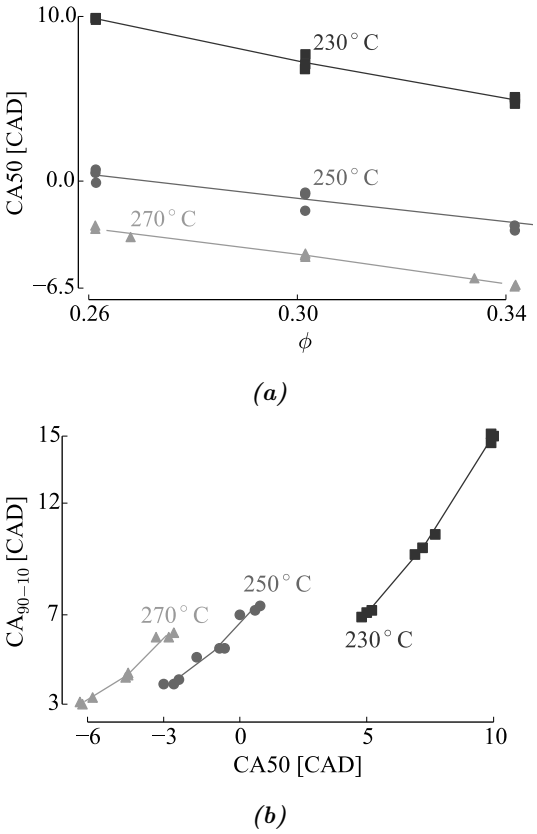


Figure 4.12: *Effects of T_{in} on the CA50 and the combustion duration. At lower T_{in}, the slow combustion results in late CA50 and larger combustion duration. However, at high T_{in}=270° C, the CA50 is too advanced giving rise to extremely short combustion durations.*

by 20°C from 230-250°C results in a jump in MPRR from 1.34 bar/CAD to 5.6 bar/CAD, an increase of more than 300%. This jump in the MPRR increases to about 500% from 230-270°C. As the fueling rate increases, the corresponding increases in the MPRR for higher T_{in} will be significantly higher. The effect on IMEP can be see in Figure 4.13b where the lower intake temperatures record a higher rate of increase in the IMEP for a certain increase in the FuelMEP. This shows that IMEP is impacted by optimum combustion phasing, which is significantly better for lower intake temperatures than at higher temperatures.

The parameter T_{in} drastically affects the HCCI combustion, with better performance being achieved at lower temperatures. The lower limit of T_{in} however must be based on the tar dew point, which depends on the chemical composition as well as the concentration of the tars. The gasification setup upstream can be optimized for lower tar dew point without the constraint on

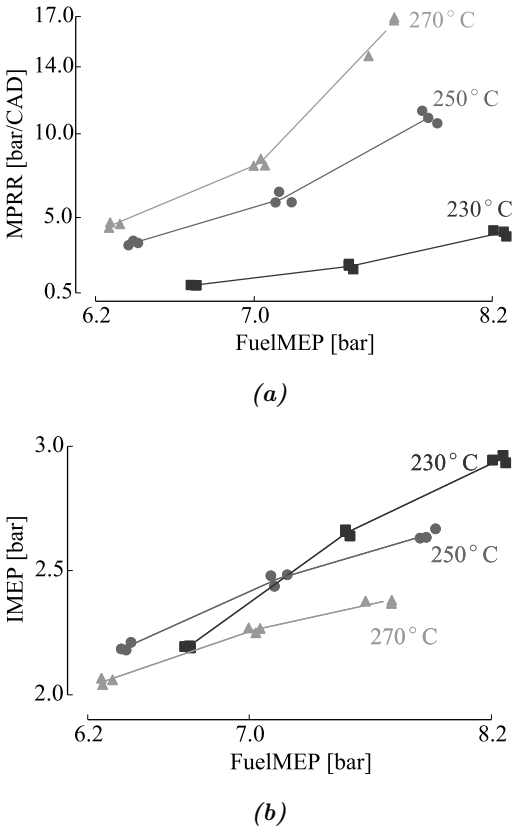


Figure 4.13: *T_{in} has drastic effects on the MPRR and the IMEP for the same amount of fuel used. The lower the T_{in} the better the performance.*

tar quantities due to the increased tar tolerances of this concept.

4.3 Conclusion

The key findings of this chapter can be summarized as follows:

- In terms of variations in the dry syngas composition, a CE >90% and an IE >30% were achieved for compositions with the H_2/CO ratios of 0.43, 0.82 and 1.22 for ϕ >0.3. The corresponding IMEP was above 2.5 bar.
- The early combustion initiated by the H_2 component of syngas resulted in increased MPRR and decreased IE and IMEP values. The maximum range of ϕ was limited to 0.34 due to the MPRR limits of 10 bar/CAD being crossed by the H_2-rich syngas (H_2/CO=1.22). Thus, syngas with low H_2 content is preferred for better performance, at least in the cases of open-loop HCCI operation.

- HCCI combustion with wet syngas with varying proportions of moisture content showed positive effects resulting from delay in the combustion caused by the damping effect of water on the rate of chemical reactions. However, a slight penalty of a decrease in the CE was observed.
- Experiments with representative tar compounds of toluene and naphthalene, up to an unrealistically high 17 g/Nm^3, were carried out. Their effect on the HCCI combustion phasing was found to be positive in the sense of increased FuelMEP without encountering an advance in combustion phasing, in contrast to pure syngas.
- To improve the performance, in terms of efficiencies and IMEP, higher p_{in} and lower T_{in} could be used. However, more research on the tar dew point needs to be carried out specific to the gasifier configuration, in order to optimize the T_{in}.

The conclusions show the positive potential of this novel pathway, however with limitations of power derating (low IMEP). Many of the challenges faced in the experiments discussed in this chapter could be boiled down to lack of an effective control strategy. The next chapter focuses on this aspect through the use of Exhaust Gas Recirculation.

Chapter 5

Exhaust Gas Recirculation for control of HCCI combustion

This chapter is an expanded/updated version of

Subir Bhaduri, Hervé Jeanmart, Ernst Breuer, and Francesco Contino. Studies of EGR in Biomass Syngas fueled tar tolerant HCCI engines. In *Ninth Mediterranean Combustion Symposium*, Rhodes, Greece, 2015

The concept of HCCI engines being operated at temperatures higher than the tar dew point of impure syngas, faces several challenges, one of which is the control of combustion phasing in response to changing syngas compositions or operating conditions. Of the many methods to achieve an effective control handle, the method of Exhaust Gas Recirculation was chosen for this application.

The effects of EGR in HCCI engines have been explored in many works, for example see [118, 119, 120]. In an HCCI engine, the use of a higher fueling rate (or equivalence ratio) advances the combustion phasing, leading to an increase in ringing and MPRR due to non-optimal phasing. In such situations, the EGR technique can be used, which modulates the ignition delay to compensate for the changes in the factors causing the shifts. Additionally, since the IMEP is directly linked to the fueling rate, the use of such a control technique increases the possibility of achieving higher performance than would have been possible in the absence of any control. It must be noted that a control system cannot be complete without an associated closed-loop feedback unit, which modulates the controllable parameter, in this case the EGR rate. As an example, Olsson et al. [121] discuss a closed-loop HCCI control system which uses real-time estimated

CA50 position as a feedback to control the combustion phasing, by changing the fuel composition consisting of two fuels, each with different combustion characteristics. However, such a feedback and action closed-loop control unit was not developed or used in this thesis.

The focus of this chapter is to explore the effectivity of the EGR technique as a control method for an HCCI engine used in the context of syngas gasification, especially at the high intake temperatures to avoid tar deposition. EGR related aspects of charge dilution and thermal effects have been studied. This chapter is divided into four broad sections. Section 5.1 reviews some of the basic fundamentals of using EGR, followed by Section 5.2 which discusses the formulation of EGR used in this chapter. Further, Section 5.3 discusses the various dilution effects caused by the use of EGR and the ways to counter them. And finally, Section 5.4 presents the experimental results achieved with simulated syngas and simulated EGR.

5.1 A brief overview of the EGR technique

The EGR is represented in schematic form in Figure 5.1. Fresh intake gas mixture consisting of air and fuel enters the intake manifold with a fuel to air equivalence ratio, represented in this chapter as ϕ_{FIN}, the subscript FIN standing for '*Fresh INtake*'. Thereafter, this fresh mixture is mixed with EGR gases which are post-combustion gases that would normally exit the engine through the exhaust. Since these gases contain some oxygen due to the lean operation of HCCI engines, the equivalence ratio of the air+fuel+EGR mixture changes to $\phi_{FIN+EGR}$. There also exists the RGF fraction of exhaust gases that are inherently recirculated and mixed with the fresh as well as EGR gases. As discussed in Section 3.1 of Chapter 3, the RGF gases are trapped in the dead volume at the TDC and are mixed with the fresh charge. Although it has the same effect as EGR, the RGF will not be treated as a control parameter in this chapter.

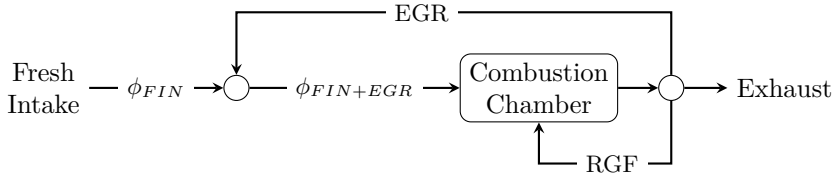


Figure 5.1: *Schematic representation of EGR in an engine. The equivalence ratio before the EGR is added to the mixture (ϕ_{FIN}) is diluted by the addition of EGR diverted from the exhaust flow, resulting in a new mixture with equivalence ratio $\phi_{FIN+EGR}$. The RGF acts as an inherent EGR, however its effect is small and cannot be modulated to act as a control technique in normal engines.*

EGR can be implemented as internal and external EGR. Continuing from

the discussion on RGF, the technique of Variable Valve Timing can be implemented to attain a Negative Valve Overlap (NVO) condition, in contrast to the Positive Valve Overlap (PVO) condition which is the case in the current engine. While the PVO condition results in the RGF gas amount and composition governed by the conditions near the intake and exhaust processes, in NVO, the exhaust valve closes much earlier in the cycle while the intake valve is yet to open. This results in trapping a larger amount of exhaust gases, over and above the RGF. As an example, Kozarac et al. [122] discussed the use of internal EGR through the NVO technique in an HCCI engine fueled by biogas. Since, biogas contains high proportions of the methane and CO_2, its auto-ignition requires higher temperatures and thus the intention of Kozarac et al. was to utilize the high temperatures of the trapped exhaust gases to achieve HCCI operation, with reduced amounts of intake gas heating. In contrast to internal EGR, external EGR channels the flow from the exhaust manifold into the intake manifold, via an external loop. The advantage of external EGR is that an intermediate cooler can be used for cases where the associated charge heating effect of internal EGR is not needed, thus resulting in an improved effectivity of EGR gases in damping the combustion rates due to lower charge temperatures.

In summary, the effects of EGR can be classified into four categories:

Modifying the charge temperature: The EGR may influence the temperature of the charge, depending on whether EGR is implemented in the form of external cooled or uncooled recirculation or in the form of internal recirculation, as discussed in the previous paragraph.

Dilution effects: In HCCI engines, the EGR is implemented in lean conditions with excess air and thus it reduces the fuel-to-air equivalence ratio from the original ϕ_{FIN} (Fresh INtake with normal air and syngas), to the effective $\phi_{FIN+EGR}$ (FIN with EGR gases), as seen in Figure 5.1. This dilution effect has to be mitigated so as to avoid decreased fuel flow into the engine per engine cycle.

Thermodynamic damping: EGR mostly consists of gases CO_2, N_2, H_2O and O_2 depending on the operating equivalence ratio. As discussed in the works reviewed in Section 1.2.2 before, the CO_2, due to its high specific heat capacity, delays and dampens the combustion process, thus causing the combustion to spread over many crank angle degrees. This is the main effect aimed to be exploited by the use of EGR.

Influence on the chemical kinetics: EGR gases such as H_2O, CO_2, CO, NO_x may also influence the HCCI combustion through chemical kinetic pathways, for example see [120, 123].

In the current context of HCCI operation with syngas above the tar dew point, the high temperatures of internal EGR seem to be more beneficial since it will aid to maintain an overall mixture temperature above the tar dew point.

However, since EGR temperatures can be higher than the tar dew point, adjustments to the intake temperature would have to be made to result in an optimal mixture at an optimal temperature. Thus, the use of internal EGR will have to be considered under the following foreseeable challenges/constraints:

- The mixture temperature must be optimum to have proper combustion phasing.
- The required intake air temperature should not fall below the tar dew point.
- The amount of EGR gases must be such that sufficient EGR related combustion delay/damping can occur in the face of changing conditions.
- Internal EGR temperature and species concentrations in turn depend on the intake conditions, gases and combustion phasing.

Although, these operational challenges have not been discussed further in this thesis, they ahve been mentioned here in order to bring forward the potential challenges with this approach. The EGR experiments described in this chapter are carried out using simulated EGR gases with simulated syngas in order to clearly identify the combustion damping/delaying effects.

5.2 Formulation

The formulation of EGR, as used in this chapter, has the following objectives:

1. Define what EGR is in terms of the Balanced Chemical Equation (BCE).
2. Understand the diluting influences of EGR and determine ways to compensate for it.
3. Determine and interpret experimental information regarding the flow of gases (intake and exhaust) through the system. Based on the BCE formulation, the various data such as molar fractions of gases, combustion efficiency, LHV, etc can be computed.

Many variations in the formulations of EGR exist, for which the reader may refer to Müller [124]. On a fundamental level, the EGR can be defined in the form of recirculated ratio, either in terms of recirculated mass or recirculated moles of the exhaust gas:

$$EGR = \frac{m_{EGR}}{m_{exhaust}} = \frac{n_{EGR}}{n_{exhaust}} \tag{5.1}$$

Here, m and n stand for the mass and the number of moles of the gas involved in a single cycle. A way of estimating the effective EGR can be through the use the ratio between measured CO_2 concentrations at the intake and exhaust of an engine. This is useful in cases where the fuel is devoid of any CO_2, unlike biomass syngas which contains a large amount of CO_2 (approximately 11%

in this case). In the context of this chapter where the EGR gases are being simulated using MFCs and pumps, such measurements are not necessary.

Similar to Chapter 4, the EGR gases have also been assumed to have the same composition as RGF gases. This assumption leads to EGR consisting of CO_2, N_2, H_2O and O_2 components, which are products from a lean and complete combustion process (no CO), henceforth termed as Complete Combustion Products (CCP). The BCE capturing all the chemical information related to the EGR, the air and the syngas can be expressed as Eq. (5.2).

$$\begin{aligned}
&\underbrace{\begin{pmatrix} n_{S,N_2}\,N_2 + n_{S,CO_2}\,CO_2 + n_{S,CO}\,CO \\ + n_{S,H_2}\,H_2 + n_{S,CH_4}\,CH_4 \end{pmatrix}}_{\text{dry syngas}} \\
&+ \frac{n_{O_2,stoic}}{\phi_{FIN}}(O_2 + 3.76N_2) \\
&+ (EGR(1-RGF) + RGF)\underbrace{\begin{pmatrix} \overline{n_{E,H_2O}}H_2O + \overline{n_{E,CO_2}}CO_2 \\ + \overline{n_{E,O_2}}O_2 + \overline{n_{E,N_2}}N_2 \end{pmatrix}}_{\text{CCP}} \\
&\xrightarrow{combustion} \\
&\quad n_{E,H_2O}H_2O + n_{E,CO_2}CO_2 + n_{E,CO}CO + n_{E,O_2}O_2 + n_{E,N_2}N_2
\end{aligned} \tag{5.2}$$

Here, the '$EGR(1-RGF)$' term represents the fraction of the exhaust gas quantity which is deliberately recirculated, in contrast to the RGF component which is inherently present within the engine. As done in the previous chapter, the EGR and RGF gases are considered to be products of complete combustion, and thus have been marked with an $\overline{overline}$. These product components can be analytically determined based on the information of the intake gases (reactants) and are thus distinct from the product gases determined experimentally by the Exhaust Gas Analyzer (EGA) (see Appendix D.1).

In contrast to the previous chapter where only two definitions of the equivalence ratio were used, ϕ and ϕ_{BCE}, there are three distinct definitions considered in this chapter, ϕ_{FIN} (Eq. (5.3) from Eq. (D.22)), $\phi_{FIN+EGR}$ (Eq. (5.4)) and ϕ_{BCE} (Eq. (5.5)). As explained previously, the ϕ_{FIN} corresponds to the fuel-to-air relationship of the Fresh INtake gases before any mixing with EGR gases takes place. The $\phi_{FIN+EGR}$ corresponds to the new relationship formed between the syngas and the air contained in the mixture of fresh intake gases and EGR gases, due to the presence of excess oxygen in the EGR gases. The ϕ_{BCE} is obtained by solving the BCE Eq. (5.2) and in ideal circumstances $\phi_{BCE} = \phi_{FIN}$, irrespective of the EGR value. However, due to experimental uncertainties and differences, this is often not the case and the discrepancy amounts to a consistent $\phi_{FIN} - \phi_{BCE} \approx 0.02$. Despite the three different equivalence ratios, only the ϕ_{FIN} and $\phi_{FIN+EGR}$ are used, while the role of ϕ_{BCE} is limited to forming a part of the solved BCE Eq. (5.2), from which various other parameters are deduced.

$$\phi_{FIN} = \frac{n_{syngas}}{n_{FIN,air}} \cdot AF_{n,stoic} \tag{5.3}$$

$$\phi_{FIN+EGR} = \frac{n_{syngas}}{n_{FIN,air} + n_{EGR,air}} \cdot AF_{n,stoic} \tag{5.4}$$

$$\phi_{BCE} = \frac{n_{syngas}}{n_{BCE,air}} \cdot AF_{n,stoic} \tag{5.5}$$

The BCE Eq. (5.2) is solved according to the procedure detailed in Appendix D. As mentioned previously, the solved BCE can be used for determining the following important parameters:

1. Composition of the reactants and their products in terms of their molar concentrations. This is crucial for computing the temperature and species dependent evolution of the ratio of specific heats for heat release analysis, γ, as discussed in Section 3.2.1 in Chapter 3.
2. LHV informations: LHV_{FIN} of the Fresh INtake (FIN) syngas+air mixture before mixing with the EGR gases and the $\text{LHV}_{FIN+EGR}$ of the syngas+air+EGR mixture.
3. The values of the various equivalence ratios: ϕ_{FIN}, $\phi_{FIN+EGR}$ and ϕ_{BCE}. Especially, an important relationship between ϕ_{FIN} and $\phi_{FIN+EGR}$ is obtained from Eq. (D.24) of Appendix D.1.2:

$$\phi_{FIN+EGR} = \frac{1 - EGR}{\frac{1}{\phi_{FIN}} - EGR} \tag{5.6}$$

4. Determination of total fuel flow to obtain IE and FuelMEP.

Additionally, the uncertainty analysis of the BCE is also discussed in Appendix D.2. This results in the uncertainties in ϕ_{FIN}, $\phi_{FIN+EGR}$, CE and IE, as discussed in Section 3.4.

5.3 The diluting effects of EGR

For all the experiments considered in this chapter, the intake temperature, the intake pressure and the RPM were maintained constant, irrespective of the EGR addition to the flow. This allowed to have data which are comparable with each other in terms of operating conditions. With this background, consider the total intake mass per engine cycle, m_{intake}. Since the experiments are conducted at lean equivalence ratios, where the charge is per-dominantly constituted of N_2 gas (irrespective of the change in EGR and ϕ_{FIN}), the value of m_{intake} can be assumed to be a constant. Thus, two cases can be imagined, with (subscripted as $EGR = 0$) and without (subscripted as $EGR \neq 0$) the

presence of EGR gases:

$$m_{intake} = \begin{cases} m_{syngas,EGR=0} + m_{air,EGR=0} & EGR = 0 \\ m_{syngas,EGR\neq 0} + m_{FIN,air,EGR\neq 0} + m_{EGR} & EGR \neq 0 \end{cases} \tag{5.7}$$

In the case of $EGR \neq 0$, it must be noted that $m_{FIN,air,EGR\neq 0}$ is disctinct from the mass of air contained within the m_{EGR}, hence the subscript contains the annotation FIN. From the definition of EGR in Eq. (5.1) and the fact that $m_{intake} = m_{exhaust}$ (assuming no blow-by losses), for the case of EGR$\neq$ 0 in Eq. (5.7), it follows that :

$$m_{intake} = \frac{m_{syngas,EGR\neq 0} + m_{FIN,air,EGR\neq 0}}{1 - EGR} \tag{5.8}$$

Further, using the definition of equivalence ratio and denoting the mass ratio of air to syngas at stoichiometric conditions as $AF_{m,stoic}$, the two cases in Eq. (5.7) can be simplified. The simplified forms can be equated based on the hypothesis that $m_{intake} = constant$:

$$m_{syngas,EGR=0} \cdot \left(1 + \frac{AF_{m,stoic}}{\phi_{EGR=0}}\right) = \frac{m_{syngas,EGR\neq 0}\left(1 + \frac{AF_{m,stoic}}{\phi_{FIN,EGR\neq 0}}\right)}{1 - EGR} \tag{5.9}$$

Here $\phi_{EGR=0}$ is the simple equivalence ratio when no EGR is included, which is distinct from $\phi_{FIN,EGR\neq 0}$ which is the equivalence of the fresh intake syngas+air mixture which is yet to be mixed with EGR gases. Based on Eq. (5.9), the influences of dilution caused by EGR can be examined. Three special cases can be considered:

Case 1: Normal flow substitution - In this case the EGR gases displace and reduce the normal flow of the syngas and air, without changing the original ϕ_{FIN} relationship between the total fresh intake flow of syngas and air. In such a case, it follows that $\phi_{EGR=0} = \phi_{FIN,EGR\neq 0}$. Thus, from Eq. (5.9) it is observed that the mass of syngas inside the chamber reduces by a factor of (1-EGR) due to EGR addition:

$$m_{syngas,EGR\neq 0} = (1 - EGR) \cdot m_{syngas,EGR=0} \tag{5.10}$$

The fuel contained in a cycle expressed as $Q_{fuel/cycle} = LHV_{syngas} \cdot m_{syngas}$, also reduces by the same factor.

$$Q_{fuel/cycle,EGR\neq 0} = (1 - EGR) \cdot Q_{fuel/cycle,EGR=0} \tag{5.11}$$

Due to the presence of excess air in the lean burning HCCI cycles, the overall equivalence ratio $\phi_{FIN+EGR}$ decreases according to Eq. (5.6). Additionally, the LHV of the gas mixture (syngas + fresh air + EGR) can be expressed as:

$$LHV_{FIN+EGR} = LHV_{syngas} \frac{m_{syngas}}{m_{intake}} \tag{5.12}$$

And thus, based on Eq. (5.9), Eq. (5.13) can be obtained which also shows the consequent decrease in the LHV due to EGR addition:

$$LHV_{FIN+EGR} = LHV_{syngas} \cdot \frac{1}{1 + \frac{AF_{m,stoic}}{\phi_{FIN}}} \cdot (1 - EGR) \tag{5.13}$$

The dilution effects can be compensated for, by increasing the ϕ_{FIN} in accordance with the EGR values, as described in the next two cases.

Case 2: Compensating for ϕ dilution- In this case the ϕ_{FIN} is adjusted such that $\phi_{FIN+EGR} = \phi_{EGR=0}$, throughout the values of EGR. Thus, based on the relationship between ϕ_{FIN} and $\phi_{FIN+EGR}$ (see Eq. (5.6)), the following relationship results which compensates for dilution of the equivalence ratio due to EGR:

$$\phi_{FIN,const.\phi} = \frac{1}{\frac{1-EGR}{\phi_{EGR=0}} + EGR} \tag{5.14}$$

Case 3: Compensating for LHV dilution- In such a case, the substitution of $m_{syngas,EGR\neq0} = m_{syngas,EGR=0}$ in Eq. (5.7) results in the following equality:

$$\phi_{FIN,const.LHV} = \frac{\phi_{EGR=0}}{1 - EGR(1 + \frac{\phi_{EGR=0}}{AF_{m,stoic}})} \tag{5.15}$$

It must be noted here that constant LHV of the mixture also implies a constant FuelMEP.

Without compensatory efforts, the aims of EGR utilization as a control parameter are lost.

In cases where EGR=0%, the equivalence ratio, $\phi_{EGR=0}$, is crucial for HCCI combustion since it represents the energy content, the oxygen available for the combustion as well as the thermal effects related to the altering of specific heat capacities [125]. However, as the EGR is included, the entry equivalence ratio, ϕ_{FIN}, can no longer represent the energy content ($\text{LHV}_{FIN+EGR}$) or the effective equivalence ratio ($\phi_{FIN+EGR}$). Since the main objective of using EGR is to optimize and maintain the combustion phasing at the *given fueling rate*, it makes sense to eliminate the energy dilution effect of EGR.

The following section describes the details of the experimental work carried

H_2	0.18
CO	0.22
N_2	0.48
CO_2	0.11
CH_4	0.01
H_2/CO	0.82
H_2/CO_2	1.64
$AF_{m,stoic}$ [kg_{air}/kg_{fuel}]	1.21
LHV_{syngas} [MJ/kg]	4.52
$LHV_{mix,FIN}$ at ϕ_{FIN}=1 [MJ/kg]	2.04
$LHV_{mix,FIN}$ at ϕ_{FIN}=0.4 [MJ/kg]	1.13

Table 5.1: *Composition and energy details of the dry syngas composition used during the EGR experiments.*

out in this chapter.

5.4 Experimental Details

The HCCI operation is achieved with simulated dry syngas as carried out in the previous chapter. The same MFC and pump systems have also been used to implement the simulated EGR, the process of calculating the flow rates is elaborated in Appendix D.1.1. The overall flow rates of the gases were controlled so that a constant $p_{in} = 1.2 \pm 0.02$ bar and $T_{in} = 250 \pm 5°C$ were maintained. In departure from the experimental conditions of the previous chapter, the EGR studies presented in this chapter were carried out at 1000 RPM, so that a sufficient range of EGR could be tested with the current MFC system. Thus, in comparison to the 1500 RPM experiments in the previous chapter, the wall heat losses would increase in this case, reducing the thermal efficiency. Additionally, to achieve the same combustion phasing as in previous experiments, higher T_{in} would probably be needed. However, these effects were not considered during the experiments and the experimental procedure followed throughout this chapter was similar to that in the previous chapter. At each setting of the EGR value, sweeps of the intake equivalence ratio ϕ_{FIN} were repeated thrice in a randomly intermixed pattern combined with different experimental points.

The composition of syngas used during these experiments, presented in Table 5.1, corresponds to the nominal syngas composition used in Chapter 4 (see Table 4.1).

In order to depict the dilution and compensation of LHV, Figure 5.2 is plotted which displays the corresponding values of all experiments performed in this chapter. The points are marked on a ϕ_{FIN}-EGR space with the contours corresponding to constant $LHV_{FIN+EGR}$, based on Eq. (5.15). The contours

of LHV depict the required ϕ_{FIN} for each EGR substitution of the charge, such that the effects of energy dilution are eliminated. This implies that the LHV of the charge at a certain EGR value remains equal to when EGR=0. For example, starting from an initial condition of EGR=0% and $\phi_{FIN} = 0.4$ where the charge mixture has an $\text{LHV}_{FIN+EGR,EGR=0}$ of about 1.133 MJ/kg, as the EGR substitution is increased, the corresponding increase in the ϕ_{FIN} following the LHV contour would result in maintaining the effective LHV of the intake charge, $\text{LHV}_{FIN+EGR}$ =1.133 MJ/kg.

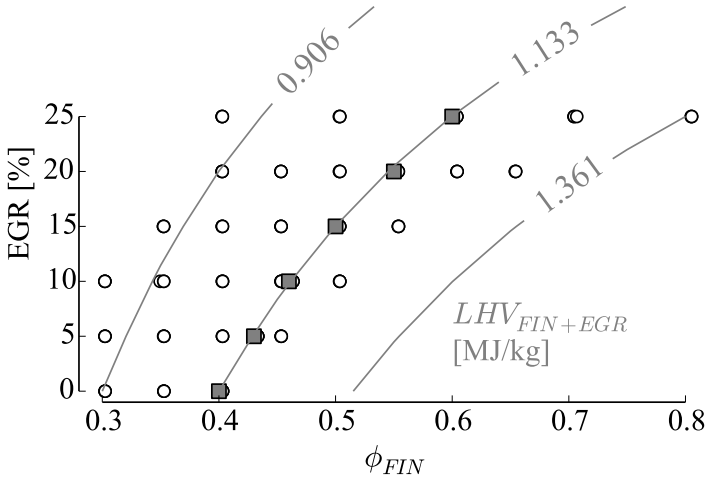


Figure 5.2: *Experimental data points plotted on the ϕ_{FIN}-EGR space with contours indicating the compensatory increases in ϕ_{FIN} so as to maintain a constant $LHV_{FIN+EGR}$.*

In order to understand the thermal effects of EGR, indeed it is necessary to compare cases with different EGR levels, but having the same charge energy density ($\text{LHV}_{FIN+EGR}$=constant) i.e. experiments where the charge energy dilution have been eliminated. Section 5.5.1 discusses six such experiments, distributed along the contour of $\text{LHV}_{FIN+EGR}$=1.133 MJ/kg and starting at ϕ_{FIN}=0.4 at EGR=0, as seen in Figure 5.2. Along with exploring the thermal effects, the possible chemical kinetic influence of the H_2O component of EGR has also been examined. Based on the developed insights, Section 5.5.2 discusses the effects of EGR across all the experimental points shown in Figure. 5.2.

5.5 Experimental results

5.5.1 Thermal effects of EGR

Figure 5.3a plots the mean and filtered in-cylinder pressure curves for six experimental points, each point corresponding to a different EGR value and yet having an average $\text{LHV}_{FIN+EGR}$ of 1.138 MJ/kg with a standard deviation of ± 0.003[1]. The peak pressure positions are delayed while their magnitudes decrease, as the EGR is increased. At EGR=0%, the bulk of heat release is completed well before the TDC, causing a steep rise in the pressure. As the EGR is increased, the increased thermal inertia slows the combustion rate and distributes the heat release over larger crank angle degrees, allowing for a bulk of the pressure to be sustained late into the cycle. In terms of the pressure-volume (pV) diagram corresponding to these experiments (see Figure 5.3b), while the 'width' of the pV trace remains essentially constant due to the constant energy input, the EGR gases effectively control the phasing of the release of heat and thus the area of the pV plot. Thus, EGR can be used to optimize the phasing or the CA50 position and in turn maximize pV area. In the Figure 5.3b, an EGR value between 0 and 15% would result in optimum combustion phasing.

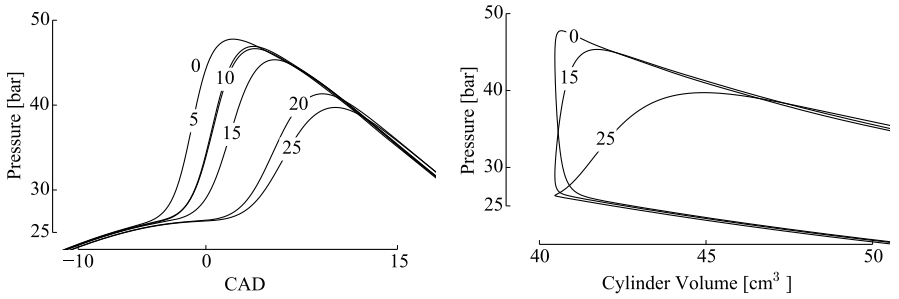


Figure 5.3: *Experimental in-cylinder pressure traces with equivalent fuel energy, but at different EGR substitution rates (EGR in %). (a) The thermal damping, due the presence of EGR gases, delays the heat release event, delaying and decreasing the peak pressure of the cycle. The corresponding pressure rise rates decrease significantly. (b) pV traces, corresponding to EGR values of 0, 5 and 25% are plotted on a pressure-volume diagram. EGR can thus effectively be used to optimize the combustion phasing to realize the desired performance.*

The main reason behind such an effect of delayed heat release can be attributed to the thermal effects. Assuming the compression phase of the engine follows a polytropic compression process, polytropic exponents for each of the

[1]The minor difference in the LHV as compared to the contour plotted in Figure. 5.2 corresponding to 1.133 MJ/kg is caused by the minor difference in the ϕ_{FIN} and the ϕ_{BCE}

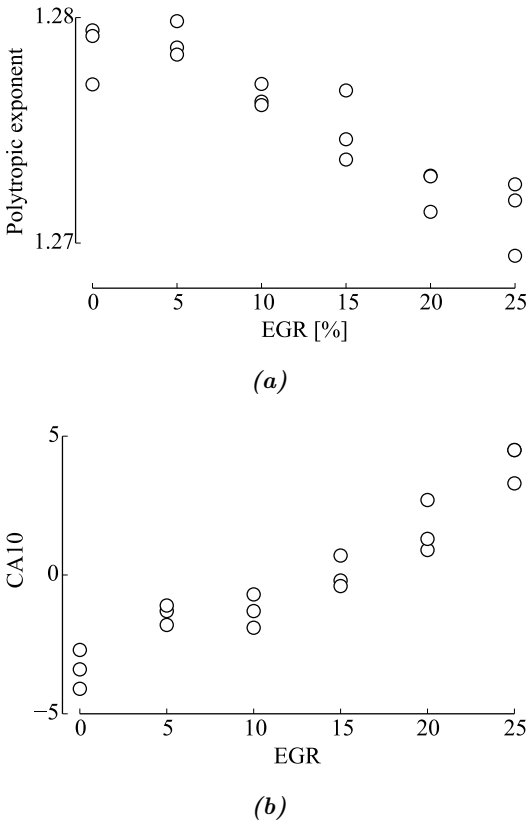


Figure 5.4: *Effects of differing EGR values on HCCI combustion with charges having equal LHV of mixture ($LHV_{FIN+EGR}$=constant). (a) The polytropic exponent, computed for the compression phase (from IVC to -9 CAD) of different charges plotted as a function of the respectively used EGR rates. The decreasing trend of polytropic exponent implies that with increasing EGR, the temperatures attained through compression decrease. (b) As a consequence, this delays the onset of ignition, represented by the CA10.*

six cases were computed between the positions of IVC and -9 CAD before the TDC, which is before the start of combustion (as can be seen in the pressure plots in Figure 5.3a). These exponents are plotted against the respective EGR values in Figure 5.4a. This technique eliminates the differences between the initial conditions for the different cycles considered here, and thus brings out clear trends. The trend in Figure 5.4a implies that as the EGR increases, the temperature achieved through the compression decreases due to the increased heat capacity of the gas mass, mainly because of the increasing CO_2 and H_2O concentrations. From EGR=0 to EGR=25%, the ΔT produced due to compression (from IVC to -9 CAD) decreases by about 15 K, which can significantly effect the autoignition conditions. Indeed, as seen in Figure 5.4b,

the combustion initiation, represented by the CA10, can be seen to respond accordingly to the trend in the polytropic exponents. The almost linear response of combustion timing to EGR along with the high correlation with the polytropic exponent signifies the effectiveness of the EGR in controlling the combustion timing. As a comparison, if it was possible to modulate the T_{in} instead of EGR, it would have the same effect. However, for the tar dew point constraint, modulating the T_{in} is not feasible in this application.

The slowing down of the combustion may be contributed by thermal as well as chemical kinetic effects. In this study, the potential magnitudes of thermal and kinetic effects of H_2O were explored further. For this reason additional experiments were performed while attempting to keep the LHV value near constant as before, but where the water in the EGR of the BCE (represented in Eq. (5.2)) was removed, resulting in the modified BCE represented by Eq. (5.16) below. This reduction was compensated by an increased flow rate into the engine, so as to keep the net flow constant and thus not change the input conditions of $p_{in} = 1.2$ bar and $T_{in} = 250°C$. The resulting LHV was slightly affected but was well within the uncertainties of the experimental LHV, $\approx \pm 0.025$ MJ/kg . However, the technique of using the polytropic exponents to compare different cases during compression, can be assumed to be less sensitive to the LHV and initial condition variations.

$$
\begin{aligned}
&\left(\begin{array}{l} n_{S,N_2}\,N_2 + n_{S,CO_2}\,CO_2 + n_{S,CO}\,CO \\ + n_{S,H_2}\,H_2 + n_{S,CH_4}\,CH_4 \end{array}\right)_{\text{dry syngas}} \\
&+ \frac{1}{\phi_{FIN}} \cdot n_{O_2,stoic} \cdot (O_2 + 3.76N_2) \\
&+ (EGR(1-RGF) + RGF) \left(\begin{array}{l} \overline{n_{E,CO_2}} CO_2 \\ + \overline{n_{E,O_2}} O_2 + \overline{n_{E,N_2}} N_2 \end{array}\right) \\
&+ RGF\,\overline{n_{E,H_2O}} H_2O \\
&\xrightarrow{\text{combustion}} \\
&\qquad \left(\begin{array}{c} n_{E,H_2O} H_2O + n_{E,CO_2} CO_2 + n_{E,CO} CO \\ + n_{E,O_2} O_2 + n_{E,N_2} N_2 \end{array}\right)
\end{aligned}
\tag{5.16}
$$

Figure 5.5a is a modification of Figure 5.4b, where the polytropic coefficients of cases with EGR devoid of water have been added. The lack of H_2O in the EGR follows the similar decreasing trend of the polytropic coefficients with increase EGR value, but with lesser sensitivity as compared to cases where EGR contained water. This implies that the effectivity of EGR is decreased when the H_2O component (and its associated cooling potential attributed to its higher specific heat capacity) is removed. The corresponding points of combustion initiation, represented here by the CA10, are plotted in Figure

5.5b. It is thus clear that H_2O is an important EGR constituent. However, it remains to be seen if this role of H_2O is due to its thermal inertia (high specific heat capacity) or due to its kinetic influences.

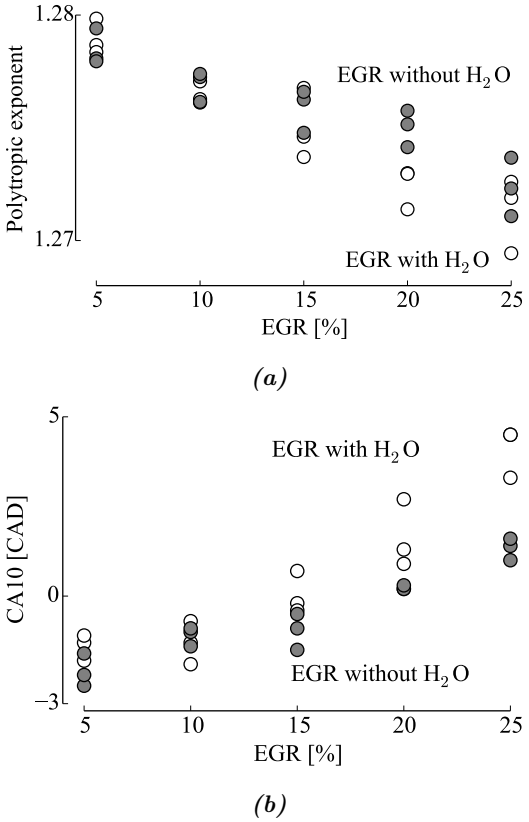


Figure 5.5: *The effects of EGR with and without containing H_2O as an EGR constituent. The trends are not as clear due to experimental irregularities, but general observations can be made. (a) The decreasing trend of polytropic exponent due to lack of H_2O in EGR is similar to cases where EGR contained H_2O. However, the rates of the trend are different in both the cases, with the EGR containing H_2O showing a greater cooling effect than without it. (b) As a consequence, EGR with H_2O is more effective in delaying the combustion, as compared to EGR without H_2O. This implies the significant effect of H_2O component of EGR.*

Due to the wide fluctuations from experimental data, as seen in Figure 5.5, it was decided to investigate further the role of H_2O through computational methods. To discriminate between the effects of thermal inertia and chemical kinetics, ignition delay simulations of syngas combustion were performed at various EGR rates by F. Contino, a co-author of Bhaduri et al. [117], which represents the work related to this chapter. For these simulations, the GRI-MECH 3.0 mechanism was used [73]. The simulations were performed in a

constant volume vessel with the TDAC method [76, 77, 78]. The mass fractions of the compressed mixture were obtained from the six experimental cases discussed in this section, which corresponded to constant $\mathrm{LHV}_{FIN+EGR}$ conditions. They were further adjusted to remove the minor variations in the LHV originating from the experiments. Further, the experimental differences in the intake conditions (p_{in} and T_{in}) were reduced by extracting the respective polytropic coefficients of the compression phases for each of the six cases, as done before in Figure 5.5a. These coefficients were then used to construct polytropic compression curves, but based on fixed inlet conditions of $\mathrm{p}_{in} = 1.2$ bar and $\mathrm{T}_{in} = 250°\mathrm{C}$. These re-constructed compression pressure curves were used as inputs for the simulating of the ignition delays.

The overall ignition delay caused by the combination of thermal and kinetic effects of the EGR gases, is plotted in Figure 5.6. To isolate the kinetic effects of H_2O, the same pressure and temperature profile as in the case of EGR=0 was assumed, but containing the usual EGR gases. Two cases, with and without H_2O were simulated with this technique. In the case where H_2O was replaced with N_2, the effect of EGR can be seen to be basically nullified in Figure 5.6, thus indicating that the H_2O has a significant thermal effect. As for the kinetic effect, it is significantly lesser compared to the bulk thermal effect, thus concluding that for all practical purposes, the main effect of the water content of EGR is thermal in nature.

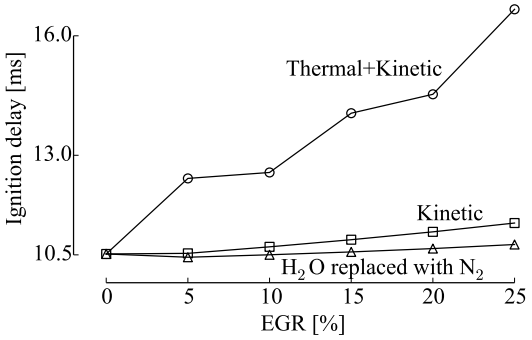


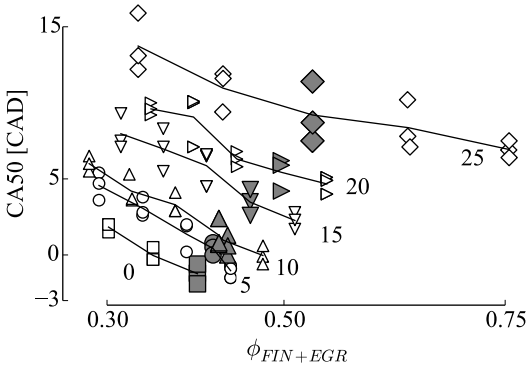
Figure 5.6: *Simulations of ignition delay at constant $LHV_{FIN+EGR}$ condition so as to isolate chemical kinetic effects from the bulk thermal effects. The strong trend of bulk effects (thermal+kinetic) dominates over kinetic effects contributed by H_2O. The EGR effect is nullified if thermal and kinetic effects are removed (flat trend with least slope).*

5.5.2 Global trends due to EGR

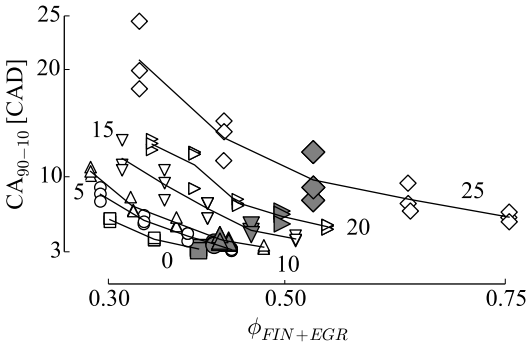
In this section, the effects of EGR throughout the experimental range are discussed. Experimental points of constant $\mathrm{LHV}_{FIN+EGR}$, as considered in the

previous section, are shaded to distinguish them from the rest of the points.

In Figure 5.7a, the CA50 is plotted against the realistic $\phi_{FIN+EGR}$ instead of the ϕ_{FIN}. As $\phi_{FIN+EGR}$ increases, the CA50 advances due to the increased combustion rates resulting from larger temperatures achieved by higher amounts of fuel. On the other hand, as the EGR increases, the larger thermal inertia increases the ignition delay and consequently retards the CA50. The CA50 corresponding to the constant $\text{LHV}_{FIN+EGR}$ points (as marked by shaded markers) are progressively delayed with increasing EGR, even as the corresponding $\phi_{FIN+EGR}$ increases. Thus, a combination of $\phi_{FIN+EGR}$ and EGR can be used to position the CA50 for optimal performance, while keeping the energy content constant, thus proving as an effective control strategy.



(a)



(b)

Figure 5.7: *CA50 and burn duration plotted as a function of $\phi_{FIN+EGR}$ with various levels of EGR (in %). The dominant effect of EGR delays and spreads the combustion increasing the potential for higher $\phi_{FIN+EGR}$.*

As the $\phi_{FIN+EGR}$ increases, the combustion is accelerated resulting in shorter burn durations as seen in 5.7b, represented by the absolute difference between the CA90 and CA10. However, the EGR slows the combustion reac-

tions causing the combustion to be spread over larger crank angle degrees. As the combustion shifts later in the cycle the effects of volume expansion further slow down the chemical reactions which increases the combustion duration.

The delay in CA50 and the subsequent spread in the combustion due to the addition of EGR decreases the cycle temperatures represented here by the peak cylinder temperature (T_{max}) as seen in Figure 5.8a. The experiments of constant $LHV_{FIN+EGR}$ show a sharp decrease in T_{max} with increasing EGR. The decrease in T_{max} directly influences the temperature sensitive and slow burning CO component of the syngas resulting in increasing CO emissions and subsequent decrease in the Combustion Efficiency (CE) as seen in Figure 5.8b.

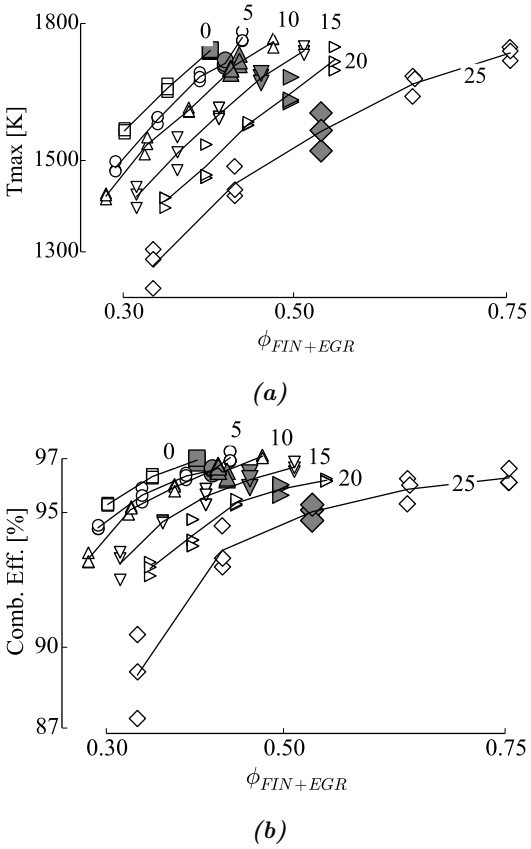


Figure 5.8: *Peak cycle temperatures and combustion efficiency as a function of $\phi_{FIN+EGR}$ for various levels of EGR. Although EGR decreases the T_{max} and the combustion efficiency for a particular energy content ($LHV_{FIN+EGR}$), higher $\phi_{FIN+EGR}$ mixtures could be used to restore the optimal values.*

As seen in the last chapter, the CE signifies the completeness of the combustion whereas the IE indicates the efficiency of the engine (including the CE

factor) in converting the input fuel into cyclic work. Figure 5.9a indicates the CA50 where the maximum IE is achieved, which lies at about 5 CAD after the TDC. As the $\phi_{FIN+EGR}$ is increased, the CA50 advances before the TDC, causing the $p\Delta V$ contributions from this region (see Eq. 3.6), to have larger negative values than would have otherwise been if the combustion would occur after the TDC. Thus, the end sum of total cyclic work decreases resulting in the consequent decrease in the IE. In physical terms, when the pressure rises before the TDC, it opposes the piston motion which dissipates the available potential of work and also increases the heat losses to the walls due to high gas densities and temperatures. With the addition of EGR and the retarding of the combustion, the indicated work can be maximized resulting in the maximum IE. With higher EGR, the CA50 is retarded much farther than the optimum position and the volume expansion causes a decrease in the overall pressure and temperature which lead to decreased combustion efficiency. As seen for the case of EGR=25% in the pressure-volume plot in Figure 5.3b, this reduces the pV indicated work area and subsequently causes a decrease in the IE. The maximum IE occurs at a CA50 of 5 CAD and not before in order to accommodate for the rest of combustion, which must begin ideally after the TDC and finish before the effects of expansion are felt, similar to the conclusion that was drawn in Section 4.2.1 of the previous chapter.

Figure 5.9b shows the linear relationship between the FuelMEP and the resulting IMEP. The use of EGR, through its effective phasing ability allows for the IMEP to be increased further than previously possible. This is more evident through Figure 5.9c. At EGR=0, the FuelMEP was limited. However, as EGR was introduced the MPRR limit effectively vanishes. The figure shows that significant fuel amounts can now be used by the same engine, thus allowing much higher IMEP to be achieved. For cases with constant $\text{LHV}_{FIN+EGR}$ (shaded points), the MPRR decreases significantly from about 10 bar/CAD at EGR=0% to about 0.8 bar/CAD for EGR=25%. This significant decrease can be attributed to the increase in the combustion duration due to the thermal damping caused by EGR gases. The trends in Figure 5.9c also indicate the decreasing sensitivity of the MPRR to the increasing fueling rates as a result of EGR.

Figures 5.9b and 5.9c are the key results of interest in this chapter. It can be concluded that EGR, through its singular effect of delaying the combustion, increases the knock or ringing limited equivalence ratio significantly. As compared to Figure 5.9b, for the cases of constant $\text{LHV}_{FIN+EGR}$, the IMEP increases from about maximum of 2.8 bar at EGR=0 and ϕ_{FIN}=0.4 to a maximum of 3.4 bar at EGR=25%, a gain of about 25%. Further, as seen in Figure 5.9c, the use of EGR opens up the space for either more fueling rate, or higher intake boosting or increasing the compression ratio, all because the MPRR limit is effectively nullified. As a rough estimate, a maximum IMEP of 4 bar could be expected through the use of increased fueling rate, within the boundaries

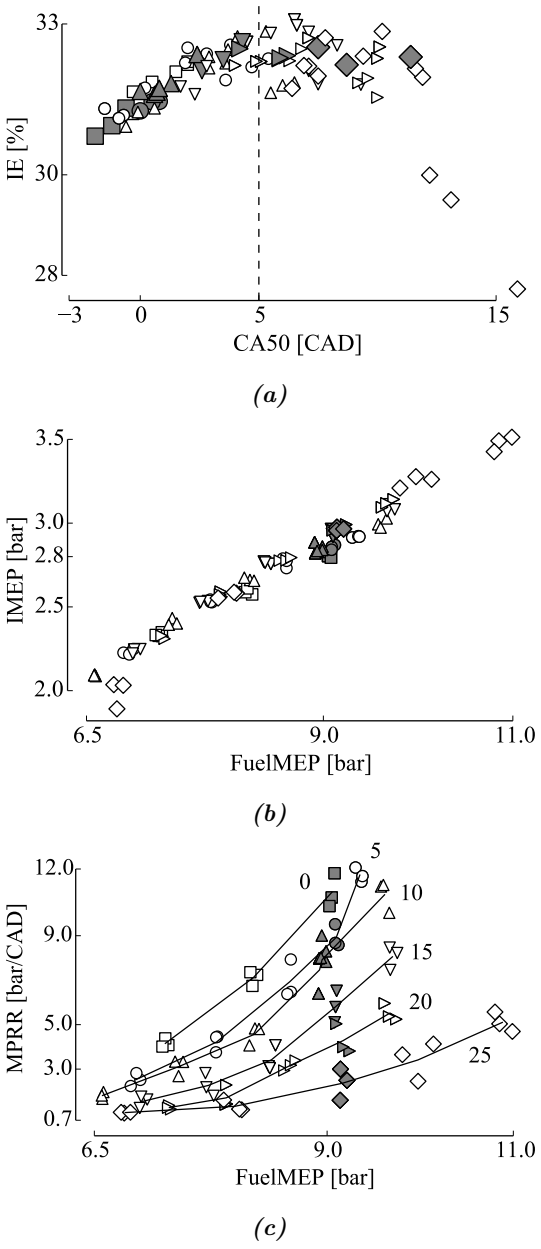
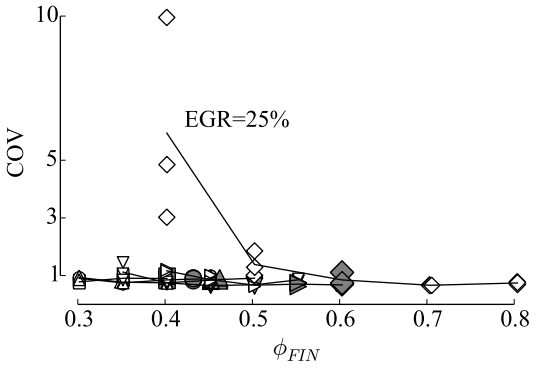


Figure 5.9: *Effects of EGR on IE, IMEP and MPRR. (a) Maximum IE is achieved near 5 CAD, and falls if combustion advances or delays further indicating where an optimal region lies. (b) However, in terms of power output, the more the fuel rate (shown here by the FuelMEP), the more the IMEP available. (c) The increased IMEP potential is because the use of EGR effectively eradicates the MPRR constraint.*

defined by the limits $\phi_{FIN} \leq 1$, MPRR <10 bar/CAD and the CoV limited EGR ≤25%.

The experiments in this chapter could not take advantage of the increased potential through the use of EGR as the increased combustion at high ϕ_{FIN} resulted in increasing cylinder wall temperatures. Due to the air-cooled engine, the temperature had to be constrained below the limit of 115°C set for this study. This experimental limitation, however could be eliminated by using a water-cooled HCCI engine.

During the experiments it was found that beyond EGR>25%, the very late and widely distributed combustion became quite unstable for any scientific analysis, even when the ϕ_{FIN} was increased to a maximum of 1. Otherwise, the CoV in Figure 5.10a remains stable for all the experimented range, except for EGR=25% at low ϕ_{FIN}=0.4. Therefore, the maximum EGR possible for the current setup can be concluded as 25%.



(a)

Figure 5.10: *The CoV remains well below the maximum of 5% for all cases except for EGR=25% at low $\phi_{FIN} = 0.4$. At EGR=30% (not shown in the figure), the CoV becomes too high, even at high ϕ_{FIN}.*

5.6 Conclusion

The potential of controlling and extending the operating range and performance of a tar tolerant HCCI engine system for syngas applications, achieved through the use of EGR, has been explored in this chapter. Experiments were carried out at 1000 RPM with EGR levels varying from 0 to 25% at an intake temperature of 250°C and intake pressure of 1.2 bar. The key observations were:

- For cases where the LHV of the mixture were kept constant, the EGR successfully delayed the combustion along with increasing the combustion

duration.

- This resulted in a decrease of MPRR from about 12 bar/CAD at EGR=0% to about 0.8 bar/CAD at EGR=25%, a drop of about 90%. The maximum fueling rates in the experiments were thus limited by the MPRR at the lower end of EGR rate, and by the engine body temperature exceeding the 115°C limit at the higher end.
- Similarly, the maximum IMEP increased from 2.8 bar at EGR=0 to 3.5 bar at EGR=25%, a gain of about 25%.
- A maximum IE of 33% was achieved with the maximum occurring at 5 CAD after the TDC for all cases.

Further increase in the IMEP for the same EGR levels was limited by the experimental inabilities of the test-bench instead of the MPRR. For the case of EGR=25%, if the issue of engine body temperature could be avoided, a potential maximum IMEP of 4 bar could be expected.

Chapter 6

Experiments with real, cooled and purified syngas

6.1 Introduction

As a step closer to the real application of the concept, experiments were carried out with a real gasifier and its fluctuating syngas characteristics. Previously, in Chapter 4, the HCCI response to various compositions, moisture, tar and operational conditions of T_{in} and p_{in} were explored. However, these were static and controlled experiments, which did not include the complexity of time variations. Both kinds of experimental investigations are needed and hence the work described in this chapter.

To do so, it was decided to split the task of testing the concept of HCCI operation with high temperature syngas from a gasifier, into two parts. The first part would focus on the operation of the HCCI engine test bench with a supply of conventional syngas which has been cooled and purified, but which is re-heated at the test bench to simulate a high temperature syngas. The second part would focus on the direct and unconventional use of hot and impure syngas in an HCCI engine. The experiments of the first part are the subject of this chapter, while the studies about the second part could not be carried out in the duration of this thesis.

In this chapter, Section 6.2 describes the characteristics and operational details of the biomass gasifier installed at the Université catholique de Louvain. Section 6.3 provides a description of the test bench adapted to run on real syngas and also presents the experimental objectives of this chapter. Thereafter, the experimental results are presented in Section 6.4.

6.2 The two-stage downdraft gasifier

The downdraft gasifier produces gases with the least tar content amongst the other gasifiers, as discussed in Chapter 1. The tar levels are generally in the order of 1 g/Nm^3 for a single stage gasifier. However, for the engines, tar content less than 50 mg/Nm^3 are required, thus necessitating the use of elaborate cleaning mechanisms. In-order to reduce the load on the secondary processes, the two-stage downdraft gasifier was developed, examples of which can be found in Bhattacharya et al. [30] and Henriksen et al. [34].

A modern two-stage downdraft gasifier of about 200 kW$_{thermal}$ capacity is installed at the author's laboratory [126]. It is a scaled down version of a commercial 1 MW$_{thermal}$ NOTAR® 1000 industrial gasifier designed by Xylowatt s.a[1] of Belgium, in collaboration with the Université catholique de Louvain. A representation of this gasifier is presented in Figure 6.1. In this two stage gasifier, the pyrolysis stage is at the top end of the system which is also the starting point for the biomass feedstock. It is heated through partial oxidation of the biomass caused by a supply of *primary air* to the pyrolysis zone. The resulting pyrolysis gases, tars and char flow downward towards the reduction chamber. The free space between the pyrolysis chamber and the reduction chamber sustains the secondary partial oxidation reactions supplied by the *secondary air*. This gaseous separation is critical for the thermal decomposition of the tars. Further, the main char gasification takes place after the partial oxidation zone. The large availability of active char in the reduction zone acts as a catalyst for further conversion of the tars into the desired simple syngas components [32].

The Xylowatt gasifier uses a mechanical moving separator at the end of pyrolysis stage, which helps maintain the separation between the two stages and the level of char bed in the reduction chamber. Due to this contraption, a stable gas composition is achieved. It produces a syngas with a tar content less than 20 mg/Nm^3 [29]. However, to stabilize the syngas quality during transient stages, such as at the warm-up time or other transients, intermediate syngas cooling and conditioning processes have to be used, as detailed in Berger et al. [29, 127], Berger and Peregrina [128]. Table 6.1 summarizes the main nominal characteristics of operation of the laboratory version of the Xylowatt NOTAR® gasifier.

6.3 Test Bench and experimental changes

The test bench modification is shown in Figure 6.2 where the MFCs supplying syngas components were disconnected. Due to the gasifier being operated near the atmospheric pressure, the outlet pressure is low and can reach a maximum of only 0.02 bar above the atmosphere. Hence, the suction or throttling method

[1] http://www.xylowatt.com

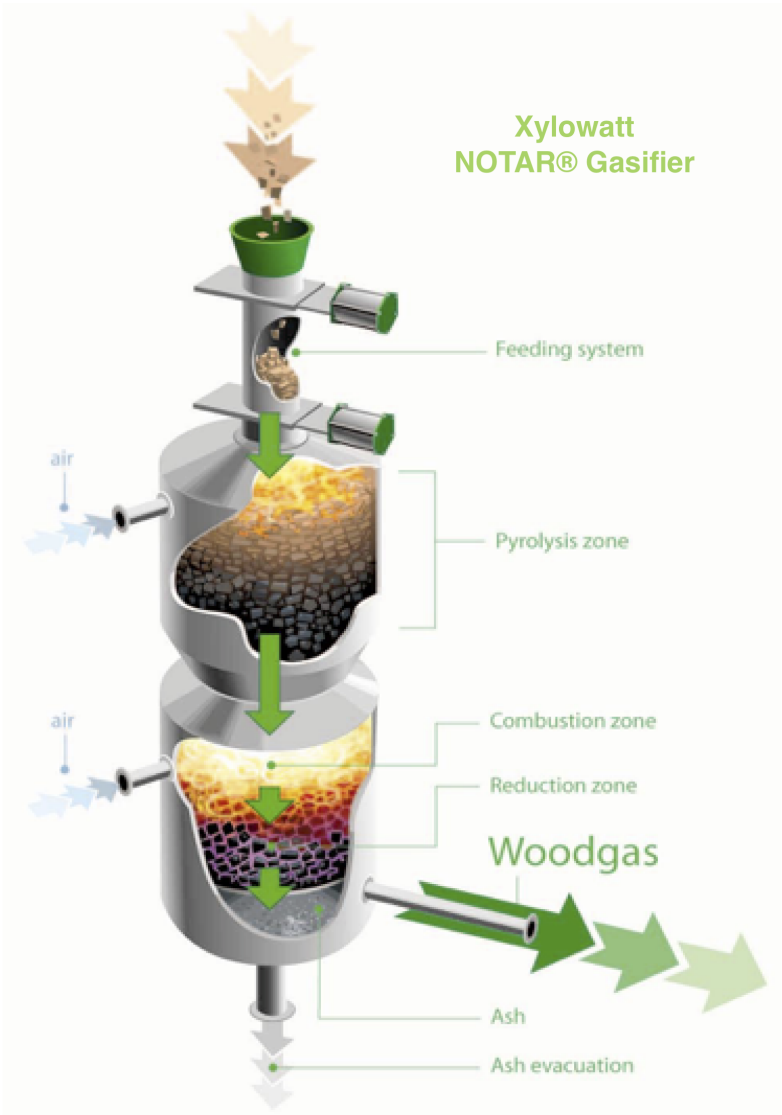


Figure 6.1: *The Xylowatt NOTAR® 2-stage biomass gasifier. The pyrolysis zone (at the top), which receives its heat from combustion with primary air, is separated from the main reduction zone (at the bottom), the heat supply of which is due to combustion by secondary air. The intermediate combustion zone is responsible for cracking all of the pyrolysis vapors (tars) resulting in relatively tar free syngas (*Woodgas *in image). Image credits: ©Xylowatt.*

of intake for the syngas into the HCCI engine was used, similar to a naturally aspirated port fueled SI engine. The air flow to the engine was controlled by a MFC, as done in the previous experiments, which allowed for the control of

Type	2-stage Downdraft gasifier
Gasification agent	air, atmospheric pressure
Biomass Type	Wood
Nominal Mass flow rate	49 kg/h
Primary/Secondary Air ratio	0.477
Gasification equivalence ratio (ϕ_g)	≈ 0.26
Pyrolysis Zone Temperature	≈ 500 °C
Combustion Zone Temperature	≈ 1000 °C
Reduction Zone Temperature	≈ 800 °C
Approx. Cold gas efficiency	≈ 70 %

Table 6.1: *Some aspects of the two-stage downdraft gasifier and some gasification conditions during the tests.*

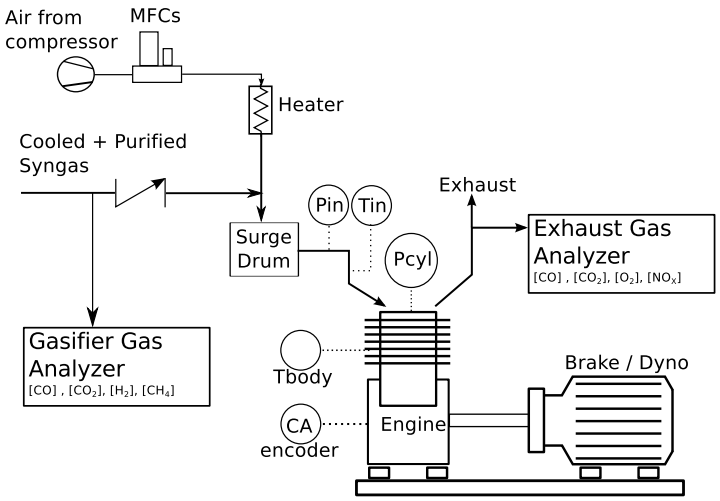


Figure 6.2: *Modified test bench for the real cooled and purified syngas tests.*

the fuel to air equivalence ratio, ϕ. A Gasifier Gas Analyzer (GGA) measured the concentrations of the main syngas components CO, CO_2, H_2 and CH_4 and the syngas was sampled at the point of its entry into the test bench. Also, due to the cold condition of syngas, moisture content was assumed to be negligible. Neglecting trace gases and minor concentrations of tars, it was assumed that input syngas composition was fully known through the information provided by the GGA. A safety check valve prevented any possibility of back flow of hot air and gas mixtures into the syngas supply line. Similar to the procedure followed in the previous chapters, the air supply was heated before being mixed with the cold syngas. The engine was heated in a motoring condition before the syngas flow was allowed.

The equivalence ratio depends on the composition of syngas and the respective volumes of syngas and air being sucked by the engine, of which the air flow

was known from the MFC reading. From the known composition of syngas, air and the emission data, the value of syngas flow was estimated by solving the BCE in an iterative fashion. For the starting value of syngas flow, a volumetric efficiency of 100% was assumed. The following set of equations were used to determine the volume of syngas:

$$VE = \frac{m_{\text{charge}}}{\rho_{\text{charge}} \cdot V_{\text{stroke}}} \tag{6.1}$$

$$V_{\text{m}^3/\text{cycle}} = VE \cdot V_{\text{stroke}} \cdot \frac{RPM}{60 \cdot 2} \tag{6.2}$$

$$V_{syngas} = V_{\text{m}^3/\text{cycle}} - V_{\text{air}} \tag{6.3}$$

As shall be seen in the results, the HCCI combustion was unstable due to undetermined sources. To understand these instabilities, it was interesting to know the cycle-by-cycle mass variations, computed through the method discussed in Section 3.2.3 of Chapter 3. During all the experiments described in this chapter, the air flow was kept constant, and this implied that the varying mass was a consequence of varying syngas flow. Based on this assumption, the parameters requiring the mass of syngas flow were recomputed, on a cycle by cycle basis, for example the IE.

While the GGA used in these experiments provided the concentrations of the input syngas necessary to solve the BCE, the uncertainties of individual modules contained within the GGA could not be determined due to the old make of the unit. Additionally, the available calibration gas bottle for the GGA, consisting of a typical calibrated syngas mixture with CO, CO_2, H_2 and CH_4 gases, had been observed (as tested with another gas analyzer) to contained a lower amount of H_2 than specified. Thus, the calibration quality of the GGA could not be guaranteed. In summary, the uncertainties in the BCE and consequently in the LHV of the syngas and the syngas-air mixture, the CE or the IE (as IE depends on $Q_{fuel/cycle}$) could not be determined for the experiments carried out in this chapter. Thus, the results discussed in this chapter must be interpreted for their trends and not for their absolute values.

The only fast control available in such a setup was of changing the air flow, which would eventually affect the ϕ, and thus could be used to compensate for a changing syngas composition or to stop the overheating of the air-cooled engine. Other controls such as that of the intake temperature T_{in} and engine body temperature T_{body} (through manually adjusting the engine fan opening) were also possible. At this point it must mentioned that no automated control loops regarding the controls of ϕ, T_{in} or T_{body} were added to the LabVIEW control system. Thus, the experiments described in this chapter are all based on manual controls (if any) carried out by the operator, the author in this case.

6.4 Experiments and results

Two major experiments were performed as described here:

3h test- The first was a 3 hour continuous running test, which was carried out with the gasifier undergoing a startup stage. In such a startup phase of the gasifier, the large thermal inertia of the system implied that the gasifier supplied a low LHV syngas with low H_2/CO ratio and whose composition changed continuously. The HCCI engine was connected and was run with such a syngas four hours after the gasifier was started from an ambient condition. The main objective here was to observe HCCI combustion with lower than usual syngas quality.

24h test- The second test was carried out in conditions when the gasifier was sufficiently heated and stabilized, i.e. as expected in a real scenario. Thus, in such conditions, relatively stable syngas compositions with a high quality, meaning high LHV and higher H_2/CO ratios, could be expected. To achieve this operating state, the gasifier was initially run for 8 continuous hours on the previous day of the 24-hour test. Due to the large thermal inertia, on the test day, the gasifier was started from a warm state, thus requiring lesser time to stabilize. The gasifier ran for about 8 hours before the HCCI engine was connected and data recording was begun only after the combustion in the HCCI engine stabilized. Thereafter, the data were recorded continuously for the next 24 hours, in intervals of 5 minutes.

In such conditions the HCCI engine was operated near its required operational conditions i.e. at the intake temperatures of 250°C (for the sake of avoiding tar condensations) and ϕ=0.3, as per the conclusions of Chapter 4. The objective during this test was to observe the potential challenges that could be faced by an HCCI engine in such conditions, without the presence of any control loop.

In both cases, no significant controls were exercised on the HCCI system by the operator, other than occasionally changing the T_{body} to keep the engine within the limits of 110±5°C. The RPM remained fixed at 1500. The data for both cases were recorded after ever 5 minutes, with each data record corresponding to 100 consecutive cycles of pressure data along with the other slowly varying parameters such as input compositions, emissions, intake pressure and intake temperatures. The following sections discuss the results.

6.4.1 The 3h test

Since the gasifier in this case was started from cold conditions, an inferior quality of syngas was to be expected. Figure 6.3 displays the syngas composition as measured by the GGA during the 3h test. As compared to the standard syngas compositions considered in Table 4.1 of Chapter 4, the gas is this case

was slightly richer in the N_2 and CO_2 concentrations while poorer in the CO, H_2 and CH_4 concentrations.

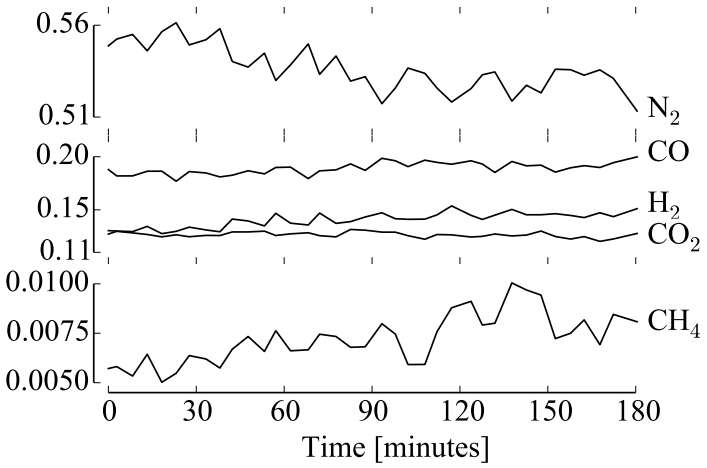


Figure 6.3: *Syngas composition during the 3 hours test, as measured by the GGA.*

Figure 6.4a charts the variations in the LHV of the syngas. It can be clearly seen that the LHV increases as the gasifier operation stabilizes with time. By the end of testing, the LHV was still lower than the expected 4-5 MJ/kg from the gasifier. In Figure 6.4b, the important H_2/CO ratio shows a increasing trend, resulting from stabilization of the gasifier operation. It is important here to notice that the value of H_2/CO ratio is similar to the one of low gas composition, considered in Table 4.1 of Chapter 4. This implies that the HCCI combustion would generally be slower (large combustion duration) and later in the cycle (late CA50), as shall be seen in the further results. Additionally, it must be noted that while the intake conditions of pressure, temperature and the equivalence ratio are interrelated and may also be strongly influenced by the combustion taking place inside the engine, the syngas properties (LHV_{syngas} and H_2/CO_2 ratios) are totally independent of the functioning of the test bench.

On the intake control side of the engine, Figure 6.5 shows the evolution of the intake temperature, T_{in}, intake pressure p_{in} and the syngas to air equivalence ratio, ϕ. The T_{in} shows a significant decrease from the required 250°C to the stable 227°C at the start of the test. The following explanation can be provided for this. The engine was connected to the syngas supply only when the intake piping, the surge drum and the engine were sufficiently hot for the HCCI combustions to occur. This was achieved through motoring of the engine using hot air from the heater. However, when the engine was connected, the air supply had to be reduced to create a suction for the syngas to be taken in from the gasifier. This reduced flow of air, decreased the ability of the 2 kW electric heater to transfer the heat, although the heater was working at its

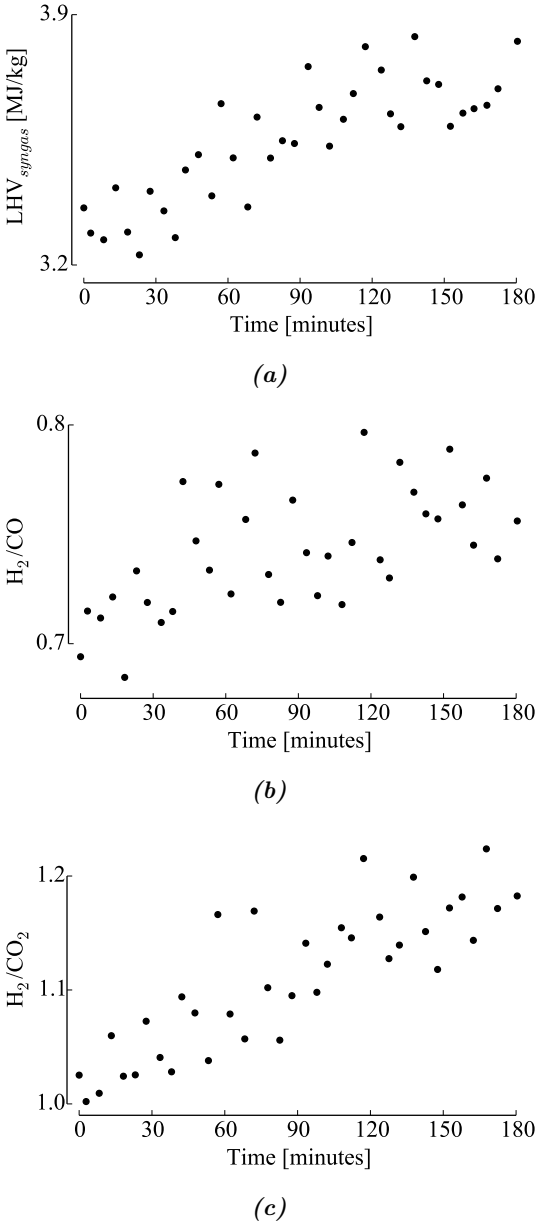


Figure 6.4: *Input syngas characteristics of LHV and H_2/CO ratio plotted against time for the 3h test. In (a) the LHV increases monotonically with time as the gasifier stabilizes, but its value is lesser than what is normally expected. In (b) the H_2/CO is of overall low value compared to what is normally expected.*

highest temperature limit ($\approx 400°C$). Additionally, it was found that a section of the tubing which conveyed the heated gases towards the engine, was not sufficiently insulated. This latter part was corrected for the 24 hours test, which resulted in testing at the required 250°C. However, despite these experiments being conducted at temperatures lower than planned, the trends in the data as a function of time are of significance.

The intake pressure could be influenced by many factors which may lead to the fluctuations and trends, as seen in Figure 6.5b. Since the T_{in} decreases with time while the intake flow of air and the RPM are held constant, this could explain the decreasing p_{in}. The ϕ (see Figure 6.5c) depends on the composition of the syngas, the air flow and also on the intake temperature. The latter is because a higher intake temperature would result in the gases having larger volumes, while the engine volumetric consumption of the gases remains fixed due to a fixed RPM. Since the air supply from the MFC also remained fixed during this testing (irrespective of downstream pressures), it would imply that the volume of syngas sucked into the intake would reduce due to increasing temperatures. The effects the changing temperature and changing composition, together may have influenced the slowly increasing trend of ϕ in Figure 6.5c.

In terms of the output parameters of the test bench, given the input conditions discussed so far, the first thing of interest was the cyclic stability. Figure 6.6a shows the CoV in the IMEP computed for each of the data points. The general spread within the points indicate the random variability within the cycles over long term, as a function of changing syngas parameters. No particular trend is observed, but the spread indicates cyclic variability and yet the value remains less than the 5% mark. Although the CoV of IMEP for these experiments indicate stable operation, the author's experience was contrary with occasional misfires observable through the engine noise and also on the live display of pressure curves on the screen. Additionally, the CoV in the IMEP for the simulated syngas experiments discussed in the past chapters (see Figures 4.6a and 5.10a) indicate that at low equivalence ratios, the CoV increases due to late burning. A similar high CoV can be observed in these real syngas experiments thus implying a late combustion, as previously predicted by the low H_2/CO ratio in Figure 6.4b.

Figure 6.6b shows the IMEP as a function of the 3h experimental time. The trend in the IMEP follows very closely the trends in the ϕ as seen in Figure 6.5c. Thus the IMEP could be said to also depend on the T_{in} and LHV values. As compared to the simulated syngas experiments in Figure 4.4b of Chapter 4, the IMEP values here are equivalent (about 2.5 bar at $\phi = 0.3$). This is even more surprising since the LHV of the syngas used in the current experiments are of lower quality in terms of their LHV and H_2/CO ratio compared to the simulated cases. This could be explained by the low intake pressure (atmospheric compared to 1.2 bar in simulated syngas studies) and low intake temperature operation in the current experiments, resulting in

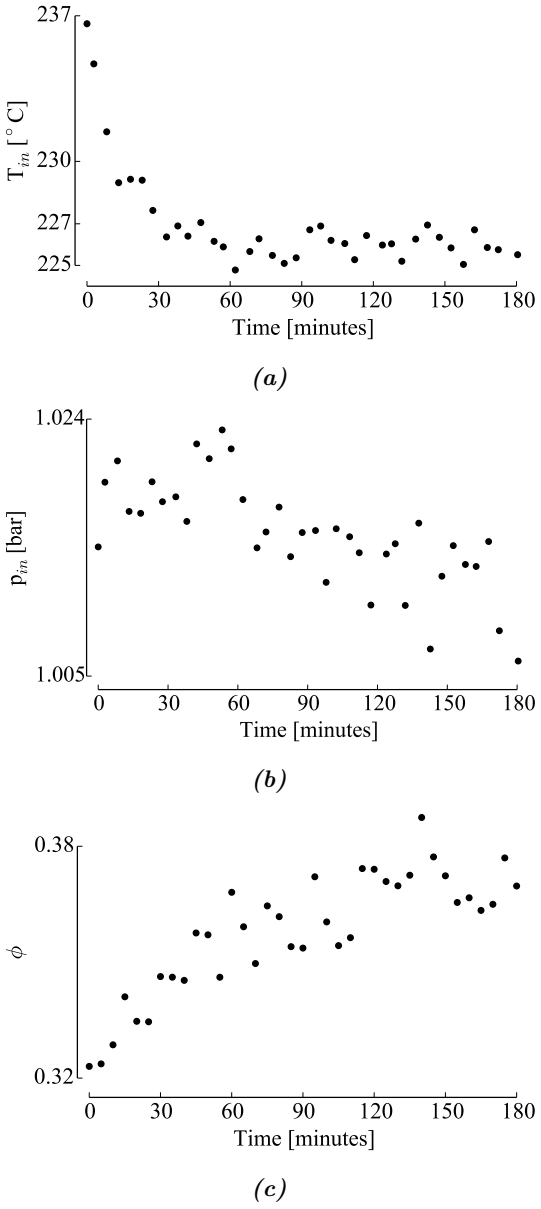


Figure 6.5: *Time evolution of the intake conditions T_{in}, p_{in} and ϕ for the 3h test.(a) The T_{in} drops due to the decrease in the flow of air and thus the effectiveness of the heater. It steadies at about 225-227° C. (b) The p_{in} decreases in time, however the trend is very small. (c) The rising ϕ could be a consequence of the decreasing T_{in} in the initial phases of the test duration, and the increasing LHV of the syngas.*

improved combustion phasing. Compared to the case of Figure 4.13b, where various T_{in} temperatures were studied, the maximum IMEP corresponded to

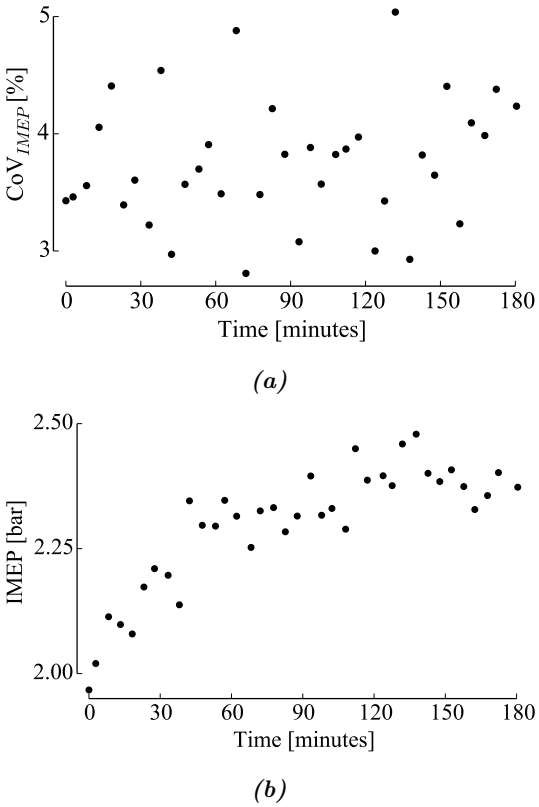


Figure 6.6: *(a) The cyclic fluctuations represented by CoV in the IMEP as a function of time. No trends can be observed and thus indicates weak or negligible effect of changing LHV or composition on the engine stability. (b) The IMEP on the other hand shows high correlation with the LHV.*

the 2.8 bar at an equivalence ratio of 0.34 and T_{in}=230°C. In the current case, slightly lower IMEP values are achieved at higher ϕ due to the low LHV syngas as well as the low H_2/CO ratio.

To understand the quality of combustion, Figure 6.7a shows an increasing combustion efficiency, CE, with the passage of time. Again, the trend of the CE follows the trends of the ϕ and LHV closely. Thus the higher LHV or a high ϕ is necessary to achieve better combustion.

The IE plotted in Figure 6.7b increases at first and then stabilizes with a lot of spread. The spread behavior of the IE can be understood by the combustion metrics, CA50 and CA_{90-10} in Figures 6.8a and 6.8b. The wide spread in the CA50 and the burn duration more clearly indicates the variations between the cycles which were not fully captured by the CoV_{IMEP} in Figure 6.6a. The similar trends show that as the LHV and the ϕ improves, the combustion

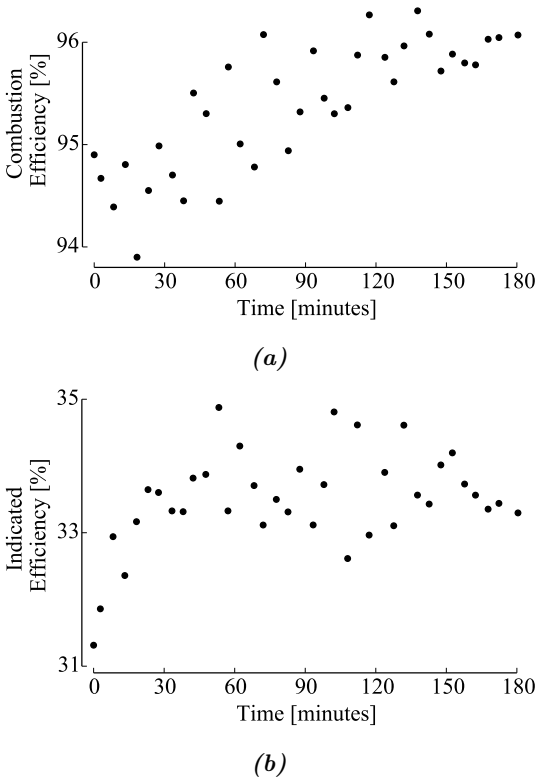


Figure 6.7: *(a) The CE indicates the improved combustion later during the experiment, most probably due to increase in the LHV. (b) However, the IE shows no particular improvement and stays around a mean value of about 34%.*

advances in the cycle and the combustion duration decreases. The subsequent decrease in the spread also indicates that the cycles are more stable around the conditions at the end of the 3 hours test. However, it must also be noted that at the beginning of the experiments, the T_{in} being high, the CA50 was quite advanced with short burn durations indicating the important influences of the T_{in} dominating over the LHV influences during that time.

The wide dispersion in the experimental results along with large number of experimental points calls for a method to express the interrelationships between the different parameters. The Spearman's correlation[2] coefficient is a statistical technique which can be used to obtain a measure of the strength and direction of association (negative or positive) between two independent variables. For this correlation analysis, the variables need not be of equivalent physical units or normalized. The Spearman's coefficient varies from its two extremes from -1 to 1, with values close to either indicating a strong positive or negative

[2]http://mathworld.wolfram.com/SpearmanRankCorrelationCoefficient.html

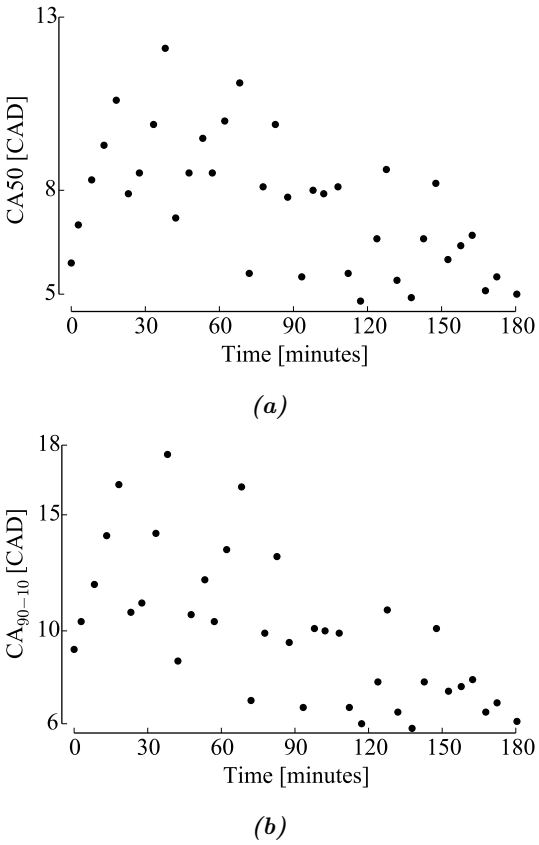


Figure 6.8: *Combustion metrics of CA50 and the burn duration indicate the variability in the combustion as well as the improvement in the combustion with the increase in time.*

correlation, while values close 0 indicates no correlation. The value of this correlation indicates if two variables have some kind of monotonic relationship, which need not be linear in nature.[3]

The experimental data was analyzed and a table of *Spearman's correlation* coefficients between the various interesting parameters were obtained, each being a function of time, as seen in Figure 6.9. The coefficients have been color coded according to their vicinity to either extremes of -1 (blue) and 1 (red). In this figure, the column headings are considered as dependent parameters which are influenced by the independent parameters mentioned as the first six row headings. Also, since the dependent parameters are interrelated with each other, additional rows have been included to present these interrelations. Since no control on the ϕ was exercised, it was considered as a dependent parameter.

[3]The correlations were computed using the *SciPy* library of the Python programming language, *scipy.stats.spearmansr(x,y)*[4].

	ϕ	CoV_{IMEP}	IMEP	CE	IE	CA50	CA_{90-10}	MPRR
LHV_{syngas}	0.91	0.0	0.84	0.9	0.1	-0.64	-0.75	0.79
H_2/CO	0.67	0.06	0.72	0.75	0.39	-0.59	-0.68	0.73
H_2/CO_2	0.85	0.03	0.82	0.93	0.13	-0.7	-0.81	0.83
T_{in}	-0.48	-0.2	-0.53	-0.39	-0.47	0.13	0.29	-0.32
p_{in}	-0.59	-0.4	-0.52	-0.6	-0.02	0.49	0.53	-0.57
T_{body}	0.55	-0.14	0.47	0.74	-0.25	-0.77	-0.78	0.73
ϕ	1.0	0.01	0.96	0.92	0.26	-0.61	-0.74	0.81
CoV_{IMEP}	0.01	1.0	-0.01	-0.04	0.05	0.13	0.1	-0.07
IMEP	0.96	-0.01	1.0	0.88	0.41	-0.65	-0.77	0.85
CE	0.92	-0.04	0.88	1.0	0.09	-0.8	-0.89	0.92
IE	0.26	0.05	0.41	0.09	1.0	0.01	-0.09	0.17
CA50	-0.61	0.13	-0.65	-0.8	0.01	1.0	0.97	-0.94
CA_{90-10}	-0.74	0.1	-0.77	-0.89	-0.09	0.97	1.0	-0.98
MPRR	0.81	-0.07	0.85	0.92	0.17	-0.94	-0.98	1.0

Figure 6.9: *Spearman's correlation coefficients between different parameters for the 3h tests.The dark blue colors indicate high negative correlation between the parameters of the respective row and column heading whereas the dark red color indicates strong positive correlation. Light colors indicate a very low correlation.*

Based on Figure 6.9, the following observations can be made:

Syngas quality (LHV, H_2/CO, H_2/CO_2) - Compared to all the independent parameters, the LHV of the syngas has the strongest influence on the critical equivalence ratio ϕ, which was evident previously from Figures 6.5c and 6.4a. However, ϕ is also strongly influenced by the ratios of H_2/CO and H_2/CO_2 in a positive manner, i.e. when the ratios increase, the ϕ increases. The H_2/CO_2 ratio and the LHV_{syngas} strongly influence the combustion efficiency, however, the H_2/CO_2 has a much stronger influence in this case. This can be understood since a high H_2/CO_2 indicates more H_2 in the syngas and thus ensures earlier and faster combustion. The strong influence of H_2/CO_2 on the CA50 and combustion duration are evidently much higher than the LHV, again implying the important influences of H_2 in advancing and shortening the combustion (hence the strong negative correlations with CA50 and combustion durations respectively). Comparing the 'popular' H_2/CO ratio and the H_2/CO_2 ratio, the latter seems to be a better parameter for understanding the HCCI combustion. This is contrary to the investigations undertaken by the author in Chapter 4, as well as the works reviewed in Section 1.2.2 of Chapter 1, where the focus was on exploring the role of the H_2/CO ratio instead. In fact, the correlations of H_2/CO_2 ratio with the dependent parameters of ϕ, IMEP, CE, CA50 and the combustion duration are slightly higher than those by the LHV of the syngas, thus reinforcing its value in the analysis of HCCI combustion with biomass syngas. This correlates well with the discussion by Yamasaki and Kaneko [72] about the H_2/CO_2 ratio (see the reviews in Section 1.2.2).

T_{in}, p_{in} and T_{body}- The intake temperature has a relatively strong negative influence on the ϕ, as has been discussed before (see Figure 6.5a). As a consequence, the IMEP is also influenced, as shall be seen further in the relationship between ϕ and the IMEP. As compared to T_{in}, the intake pressure has a much stronger influence on the dependent parameters. This is obvious as the p_{in} is directly correlated to the intake temperature and ultimately governs the amount of syngas sucked into the engine. The cylinder body temperature has a large influence on the combustion efficiency. This is not surprising as the T_{body} has a direct effect on the combustion of CO in the crevices and cold regions of the engine, which forms a crucial factor in the computation of the CE. Additionally, the T_{body} also advances the combustion and reduces the burn duration, hence the strong negative correlations with CA50 and burn duration.

Equivalence ratio ϕ - The strongest positive influence of ϕ can be found on the IMEP, much more than the LHV_{syngas} or the H_2/CO_2 ratio. This must be expected since the ϕ actually determines the amount of fuel going into the engine. The ϕ also has a strong positive influence on the combustion efficiency, but not to the extent of LHV_{syngas} or the H_2/CO_2

ratio. The influence of ϕ on the combustion phasing is relatively weaker than those exercised by the syngas factors (LHV, H_2/CO, and H_2/CO_2) as well as the body temperature. It must be noted that ϕ is influenced by both the LHV and the H_2/CO ratio, and is also equivalent to FuelMEP.

IE and CoV$_{IMEP}$ - As seen in Figures 6.6a and 6.7b, the trends in IE and CoV$_{IMEP}$ are negligible with a lot of spread. Spearman's correlation is capable of comparing monotonic relationships, which does not hold for IE since there is only a certain region around the TDC where it has a maximum. However, the same can not be said for the CoV$_{IMEP}$, which needs to be further examined.

CA50, CA$_{90-10}$ and MPRR - It is interesting to see that CA$_{90-10}$ and the CA50 have a very high positive correlation, very close to 1 (about 0.97). This implies that when the CA50 advances, the burn duration must reduce proportionally. Consequently, this short burn duration would result in increased ringing signified by the high negative correlations between the CA50 and combustion duration to the MPRR.

As a summary, the results of the 3 hours of continuous tests provided many fundamental clues to the operating or an HCCI engine with syngas. Next, the 24 hours of test are described.

6.4.2 The 24h test

For the 24 hours test, the same conditions were adhered to, as done in the 3 hours test. Only this time, the tests were begun after the cold gasifier had been preheated the previous day, which is enough to heat up the gasifier and reach optimal working conditions the following day. Additionally, the insulation at the test bench was increased to retain the heat contained within the air flow of the engine, which helped in keeping the T_{in} close to the targeted 250°C. The data acquisition was automated, with the operator overseeing the system and occasionally adjusting the engine cooling fan.

Figure 6.10 charts the varying and fluctuating syngas composition during the 24 hours test. Such a varying composition can be assumed to be a normal scenario in the domain of biomass gasification, which is why the current tests are important. The functioning of the HCCI engine, which is highly sensitive to compositional changes, could thus be disturbed, as shall be seen in the following discussion. An important point to note here is that the operation of the small engine in comparison to the size and the capacity of the gasifier makes it highly unlikely that compositional variations seen in Figure 6.10 were caused due to the engine. Additionally, the CO and CO_2 concentrations seem to be highly steady, in contrast to the other gases, thus implying that the origin of the variations are more likely to be related to the gasifier than to any gas dynamics in the tubing connecting the gasifier to the engine.

Apart from the compositional fluctuations, the first observations about this

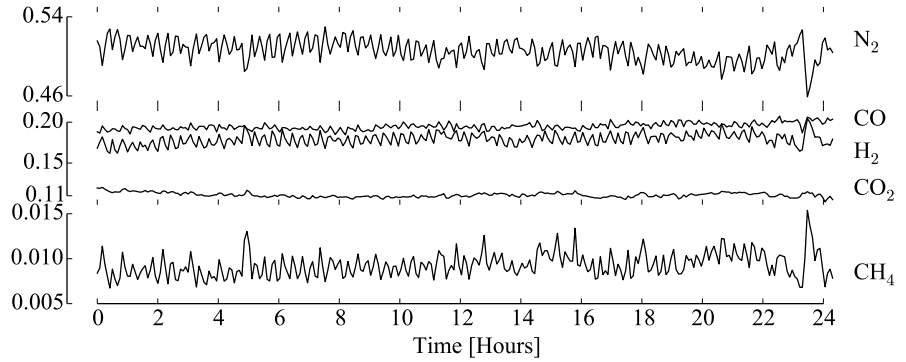


Figure 6.10: *Gas composition measured by the GGA during the 24 hours test. Note the relatively steady concentrations of CO and CO_2 as compared to the fluctuation concentrations of N_2, H_2 and CH_4.*

test were the relatively high values of the LHV_{syngas} and the H_2/CO_2 ratio, shown in Figure 6.11. The LHV_{syngas} improved over the 3h test (see Figure 6.4a) and kept increasing with time. The large variations in the LHV are also representative of the real conditions found in the domain of biomass gasification. It remains to be seen how the spread in this important factor influenced the HCCI combustion. At the end of the test duration, large variations in the LHV_{syngas} can be observed in the 22-24h period, highly correlated to the spikes in CH_4 concentration in Figure 6.10. The origins of these oscillations could not be determined.

As observed in Figure 6.9 and its subsequent discussion at the end of the last section, the discussion henceforth will use the ratio H_2/CO_2, instead of H_2/CO, due to the stronger influence of the former parameter. The H_2/CO_2 ratio fluctuated widely and as compared to the 3h test (see Figure 6.4c) which had a value between 1-1.2, the current values are much higher, from 1.4 to 1.8. A high value of H_2/CO_2 implies that the there is more of the fast burning H_2 and not enough of the combustion dampening CO_2 in the charge mixture. It can be thus predicted from the discussion in the previous section that such a charge mixture will bring about the benefits of higher combustion efficiency, but at the same time, would also advance and shorten the combustion duration leading to lower values of IE, IMEP and higher MPRR. This again calls for the closed-loop controlled operation of HCCI engine to compensate for such effects.

Based on the input syngas properties varying as a function of time, further discussions on the intake conditions can be started upon. Figure 6.12a shows the intake temperature variations as a function of time, which can be broadly divided into three segments. The first segment, eliminating the readings in the first hour, spans the 2-4th hour gap and can be seen to have a rising trend with minimal spread. This can be attributed to the slow response of the PID controller attempting to stabilize the electric heater. It remains well within the

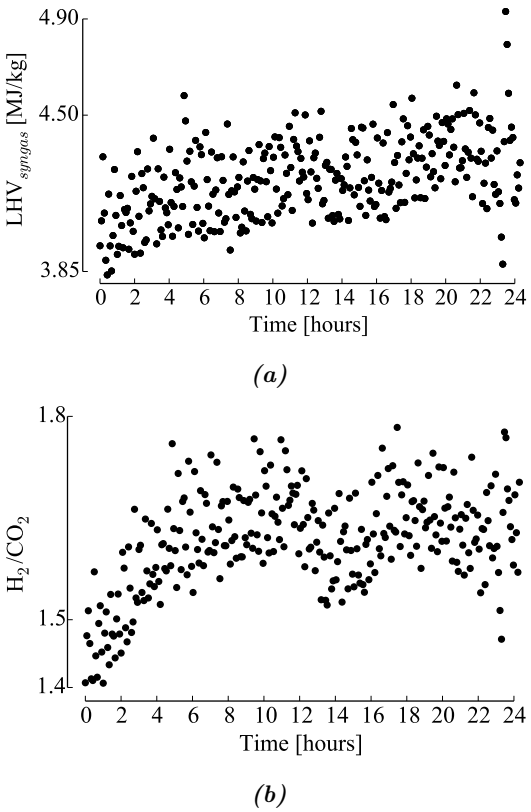


Figure 6.11: *Input syngas characteristics of LHV and H_2/CO_2 ratio plotted against time for the 24h test. (a) The LHV is much higher than the previous 3h test and increases slightly with time. (c) The H_2/CO_2 has also increased compared to the 3h tests, implying that the combustion would be more advanced and shorter.*

range of 250 ±5°C. The second section can be imaged to be between the 4th to the 16th hour interval, and consists of a stable operation with no particular trend. However, the last segment, spanning from the 16th to the 24th hour shows wide fluctuations. As mentioned before, the origins of these fluctuations are very not clear at the time of writing this thesis.

Figure 6.12b shows the steady decline of the intake pressure p_{in} as a function of time. On close observation, two segments can be identified with the first from 0-14h gap and the second for the remaining period. In the first segment the p_{in} is relatively stable, however in the second segment there is a steady declining trend in its value. It must be noted here that even if the engine was operated as throttled by the fixed supply of air and a constant RPM, the intake pressure is relatively higher than the atmospheric pressure. Part of this difference could be attributed to the 0.02 bar over-pressure at the exit of the gasifier. However, this pressure at the exit of the gasifier would not remain the same at the inlet of the

test bench, due to the pressure drops caused by the long piping and the presence of intermediate valves and turns. A hypothesis can be made here which may explain the higher than atmospheric intake pressures as due to the presence of pressure oscillations caused by the intake dynamics of the engine. The intake pressure sensor has a slow response and is connected to measure only an average pressure. Thus, there might be a phase lag between the measurement and the pressure oscillations giving rise to the wide fluctuations seen in Figure 6.12b.

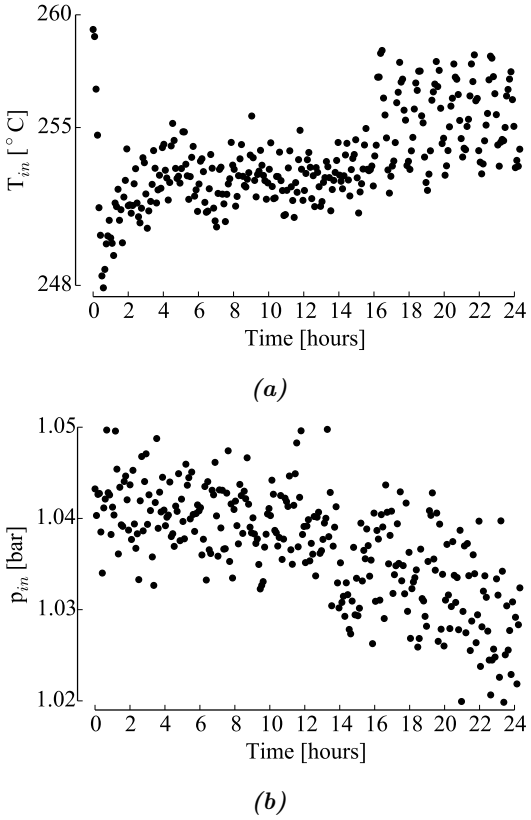


Figure 6.12: *Input conditions for the 24h tests. (a) The T_{in} has been increased from the previous $T_{in} \approx 227^\circ C$ in the 3h tests the value of interest. The changes in Tin at the end phases after the 16th hour is seen to be oscillating rapidly, probably due to back flow of combustion gases. (b) The p_{in} shows a slow but steady decline throughout the time span. The reason for such may be attributed to the oscillations in the intake.*

The ϕ, though an important control parameter, was not controlled and depended on the LHV_{syngas}, the gas composition as well as on the T_{in}. However, no particular correlation can be seen between the Figure 6.13a and the LHV_{syngas} in Figure 6.11a or the T_{in} in Figure 6.12a. The ϕ rises slightly in the 0-6h period and then steadily declines. The last part near the 24th hour shows a large fluctuation similar to the 24th hour oscillations observed

for the LHV_{syngas} and H_2/CO_2 parameters. These spikes are highly correlated to those found in Figure 6.10.

The T_{body} was the only control used by the operator, but only occasionally. Such a control can be seen in Figure 6.13b where it was exercised at 8th hour and in the 14-16th hours resulting in the abrupt shifts in the plot. The reasons for exercising such controls were, for the first control action, to stop the steady decline of the T_{body} seen in the period 0-8h, and, for the second control action, to decrease the combustion oscillations observed during time of the 16th hour and onwards. This second control action can be closely correlated to the oscillations observed in the T_{in} at the same times (see Figure 6.12a).

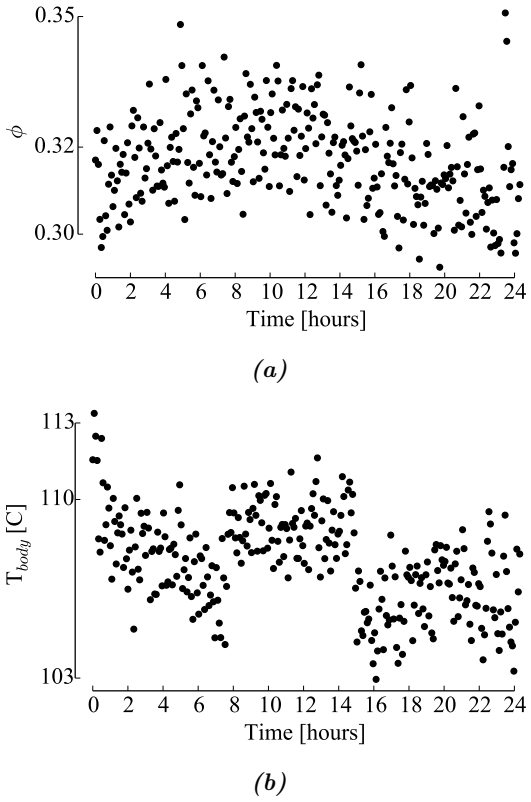
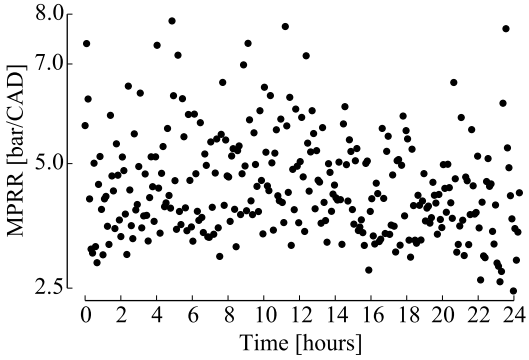
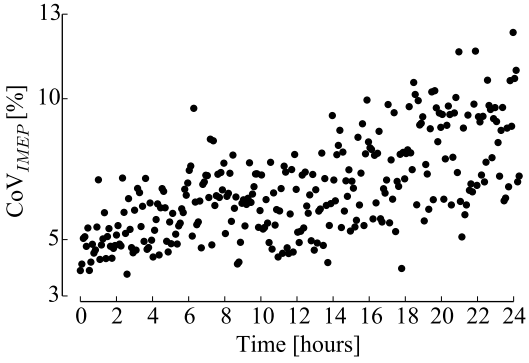


Figure 6.13: *Input conditions for the 24h tests. (a) The ϕ shows no clear trends as per the LHV and mostly keeps steady throughout the run. (b) The body temperature was the only control exercised and shows the changes made at the 8h and 14h-16h.*

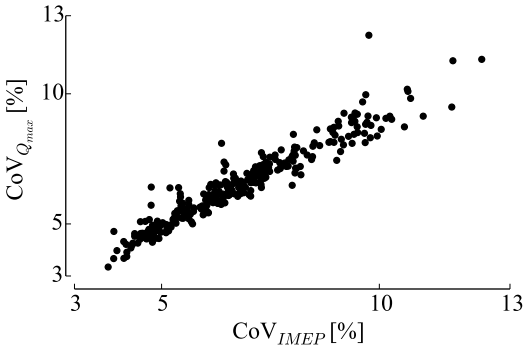
As for the MPRR, (see Figure 6.14a), a wide spread can be observed from the very low values which can be correlated to decent or poor/late combustion, to the relatively higher values which can be related to advanced combustion with the high pressure ringing. The latter was also experienced by the author during the tests. Although the limit for the MPRR during this thesis has been



(a)



(b)



(c)

Figure 6.14: *(a) Wide variations in MPRR indicate significant instabilities and implies that the cycles showed slow as well as fast burning. (b) The CoV in IMEP deteriorates over time as the combustions tend to be more unstable. (c) The CoV in the maximum heat released per cycle (Q_{max}) shows a very strong correlation with the CoV of the IMEP.*

set at 10 bar/CAD, the pressure ringing phenomenon was experienced even before, though at less amplitudes.

The net effect of the controls and conditions discussed so far should be reflected in the CoV of the IMEP as observed in the Figure 6.14b. It is no surprise that the CoV is high, compared to the 3 hours tests, since the combustion during the current tests were not stable in terms of audible noise as well as the pressure traces observed on the screen by the author. Especially in the later stages, the value of CoV_{IMEP} increases beyond what can be called an acceptable condition. The wide spread in the CoV_{IMEP} also indicates long term fluctuations not captured within the 100 cycle sample used for these calculations. The term $\mathrm{CoV}_{Q_{max}}$ indicates the intra-cycle variations in the maximum heat released, as computed from the RoHR analysis. Figure 6.14c shows a strong linear correlation between $\mathrm{CoV}_{Q_{max}}$ and CoV_{IMEP} which relates the instabilities in the engine directly to unstable combustion. A few hypotheses can be proposed to understand possible reasons why such large values of $\mathrm{CoV}_{Q_{max}}$ exist: A) The syngas composition is highly unstable, B) The combustion efficiency is varying cycle by cycle, or C) The fuel flow within the 100 cycles is unstable. Of these three, the hypothesis of rapid changes in syngas composition may not be true simply because of the inertia and volume of the gasifier. The latter reasons of varying combustion efficiency and fuel flow may be interrelated and seem to be most likely. However, no method or analysis of the available data could be devised at the time of writing which could identify the exact cause of these variations.

In terms of the IMEP as seen in Figure 6.15a, it follows closely the ϕ from Figure 6.13a which increases in the period 0-6h and thereafter steadily decreases. Similarly, oscillations are observed in the IE, as seen in Figure 6.15b, although no particular trends can be found which would help to relate with potential influencing parameters.

The influences of high H_2 content syngas are directly reflected on the HCCI combustion phasing. As seen in Figure 6.16a, the CA50 is very near the TDC throughout the 24 hours test duration. It is also interesting to note that the CA50 is not delayed in the cycle. Thus, the advanced CA50 and the narrow combustion duration in Figure 6.16b indicates that complete combustion was achieved. This observation eliminates one of the main reasons which potentially contribute to the high CoV in the IMEP as observed in Figure 6.14b, and hence the source of these variations must certainly be related to gas flow dynamics at the engine intake.

Next it would be interesting to analyze the combustion in terms of its completion and emissions. The CE in Figure 6.17a shows a high value indicating excellent combustion, even compared to the 3h tests. This correlates well with the CA50 and the short burn duration. Interestingly, the NO_x emissions increase drastically in Figure 6.17b. Likewise, in case of the T_{in}, the NO_x evolution can be divided into 3 segments, 0-8, 8-16 and 16-24h intervals. The oscillations

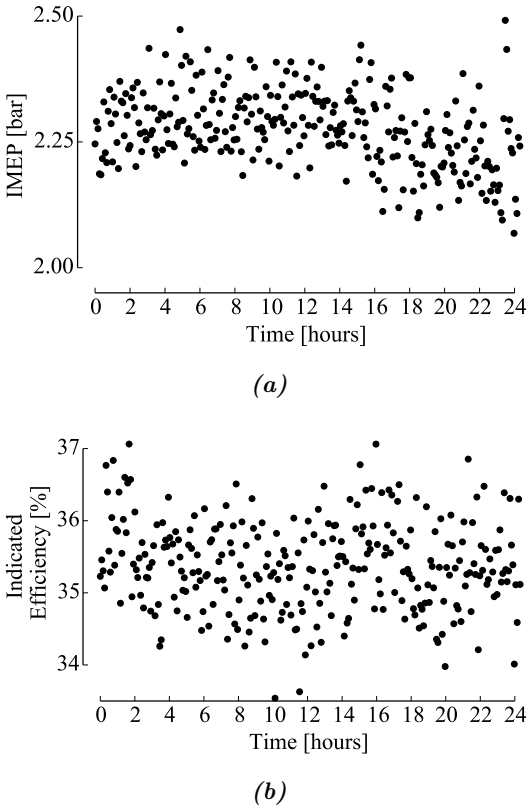


Figure 6.15: *(a) The IMEP follows a trend similar to ϕ. (b) Similar to the IMEP, the IE is also negatively affected by the relatively high LHV syngas, with high H_2 content and the high intake temperatures.*

encountered in the last segment, 16-24h, can be hypothesized to have resulted from intermittent cycles with significant combustion temperatures, which may have lead to out of normal NO_x production. As a comparison, the mean peak temperatures computed over the 100 cycles have been plotted with the corresponding NO_x emissions in Figure 6.17c. No correlation can be seen through a strong correlation must exist. This implies that the data acquisition carried out in these studies does not have sufficient resolution for such phenomena. Similar plots (not shown here) with CoV in the T_{max} also did not produce any correlation.

Finally, a Spearman's correlation table has been formed, similar to the one done for the 3 hours test section. However, due to the long experimental run and many variations within the values along with the different probable phase lags between the systems, computing a single correlation coefficient between two variables of interest would underestimate any correlation. Thus, for this long duration test, a 'boxcar' or moving correlation computation was performed

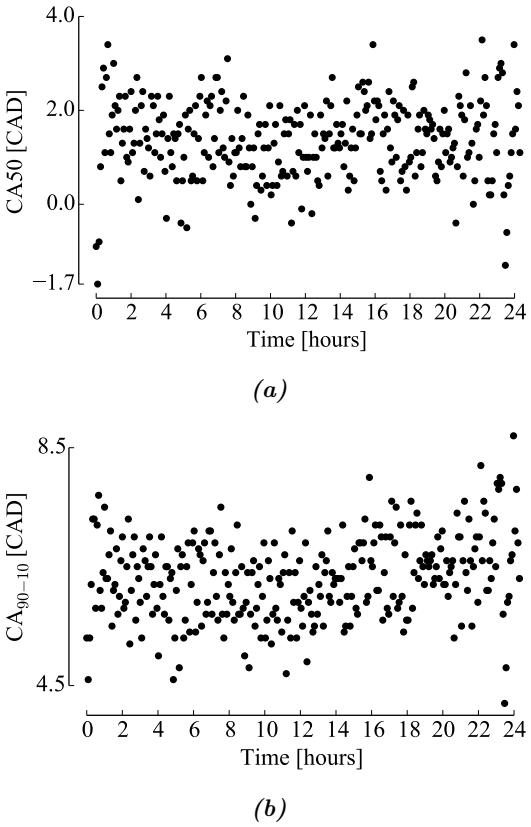


Figure 6.16: *Combustion metrics of CA50 and the burn duration indicate the variability in the combustion. However, the average values are very nearly stable for this long duration test, which point out to the potential of stable performance.*

over a sample size of 1 hour (12 data points corresponding to 5 minutes data sampling rate). The Spearman's correlation coefficients were averaged and the results are presented in Figure 6.18.

The main observations that can be made are:

- The LHV, H_2/CO and H_2/CO_2 ratios have high positive influence on the ϕ, similar to what was observed in case of the 3 hours tests. Likewise in the 3 hours tests, the syngas properties significantly influence the IMEP, CE the combustion phasing of CA50 and combustion duration. The two new parameters added are the NO_x and the MPRR, both of which show the high correlation with syngas properties. The values of IE and COV_{IMEP} do not show any significant correlation.
- Both the intake temperature and pressure seem to be uncorrelated to the rest of the dependent parameters, in contrast to the 3 hour tests. This may be due to the relative stability in these parameters over time.

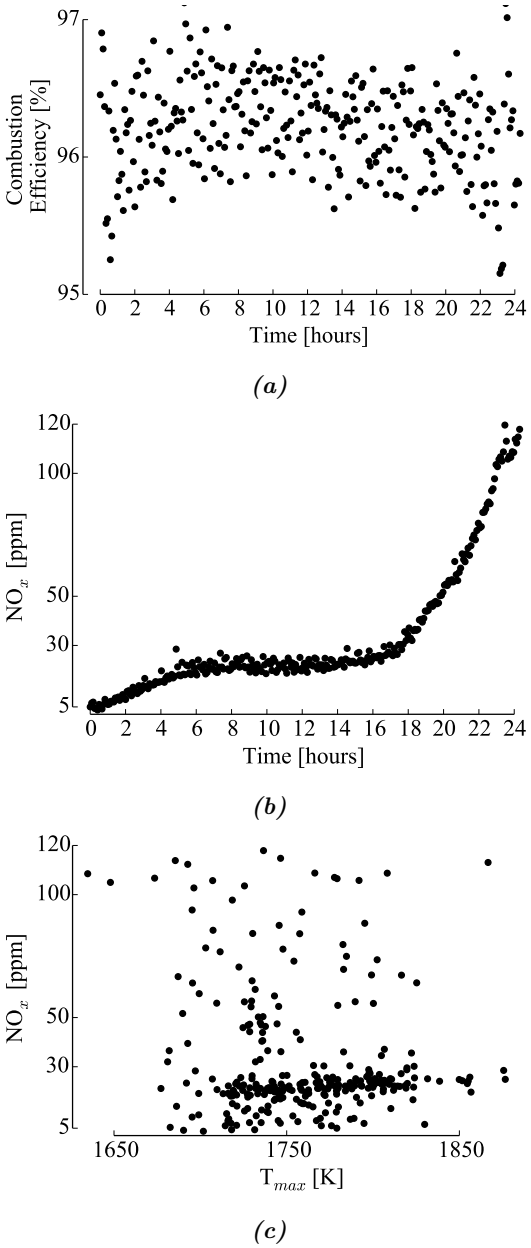


Figure 6.17: *Combustion Efficiency plotted against the time duration of the 24 hours test. The high values indicate near complete combustion resulting from the advanced CA50 and short combustion duration. The consequences of short combustion duration may cause the in-cylinder temperatures to rise and increase the emissions of NO_x. However, no correlation can be seen between the peak cylinder temperatures and the high NO_x emissions.*

	ϕ	CoV_{IMEP}	IMEP	CE	IE	CA50	CA_{90-10}	[NOx]	MPRR
LHV_{syngas}	0.87	-0.13	0.67	0.9	-0.23	-0.71	-0.76	0.62	0.77
H2/CO	0.7	-0.15	0.68	0.8	0.05	-0.72	-0.78	0.51	0.79
H2/CO2	0.75	-0.17	0.68	0.84	-0.09	-0.79	-0.81	0.62	0.81
T_{in}	-0.18	0.03	-0.26	0.05	-0.12	-0.27	-0.06	-0.05	0.04
p_{in}	0.06	-0.38	0.04	0.0	-0.01	-0.01	-0.02	0.0	0.01
T_{body}	0.63	-0.12	0.38	0.72	-0.33	-0.55	-0.54	0.4	0.53
ϕ	1.0	-0.22	0.78	0.85	-0.2	-0.63	-0.73	0.66	0.75
CoV_{IMEP}	-0.22	1.0	-0.39	-0.16	-0.25	0.26	0.31	-0.15	-0.27
IMEP	0.78	-0.39	1.0	0.68	0.3	-0.66	-0.82	0.57	0.83
CE	0.85	-0.16	0.68	1.0	-0.17	-0.83	-0.85	0.63	0.84
IE	-0.2	-0.25	0.3	-0.17	1.0	-0.12	-0.17	-0.08	0.19
CA50	-0.63	0.26	-0.66	-0.83	-0.12	1.0	0.92	-0.58	-0.92
CA_{90-10}	-0.73	0.31	-0.82	-0.85	-0.17	0.92	1.0	-0.62	-0.97
[NOx]	0.66	-0.15	0.57	0.63	-0.08	-0.58	-0.62	1.0	0.63
MPRR	0.75	-0.27	0.83	0.84	0.19	-0.92	-0.97	0.63	1.0

Figure 6.18: *Correlation coefficients between different parameters for the 24 hours test. As before, red blocks indicate high positive correlation whereas blue blocks indicate high negative correlations.*

Had the parameters changed, it can be estimated that correlations would have appeared as these are important HCCI combustion influencing parameters. As of T_{body}, it once again emerges as an important parameter strongly correlated to the ϕ and the combustion efficiency.

- As before, the ϕ strongly influences the IMEP, CE, CA50 and the burn duration. It can also be seen to be highly correlated to the NO_x emissions and the MPRR. The increase in ϕ causes the combustion to advance in the cycle. Since the combustion takes place at nearer to the TDC, the combustion duration is consequently shorter giving rise to high temperatures and pressure oscillations. The effects of high temperatures could be directly correlated to the increased NO_x emissions and high MPRR. Since the LHV, the H_2/CO_2 and H_2/CO ratios influence the ϕ, these parameters can also be seen to have high correlation to the NO_x and MPRR levels.
- The MPRR and the combustion duration show a very high and consistent correlation, similar to the 3 hours test.

It can be concluded here that the ϕ is the main influencing parameter, influencing all the parameters (except CoV_{IMEP} and the IE) to high levels. The high correlations between other values could result from high primary correlations with ϕ, which in turn would make them correlated with ϕ dependent parameters.

6.5 Conclusion and analysis

The correlations study carried out for the 3 hours and the 24 hours test point to the interesting relationships between the various parameters affecting HCCI combustion. Such a study of parameters was possible due to the large amount of data points available and the inherent spread arising due to experimental irregularities. However, the following key questions remain to be answered:

- What could be the cause of the large oscillations evident in the plots of CoV_{IMEP}, as well as experienced during the operation of the test bench for the 24 hours test case?
- What could be the reason behind the excessively high NO_x emissions found in the later stages of the 24 hours experiment?

A hypothesis for the oscillations is presented here:

In addition to the syngas compositional oscillations observed in Figure 6.10, another source of these disturbances could be attributed to engine gas exchange dynamics on the intake side, where some amount of combustion gases probably flowed back into the intake plenum resulting in an increase in the pressure, p_{in}. This increased pressure probably caused the check valve connecting the gasifier to the test bench to close, cutting off the flow of syngas. The persistent

but intermittent clapping noise originating from the check valve was noticed throughout the 24-hours experiment. Meanwhile, the air flow was maintained due to the air MFC and so was the RPM of the engine. Thus, the sensitive operation of the check valve could be a potential reason for fluctuating ϕ. An added complexity could be imagined where intermittent closure of check valve created larger than normal suction of syngas for the consecutive cycle, thereby increasing the combustion severity and leading to the production of NO_x.

For future tests the following recommendations could be made:

- The data acquisition of 100 cycles at the RPM of 1500 amounts to a data capture spanning 8 seconds. This sample size, through enough for heat release analysis, may not be sufficient to capture the short term oscillations which would be the mainstay problem with such connected gasifier-engine systems. Thus, for such tests larger sample sizes could be beneficial.
- The sensitivity of the check valve to the intake dynamics of the engine needs to be reduced, even if the hypothesis presented above has not been verified. This could be done by placing the check valve as far as possible from the test bench as well as increasing the capacity of the surge drum at the intake to absorb such oscillations. Additionally, it must be explored as to how the combustion phenomena is able to influence the intake flow conditions.
- The test of 24 hours was carried out with the intention of encountering rough operating conditions. Additional experiments could be made to run the engine and gasifier combination at stabler conditions with less values of ϕ which would result in somewhat late combustion, lower MPRR and probably lower NO_x levels.
- HCCI combustion phasing control strategies need to be used for effective operation and to avoid the onset of unstable combustion. Controls could be in the form of controlling of the air flow (and hence the ϕ) or through the use of a varying EGR rate.

Chapter 7

Conclusions and future directions

In Chapter 1, the broad context of gasification and its associated tar related issues were presented. The tars have been the most troublesome of the impurities and many efforts have been directed to address this issue. The present thesis is based on a novel concept which hinges on the fact that tar issues could be avoided by operating the processes downstream of a gasifier at conditions above the tar dew point. To this end, a HCCI engine is opted for due to it ability to operate at the required high intake temperatures. As a consequence of this novel pathway, many essential problems/challenges arise. Of these various challenges, this thesis attempted to explore the following ones:

- How does HCCI combustion behave as a function of syngas composition, including water and tar constituents, and specifically at the high temperatures of interest?
- Can EGR act as an effective control method for a HCCI engine fueled by syngas?
- What complications may arise if such an engine were to be run with a realistic condition of time varying syngas composition as well as time varying operating conditions?

Accordingly, a test bench and a set of post-processing methods were developed for this purpose, which were discussed in Chapters 2 and 3, respectively.

In the first set of experiments (Chapter 4), it was found that the H_2 content of syngas lead to an advancement of combustion, which increased the undesirable pressure ringing in the cycles and decreased the indicated efficiency as well as the IMEP. In the lack of an effective combustion control technique, it was concluded that high H_2/CO content syngas was not desirable for such an operation with HCCI engines. Further, raw syngas would not be devoid of

moisture content, and hence its effect on HCCI combustion was studied. Moisture, due to its high heat capacity, dampened the combustion and thus, it acted as a boon in the sense that such a moisture laden syngas allowed for higher equivalence ratios (resulting in higher IMEP) to be used. Raw syngas would also contain varying amounts of tars, depending on the type of gasification and the intermediate cleaning processes, upstream of the engine. Two commonly found representative tar compounds, toluene (liquid) and naphthalene (solid), were injected into the artificial syngas flow (in significant amounts) in order to observe their effects on HCCI combustion. It was found that such tar loaded syngas compositions resulted in the desirable increase in the fuel LHV, while, at the same time damping the combustion, which were opposite to the effects of using pure syngas. Within this chapter, experiments testing the effects of intake pressure and temperature were also discussed, revealing that high intake pressures and low intake temperatures resulted in higher overall performance. Thus, contrary to the requirements of conventional SI engines used in the gasification scenario, the use of HCCI engine actually benefits from the *impurities* of water and tars while being somewhat negatively sensitive to the presence of H_2. The latter aspect of H_2 content, which advances the combustion, could be mitigated through the use of closed-loop HCCI control methodologies, such as EGR.

Due to the lack of direct controls on HCCI combustion, Chapter 5 discussed experiments related to the use of EGR as a control methodology. EGR gases such as CO_2 and H_2O effectively delayed and dampened the combustion and thus, paired with the equivalence ratio, were shown as being an effective strategy for positioning the combustion phasing. Additionally, this mode of control would be very desirable for time varying syngas compositions as well as the operating conditions of intake temperature and pressure. Since the use of EGR significantly reduces the MPRR, it allows higher fueling rates to be used. However, since the limits of maximum equivalence ratio could only be up to stoichiometric, further benifits of EGR could be exploited through the use of higher compression ratios or boost pressures. The maximum IMEP was improved from 2.8 bar at EGR=0 to 3.3 bar at EGR=25%, a significant gain of about 25%. However, this value of IMEP is still low compared to a regular SI engine used in the gasification context.

Chapter 6 discussed the 3 hour and 24 hour experiments when the HCCI engine was run in an open-loop condition with real but cooled and purified syngas from a 2-stage downdraft gasifier installed at the laboratory. In the 3 hours experiments, the gasifier was in a transient starting-up stage with low but increasing LHV and produced stable combustion which was interesting in the light of the highly sensitive nature of the HCCI combustion. In contrast, during the 24 hour test, the gasifier was operating in a stable condition, supplying high LHV syngas. The 24 hour results showed significant instabilities and significantly high amounts of NO_x emissions. Direct reasons for explaining

these outcomes could not be established. Instead, it was hypothesized that the most probable reasons could either originate from instabilities in the syngas supply (from within the gasifier), or instabilities in the syngas flow due to the sensitive operation of a check valve connecting the syngas supply to the test bench. The reason for high NO_x emissions was hypothesized to be the presence of extreme combustion cycles dispersed in-between normal cycles. These hypotheses could not be verified sufficiently due to limited resolution of the various parameters acquired during the experiments, especially the low number of cycles (100) and the slow time integrating nature of few instruments. In conclusion, these experiments showed that significant instabilities would exist and an appropriate control system had to be devised for use in such circumstances. Even if the results of the 24 hour tests were far from optimum, the objectives of these experiments were met, wherein it was important to establish the ground challenges that such a system and the associated control technique would have to handle. Additionally, many insights were developed using the statistically large data collected during these experiments.

7.1 Merits and Demerits of the Concept

If the major issues within this concept could be resolved, the following benefits could be foreseen:

- Low quality syngas with significant amounts of water and tars could be used in an advantageous manner.
- This will allow low-tech gasifiers, such as the updraft gasifiers, to be used with such an engine without encountering tar problems.
- This concept provides an alternative to the traditional approach which focuses on developing high tech low tar gasification and gas conditioning systems aimed to meet the requirements of a traditional SI engine. The alternative would be pursuing the high temperature approach and focusing on using low-tech high tar producing gasification units with high-tech HCCI engine systems.
- With the use of EGR, the HCCI engine would benefit from higher compression ratios than would normally be possible with a SI engine.
- In terms of emissions, the low NO_x combustion of this concept can be very attractive.

In terms of limitations or disadvantages of this concept:

- The major limitation is the power derating arising from the two crucial pillars of this concept: 1) The use of a HCCI engine with its limited load capacity 2) The use of temperatures above the tar dew point. For the sake of comparison, consider the FuelMEPs of a SI engine used in the traditional approach and a HCCI engine used with the proposed approach

of this thesis. The FuelMEP (as defined in Eq. (3.17) and simplified in the form expressed in Eq. (1.1)) is represented here:

$$\text{FuelMEP} = \frac{p_0}{R_{\text{charge}} \cdot T_0} \cdot \frac{\text{LHV}_{\text{fuel}}}{\frac{AFR_{m,st}}{\phi} + 1} \tag{7.1}$$

Assuming both the engines operate as naturally aspirated, the only difference between the two engines are the different intake temperatures, $\text{AF}_{m,st}$ and ϕ. Thus the ratio of FuelMEP between the two engines can be reduced to the following equality:

$$\frac{\text{FuelMEP}_{\text{SI}}}{\text{FuelMEP}_{\text{HCCI}}} = \frac{T_{in,HCCI}}{T_{in,SI}} \cdot \frac{\frac{AF_{m,st}}{\phi_{HCCI}} + 1}{\frac{AF_{m,st}}{\phi_{SI}} + 1} \tag{7.2}$$

Thus, given the information $\phi_{HCCI} \approx 0.4$, $\phi_{SI} \approx 1$, $T_{in,HCCI} \approx 523\text{K}$ and $T_{in,SI} \approx 303\text{K}$ and using the usual $AF_{m,st} \approx 1.2$, the ratio results in:

$$\text{FuelMEP}_{SI} > 3 \times \text{FuelMEP}_{HCCI} \tag{7.3}$$

Thus, for an equivalent power, a HCCI engine with high intake temperature would need to be significantly larger than a SI engine.

- As shown in the studies by [51], SI engine can achieve high efficiency along with significant power.
- SI engines at ambient conditions could benefit from the use of supercharging or turbocharging, further increasing the power. However, for HCCI engine, supercharging or turbocharging at the high temperatures seems viable but with more complexities and certainly lower boost pressures.
- Other limitations would be developing monitoring and control systems since the HCCI engine is especially susceptible to many factors. These additional systems would make such a concept costly and complex, compared to the significantly simple and available SI engine.

Thus, the present concept would have to compete on many fronts to be comparable to the standard traditional SI engines used in the gasification scenario. However, if the issue of tars are the most significant and the costs and complexities of eradicating the tar related problems are significantly higher, this concept can play a key role.

7.2 Limitations of this thesis

A significant amount of time available in the duration of this thesis was spent on assembly and trouble shooting of the test bench. However, in terms of assessment, the following limitations could be pointed out:

- The most significant limitation is that not enough experiments were carried out with tars, which was the main challenge which motivated this thesis. Specifically the following questions could have been discussed:
  - Do tars get destroyed completely during the HCCI combustion?
  - Does tars deposition take place in the high temperature operating conditions?
  - Do tars polymerize into soot?
  - Representative tars, toulene and naphthalene, do not necessarily represent the condensation behavior, so which kind of tars would be the best candidates for testing tar deposition?
- The HCCI engine was operated in open-loop condition without any active control. This implies that the results discussed in this thesis would be limited to conditions where no controls are available, which is a limiting and highly unlikely scenario for using HCCI engines. Had some form of control been implemented, such as with the use of EGR resulting in consistent CA50 position for example, the data would have become more relevant to generate an operational map.
- Water cooled engine could have been used which would have helped to test full potential for EGR and as well as provide an test bench engine closer to the real application scenario.
- HC and GC/MS measurements could have been made which would have given an estimation of tar combustion.
- More experiments in Chapter 6 could have been done to give a more complete insight into the issues.

7.3 Future work

The following works have been planned or are currently in progress at the time of writing this thesis:

1. Experiments with hot and impure syngas are on the verge of beginning. These experiments will study:
   (a) Stability and response of the HCCI engine to the time variations of syngas compositions, same as those carried out in Chapter 6. However, additional complications are expected, especially with varying syngas temperatures, uncontrollable tars, tar depositions and blocking of connecting pipes, etc.
   (b) The tar destruction capability would be explored, by taking tar measurements on the intake and the exhaust of the engine.
   (c) The deposits of tars, if any, may be explored in terms of their content.

2. The test bench is planned to be upgraded to a 4-cylinder engine soon. This would allow long duration tests focusing more on the power de-rating aspect and bringing out possible maintenance issues arising with the high temperature operation. Additionally, various combustion control strategies such as EGR or variable valve timing could be tried.
3. Aspects of possible turbocharging may be looked into.
4. SI transition or Spark assisted HCCI could also be explored.
5. As a system upgrade, future systems would contain water-cooled pressure sensors, water cooled engines and HCCI with closed control strategies in place.

Bibliography

[1] Raphael Slade, Ausilio Bauen, and Robert Gross. Global bioenergy resources. *Nature Climate Change*, 4(2):99–105, 2014.

[2] Francesco Cherubini, Neil D. Bird, Annette Cowie, Gerfried Jungmeier, Bernhard Schlamadinger, and Susanne Woess-Gallasch. Energy- and greenhouse gas-based LCA of biofuel and bioenergy systems: Key issues, ranges and recommendations. *Resources, Conservation and Recycling*, 53:434–447, 2009.

[3] Peter McKendry. Energy production from biomass (part 1): overview of biomass. *Bioresource Technology*, 83(1):37–46, May 2002.

[4] Sarah Gerssen-Gondelach, Deger Saygin, Birka Wicke, and André Faaij. Competing uses of biomass - Assessment and comparison of the performance of bio-based heat, power, fuels and materials. *Renewable and Sustainable Energy Reviews*, 40(April):964–998, 2014.

[5] Pabir Basu. *Biomass Gasification and Pyrolysis - Practical Design and Theory*. Academic Press, 2010, 2010. ISBN 978-0-12-374988-8.

[6] A.V. AV Bridgwater. The technical and economic feasibility of biomass gasification for power generation. *Fuel*, 14(5):631–653, May 1995.

[7] Veronika Dornburg and A. P C Faaij. Efficiency and economy of wood-fired biomass energy systems in relation to scale regarding heat and power generation using combustion and gasification technologies. *Biomass and Bioenergy*, 21:91–108, 2001.

[8] U. Arena, F. Di Gregorio, and M. Santonastasi. A techno-economic comparison between two design configurations for a small scale, biomass-to-energy gasification based system. *Chemical Engineering Journal*, 162(2): 580–590, August 2010.

[9] Anna Skorek-Osikowska, Łukasz Bartela, Janusz Kotowicz, Aleksander Sobolewski, Tomasz Iluk, and Leszek Remiorz. The influence of the size of the CHP (combined heat and power) system integrated with a biomass

fueled gas generator and piston engine on the thermodynamic and economic effectiveness of electricity and heat generation. *Energy*, 67:328–340, 2014.

[10] TB Reed, T.B.R.A. Das, and A Das. *Handbook of Biomass Downdraft Gasifier Engine Systems*. Biomass Energy Foundation, 1988. ISBN 9781890607005.

[11] a. V. Bridgwater. Review of fast pyrolysis of biomass and product upgrading. *Biomass and Bioenergy*, 38:68–94, 2012.

[12] Nuno Couto, Abel Rouboa, Valter Silva, Eliseu Monteiro, and Khalid Bouziane. Influence of the Biomass Gasification Processes on the Final Composition of Syngas. *Energy Procedia*, 36:596–606, January 2013.

[13] Peter McKendry. Energy production from biomass (Part 3): Gasification technologies. *Bioresource Technology*, 83(1):55–63, 2002.

[14] J.a. Ruiz, M.C. Juárez, M.P. Morales, P. Muñoz, and M.a. Mendívil. Biomass gasification for electricity generation: Review of current technology barriers. *Renewable and Sustainable Energy Reviews*, 18:174–183, February 2013.

[15] Javier Gil, P Aznar, and Miguel Caballero. Biomass gasification in atmospheric and bubbling fluidized bed: Effect of the type of gasifying agent on the product distribution. *Biomass*, 17:0–14, 1999.

[16] T A Milne, N Abatzoglou, and R J Evans. Biomass Gasifier " Tars ": Their Nature , Formation , and Conversion. Technical Report November, Kemestrie, Inc. National Renewable Energy Laboratory (U.S.), 1998.

[17] B. J. Vreugdenhil, Robin Zwart, and Johannes Petrus Adrianus Neeft. Tar formation in pyrolysis and gasification. Technical Report June, ECN, The Netherlands, 2009.

[18] Luc P L M Rabou, Robin W R Zwart, Berend J. Vreugdenhil, and Lex Bos. Tar in biomass producer gas, the Energy research Centre of The Netherlands (ECN) experience: An enduring challenge. *Energy and Fuels*, 23(2):6189–6198, 2009.

[19] J.J. J Hernández, R. Ballesteros, and G. Aranda. Characterisation of tars from biomass gasification: Effect of the operating conditions. *Energy*, 50: 333–342, February 2013.

[20] Patrick C A Bergman, Sander V B Van Paasen, Harold Boerrigter, and Sander V B van Paasen. The novel OLGA technology for complete tar removal from biomass producer gas. In *Pyrolysis and Gasification of Biomass and Waste, Expert Meeting, Strasbourg, France*, 2002.

[21] R W R Zwart. Gas cleaning downstream biomass gasification. Technical Report JUNE, ECN, The Netherlands, 2009.

[22] Orgun Güralp, Mark Hoffman, Dennis Assanis, Zoran Filipi, Tang-Wei Kuo, Paul Najt, and Rod Rask. Characterizing the Effect of Combustion Chamber Deposits on a Gasoline HCCI Engine. *SAE Technical Paper 2006-01-3277*, October 2006.

[23] Jesper Ahrenfeldt, Ulrik Henriksen, Jesper Schramm, Torben K Jensen, and Helge Egsgaard. Combustion Chamber Deposits and PAH Formation in SI Engines Fueled by Producer Gas from Biomass Gasification. In *SAE Technical Paper 2003-01-1770*, 2003.

[24] M. P. Houben, H. C. De Lange, and a. a. Van Steenhoven. Tar reduction through partial combustion of fuel gas. *Fuel*, 84:817–824, 2005.

[25] Philipp Hasler and Thomas Nussbaumer. Sampling and analysis of particles and tars from biomass gasifiers. *Biomass and Bioenergy*, 18(1): 61–66, January 2000.

[26] Mohammad Asadullah. Biomass gasification gas cleaning for downstream applications: A comparative critical review. *Renewable and Sustainable Energy Reviews*, 40:118–132, December 2014.

[27] Philipp Hasler and Thomas Nussbaumer. Gas cleaning for IC engine applications from fixed bed biomass gasification. *Biomass and Bioenergy*, 16(6):385–395, June 1999.

[28] Jesper Ahrenfeldt, Tobias P. Thomsen, Ulrik Henriksen, and Lasse R. Clausen. Biomass gasification cogeneration - A review of state of the art technology and near future perspectives. *Applied Thermal Engineering*, 50(2):1407–1417, February 2013.

[29] Benjamin Berger, Alexandre Bacq, Hervé Jeanmart, and Frédéric Bourgois. Experimental and Numerical Investigation of the Air Ratio on the Tar Content in the Syngas of a Two-Stage Gasifier. In *European Biomass Conference and Exhibition Proceedings*, pages 20–25, Lyon, France, 2010.

[30] S.C Bhattacharya, A.H.Md Mizanur Rahman Siddique, and Hoang-Luong Pham. A study on wood gasification for low-tar gas production. *Energy*, 24(4):285–296, 1999.

[31] Jesper Ahrenfeldt, Ulrik Henriksen, Torben K. Jensen, Benny Gø bel, Lars Wiese, Alphons Kather, and Helge Egsgaard. Validation of a continuous combined heat and power (CHP) operation of a two-stage biomass gasifier. *Energy and Fuels*, 20(6):2672–2680, 2006.

[32] Lopamudra Devi, Krzysztof J Ptasinski, and Frans J.J.G J G Janssen. A review of the primary measures for tar elimination in biomass gasification processes. *Biomass and Bioenergy*, 24(2):125–140, February 2003.

[33] Ana Lisbeth Galindo, Electo Silva Lora, Rubenildo Viera Andrade, Sandra Yamile Giraldo, Rene Lesme Jaén, and Vladimir Melian Cobas. Biomass gasification in a downdraft gasifier with a two-stage air supply: Effect of operating conditions on gas quality. *Biomass and Bioenergy*, 61: 236–244, 2014.

[34] Ulrik Henriksen, Jesper Ahrenfeldt, Torben Kvist Jensen, Benny Gø bel, Jens Dall Bentzen, Claus Hindsgaul, and Lasse Holst Sø rensen. The design, construction and operation of a 75 kW two-stage gasifier. *Energy*, 31(10-11):1542–1553, 2006.

[35] Patrick J. Woolcock and Robert C. Brown. A review of cleaning technologies for biomass-derived syngas. *Biomass and Bioenergy*, 52:54–84, May 2013.

[36] Murari Mohon Roy, Eiji Tomita, Nobuyuki Kawahara, Yuji Harada, and Atsushi Sakane. Performance and emission comparison of a supercharged dual-fuel engine fueled by producer gases with varying hydrogen content. *International Journal of Hydrogen Energy*, 34(18):7811–7822, September 2009.

[37] John B Heywood. *Internal combustion engine fundamentals*. McGraw-Hill, 1988. ISBN 007028637X, 9780070286375.

[38] M. Pöschl and T. Sattelmayer. Influence of temperature inhomogeneities on knocking combustion. *Combustion and Flame*, 153:562–573, 2008.

[39] Bengt Johansson. Cycle to Cycle Variations in S.I. Engines - The Effects of Fluid Flow and Gas Composition in the Vicinity of the Spark Plug on Early Combustion. In *SAE Technical Paper*, number 962084, October 1996.

[40] Jennifer A Topinka, Michael D Gerty, John B Heywood, and James C Keck. Knock Behavior of a Lean-Burn , H 2 and CO Enhanced , SI Gasoline Engine Concept. *SAE Technical Paper 2004-01-0975*, 2004.

[41] Francisco V. Tinaut, Andrés Melgar, Alfonso Horrillo, and Ana Díez de la Rosa. Method for predicting the performance of an internal combustion engine fuelled by producer gas and other low heating value gases. *Fuel Processing Technology*, 87(2):135–142, January 2006.

[42] Aparna Arunachalam and Daniel B. Olsen. Experimental evaluation of knock characteristics of producer gas. *Biomass and Bioenergy*, 37:169–176, February 2012.

[43] Martin Malenshek and Daniel B. Olsen. Methane number testing of alternative gaseous fuels. *Fuel*, 88(4):650–656, 2009.

[44] S. Dasappa, D. N. Subbukrishna, K. C. Suresh, P. J. Paul, and G. S. Prabhu. Operational experience on a grid connected 100kWe biomass gasification power plant in Karnataka, India. *Energy for Sustainable Development*, 15(3):231–239, 2011.

[45] G. Sridhar, P. J. Paul, and H. S. Mukunda. Biomass derived producer gas as a reciprocating engine fuel—an experimental analysis. *Biomass and Bioenergy*, 21(1):61–72, 2001.

[46] Jesper Ahrenfeldt. Development and Test of a new Concept for Biomass Producer Gas Engines Risø-R-Report. Technical Report February, Risø-National Laboratory for Sustainable Energy, 2010.

[47] Juan J. Hernandez, Magín Lapuerta, Clara Serrano, and Andres Melgar. Estimation of the Laminar Flame Speed of Producer Gas from Biomass Gasification. *Energy & Fuels*, 19(10):2172–2178, 2005.

[48] Juan Daniel Martínez, Khamid Mahkamov, Rubenildo V. Andrade, Electo E. Silva Lora, Juan Daniel, Electo E Silva, and Juan Daniel MartÃnez. Syngas production in downdraft biomass gasifiers and its application using internal combustion engines. *Renewable Energy*, 38(1): 1–9, February 2012.

[49] Ftwi Yohaness Hagos, a. Rashid a. Aziz, and Shaharin Anwar Sulaiman. Trends of Syngas as a Fuel in Internal Combustion Engines. *Advances in Mechanical Engineering*, 2014:1–10, 2014.

[50] G. Sridhar, S. Dasappa, H. V. Sridhar, P. J. Paul, and N. K. S. Rajan. Gaseous Emissions Using Producer Gas as Fuel in Reciprocating Engines. In *SAE Technical Paper 2005-01-1732*, April 2005.

[51] Jonas Ulfvik, Matthias Achilles, Martin Tuner, Bengt Johansson, Jesper Ahrenfeldt, Franz Xaver Schauer, and Ulrik Henriksen. SI Gas Engine : Evaluation of Engine Performance , Efficiency and Emissions Comparing Producer Gas and Natural Gas. *SAE International Journal of Engines*, 4(1):1202–1209, April 2011.

[52] R.H. Williams and E.D. Larson. Biomass gasifier gas turbine power generating technology. *Biomass and Bioenergy*, 10(2-3):149–166, 1996.

[53] Ramanan Sankaran, Hong G. Im, Evatt R. Hawkes, and Jacqueline H. Chen. The effects of non-uniform temperature distribution on the ignition of a lean homogeneous hydrogen–air mixture. *Proceedings of the Combustion Institute*, 30(1):875–882, January 2005.

[54] George a. Lavoie, J. Martz, M. Wooldridge, and Dennis Assanis. A multi-mode combustion diagram for spark assisted compression ignition. *Combustion and Flame*, 157(6):1106–1110, 2010.

[55] Salvador M. Aceves, Daniel L. Flowers, Francisco Espinosa-Loza, Joel Martinez-Frias, John E. Dec, Magnus Sjöberg, Robert W. Dibble, and Randy P. Hessel. Spatial Analysis of Emissions Sources for HCCI Combustion at Low Loads Using a Multi-Zone Model. *SAE Technical Paper 2004-01-1910*, June 2004.

[56] J.a. Eng. Characterization of Pressure Waves in HCCI Combustion. *SAE Technical Paper 2002-01-2859*, (724), 2002.

[57] Samveg Saxena and Iván D. Bedoya. Fundamental phenomena affecting low temperature combustion and HCCI engines, high load limits and strategies for extending these limits. *Progress in Energy and Combustion Science*, 39(5):457–488, October 2013.

[58] Janardhan Kodavasal, George a. Lavoie, Dennis Assanis, and Jason B. Martz. The effects of thermal and compositional stratification on the ignition and duration of homogeneous charge compression ignition combustion. *Combustion and Flame*, 162(2):451–461, 2014.

[59] Magnus Christensen, Anders Hultqvist, and Bengt Johansson. Demonstrating the Multi Fuel Capability of a Homogeneous Charge Compression Ignition Engine with Variable Compression Ratio. *SAE Technical Paper 1999-01-3679*, 2009.

[60] Hå kan Persson, Bengt Johansson, and Alfredo Remón. The Effect of Swirl on Spark Assisted Compression Ignition (SACI). *SAE International*, JSAE 20077(SAE 2007-01-1856):365–375, 2007.

[61] Magnus Christensen and Bengt Johansson. Homogeneous Charge Compression Ignition with Water Injection. *SAE Technical Paper 1999-01-0182*, March 1999.

[62] Jan-Ola Olsson, Per Tunestå l, and Bengt Johansson. Boosting for High Load HCCI. *SAE Technical Paper 2004-01-0940*, March 2004.

[63] Per Risberg. *Describing the Auto-Ignition Quality of Fuels in HCCI Engines*. PhD thesis, Royal Insititute of Technology, Sweden, 2006.

[64] Xingcai Lu, Dong Han, and Zhen Huang. Fuel design and management for the control of advanced compression-ignition combustion modes. *Progress in Energy and Combustion Science*, 37(6):741–783, December 2011.

[65] Andreas Vressner, Petter Strandh, Anders Hultqvist, Per Tunestå l, and Bengt Johansson. Multiple Point Ion Current Diagnostics in an HCCI Engine. *SAE Technical Paper 2004-01-0934*, pages 1–7, March 2004.

[66] Yong Cheng, Juan Tang, Shaobo Ji, and Minli Huang. Combustion timing determination based on vibration velocity in HCCI engines. *Mechanism and Machine Theory*, 58:20–28, December 2012.

[67] Dale Edward Haggith, Andrzej Sobiesiak, Luke Warren Miller, and Grzegorz Przybyla. Experimental Indicated Performance of a HCCI Engine Fuelled by Simulated Biomass Gas. In *SAE Technical Paper 2010-01-1081*, 2010.

[68] Yudai Yamasaki, Go Tomatsu, Yuki Nagata, and Shigehiko Kaneko. Combustion Characteristics of Low-Calorific-Value Gaseous Fuels in Small Gas Engine. *Journal of Environment and Engineering*, 4(1):188–197, 2009.

[69] Matthias Achilles, Jonas Ulfvik, Martin Tuner, Bengt Johansson, Jesper Ahrenfeldt, Ulrik Henriksen, and Franz Xaver Schauer. HCCI Gas Engine: Evaluation of Engine Performance, Efficiency and Emissions - Comparing Producer Gas and Natural Gas. *SAE Technical Paper 2011-01-1196*, April 2011.

[70] Anil Singh Bika, Luke Franklin, and David B Kittelson. Homogeneous charge compression ignition engine operating on synthesis gas. *International Journal of Hydrogen Energy*, 37(11):9402–9411, June 2012.

[71] Dale Edward Haggith and Andrzej Sobiesiak. Effects of Fuel Composition Variations (H 2 :CO) for Biomass Gas HCCI Combustion. *SAE Technical Paper 2012-01-1112*, April 2012.

[72] Yudai Yamasaki and Shigehiko Kaneko. Prediction of Ignition and Combustion Development in an HCCI Engine Fueled by Syngas. *SAE Technical Paper 2014-32-0002*, 2014.

[73] Gregory P. Smith, David M. Golden, Michael Frenklach, Nigel W. Moriarty, Boris Eiteneer, Mikhail Goldenberg, C. Thomas Bowman, Ronald K. Hanson, Soonho Song, William C. Gardiner Jr., Vitali V. Lissianski, and Zhiwei Qin. GRI-MECH 3.0. URL `http://www.me.berkeley.edu/gri_mech/`.

[74] Francesco Contino, Benjamin Berger, Fabrice Foucher, Jean-Baptiste Masurier, Subir Bhaduri, Anil Singh Bika, and Hervé Jeanmart. Analysis of a syngas HCCI engine for chp biomass gasification facilities. In *The 11th International Conference on Combustion and Energy Utilization*, Coimbra, Portugal, 2012.

[75] Subir Bhaduri, Francesco Contino, Hervé Jeanmart, and Ernst Breuer. The effects of biomass syngas composition, moisture, tar loading and operating conditions on the combustion of a tar-tolerant HCCI (Homogeneous Charge Compression Ignition) engine. *Energy*, 87(0):289–302, 2015.

[76] Francesco Contino, Hervé Jeanmart, Tommaso Lucchini, and Gianluca D'Errico. Coupling of in situ adaptive tabulation and dynamic adaptive chemistry: An effective method for solving combustion in engine simulations. *Proceedings of the Combustion Institute*, 33(2):3057–3064, January 2011.

[77] Francesco Contino, Tommaso Lucchini, Gianluca D'Errico, Catherine Duynslaegher, Veronique Dias, and Hervé Jeanmart. Simulations of Advanced Combustion Modes Using Detailed Chemistry Combined with Tabulation and Mechanism Reduction Techniques. *SAE Int. J. Engines*, 5(2):185–196, April 2012.

[78] Francesco Contino, Fabrice Foucher, Philippe Dagaut, Tommaso Lucchini, Gianluca D'Errico, and Christine Mouna´im-Rousselle. Experimental and numerical analysis of nitric oxide effect on the ignition of iso-octane in a single cylinder HCCI engine. *Combustion and Flame*, 160 (8):1476–1483, August 2013.

[79] Francesco Contino, Jean-Baptiste Masurier, Fabrice Foucher, Tommaso Lucchini, Gianluca D'Errico, and Philippe Dagaut. CFD simulations using the TDAC method to model iso-octane combustion for a large range of ozone seeding and temperature conditions in a single cylinder HCCI engine. *Fuel*, 137:179–184, December 2014.

[80] G.T. Kalghatgi and R a Head. Combustion Limits and Efficiency in a Homogeneous Charge Compression Ignition Engine. *International Journal of Engine Research*, 7(3):215–236, June 2006.

[81] Jan-ola Olsson, Per Tunestå l, Jonas Ulfvik, and Bengt Johansson. The Effect of Cooled EGR on Emissions and Performance of a Turbocharged HCCI Engine. *SAE Technical Paper*, 2003-01-07, 2003.

[82] Bonnie J. McBride, Sanford Gordon, and Martin A. Reno. *Coefficients for calculating thermodynamic and transport properties of individual species*. National Aeronautics and Space Administration, Office of Management, Scientific and Technical Information Program ; National Technical Information Service, distributor] [Washington, DC] : [Springfield, Va, 1993.

[83] Francesco Contino, Fabrice Foucher, Christine Mouna´im-Rousselle, and Hervé Jeanmart. Experimental Characterization of Ethyl Acetate, Ethyl

Propionate, and Ethyl Butanoate in a Homogeneous Charge Compression Ignition Engine. *Energy & Fuels*, 25(3):998–1003, March 2011.

[84] J. A. Gatowski, E. N. Balles, K. M. Chun, F. E. Nelson, J. A. Ekchian, and John B. Heywood. Heat Release Analysis of Engine Pressure Data. *SAE Technical Paper 841359*, October 1984.

[85] Michael F.J. Brunt, Harjit Rai, and Andrew L. Emtage. The Calculation of Heat Release Energy from Engine Cylinder Pressure Data. In *SAE Technical Paper 981052*, February 1998.

[86] Rolf Egnell. Combustion Diagnostics by Means of Multizone Heat Release Analysis and NO Calculation. *Sae*, (981424), 1998.

[87] Junseok Chang, Orgun Güralp, Zoran Filipi, Dennis Assanis, Tang-Wei Kuo, Paul Najt, and Rod Rask. New Heat Transfer Correlation for an HCCI Engine Derived from Measurements of Instantaneous Surface Heat Flux. *SAE Technical Paper 2004-01-2996*, October 2004.

[88] Miguel Torres García, Francisco José Jiménez-Espadafor Aguilar, Tomás Sánchez Lencero, and José Antonio Becerra Villanueva. A new heat release rate (HRR) law for homogeneous charge compression ignition (HCCI) combustion mode. *Applied Thermal Engineering*, 29(17-18): 3654–3662, December 2009.

[89] H.S. S Soyhan, H. Yasar, H. Walmsley, B. Head, G.T. Kalghatgi, and C. Sorusbay. Evaluation of heat transfer correlations for HCCI engine modeling. *Applied Thermal Engineering*, 29(2-3):541–549, February 2009.

[90] Morteza Fathi, R. Khoshbakhti Saray, and M. David Checkel. Detailed approach for apparent heat release analysis in HCCI engines. *Fuel*, 89 (9):2323–2330, September 2010.

[91] Stijn Broekaert, Thomas De Cuyper, Michel De Paepe, and Sebastian Verhelst. Assessment of Empirical Heat Transfer Models for a CFR Engine Operated in HCCI Mode. *SAE Technical Paper 2015-01-1750*, 2015.

[92] Per Tunestål. Self-tuning gross heat release computation for internal combustion engines. *Control Engineering Practice*, 17(4):518–524, April 2009.

[93] Magnus Sjöberg and John E Dec. An Investigation of the Relationship Between Measured Intake Temperature, BDC Temperature, and Combustion Phasing for Premixed and DI HCCI Engines. *SAE Technical Paper 2004-01-1900*, 113(4):1271–1286, 2004.

[94] J. M. Desantes, J. Galindo, C. Guardiola, and V. Dolz. Air mass flow estimation in turbocharged diesel engines from in-cylinder pressure measurement. *Experimental Thermal and Fluid Science*, 34(1):37–47, 2010.

[95] Ivan Arsie, Rocco Di Leo, Cesare Pianese, and Matteo De Cesare. Estimation of in-cylinder mass and AFR by cylinder pressure measurement in automotive Diesel engines. In *19th World Congress of the International Federation of Automatic Control*, Cape Town, South Africa, 2014.

[96] José Manuel Luján, Carlos Guardiola, Benjamín Pla, and Pau Bares. Estimation of trapped mass by in-cylinder pressure resonance in HCCI engines. *Mechanical Systems and Signal Processing*, pages 1–13, 2015.

[97] Alberto Broatch, Carlos Guardiola, Benjamín Pla, and Pau Bares. A direct transform for determining the trapped mass on an internal combustion engine based on the in-cylinder pressure resonance phenomenon. *Mechanical Systems and Signal Processing*, 62-63:480–489, 2015.

[98] C S Draper. The physical effects of detonation in a closed cylindrical chamber. Technical report, NACA, 1935.

[99] K. Stricker, L. Kocher, E. Koeberlein, D. Van Alstine, and G. M. Shaver. Estimation of effective compression ratio for engines utilizing flexible intake valve actuation. *Proceedings of the Institution of Mechanical Engineers, Part D: Journal of Automobile Engineering*, 226(8):1001–1015, August 2012.

[100] Adrian Irimescu, Cinzia Tornatore, Luca Marchitto, and Simona Silvia Merola. Compression ratio and blow-by rates estimation based on motored pressure trace analysis for an optical spark ignition engine. *Applied Thermal Engineering*, 61(2):101–109, November 2013.

[101] E. Abdi Aghdam and M.M. Kabir. Validation of a blowby model using experimental results in motoring condition with the change of compression ratio and engine speed. *Experimental Thermal and Fluid Science*, 34(2):197–209, February 2010.

[102] Marcus Klein, Lars Eriksson, Jan Å slund, and Jan Ã. . . slund. Compression ratio estimation based on cylinder pressure data. *Control Engineering Practice*, 14(3):197 – 211, March 2006.

[103] Michael F. J. Brunt and Andrew L. Emtage. Evaluation of IMEP Routines and Analysis Errors. *SAE Technical Paper 960609*, February 1996.

[104] Hanbao Chang, Yusheng Zhang, and Lingen Chen. An applied thermodynamic method for correction of TDC in the indicator diagram and its experimental confirmation. *Applied Thermal Engineering*, 25(5-6):759–768, April 2005.

[105] Emiliano Pipitone and Alberto Beccari. Determination of TDC in internal combustion engines by a newly developed thermodynamic approach. *Applied Thermal Engineering*, 30(14-15):1914–1926, October 2010.

[106] Emiliano Pipitone, Alberto Beccari, and Stefano Beccari. Reliable TDC position determination: a comparison of different thermodynamic methods through experimental data and simulations. *SAE Technical Paper 2008-36-0059*, October 2008.

[107] Mohand Tazerout, Olivier Le Corre, and S Rousseau. TDC Determination in IC Engines Based on the Thermodynamic Analysis of the Temperature-Entropy Diagram. *SAE Technical Paper 1999-01-1489*, 108 (4):936–945, May 1999.

[108] Per Tunestål. TDC Offset Estimation from Motored Cylinder Pressure Data based on Heat Release Shaping. *Oil & Gas Science and Technology - Revue d'IFP Energies nouvelles*, 66(4):705–716, October 2011.

[109] Per Tunestål. *Estimation of the in-cylinder air/fuel ratio of an internal combustion engine by the use of pressure sensors.* Dissertation (monograph), Lund Institute of Technology, 2001.

[110] Kangyoon Lee, Maru Yoon, and Myoungho Sunwoo. A study on pegging methods for noisy cylinder pressure signal. *Control Engineering Practice*, 16(8):922–929, August 2008.

[111] Rakesh Kumar Maurya, Dev Datt Pal, and Avinash Kumar Agarwal. Digital signal processing of cylinder pressure data for combustion diagnostics of HCCI engine. *Mechanical Systems and Signal Processing*, 36 (1):95–109, March 2013.

[112] F. Payri, P. Olmeda, C. Guardiola, and J. Martín. Adaptive determination of cut-off frequencies for filtering the in-cylinder pressure in diesel engines combustion analysis. *Applied Thermal Engineering*, 31(14-15): 2869–2876, October 2011.

[113] Juan J. Hernandez, Clara Serrano, Javier Perez, Avenida Camilo Jose, S N Cela, and Ciudad Real. Prediction of the Autoignition Delay Time of Producer Gas from Biomass Gasification. *Energy & Fuels*, 20(2):532–539, March 2006.

[114] O Stenlåå s, M Christensen, R Egnell, P Tunestå l, Bengt Johansson, and F. Mauss. Reformed Methanol Gas as Homogeneous Charge Compression Ignition Engine Fuel. In *SAE Technical Paper 2004-01-2991*, number 724, October 2004.

[115] R Lanzafame. Water Injection Effects In A Single-Cylinder CFR Engine. *SAE Technical Paper 1999-01-0568*, March 1999.

[116] Chunshan Li and Kenzi Suzuki. Tar property, analysis, reforming mechanism and model for biomass gasification—An overview. *Renewable and Sustainable Energy Reviews*, 13(3):594–604, April 2009.

[117] Subir Bhaduri, Hervé Jeanmart, Ernst Breuer, and Francesco Contino. Studies of EGR in Biomass Syngas fueled tar tolerant HCCI engines. In *Ninth Mediterranean Combustion Symposium*, Rhodes, Greece, 2015.

[118] Hua Zhao, Z. Peng, J. Williams, and N. Ladommatos. Understanding the Effects of Recycled Burnt Gases on the Controlled Autoignition (CAI) Combustion in Four-Stroke Gasoline Engines. *SAE Technical Paper 2001-01-3607*, September 2001.

[119] Rui Chen and Nesa Milovanovic. A computational study into the effect of exhaust gas recycling on homogeneous charge compression ignition combustion in internal combustion engines fuelled with methane. *International Journal of Thermal Sciences*, 41(9):805–813, July 2002.

[120] Magnus Sjöberg and John E. Dec. Effects of EGR and its constituents on HCCI autoignition of ethanol. *Proceedings of the Combustion Institute*, 33(2):3031–3038, January 2011.

[121] Jan-Ola Olsson, Per Tunestå l, and Bengt Johansson. Closed-Loop Control of an HCCI Engine. *SAE Technical Paper 2001-01-1031*, (724), March 2001.

[122] Darko Kozarac, David Vuilleumier, Samveg Saxena, and Robert W. Dibble. Analysis of benefits of using internal exhaust gas recirculation in biogas-fueled HCCI engines. *Energy Conversion and Management*, 87 (x):1186–1194, May 2014.

[123] Hatim Machrafi, Simeon Cavadias, and Philippe Guibert. An experimental and numerical investigation on the influence of external gas recirculation on the HCCI autoignition process in an engine: Thermal, diluting, and chemical effects. *Combustion and Flame*, 155(3):476–489, November 2008.

[124] Martin Müller. General air fuel ratio and EGR definitions and their calculation from emissions. *SAE Technical Paper 2010-01-1285*, 2010.

[125] Hatim Machrafi and Simeon Cavadiasa. An experimental and numerical analysis of the influence of the inlet temperature, equivalence ratio and compression ratio on the HCCI auto-ignition process of Primary Reference Fuels in an engine. *Fuel Processing Technology*, 89(11):1218–1226, November 2008.

[126] Hervé Jeanmart, F Bourgois, A Bacq, and X Kuborn. Impact of the pyrolysis quality on the tar concentration of in the syngas. In *16th European Biomass Conference & Exhibition - Proceedings*, pages 1–6, Valencia,Italy, June 2008. ETA-Florence Renewable Energies.

[127] Benjamin Berger, Alexandre Bacq, Hervé Jeanmart, and Frédéric Bourgois. Experimental Investigation on the Gasification of Creosoted Wood Using a Two-Stage Gasifier. In *19th European Biomass Conference and Exhibition*, pages 899 – 906, Berlin, Germany, 2011.

[128] Benjamin Berger and C Peregrina. Experimental investigation of sewage sludge gasification using a two-stage fixed bed downdraft gasifier. In *Fourth International Symposium on Energy from Biomass and Waste*, Venice, 2012.

[129] Bipm.org and Http://www.bipm.org. Evaluation of measurement data – Guide to the expression of uncertainty in measurement. Technical Report September, bipm, 2008.

Appendix A

Schematic of LabVIEW codes

LabVIEW is a visual programming language where different modules, data and functions are linked through virtual wires and each object is graphically represented, similar to an electronic circuit board. In the present implementation the programs for the CompactRIO RTOS controller as well as the FPGA codes are developed in LabVIEW and special Labview softwares convert these programs into respective machine language codes. The IO modules are directly interfaced by the code as written in the FPGA, while the code for the RTOS takes care of top level computations and interactions with the human operator. The division of computation tasks between the RT system and the FPGA system is based mostly on the consideration of computing power versus the speed. The RT system can carry out complex computations such as required by any mathematical codes, while the FPGA expertises in low computation capabilities but at vastly high speeds of interfacing with the IO modules.

A.1 RTOS code

Beginning with the RTOS code, it consists of three main parts and few other supportive sections which are not discussed here for the sake of clarity. One of the most important parts is the main loop, as depicted in Figure A.2a. The main loop is responsible for interacting with the FPGA and acquiring/controlling all the slow IO parameters such as the intake pressure, temperatures, gas flow rates, emissions, etc. This acquisition section is depicted in the left most branch on the flowchart. A running average of the data is performed and the data is sent to the interface for the human operator to interpret. The interface program (see Figure A.2b) simply updates and plots trends on the human interface along with taking operator inputs such as changes in ϕ, the overall flow rate

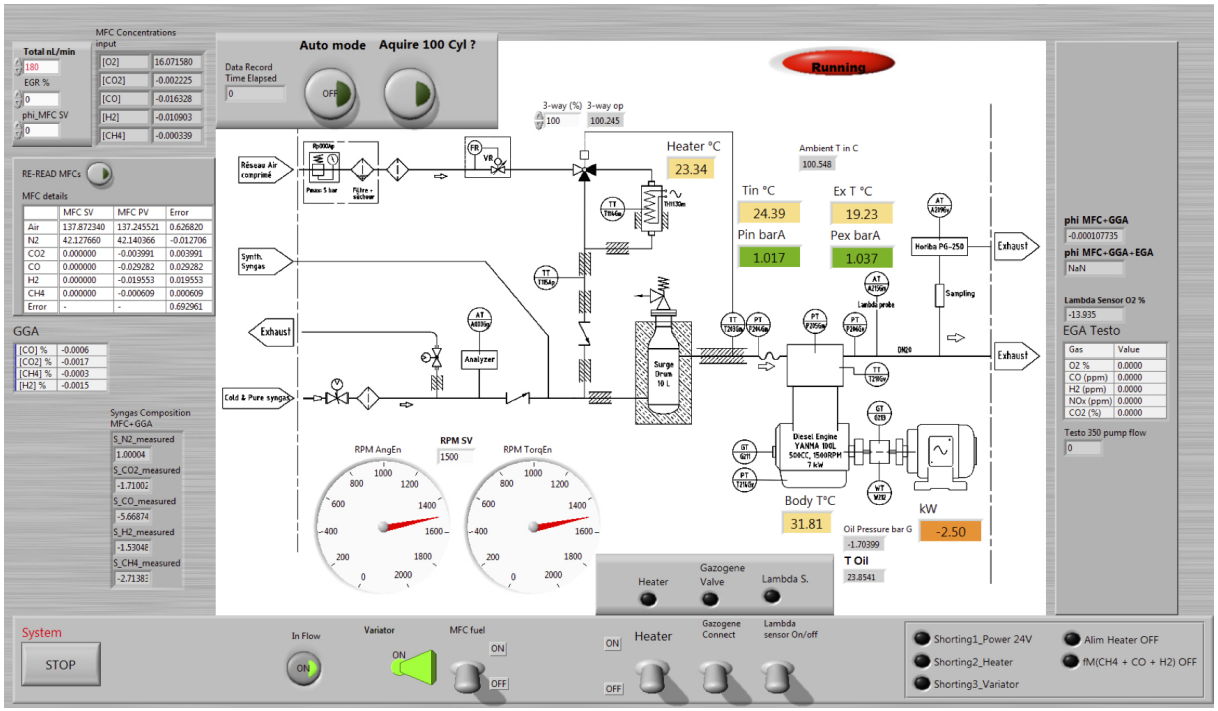


Figure A.1: *The front end LabVIEW® interface for the operator displaying all the slow acquisition data such as RPM, intake temperature and pressure, MFC measured flows, emission measurements as well as providing controls such as the total flow rate, RPM set point, equivalence ratio, and others. The interface also provides an option to record the latest 100 cycles data.*

to change the p_{in} and others. For example, a change in the user specified ϕ is used to adjust the flow rates for all the MFCs, which is relayed as a control signal back to the RT main loop. Th interface loop is called for each iteration of the main loop. The main loop reads the data sent by the interface and passes them on to the FPGA code which modulates the control instruments such as the MFCs, pumps and the RPM. The LabVIEW interface, as visible to the operator of the test bench, can be seen in Figure A.1.

The main loop also interfaces the FPGA for high speed data such as the pressure and torque measurements as depicted in the right most branch of Figure A.2a. When data is acquired by the FPGA, it is stored in a high speed First In First Out (FIFO) memory segment of the inbuilt RAM, which is accessible to the RTOS directly. Due to time efficiency achieved by data transfer in bulk form instead of as a continuous stream, it is necessary to acquire a large quantity of data and transfer it in batches. Thus, in the current implementation, the FIFO is sized to contain pressure data of five 4-stroke cycles, which amounts to 5×7200=36000 pressure data points. Since the data is synchronized with the TDC, it is necessary to ensure that during the acquisition, 5 complete cycles are acquired. Thus, in the main loop, the FIFO size is checked constantly with some delay. If 5 cycles are found to be available, the data is downloaded from the FIFO of the FPGA in to the RAM of the RTOS. Once in the RTOS, the data is split into two copies, the first one is reduced in resolution from 7200 points/cycle to 720 points/cycle and sent to a plotting program for the live displace of the pressure cycles on the human interface. The other copy is used to replace 5 oldest cycles from a 100 cycle pre-initialized array of pressure data which assures that the latest 100 cycles are always readily available. Finally, when the human operator finds the slow as well as the fast data are satisfactory, a download of all the data is initiated from the memory in to the internal storage of the RTOS.

A.2 FPGA codes

The FPGA has three main parts of the code. A slow interaction and communication section, a Crank Angle Encoder (CAE) section which gives vital synchronization outputs and finally the fast cycle sampling section which reads the pressure or torque data as per the triggers supplied by the CAE section.

In Figure A.3a, the CAE section is shown. The CAE produces three outputs as discussed in previous section, A, B and Z. In the current system the signal A is used as the trigger, while B is used to check the direction of rotation. If the direction is OK and the signal A has a RiSing Edge (RSE), then a tick is broadcast or announced. For such a crucial announcement such as the synchronization of signals, something called 'occurrences' are used in this implementation which is a crucial information to be mentioned in the context of LabVIEW. Occurrences are special LabVIEW constructs that have the ability

to communicate between while loops, something like a 'global variable' used in the programming languages. Occurrences avoid the need to use the resource intensive polling method of checking if an update is available. Once the correct direction is checked by the reception of an occurrence signal, the time delay between the pulses are recorded and is used to determine the RPM of the shaft. As for the channel Z, it is first necessary to identify between the two RSE signals corresponding to the two revolutions of the shaft for each 4-stroke cycle. After the right Z signal is identified, it is broadcast, thus terminating a cycle.

The pressure acquisition loop is shown in Figure A.3b. Here the occurrence of a TDC signal (signal Z) is waited for before the loop can begin. Once the TDC occurs, it happens such that the CAD signal from channel A is also available and the first pressure data is recorded from the voltage of the Charge Amplifier. This data point is passed on to the FIFO and the system then waits for next 'tick' from the channel A. This carries on until 7200 points are received after which the loop terminates completing the acquisition of a single 4-stroke cycle. Such a pressure loop is repeated for 5 cycles after which the FIFO data is transfered to the RTOS which also empties the FIFO and the acquisition of the next 5 cycles begin.

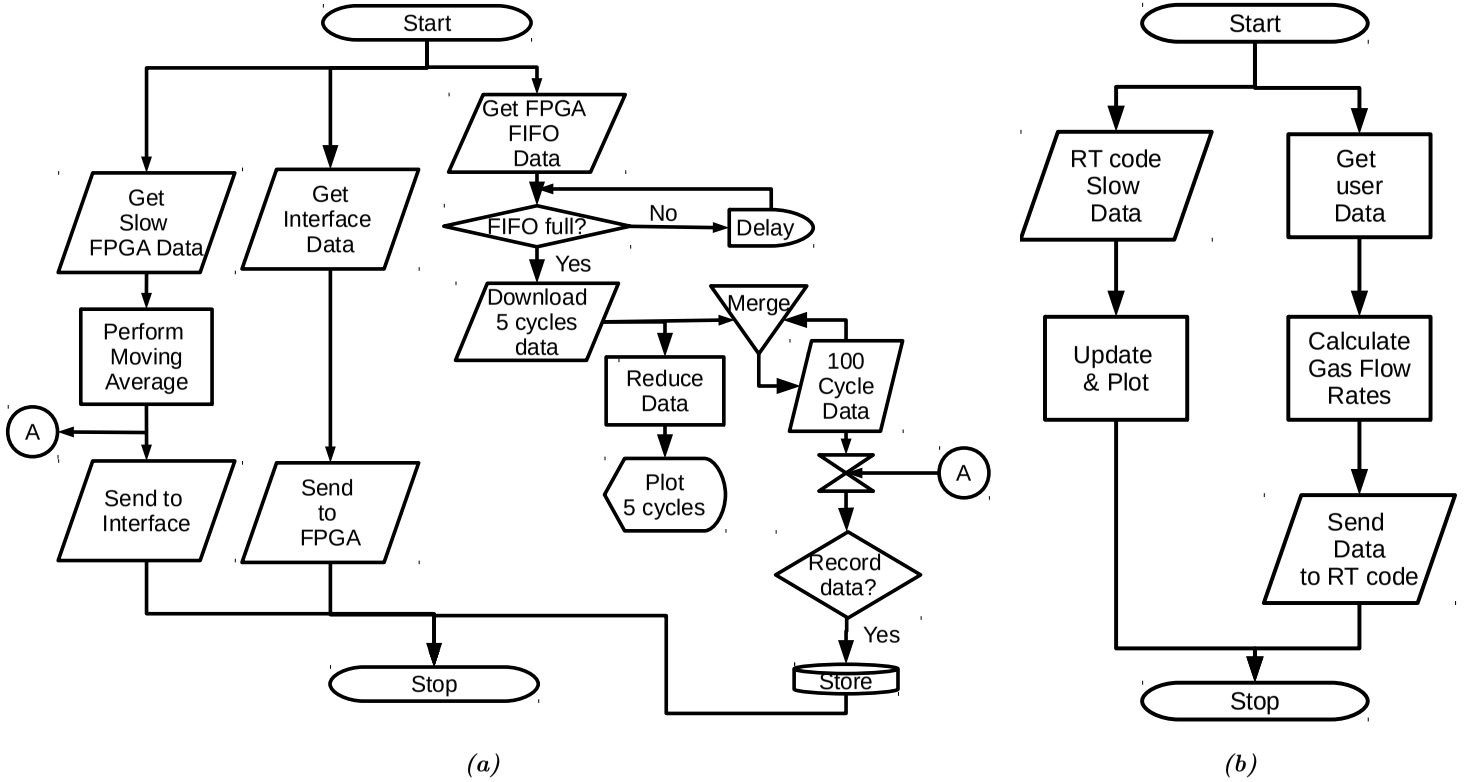


Figure A.2: *(a)The main RTOS loop that has three main acquisitions. The extreme left branch indicates the slow data path which acquires data such as the intake and exhaust pressures, various temperatures, MFC values and emission data and others. The middle branch is responsible for getting the operator controls and transferring them the FPGA for their final execution. The last branch is responsible for the continuous acquisition of in-cylinder pressure data and display the data on the interface. (b) The user interface LabVIEW loop.*

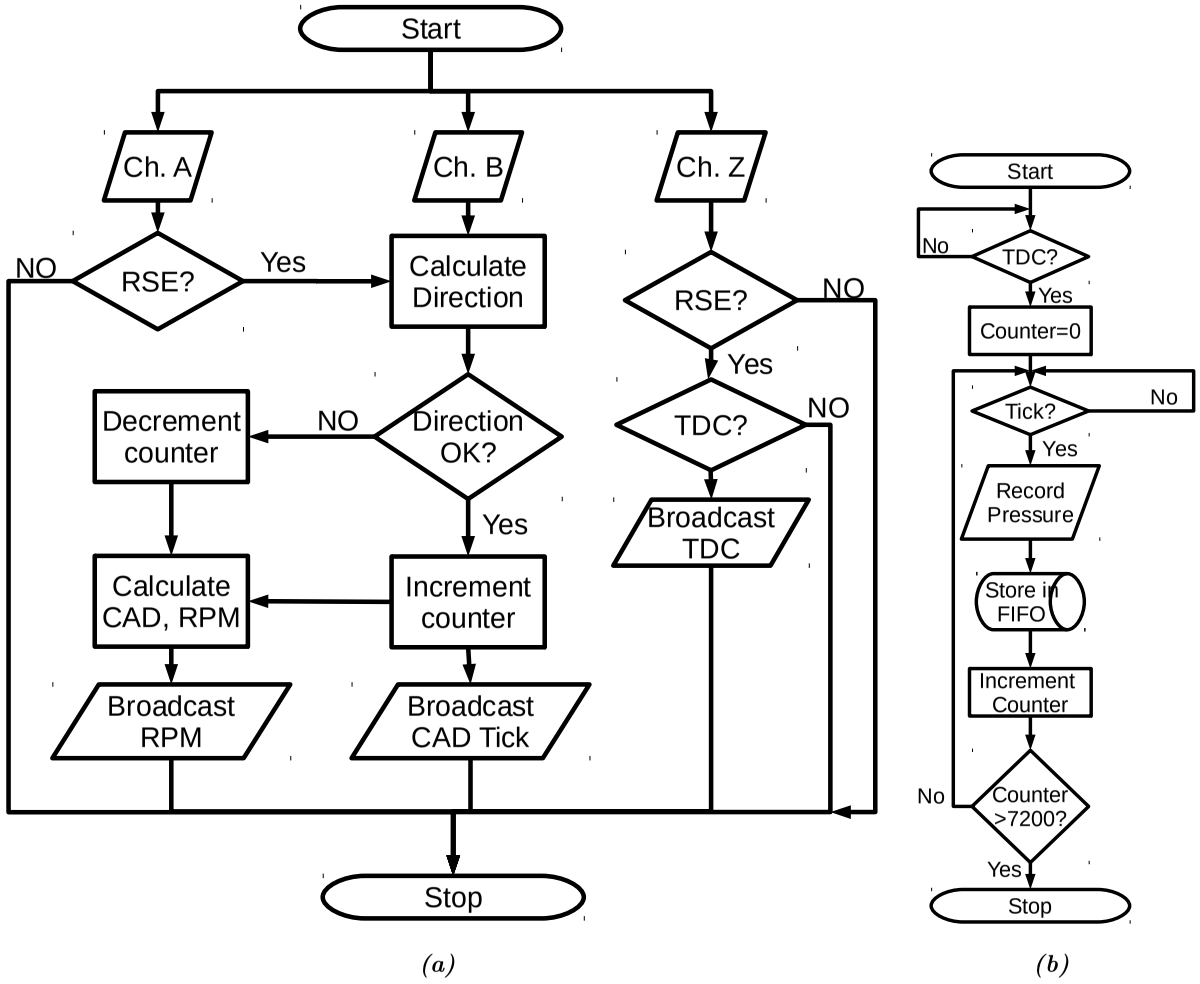


Figure A.3: *(a)A schematic of the rotary encoder loop implemented at the FPGA level which interfaces with the 3 digital channels to detect a change in the CAD, to identify the direction of rotation and the absolute current position of the shaft in terms of the CAD. (b) A schematic depicting the pressure acquisition process implemented at the FPGA level.*

Appendix B

Uncertainty formulations

The uncertainty '$U_{x,p}$' of a measured or a calculated parameter 'x' is the region of $\pm U$ around the nominal value, $x_{nominal}$, where if repeated measurements are carried out, the outcomes would lie within this region with a probability of p. In other words, $\pm U_{x,95}$ means that if 100 measurements of x were made in similar conditions, 95 of those measured values would lie within $\pm U$ of $x_{nominal}$. According to the *Guidelines to Uncertainty Measurement* (GUM) [129] the uncertainty analysis must be carried out with the base of one standard deviation. The uncertainty can be estimated in two ways, Type A and Type B. Type A uncertainty assessment is based on drawing a random sample from an entire population of possible measurements and its subsequent analysis. On the other hand, Type B uncertainty analysis are made from specified tolerance limits obtained from manufacturer datasheets which in themselves can be thought to have originated from Type A assessments carried out by the manufacturer. Finally, to obtain the uncertainty of parameters derived from instrument level parameters, the respective uncertainties are combined together which is termed as *propagation of uncertainties*.

The sections below first discuss the uncertainty in the instruments which are Type B uncertainties obtained from the respective manufacturer datasheets. The in-cylinder pressure is acquired for 100 consecutive cycles and thus the mean pressure can be treated with a Type A uncertainty analysis combined with the Type B of the pressure measurement system. Finally when all the fundamental uncertainties are recovered, they are combined together to evaluate the uncertainties of the derived parameters (refer to Figure 3.15).

B.1 Uncertainties from the MFC and EGA

The MFCs control the flow of gases into the system and the mass and volume flow rates can be expressed as:

$$\dot{m} = \sum_{x}^{allMFCs} \dot{m}_x \quad \text{and} \quad \dot{V} = \sum_{x}^{allMFCs} \dot{V}_x \tag{B.1}$$

The uncertainty in the flow rates can be written as:

$$u_{\dot{m}} = \sqrt{\sum_{x}^{allMFCs} u_{\dot{m},x}^2} \quad \text{and} \quad u_{\dot{V}} = \sqrt{\sum_{x}^{allMFCs} u_{\dot{V},x}^2} \tag{B.2}$$

For each MFC_x the uncertainties emerge from various sources such as repeatibility, temperature effect, linearity and so on which are listed with upper and lower bounds in the datasheet. As discussed in previous section, the final uncertainty is derived as:

$$u_x = \sqrt{u_{accuracy}^2 + u_{repeatability}^2 + u_{\text{T effect on zero}}^2 + u_{\text{T effect on Span}}^2} \tag{B.3}$$

with each uncertainty source (repeatibility, accuracy, etc) derived as

$$u_{source} = \frac{\pm L_{source}}{\sqrt{3}} \tag{B.4}$$

A similar treatment can be used to determine the uncertainties of the exhaust gas analyser (EGA).

B.2 Uncertainties in the Balanced Chemical Equation

Uncertainties in the BCE and the subsequent parameters such as the ϕ, the ϕ_{BCE}, the LHV of the gas mixture, the fuel input to the cycle and CE are calculated in the respective chapters (Appendices C and D), due to their non-generic nature.

B.3 Uncertainty in the pressure data

Assume a very simple pressure sensing model with piezoelectric sensor 'PZT', charge amplifier, 'ChA', and 'G' as sensor gain in pC/bar. Thus:

$$p_{ChA} = p_{PZT} \cdot \frac{G_{PZT}}{G_{ChA}} \tag{B.5}$$

The output pressure from the charge amplifier (ofcourse assuming the intermediate conversions of voltage to pressure have no errors) is pegged by DC offset Δp_{peg}. Thus:

$$p_{measured} = p_{ChA} + \Delta p_{peg} \tag{B.6}$$

$$= p_{PZT} \cdot \frac{G_{PZT}}{G_{Ch}} + \Delta p_{peg} \tag{B.7}$$

Since the pressure data are acquired when trigged by the crank angle encoder, and error in the positioning of the encoder, the TDC offset error (see Section 3.3.2), is added to the pressure signal. Thus, the final data uncertainty in the pressure signal, which includes the uncertainty contributions from the amplifier, the pegging offset Δp and the TDC offset α results in:

$$p_{measured} + \epsilon_{measured} = \begin{pmatrix} (p_{PZT} + \epsilon_{PZT,linearity} \\ + \epsilon_{PZT,Tshock} + \epsilon_{PZT,Tdrift}) \\ \times \dfrac{G_{PZT} + \epsilon_{PZT,G,TSC}}{G_{ChA}} \\ + \epsilon_{ChA,linearity} + \Delta p_{peg} + \epsilon_{\Delta p,peg} \end{pmatrix} \tag{B.8}$$

Here, 'Tshock' represents the thermal shock experienced by the pressure sensor due to steep temperature changes, 'Tdrift' represents the thermal cyclic drift of the sensor while 'TSC' stands for Thermal Sensitivity Changes which occur due to the temperature at the sensing element. These sources of error act on the PZT to change its signal. The true+error signal from the PZT is converted by the charge amplifier, however the conversion has a linearity error. Finally, the pegging method adds some error, mostly coming from the uncertainty of the input pressure sensor, if it is used for pegging. Since the uncertainty in the Tunestål method for pegging, discussed in Section.

Finally, assuming $G_{PZT} = G_{ChA}$, the Eq. (B.8) can be expressed as :

$$p_{measured} + \epsilon_{measured} \approx \begin{pmatrix} p_{PZT} + \epsilon_{PZT,linearity} + \epsilon_{PZT,Tshock} \\ + \epsilon_{PZT,Tdrift} + p_{PZT} \\ + \dfrac{\epsilon_{PZT,G,TSC}}{G_{ChA}} + \epsilon_{ChA,linearity} \\ + \Delta p_{peg} + \epsilon_{\Delta p,peg} \end{pmatrix} \tag{B.9}$$

Thus, the uncertainty is:

$$u_{p,measured} = \sqrt{\begin{array}{l} u^2_{p,PZT,linearity} + u^2_{p,PZT,Tshock} + u^2_{p,PZT,Tdrift} + \\ (\dfrac{p_{PZT}}{G_{PZT}} \cdot u_{G,PZT,TSC})^2 + u^2_{ChA,linearity} + u^2_{\Delta p,peg} \end{array}} \tag{B.10}$$

Where, the uncertainties are:

$$u_{p,PZT,linearity} = \pm\frac{a_{p,PZT,linearity}}{\sqrt{3}}$$
$$u_{p,PZT,Tshock} = \pm\frac{a_{p,PZT,Tshock}}{\sqrt{3}}$$
$$u_{p,PZT,Tdrift} = \pm\frac{a_{p,PZT,Tdrift}}{\sqrt{3}}$$
$$u_{G,PZT,TSC} = \pm\frac{a_{G,PZT,TSC}}{\sqrt{3}}$$
$$u_{ChA,linearity} = \pm\frac{a_{ChA,linearity}}{\sqrt{3}}$$
$$u_{\Delta p,peg} = \pm\frac{a_{\Delta p,peg}}{\sqrt{3}}$$

Additionally, since the pressure data are acquired when trigged by the crank angle encoder, and error in the positioning of the rotary encoder (α, from Section 3.3.2) is added to the pressure signal. Thus, the final Type B uncertainty in the pressure signal can be represented in Eq. (B.11).

$$u_{p,Type\,B} = \sqrt{u^2_{p,measured} + \left(\frac{\partial p}{\partial \alpha}u_\alpha\right)^2} \tag{B.11}$$

After acquiring 100 cycles of raw pressure, averaging and filtering is carried out to produce a mean and filtered pressure signal $p_{cyl,mfp}$. Uncertainty of the Type A can be attributed to the 100 cycles sample for which the ultimate requirement is an uncertainty on the mean of the 100 cycles:

$$u_{p,Type\,A} = \sqrt{\frac{\sum(p_i - \bar{p})^2}{n(n-1)}} \tag{B.12}$$

Here, i is the cycle number with n=100. So finally, combined with the uncertainty in the raw pressure data (Eq. (B.11)), the uncertainty in the final pressure signal is:

$$u_{p,mfp} = \sqrt{u^2_{p,Type\,B} + u^2_{p,Type\,A}} \tag{B.13}$$

B.4 Volume

The uncertainty in the volume measurement comes mainly from the uncertainty in the compression ratio r_c determined in Section 3.3.1, and the finite resolution of the rotary encoder. It must be noted that the TDC error α has already been accounted for in the pressure uncertainty analysis in the last section. This is so because it is the pressure signal and its referencing which is shifted instead

of the actual volume. The crank angle θ can be expressed as:

$$\theta = \theta_{real} + \epsilon_{\theta,LC} \tag{B.14}$$

$$\therefore u_\theta = u_{\theta,LC} \tag{B.15}$$

Recalling the volume and its derivative (see Eq. (3.3) and Eq. (3.4)):

$$\begin{aligned} V(\theta) &= \frac{V_{stroke}}{r_c - 1} + \frac{V_{stroke}}{2}\left(L/r + 1 - cos(\theta) - \sqrt{(L/r)^2 - sin^2(\theta)}\right) \\ \frac{\partial V}{\partial \theta} &= V_{stroke}\frac{sin(\theta)}{2} \cdot \left(1 + \frac{cos(\theta)}{\sqrt{(L/r)^2 - sin^2(\theta)}}\right) \end{aligned} \tag{B.16}$$

The derivative volume can be converted to discrete data where it must be emphasized that the computations must be reconverted from radians to degrees appropriately. The discrete differential volumes can be expressed as:

$$\Delta V = \left[V_{stroke}\frac{sin(\theta_i)}{2} \cdot (1 + \frac{cos(\theta_i)}{\sqrt{(L/r)^2 - sin^2(\theta_i)}})\right]_{degrees} \times \delta\theta_{degrees} \tag{B.17}$$

Finally, the uncertainties in the volume involves the uncertainties in the θ as well as the uncertainty in the r_c. It can be noted that since the dV is independent of r_c so its uncertainty only depends on θ. The uncertainty in volume can be expressed as:

$$u_V = \sqrt{\left(\frac{\partial V}{\partial \theta} \cdot u_\theta\right) + \left(\frac{\partial V}{\partial r_c} \cdot u_{r_c}\right)^2} = \sqrt{\left(\frac{\partial V}{\partial \theta} \cdot u_\theta\right)^2 + \left(-\frac{V_{stroke}}{(r_c - 1)^2} \cdot u_{r_c}\right)^2} \tag{B.18}$$

While the uncertainty in the discrete differential volumes can be evaluated as:

$$\begin{aligned} u_{\Delta V} &= \frac{\partial(\Delta V)}{\partial \theta} \cdot u_\theta \\ &= \frac{V_{stroke}}{2} \cdot \left(\begin{array}{l} cos(\theta)\left(1 + \dfrac{cos(\theta)}{\sqrt{(L/r)^2 - sin^2(\theta)}}\right) \\ \\ + sin^2(\theta)\dfrac{1 - (L/r)^2}{((L/r)^2 - sin^2(\theta))^{3/2}} \end{array}\right) \delta\theta \cdot u_\theta \end{aligned} \tag{B.19}$$

B.5 Indicated Efficiency IE

The formula for gross IE, from Eq. (3.6) is re-written here :

$$IE = 100 \cdot \frac{\sum_{\theta=-180}^{180} p\Delta V}{Q_{fuel/cycle}} = 100 \sum_{\theta=-180}^{180} A(\theta) \quad \text{with} \quad A(\theta) = \frac{p(\theta)\Delta V(\theta)}{Q_{fuel/cycle}} \tag{B.20}$$

The uncertainty in A can be expressed with the sensitivities S:

$$u_A = \sqrt{\begin{array}{l}(S_p \cdot u_p)^2 + (S_{\Delta V} \cdot u_{\Delta V})^2 \\ + (S_{Q_{fuel/cycle},\theta} \cdot u_{Q_{fuel/cycle}})^2\end{array}} \tag{B.21}$$

Note that the uncertainty over the fuel, $u_{Q,fuel/cycle}$, is constant for the cycle, though the sensitivity of IE to its error is not. The sensitivities can be expressed as:

$$S_p = \frac{\partial A}{\partial p} = \frac{\Delta V}{Q_{fuel/cycle}} \tag{B.22}$$

$$S_{\Delta V} = \frac{\partial A}{\partial \Delta V} = 100 \frac{p}{Q_{fuel/cycle}} \tag{B.23}$$

$$S_{Q_{fuel/cycle}} = \frac{\partial A}{\partial Q_{fuel/cycle}} = -\frac{p\Delta V}{Q^2_{fuel/cycle}} \tag{B.24}$$

Thus the final uncertainty in IE is:

$$u_{IE} = 100 \sqrt{\sum_{\theta=-180}^{180} u^2_{A(\theta)}} \tag{B.25}$$

B.6 IMEP

The equation for IMEP can be recalled From Eq. (3.8):

$$IMEP = \sum_{\theta=-180}^{180} \frac{P(\theta)\Delta V(\theta)}{V_{stroke}} = \sum_{\theta=-180}^{180} A(\theta) \tag{B.26}$$

The uncertainty in term $A(\theta)$ can be written as:

$$u_A = \sqrt{\left(\frac{\partial A}{\partial p}u_p\right)^2 + \left(\frac{\partial A}{\partial \Delta V}u_{\Delta V}\right)^2 + \left(\frac{\partial A}{\partial V_{stroke}}u_{V_{stroke}}\right)^2} \tag{B.27}$$

$$= \sqrt{\begin{array}{l}(\Delta V_i \cdot u_{p,i})^2 + (p_i \cdot u_{\Delta V,i})^2 \\ + \left(\frac{A}{V_{stroke}}\right)^2 \cdot u^2_{V_{stroke}}\end{array}} \tag{B.28}$$

Thus, the total uncertainty in the $IMEP$ can be written as:

$$u_{IMEP} = \sqrt{\sum_{\theta=-180}^{180} u_A^2} \tag{B.29}$$

B.7 Cumulative gross heat release, Q_{net}

The uncertainty analysis of the Heat release computation procedure assumes that the uncertainties over the gas temperatures, the γ, as well as the heat loss, cannot be computed and hence are excluded from the following analysis. The RoHR equation Eq. (3.27) is recalled here as a function of the ratio of specific heat γ, pressure p and volume V. For the sake of clarity, the subscript θ has been dropped.

$$\frac{dQ_\theta}{d\theta} = \frac{\gamma_\theta}{\gamma_\theta - 1}p_\theta\frac{dV_\theta}{d\theta} + \frac{1}{\gamma_\theta - 1}V\frac{dp_\theta}{d\theta} \tag{B.30}$$

In order to avoid noise due to differentiation of p_θ, the following simplification is used:

$$\frac{d(p_\theta V_\theta)}{d\theta} = p_\theta\frac{dV_\theta}{d\theta} + V_\theta\frac{dp_\theta}{d\theta} \tag{B.31}$$

$$\text{Thus} \quad \frac{dQ_\theta}{d\theta} = \frac{1}{\gamma_\theta - 1}\frac{d(p_\theta V_\theta)}{d\theta} + p_\theta\frac{dV_\theta}{d\theta} \tag{B.32}$$

Due to discrete data, the heat release Q_θ must be evaluated in terms of finite sums, i.e.

$$\Delta Q_\theta = \frac{1}{\gamma_\theta - 1}\Delta(p_\theta V_\theta) + p_\theta \Delta V_\theta \tag{B.33}$$

Therefore, the Q_θ at a certain point between the $SOC \leq j \leq EOC$ can be written as:

$$Q_\theta = \sum_{\theta=SOC}^{j} \Delta Q_\theta$$
$$\text{And} \quad u_{Q_\theta} = \sqrt{\sum_{\theta=SOC}^{j} u^2_{\Delta Q_\theta}} \tag{B.34}$$

Where...

$$u^2_{\Delta Q_\theta} = (\frac{1}{\gamma_\theta - 1} u_{\Delta(p_\theta V_\theta)})^2 + (p_\theta \cdot u_{\Delta V_\theta})^2 + (\Delta V_\theta \cdot u_{p_\theta})^2 \tag{B.35}$$

$$u^2_{\Delta(p_\theta V_\theta)} = \frac{1}{4}\left[\begin{matrix}(V_{\theta+\delta\theta} \cdot u_{p_{\theta+\delta\theta}})^2 + (p_{\theta+\delta\theta} \cdot u_{V_{\theta+\delta\theta}})^2 + \\ (V_{\theta-\delta\theta} \cdot u_{p_{\theta-\delta\theta}})^2 + (p_{\theta-\delta\theta} \cdot u_{V_{\theta-\delta\theta}})^2\end{matrix}\right] \tag{B.36}$$

B.8 CA50

The CA50 is associated with the $Q50$ which is the 50% energy of the complete heat release which is calculated as:

$$Q50 = 0.5 \cdot (Q_{max} - Q_{min})$$
$$\therefore u_{Q50} = 0.5\sqrt{u^2_{Q_{max}} + u^2_{Q_{min}}} \tag{B.37}$$

Uncertainties in the Q_{max} and Q_{min} are readily obtained from the Eq. (B.34). Finally, the uncertainty in CA50 is defined as the difference between the crank angles associated with $Q50$ and $Q50 + u_{Q50}$:

$$u_{CA50} = CA_{(Q50+u_{Q50})} - CA_{CA50} \tag{B.38}$$

Two cases of cumulative gross heat release rates are plotted in Figure B.1. These cases have very different equivalence ratio (ϕ=0.34 and 0.22). Additionally, uncertainties in the heat release, computed according to Eq. B.34, and using either Type A pressure uncertainties (Eq. B.12) or the combination of Type A and Type B pressure uncertainties (Eq. B.12) have been plotted. It can be observed that the uncertainties do not change much with the equivalence ratio or with the shape of the heat release curves. The observation here is, that uncertainties calculated for fast combustion reactions, such as at higher ϕ would have small magnitudes as compared to uncertainties computed for slow combustion durations. In terms of the data presented, the U_{95} uncertainty in the CA50 for the case of $\phi = 0.22$ is about 12 CAD, where as, for the case of $\phi = 0.22$ is only about 0.8 CAD. The large difference is thus very surprising as it makes no physical sense. However, if the uncertainties in the heat release are computed taking into account only the pressure variations in the 100 cycles,

i.e. only Type A uncertainties in the pressure (from Eq. B.12), then the U_{95} uncertainties in the CA50 for ϕ of 0.34 and 0.22 reduce significantly to 0.8 CAD and 0.2 CAD, respectively. Since the heat release computation is itself based on many assumptions (evolution of burn fraction, zero dimensional heat model, etc), it would not make sense to have a rigorous estimation of the uncertainty in this parameter. Instead, Type A based heat release uncertainties have a direct relation to the variations in the 100 pressure cycles and thus can be related to.

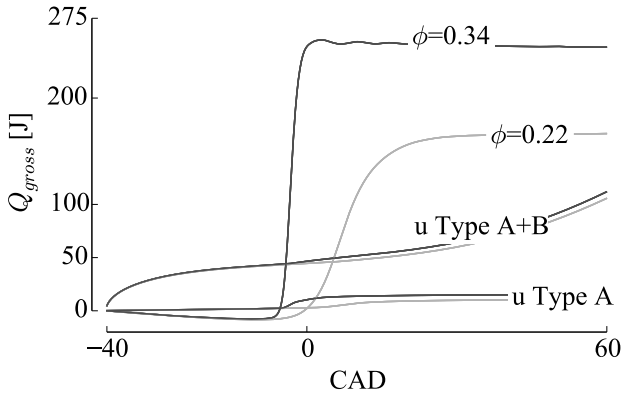


Figure B.1: *Gross cumulative heat release curves plotted for two cases,* $\phi = 0.34$ *and*$\phi = 0.22$ *along with the respective uncertainties computed from either Type A pressure uncertainties or Type A and Type B combined pressure uncertainties. The large uncertainty from Type A+B combination makes little physical sense.*

Thus, in this thesis, the values of uncertainties in the heat release related terms, CA50 and CA10, would be based on Type A pressure uncertainties.

Appendix C

BCE formulation, calibration of pumps and uncertainties for Chapter 4

C.1 General BCE formulation

THE BCE for the experiments carried out in Chapter 4 can be recalled as :

$$
\begin{aligned}
&\left(\begin{array}{l} n_{S,N_2}\,N_2 + n_{S,CO_2}\,CO_2 + n_{S,CO}\,CO \\ + n_{S,H_2}\,H_2 + n_{S,CH_4}\,CH_4 \end{array}\right)_{\text{dry syngas}} \\
&+ \left(\begin{array}{l} n_{S,C_7H_8}\,C_7H_8 \\ + n_{S,C_{10}H_8}\,C_{10}H_8 \\ + n_{S,H_2O}\,H_2O \end{array}\right)_{\text{tars and moisture}} \\
&+ \frac{1}{\phi_{BCE}}\,n_{O_2,stoic}\,(O_2 + 3.76N_2) \\
&+ RGF\left(\begin{array}{l} \overline{n_{E,H_2O}}\,H_2O + \overline{n_{E,CO_2}}\,CO_2 \\ + \overline{n_{E,O_2}}\,O_2 + \overline{n_{E,N_2}}\,N_2 \end{array}\right) \\
&\xrightarrow{combustion} \\
&\left(\begin{array}{l} n_{E,H_2O}\,H_2O + n_{E,CO_2}\,CO_2 \\ + n_{E,CO}\,CO + n_{E,O_2}\,O_2 + n_{E,N_2}\,N_2 \end{array}\right)
\end{aligned}
\tag{C.1}
$$

In this equation, as a starting point, the dry syngas quantities are known, along with the quantities of tars and the added moisture. The rest of the terms are derived as follows. With the assumption of complete combustion of a stoichiometric mixture, the stoichiometric moles of O_2 required for the syngas

content n_{syngas} can be determined as:

$$n_{O_2,stoic} = \frac{n_{S,H_2} + 4n_{S,CH_4} + n_{S,CO} + 18n_{S,C_7H_8} + 24n_{S,C_{10}H_8}}{2} \tag{C.2}$$

In order to determine the RGF terms, a modification of the Eq. (C.1) can be considered where the products of incomplete combustion as in Eq. (C.1) have been replaced by products from complete combustion in Eq. (C.3).

$$\begin{aligned}
&\begin{pmatrix} n_{S,N_2}\,N_2 + n_{S,CO_2}\,CO_2 + n_{S,CO}\,CO \\ + n_{S,H_2}\,H_2 + n_{S,CH_4}\,CH_4 \end{pmatrix}_{\text{dry syngas}} \\
&+ \begin{pmatrix} n_{S,C_7H_8}\,C_7H_8 \\ + n_{S,C_{10}H_8}\,C_{10}H_8 \\ + n_{S,H_2O}\,H_2O \end{pmatrix}_{\text{tars and moisture}} \\
&+ \frac{1}{\phi}\,n_{O_2,stoic}\,(O_2 + 3.76N_2) \\
&+ RGF \begin{pmatrix} \overline{n_{E,H_2O}}\,H_2O + \overline{n_{E,CO_2}}\,CO_2 \\ + \overline{n_{E,O_2}}\,O_2 + \overline{n_{E,N_2}}\,N_2 \end{pmatrix} \\
&\xrightarrow{\text{complete combustion}} \\
&\qquad \begin{pmatrix} \overline{n_{E,H_2O}}\,H_2O + \overline{n_{E,CO_2}}\,CO_2 \\ + \overline{n_{E,O_2}}\,O_2 + \overline{n_{E,N_2}}\,N_2 \end{pmatrix}
\end{aligned} \tag{C.3}$$

It must be noted here that the equivalence ratio in this case is ϕ, and is computed based in the inputs of gases from the MFCs and pumps in contrast to the ϕ_{BCE} in Eq. (C.1), which is computed from solving the BCE. The resulting equalities from analysis of Eq. (C.3) are:

$$\overline{n_{E,CO_2}} = \frac{n_{S,CO_2} + n_{S,CO} + n_{S,CH_4} + 7n_{S,C_7H_8} + 10n_{S,C_10H_8}}{1 - RGF} \tag{C.4}$$

$$\overline{n_{E,H_2O}} = \frac{n_{S,H_2} + 2n_{S,CH_4} + 4n_{S,C_7H_8} + 4n_{S,C_{10}H_8} + n_{S,H_2O}}{1 - RGF} \tag{C.5}$$

$$\overline{n_{E,O_2}} = \frac{1}{1 - RGF} \cdot \left(\frac{1}{\phi_{FIN}} - 1\right) \cdot n_{O_2,stoic} \tag{C.6}$$

$$\overline{n_{E,N_2}} = \frac{n_{S,N_2} + \frac{1}{\phi_{FIN}} n_{O_2,stoic} \cdot 3.76}{1 - RGF} \tag{C.7}$$

Thus, the products of complete combustion can be computed with knowledge of only the intake side. The Exhaust Gas Analyzer (EGA) measures the concentrations of emissions on a dry basis. Thus the total dry moles on the product side of the BCE of Eq. (C.1), $n_{total,p,dry}$, needs to be established for converting

the emission concentrations (of the form $[x]$) into moles. This is derived as:

$$n_{total,p,dry} = \frac{1}{1 - RGF} \cdot \frac{\begin{pmatrix} n_{S,CO_2} + n_{S,CO} + n_{S,CH_4} + \\ 7n_{S,C_7H_8} + 10n_{S,C_{10}H_8} \end{pmatrix}}{[CO_2] + [CO]} \tag{C.8}$$

Thus, the experimentally determined exhaust components including the CO emissions, in contrast to the RGF components (see Eq. (C.4) and Eq. (C.6)), can be computed as:

$$n_{E,CO_2} = n_{total,p,dry} \cdot [CO_2] \tag{C.9}$$
$$n_{E,O_2} = n_{total,p,dry} \cdot [O_2] \tag{C.10}$$
$$n_{E,CO} = n_{total,p,dry} \cdot [CO] \tag{C.11}$$
$$n_{E,N_2} = n_{total,p,dry} \cdot (1 - [CO] - [O_2] - [CO_2]) \tag{C.12}$$

The last equality assumes that the dry sample is constituted only of O_2, CO_2, CO and N_2. Further, the water content of the exhaust gases can not be measured by the existing EGA and thus has to be estimated from the BCE while also incorporating the water trapped as RGF:

$$n_{E,H_2O} = \begin{pmatrix} n_{S,H_2} + 2n_{S,CH_4} + 4n_{S,C_7H_8} + 4n_{S,C_{10}H_8} \\ + n_{S,H_2O} + RGF \cdot \overline{n_{E,H_2O}} \end{pmatrix} \tag{C.13}$$

$$= \frac{1}{1 - RGF} \cdot \begin{pmatrix} n_{S,H_2} + 2n_{S,CH_4} \\ + 4n_{S,C_7H_8} + 4n_{S,C_{10}H_8} \\ + n_{S,H_2O} \end{pmatrix} \tag{C.14}$$

Finally, the ϕ_{BCE} is evaluated:

$$\frac{1}{\phi_{BCE}} = \frac{\begin{pmatrix} n_{E,H_2O} + 2n_{E,CO_2} + n_{E,CO} + 2n_{E,O_2} \\ RGF(\overline{n_{E,H_2O}} + 2\overline{n_{E,CO_2}} + 2\overline{n_{E,O_2}}) \\ - 2n_{S,CO_2} - n_{S,CO} - n_{S,H_2O} \end{pmatrix}}{2 \cdot n_{O_2,stoic}} \tag{C.15}$$

It must be noted here that an additional term estimating the $n_{E,N2}$ can be obtained from the analysis of N_2 in the BCE Eq. C.1

$$n_{E,N_2,BCE} = \frac{1}{1 - RGF} \cdot \left(n_{S,N_2} + \frac{1}{\phi_{BCE}} n_{O_2,stoic} \cdot 3.76 \right) \tag{C.16}$$

The $n_{E,N_2,BCE}$ is not a measured quantity but is inferred from the reactants side of the BCE. Thus, the Eq. (C.12) and (C.16) can be compared to obtain

a *Compatibility* equation which ideally should be equal to 1. Thus:

$$\text{Compatibility}_{EGA/BCE} = \frac{n_{E,N_2}}{n_{E,N_2,BCE}} \tag{C.17}$$

Additionally, another n_{E,N_2} can be arrived which has been previously computed as the $\overline{n_{E,N_2}}$. Since the N2 does not undergo combustion, ideally $n_{E,N_2} = \overline{n_{E,N_2}}$. And thus, another compatibility equation can be written:

$$\text{Compatibility}_{intake/BCE} = \frac{\overline{n_{E,N_2}}}{n_{E,N_2,BCE}} \tag{C.18}$$

Due to experimental irregularities, the compatibility values are often lower or higher than 1. Based on these formulations, the molar fractions of reactants and products can be evaluated, which are necessary for the calculation of the ratio of specific heat, γ (see Section. 3.2.1). Also the ϕ_{BCE} and the Compatibility values help in detecting flaws in the process chain by evaluating how they compare with the ϕ (Eq. (3.12)) and 1, respectively.

C.2 Calibration of Syringe and Peristaltic Pumps

C.2.1 Syringe Pump

The syringe pump consists of a 4-step stepper linear motor and a 10 ml syringe (Hamilton Gastight 1010, 10 ml) syringe. The procedure is as follows:

1. The syringe had 5 divisions/ml, and therefore the least count LC=0.2 ml.
2. The syringe pump delivered a volume rate flow $\dot{V}$ (in ml/min) based on the time interval set up between the 4-step stepper motor, T_{step} (in ms).
3. At each value of T_{step}, for a fixed time Δt, a volume ΔV was measured. Such steps were repeated for 4 times, and also for various T_{step} values. The data is reported in Table C.1 and is plotted in Figure C.1.
4. The trend lines in Figure C.1 follow the power function of the form

$$\dot{V} = \text{Mul} \cdot T_{step}^{\text{Exp}}$$

5. The following procedure was used to determine a model for the pump, using the spreadsheets software *LibreOffice Calc* and its functions SLOPE, and INTERCEPT.
6. A logarithm of the power function on both sides results in a linear equation:

$$\begin{aligned} log(\dot{V}) &= log(\text{Mul}) + \text{Exp} \cdot log(T_{step}) \\ \therefore log(\dot{V}) &= \text{INTERCEPT} + \text{SLOPE} \cdot log(T_{step}) \end{aligned} \tag{C.19}$$

Thus...

$$\text{Mul} = e^{\text{INTERCEPT}} \tag{C.20}$$

$$\text{Exp} = \text{SLOPE} \tag{C.21}$$

7. The resulting model data from this analysis is expressed in Table C.2. The analytical form or the model for syring pump is thus:

$$\dot{V}_{ml/min} = 312.53 \cdot T_{step,ms}^{-1.033}$$

8. Based on this model the flow of tars can be determined, using the respective molecular weight M_{tars} and density ρ_{tars} of the tar solution:

$$\dot{n}_{tars} = \frac{\rho_{tars}\dot{V}}{M_{tars}}$$

9. The repeatability error,Type A error or the *standard error* is less than the LC. It is calculated by the following formula where $\dot{V}_{i,data}$ and $\dot{V}_{i,model}$ are the experimental data and the model data calculated for a particular T_{step} and N are the total number of readings, which in this case is 20. The degrees of freedom $(N-2)$ accommodates for the calculation of SLOPE and INTERCEPT which went into constructing the the model.

$$\text{Std. Error} = u_{\dot{V},repeatibility} = \sqrt{\frac{\sum_{i}^{N}(\dot{V}_{i,data} - \dot{V}_{i,model})^2}{N-2}}$$

X	Y $\dot{V}_{additives}$ (ml/min)			
T_{step} (ms)	1	2	3	4
600	0.4138	0.4167	0.4211	0.4211
800	0.3243	0.3077	0.3200	0.3200
1000	0.2449	0.2400	0.2526	0.2449
1200	0.2000	0.2087	0.2000	0.2087
1400	0.1714	0.1791	0.1832	0.1714

Table C.1: *Syringe flow calibration data*

Exp	-1.033
Mul	312.53
Std. Error in $\dot{V} = u_{\dot{V},TypeA}$	0.006
$U_{95,\dot{V},TypeA}$ (ml/min)	0.012

Table C.2: *Syringe pump Coefficients and their uncertainty from calibration experiments*

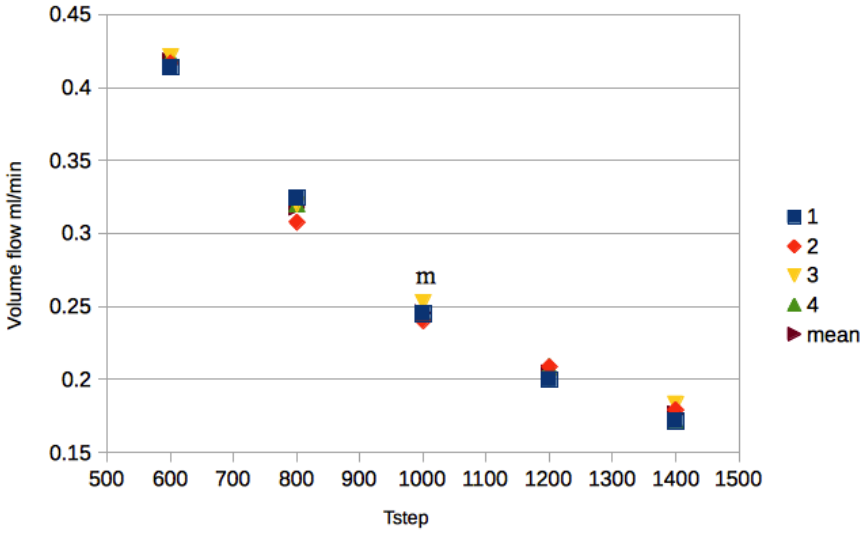


Figure C.1: *Syringe pump calibration data plotted.*

Uncertainty analysis

The uncertainty in the volume flow due to the syringe pump, $u_{\dot{V}}$, can be expressed as:

$$u_{\dot{V}} = \sqrt{u^2_{\dot{V},TypeA} + u^2_{\dot{V},Cal.}} \tag{C.22}$$

The operator error occurs during the calibration process, resulting in the calibration uncertainty $u_{\dot{V},Cal.}$. The sources of such errors are the subjective judgement of the changing volume displacement of the syring, or the error between starting and stopping the stop watch. The operator error contribution to calibration uncertainty can be assumed, based on the author's subjective guesses, as:

$$u_{\Delta V} \approx \pm(0.1 \text{ ml} + LC/\sqrt{3}) = 0.2 \text{ ml} \tag{C.23}$$

$$u_{\Delta t} \approx \pm 5s = \pm 0.083 \text{ min} \tag{C.24}$$

The $\dot{V}_{Cal.}$ are the calibration values, and they are calculated as

$$\dot{V}_{Cal.} = \frac{\Delta V}{\Delta t} \tag{C.25}$$

$$\therefore u_{\dot{V},Cal.} = \sqrt{(\frac{1}{\Delta t} \cdot u_{\Delta V})^2 + (\frac{-\Delta V}{\Delta t^2} \cdot u_{\Delta t})^2} \tag{C.26}$$

Thus based on these equations the uncertainty in the volume flow can be deduced. Thus the uncertainty in the i'th component of n component tar mixture can be written as:

$$u_{\dot{n},tars,i} = x_{\text{i in n}} \frac{\rho_{tars}}{M_{tars}} u_{\dot{V}} \tag{C.27}$$

The uncertainties in ρ and the molar fraction x are neglected.

C.2.2 Peristaltic Pump

The peristaltic pump (Sartorius Practum 2102-1s) is used for larger flow rates. The pump system and its calibration is as follows:

1. The pump is run with a known voltage v and is connected to a reservoir placed on a sensitive weighing scale.
2. Calibrations for various v are repeated recording the corresponding Δm pumped in time interval Δt. Data is presented in Table C.3 and Figure C.2, which shows a linear form

$$\dot{m} = SLOPE \cdot v + INTERCEPT$$

3. Using spreadsheet functions of SLOPE() and INTERCEPT(), the resulting data is presented in Table C.4 and the pump model can be written as:

$$\dot{m}_{g/min} = 0.48 \cdot v - 0.342$$

X	Y $\dot{m}$ in g/min		
Volt v	1	2	3
10	4.5	4.5	4.5
9	4	4	4
8	3.47	3.53	3.54
7	3	2.98	2.95
6	2.57	2.6	2.6
5	2.1	2.06	2.07

Table C.3: *Calibration data for Peristaltic pump*

The possible uncertainties encountered in this pumps are:

1. The least count in the weighing scale where the LC=0.01 g. This error contributes to the error in calibration experiments, $u_{\dot{m},Cal.}$.
2. Random errors encountered during the experiments, Type A, $u_{\dot{m},TypeA}$.
3. Operator errors during in calibration experiments adds to $u_{\dot{m},Cal.}$.
4. The following errors are neglected
   (a) Variations in the flow rate due to uneven rollers in the pump.

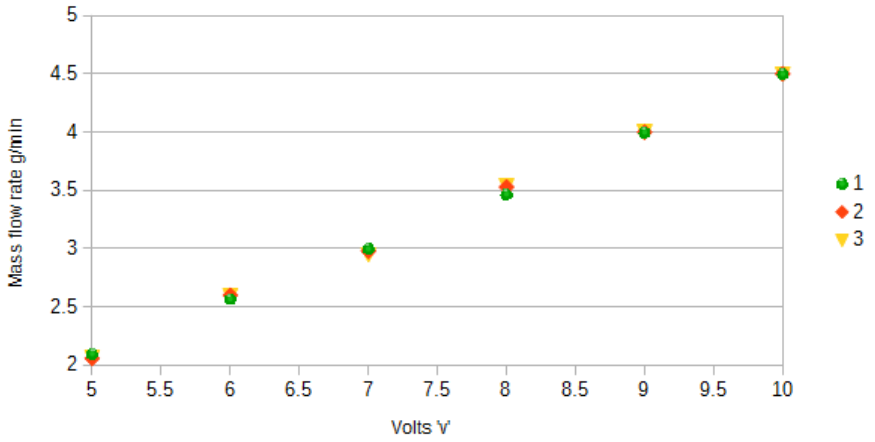


Figure C.2: *Peristaltic pump calibration data plotted.*

SLOPE	0.48
INTERCEPT	-0.342
R^2	0.998
$u_{\dot{m},TypeA}$(g/min)	0.036
$U_{95,\dot{m},TypeA}$ (g/min)	0.073

Table C.4: *Peristaltic Pump Coefficients and their uncertainty from calibration experiments*

(b) Increases in the errors caused due to reduce in the pump speed.
(c) Errors in the voltage supply.
(d) Errors due to test bench vibrations affecting the balance.

The uncertainty in the calibration errors are due to operator (as per subjective experience), as well as the least count. Thus:

$$u_{\Delta m} \approx \pm 2\% \text{ of value, for example } 5 \text{ g} + LC = 0.1 + 0.01 \text{ g} \tag{C.28}$$

$$u_{\Delta t} \approx \pm 5 \text{ s} = \pm 0.083 \text{ min} \tag{C.29}$$

During calibration, the values of $\dot{m}$ can be arrived at by using the following form:

$$\dot{m}_{Cal.} = \frac{\Delta m}{\Delta t} \tag{C.30}$$

Thus

$$u_{\dot{m},Cal.} = \sqrt{(\frac{1}{\Delta t} \cdot u_{\Delta m})^2 + (\frac{-\Delta m}{\Delta t^2} \cdot u_{\Delta t})^2} \tag{C.31}$$

Finally, the combined uncertainty in the peristaltic pump can be expressed as:

$$u_{\dot{m}} = \sqrt{u^2_{\dot{m},TypeA} + u^2_{\dot{m},Cal.}} \tag{C.32}$$

C.3 Uncertainties in the BCE

The main uncertainties of interest are related to the LHV of the intake gases, the combustion efficiency and the fuel amount heat contained in the cycle. For these values, the uncertainty in the main BCE parameters are essential. Based on the uncertainties in the MFCs and the EGA discussed in Section B.1, and the uncertainties from the pumps discussed in the previous sections, the uncertainties in the BCE can be derived:

$$u_{n,O_2,stoic} = \sqrt{\begin{matrix}(0.5\,u_{n,S,H_2})^2 + (2\,u_{n,S,CH_4})^2 + (0.5\,u_{n,S,CO})^2 \\ + (9\,u_{n,S,C7H8})^2 + (12\,u_{\dot{n},S,C10H8})^2\end{matrix}} \tag{C.33}$$

$$u_{\phi} = 4.76 \cdot \sqrt{\left(\frac{1}{n_{air}} u_{n,O_2,stoic}\right)^2 + \left(\frac{n_{O_2,stoic}}{n^2_{air}} u_{n_{air}}\right)^2} \tag{C.34}$$

$$u_{n,total,p,dry} = \sqrt{\begin{matrix}\frac{\left(\begin{matrix}u^2_{n,S,CO_2} + u^2_{n,S,CO} + u^2_{n,S,CH_4} \\ + 49u^2_{n,S,C_7H_8} + 100u^2_{\dot{n},S,C_{10}H_8}\end{matrix}\right)}{(1-RGF)([CO_2]+[CO])^2} \\ + \left(\frac{\dot{n}_{total,p,dry}}{[CO_2]+[CO]}\right)^2 \cdot (u^2_{[CO_2]} + u^2_{[CO]})\end{matrix}} \tag{C.35}$$

$$u_{n,E,CO_2} = \sqrt{([CO_2] \cdot u_{n,total,p,dry})^2 + (n_{total,p,dry} \cdot u_{[CO_2]})^2} \tag{C.36}$$

$$u_{n,E,CO} = \sqrt{([CO] \cdot u_{n,total,p,dry})^2 + (n_{total,p,dry} \cdot u_{[CO]})^2} \tag{C.37}$$

$$u_{n,E,O_2} = \sqrt{([O_2] \cdot u_{n,total,p,dry})^2 + (n_{total,p,dry} \cdot u_{[O_2]})^2} \tag{C.38}$$

$$u_{[N_2]} = \sqrt{u^2_{[O_2]} + u^2_{[CO_2]} + u^2_{[CO]}} \tag{C.39}$$

$$u_{n,E,N_2} = \sqrt{([N_2] \cdot u_{n,total,p,dry})^2 + (n_{total,p,dry} \cdot u_{[N_2]})^2} \tag{C.40}$$

$$u_{n,E,H_2O} = \frac{1}{1-RGF} \cdot \sqrt{u^2_{S,H_2} + 4u^2_{S,CH_4} + 16u^2_{S,C_7H_8} + 16u^2_{S,C_{10}H_8} + u^2_{S,H_2O}} \tag{C.41}$$

$$\tag{C.42}$$

These uncertainties can be further utilized in determining the uncertainties

in the CE and the LHV of the mixtures.

C.3.1 Heat input per cycle

Let B_x represent:

$$B_x = \frac{M_x}{1000} \cdot LHV_x \tag{C.43}$$

Where B_x is the LHV/mole of species x, with molar mass M_x in g/mol and LHV_x in Joules/kg. Thus the heat per cycle is give by:

$$Q_{fuel/cycle} = \begin{pmatrix} n_{S,CO} \cdot B_{CO} + n_{S,H_2} \cdot B_{H_2} + n_{S,CH_4} \cdot B_{CH_4} \\ + n_{S,C_7H_8} \cdot B_{C_7H_8} + n_{S,C_{10}H_8} \cdot B_{C_{10}H_8} \end{pmatrix} \tag{C.44}$$

Thus, the uncertainty is:

$$u_{Q_{fuel/cycle}} = \sqrt{\begin{array}{l} (u_{n_{S,CO}} \cdot B_{CO})^2 + (u_{n_{S,H_2}} \cdot B_{H_2})^2 + (u_{n_{S,CH_4}} \cdot B_{CH_4})^2 \\ + (u_{n_{S,C_7H_8}} \cdot B_{C_7H_8})^2 + (u_{n_{S,C_{10}H_8}} \cdot B_{C_{10}H_8})^2 \end{array}} \tag{C.45}$$

C.3.2 LHV of air+fuel mixture

The calculation of LHV and its uncertainty can be done in the context of the BCE.

$$LHV_{mix} = \frac{\sum_{x}^{LHV>0} n_x \cdot \frac{M_x}{1000} \cdot LHV_{x,MJ/kg}}{\sum_{y}^{BCE} n_y \cdot \frac{M_y}{1000}} = \frac{B}{A}$$

Therefore the uncertainty:

$$u_{LHV,mix} = \sqrt{\sum_{x}^{LHV>0} C_x^2 \cdot u_{n,x}^2 + \sum_{x}^{LHV=0} C_x^2 \cdot u_{n,x}^2} \tag{C.46}$$

Where...

$$\begin{aligned} C_{x\in[LHV>0]} &= \frac{\partial LHV_{mix}}{\partial n_x} = \frac{A \cdot \frac{M_x}{1000} \cdot LHV_x - B \cdot \frac{M_x}{1000}}{A^2} \\ C_{x\in[LHV=0]} &= \frac{\partial LHV_{mix}}{\partial \dot{n}_x} = \frac{-B \cdot \frac{M_x}{1000}}{A^2} \end{aligned} \tag{C.47}$$

C.3.3 Combustion Efficiency

Combustion efficiency is recalled from Eq. 3.19

$$CE = (1 - \frac{Q_p}{Q_r}) \cdot 100 \tag{C.48}$$

$$u_{CE} = 100 \cdot \sqrt{(-\frac{Q_p}{Q_r^2} \cdot u_{Q,r})^2 + (\frac{1}{Q_r} \cdot u_{Q,p})^2} \tag{C.49}$$

Let

$$B_{xx} = \frac{M_{xx,g/mol}}{1000} \cdot LHV_{J/kg}$$

Thus Q_p is:

$$\begin{aligned} Q_p &= n_{E,CO} \cdot B_{CO} \\ u_{Q_p} &= u_{n_{E,CO}} \cdot B_{CO} \end{aligned} \tag{C.50}$$

And, Q_r and its uncertainty is:

$$\begin{aligned} Q_r = {} & n_{S,CO} \cdot B_{CO} + n_{S,H_2} \cdot B_{H_2} + n_{S,CH_4} \cdot B_{CH_4} + \\ & n_{S,C_{10}H_8} \cdot B_{C_{10}H_8} + n_{S,C_7H_8} \cdot B_{C_7H_8} \end{aligned} \tag{C.51}$$

$$\begin{aligned} \therefore u_{Q_r} = \sqrt{} & (B_{CO} \cdot u_{n_{S,CO}})^2 + (B_{H_2} \cdot u_{n_{S,H_2}})^2 + (B_{CH_4} \cdot u_{n_{S,CH_4}})^2 + \\ & (B_{C_{10}H_8} \cdot u_{n_{S,C_{10}H_8}})^2 + (B_{C_7H_8} \cdot u_{n_{S,C_7H_8}})^2 \end{aligned} \tag{C.52}$$

Appendix D

BCE formulation for Chapter 5

D.1 Formulation of EGR : BCE assuming complete combustion

In this section, the objective is to determine the amounts of respective gases required to simulate the EGR conditions, so that flow rates for the MFCs and the pump can be specified. The BCE, with the assumption of complete combustion, is presented in Eq. (D.1). It describes the transformation of the reactants (syngas, fresh air, RGF and EGR fractions) on the right hand side into the products composed of complete combustion products (no unburnt CO) on the left hand side, during a single HCCI combustion cycle.

$$\begin{aligned}
&\underbrace{\begin{pmatrix} n_{S,N_2}\, N_2 + n_{S,CO_2}\, CO_2 + n_{S,CO}\, CO \\ + n_{S,H_2}\, H_2 + n_{S,CH_4}\, CH_4 \end{pmatrix}}_{\text{dry syngas}} \\
&+ \frac{1}{\phi_{FIN}} \cdot n_{O_2,stoic} \cdot (O_2 + 3.76 N_2) \\
&+ (EGR(1-RGF) + RGF) \begin{pmatrix} \overline{n_{E,H_2O}} H_2O + \overline{n_{E,CO_2}} CO_2 \\ + \overline{n_{E,O_2}} O_2 + \overline{n_{E,N_2}} N_2 \end{pmatrix} \\
&\xrightarrow{\text{complete combustion}} \\
&\quad \begin{pmatrix} \overline{n_{E,H_2O}} H_2O + \overline{n_{E,CO_2}} CO_2 \\ + \overline{n_{E,O_2}} O_2 + \overline{n_{E,N_2}} N_2 \end{pmatrix}
\end{aligned} \tag{D.1}$$

The analysis of Eq. (D.1) results in the following relations:

$$n_{O_2,stoic} = \frac{n_{S,H_2} + n_{S,CO} + n_{S,CH_4}}{2} \tag{D.2}$$

$$\overline{n_{E,CO_2}} = \frac{n_{S,CO_2} + n_{S,CO} + n_{S,CH_4}}{(1-EGR)(1-RGF)} \tag{D.3}$$

$$\overline{n_{E,H_2O}} = \frac{n_{S,H_2} + 2n_{S,CH_4}}{(1-EGR)(1-RGF)} \tag{D.4}$$

$$\overline{n_{E,O_2}} = \frac{1}{(1-EGR)(1-RGF)} \cdot \left(\frac{1}{\phi_{FIN}} - 1\right) \cdot n_{O_2,stoic} \tag{D.5}$$

$$\overline{n_{E,N_2}} = \frac{n_{S,N_2} + 3.76\frac{1}{\phi_{FIN}} n_{O_2,stoic}}{(1-EGR)(1-RGF)} \tag{D.6}$$

D.1.1 Specifying the inputs

To maintain the intake conditions of intake temperature T_{in} and pressure p_{in}, a fixed flow of gases n_{intake} was necessary for the experiments. It must be noted that the total moles of gases reacting within the cycle, $n_{total,r}$, is greater than the intake amount, n_{intake}, due to the trapped RGF fraction. This n_{intake} can be expressed as:

$$n_{intake} = n_{syngas} + n_{FIN,air} + n_{EGR} \tag{D.7}$$

n_{syngas} is the total syngas component, the $n_{FIN,air}$ represents the Fresh INtake amount of air and n_{EGR} represents the EGR fraction of exhaust gases. On substitution from Eq. (D.3) to Eq. (D.6), the Eq. (D.7) can be simplified further:

$$n_{intake} = n_{syngas} + n_{FIN,air} + \frac{EGR}{1-EGR}\left(n_{syngas} + n_{FIN,air} + 2n_{S,CH_4} - n_{O2,stoic}\right) \tag{D.8}$$

The syngas composition of interest is known before hand, represented by molar fractions '$x_{S,y}$' with y being any of the syngas species N_2,CO_2,CO,H_2,CH_4. Thus, utilizing the knowledge of syngas composition and the definition of ϕ_{FIN} to determine the air to fuel molar stoichiometric ratio '$AF_{n,stoic}$', further simplifications of Eq. (D.8) can be made such that:

$$n_{intake} = \frac{n_{syngas}}{1-EGR}\left(1 + \frac{AF_{n,stoic}}{\phi_{FIN}} - 0.5 \cdot EGR \cdot (x_{H_2} + x_{CO})\right) \tag{D.9}$$

Eq. D.9 can be used to determine the n_{syngas}, based on the parameters n_{intake}, ϕ_{FIN}, EGR and the syngas composition. Correspondingly the quantities n_{S,N_2}, n_{S,CO_2}, $n_{S,CO}$, n_{S,H_2} and n_{S,CH_4} can be determined.

The final intake amounts of gases per cycle of the HCCI engine gases (with

subscript *intake*), are derived next. It should be noted that the fresh component of air (subscript FIN) and the syngas components of N_2 and CO_2 (subscript S) are supplied by the same MFCs which also supply the respective EGR components (subscript EGR).

$$n_{intake,air} = n_{FIN,air} + n_{EGR,air} \tag{D.10}$$

Based on Eq. (D.1), Eq. (D.10) results in:

$$n_{intake,air} = \frac{n_{O_2,stoic} \cdot 4.762}{\phi_{FIN}} + 4.762 \cdot EGR(1 - RGF) \cdot \overline{n_{E,O_2}} \tag{D.11}$$

Note that only the fresh air (FIN) and the simulated EGR component of air are supplied from the MFCs, neglecting the trapped RGF amount. Further, using Eq. (D.5) the final amount of air intake per cycle is determined as:

$$n_{intake,air} = \frac{n_{O_2,stoic} \cdot 4.76}{1 - EGR} \cdot \left[\frac{1}{\phi_{FIN}} - EGR\right] \tag{D.12}$$

In a similar fashion the intake amounts of N_2 and CO_2 can be determined.

$$n_{intake,N_2} = n_{S,N_2} + n_{EGR,N_2} \tag{D.13}$$

$$= n_{S,N_2} + \frac{EGR}{1 - EGR}(n_{S,N_2} + 3.762 \cdot n_{O_2,stoic}) \tag{D.14}$$

$$n_{intake,CO_2} = n_{S,CO_2} + n_{EGR,CO_2} \tag{D.15}$$

$$= n_{S,CO_2} + \frac{EGR}{1 - EGR}(n_{S,CO_2} + n_{S,CO} + n_{S,CH_4}) \tag{D.16}$$

The EGR component of water is supplied by a peristaltic pump and specified as:

$$n_{intake,H_2O} = \frac{EGR}{1 - EGR}(n_{S,H_2} + 2n_{S,CH_4}) \tag{D.17}$$

The other gases do not contribute to the EGR gases and thus specifying their amounts are trivial as follows:

$$n_{intake,CO} = n_{S,CO} \tag{D.18}$$

$$n_{intake,H_2} = n_{S,H_2} \tag{D.19}$$

$$n_{intake,CH_4} = n_{S,CH_4} \tag{D.20}$$

D.1.2 Decoding data from flow measurements

Due to some inherent differences present in the specified set point values and the measured process values returned by the MFCs, the assumption of known syngas composition, ϕ_{FIN} and EGR value can not be made while trying to

determine the quantities $n_{FIN,air}$, n_{S,N_2}, n_{S,CO_2}, $n_{S,CO}$, n_{S,H_2} and n_{S,CH_4} from experimental measurement data of $n_{intake,air}$, n_{intake,N_2}, n_{intake,CO_2}, $n_{intake,CO}$, n_{intake,H_2} and n_{intake,CH_4}. Thus the following technique has been used.

The value of EGR is assumed to be an experimental constant whereas the syngas composition is assumed to have been varied by the MFCs. The first step is to formulate the relationship between parameters ϕ_{FIN} and $\phi_{FIN+EGR}$ which are linked by the EGR fraction. The overall $\phi_{FIN+EGR}$ of the gas mixture at the IVC can be determined from experimental data as expressed here:

$$\phi_{FIN+EGR} = \frac{n_{syngas}}{n_{intake,air}} \times \frac{n_{O_2,stoic} \cdot 4.762}{n_{syngas}} = \frac{n_{O_2,stoic} \cdot 4.762}{n_{intake,air}} \tag{D.21}$$

The $\phi_{FIN+EGR}$ can be determined from experimental data since the term $n_{O_2,stoic}$ is experimentally determined (see Eq. (D.2)). The ϕ_{FIN} on the other hand is unknown due to lack of knowledge about $n_{FIN,air}$ which can be expressed as:

$$\phi_{FIN} = \frac{n_{O_2,stoic} \cdot 4.762}{n_{FIN,air}} \tag{D.22}$$

Based on the equations Eq. (D.10), Eq. (D.21) and Eq. (D.22), the following combination results:

$$\begin{aligned} \phi_{FIN+EGR} &= \frac{n_{O_2,stoic} \cdot 4.76}{n_{FIN,air} + n_{EGR,air}} \\ &= \frac{n_{O_2,stoic}}{\frac{1}{\phi_{FIN}} n_{O_2,stoic} + EGR(1 - RGF) \cdot \overline{n_{E,O2}}} \end{aligned} \tag{D.23}$$

Further substitution from Eq. (D.5) results in:

$$\phi_{FIN+EGR} = \frac{1 - EGR}{\frac{1}{\phi_{FIN}} - EGR} \tag{D.24}$$

Eq. (D.24) can thus be used to determine the ϕ_{FIN}, given a value of EGR. Once ϕ_{FIN} is known, the other terms in Eq. (D.1) can be determined accordingly.

D.1.3 Formulation of the BCE with incomplete combustion

The BCE with real combustion includes the emission results from the exhaust analysis, which also includes the non-negligible amounts of unburnt CO, as presented in Eq. (D.25). The recirculation gas amounts, being determined from the assumption of complete combustion in the previous section, retain their overline markings. Also, it must be noted that the ϕ_{BCE} term has been

mentioned, rather than the ϕ_{FIN}.

$$\begin{pmatrix} n_{S,N_2}\,N_2 + n_{S,CO_2}\,CO_2 + n_{S,CO}\,CO \\ + n_{S,H_2}\,H_2 + n_{S,CH_4}\,CH_4 \end{pmatrix} + \frac{n_{O_2,stoic}}{\phi_{FIN}}(O_2 + 3.76N_2) + (EGR(1-RGF)+RGF)\begin{pmatrix} \overline{n_{E,H_2O}}H_2O + \overline{n_{E,CO_2}}CO_2 \\ + \overline{n_{E,O_2}}O_2 + \overline{n_{E,N_2}}N_2 \end{pmatrix} \xrightarrow{combustion}$$

$$n_{E,H_2O}H_2O + n_{E,CO_2}CO_2 + n_{E,CO}CO + n_{E,O_2}O_2 + n_{E,N_2}N_2 \quad \text{(D.25)}$$

Analysis of Eq. (D.25) reveals the following equalities. The first parameter, $n_{total,p,dry}$, indicates the dry moles of combustion products contained within the combustion chamber.

$$n_{total,p,dry} = \frac{1}{(1-EGR)(1-RGF)} \cdot \frac{n_{S,CO_2} + n_{S,CO} + n_{S,CH_4}}{[CO_2] + [CO]} \quad \text{(D.26)}$$

The emission concentrations, measured by the EGA, can then be used to determine the molar content of the respective products in the combustion chamber.

$$n_{E,CO_2} = n_{total,p,dry} \cdot [CO_2] \quad \text{(D.27)}$$

$$n_{E,O_2} = n_{total,p,dry} \cdot [O_2] \quad \text{(D.28)}$$

$$n_{E,CO} = n_{total,p,dry} \cdot [CO] \quad \text{(D.29)}$$

$$n_{E,N_2} = n_{total,p,dry} \cdot [N_2] \quad \text{(D.30)}$$

$$n_{E,H_2O} = \frac{1}{(1-EGR)(1-RGF)} \cdot (n_{S,H_2} + 2n_{S,CH_4}) \quad \text{(D.31)}$$

Finally, the parameter ϕ_{BCE} can be computed (Eq. (D.32)) which helps to correlate with ϕ_{FIN} in order to determine the closeness between the experimental measurements and the intake gas quantities:

$$\frac{1}{\phi_{BCE}} = \frac{\begin{pmatrix} n_{E,H_2O} + 2n_{E,CO_2} + n_{E,CO} + 2n_{E,O_2} \\ - (EGR(1-RGF)+RGF)\cdot(\overline{n_{E,H_2O}} + 2\overline{n_{E,CO_2}} + 2\overline{n_{E,O_2}}) \\ - 2n_{S,CO_2} - n_{S,CO} \end{pmatrix}}{2 \cdot n_{O_2,stoic}} \quad \text{(D.32)}$$

The determination of n_{E,N_2} from experiments (Eq. (D.30)) must match the value determined from the from the BCE, presented in Eq. (D.33). This *Com-*

patibility is measured in Eq. (D.34).

$$n_{E,N_2,BCE} = \frac{n_{S,N_2}}{(1-EGR)(1-RGF)} + 3.76 \cdot n_{O_2,stoic}\left[\frac{1}{\phi_{BCE}} + \frac{(EGR(1-RGF)+RGF)}{(1-EGR)(1-RGF)}\frac{1}{\phi_{FIN}}\right] \tag{D.33}$$

$$Compatibility = \frac{n_{E,N_2}}{n_{E,N_2,BCE}} \tag{D.34}$$

D.2 Uncertainties in the BCE

Uncertainties computed for the BCE are required for determining the uncertainties in the LHV of the mixture, CE and the IE. Considering that all the flows to the system are controlled through the MFCs and the pump, a similar formulation as done for the uncertainties in Chapter 4 can be carried out. It must be noted here that the uncertainty calculations in this case not make any distinction between EGR and fresh components as the quantities $\text{LHV}_{FIN+EGR}$, CE and IE and independent of these values.